KATHOLIEKE UNIVERSITEIT LEUVEN
FACULTEIT TOEGEPASTE WETENSCHAPPEN
DEPARTEMENT ELEKTROTECHNIEK (ESAT)
AFDELING PSI
Kasteelpark Arenberg 10, B-3001 Leuven-Heverlee (Belgium)

FACULTEIT GENEESKUNDE
DEPARTEMENT MORFOLOGIE EN MEDISCHE BEELDVORMING, AFDELING NUCLEAIRE GENEESKUNDE
Herestraat 49, B-3000 Leuven (Belgium)

MICROSPECT IMAGING OF SMALL LABORATORY ANIMALS

Promotoren:
Prof. dr. ir. J. Nuyts
Prof. dr. ir. P. Suetens

Proefschrift voorgedragen tot
het behalen van het doctoraat
in de toegepaste wetenschappen

door

Dirk BEQUE

januari 2005

KATHOLIEKE UNIVERSITEIT LEUVEN
FACULTEIT TOEGEPASTE WETENSCHAPPEN
DEPARTEMENT ELEKTROTECHNIEK (ESAT)
AFDELING PSI
Kasteelpark Arenberg 10, B-3001 Leuven-Heverlee (Belgium)

FACULTEIT GENEESKUNDE
DEPARTEMENT MORFOLOGIE EN MEDISCHE BEELD-
VORMING, AFDELING NUCLEAIRE GENEESKUNDE
Herestraat 49, B-3000 Leuven (Belgium)

MicroSPECT Imaging of Small Laboratory Animals

Leden van de jury:
Prof. dr. ir. H. Neuckermans (voorzitter)
Prof. dr. ir. J. Nuyts (promotor)
Prof. dr. ir. P. Suetens (promotor)
Prof. dr. sc. P. Dupont (assessor)
Prof. dr. ir. D. Vandermeulen (assessor)
Prof. dr. sc. M. Defrise
(Vrije Universiteit Brussel)
Prof. dr. sc. I. Lemahieu
(Vrije Universiteit Gent)

Proefschrift voorgedragen tot
het behalen van het doctoraat
in de toegepaste wetenschappen

door

Dirk BEQUE

U.D.C. 681.3*14:59.084

januari 2005

ISBN 90-5682-581-X
D/2005/7515/15

Acknowledgements

In 1999, I put my first steps in the world of medical imaging as a student in medical radiation physics. Soon I got closer involved with research on nuclear medicine imaging and I was given the opportunity to go further along that road. This eventually resulted in this work. Along the way, I have got in touch with many other people and a word of thanks to them is here in place.

First of all, I would like to thank all the *members of the jury*, for the interest they have shown in my work and for their flexibility in determining the date of my Ph.D. defense.

In particular, I would like to thank my promoters *Prof. Paul Suetens* and *Prof. Johan Nuyts* for giving me the chance to do research as a Ph.D. student in the field of nuclear medicine imaging. Showing great confidence in me, they have always inspired and supported me to go my own way in research. Nevertheless they were there for guidance and advice when I needed so. I am further grateful to Johan Nuyts for the many practical programming tips he gave me, the various phantoms he managed to produce at his home and for our weekly snooker sessions.

I also thank my assessors *Prof. Patrick Dupont* and *Prof. Dirk Vandermeulen*. Patrick Dupont has often been closely involved in my research in various ways. I also found great pleasure in solving with him and Kristof Baete the "other great problems of the world"during lunch time. Dirk Vandermeulen was further a regular attendee of the seminars I gave, and his questions and remarks were of great value to me and my work.

I further thank *Prof. Mortelmans*, Head of the Department of Nuclear Medicine, and Chief Technologist *Ludo Verhaegen* for welcoming me at their department as a researcher. Despite the constant changes at the department, they made sure that I always had a place to work. They further trusted me in using the camera systems of the department, which allowed me to perform the various experiments that contributed to this work.

In relation to those experiments, I would also like to thank *Prof. Guy Bormans* and *Bert Vanbillioen, Ph.D.* of Radiopharmacy. They have been helpful numerous times with the creation and preparation of phantoms and by providing the tracers for the laboratory animal experiments. I also thank *Prof. Koen Van Laere* and *Peter Vermaelen*, research technologist, for the nice cooporation in planning and conducting those animal experiments.

I owe many thanks to *Kristof Baete*, who started his PhD research at the department at approximately the same time I did. I enjoyed our many lively discussions, both those about our research as those about the other important things in life. I am also grateful to him and to *Engineer Stefaan Vleugels* for solving the various computer related and other practical problems that I encountered from time to time.

I am also very grateful too to *Prof. Michel Defrise* (member of the jury), *Chris Vanhove, Ph.D.* and *Andriy Andreyev* of the Vrije Universiteit Brussel. Our common interest in pinhole imaging goes back a long time and has resulted in a firm collaboration. I have enjoyed the many meetings and discussions we have had and I am grateful for the experiments conducted at the nuclear medicine department of your university.

Special thanks goes to *Nuclear Fields International BV* (The Netherlands) in general and to *Pieter-Jan van Mullekom* and *Pieter van Mullekom* in particular, for their help in the realization of a prototype multipinhole collimator. I further thank *Siemens Medical Solutions* (Belgium) and *Ronnie (Ronald) Lubon* in particular for the actual installation of this prototype collimator on our camera system.

I want to express my appreciation for the work of *Francine Reniers*, *Kim De Wolf* and *Annitta De Messemaeker*, who have been indispensable at many occasions. I also would like to thank all my direct colleagues, friends and family for your support, suggestions, discussions, for joining me on my coffee break, ...

For their financial support, I thank the Katholieke Universiteit Leuven (grant OT-00/32 and grant IDO/02/012), the Flemish Fund for Scientific Research (F.W.O., grant G.0174.03) and the Institute for the Promotion of Innovation by Science and Technology in Flanders (I.W.T., grant SBO-ANIMONE).

Mijn laatste woorden van dank gaan naar mijn familie. In de eerste plaats wil ik mijn ouders bedanken voor de aandacht die ze altijd besteed hebben aan goed onderwijs voor mijn broers en mijzelf, voor de kansen die ze ons daardoor gegeven hebben en voor hun onvoorwaardelijke steun bij onze studiekeuzes. Dit doctoraat heb ik voor een groot deel aan jullie te danken en ik kan jullie daar onmogelijk genoeg voor BEdanken. Ook wil ik mijn beide broers, Luk en Rik bedanken. Ontspanning is al even belangrijk als inspanning, en laat jullie nu juist ook in dat eerste bijzonder bedreven zijn. Bedankt!

Abstracts

MicroSPECT Imaging of Small Laboratory Animals

Pinhole and also multipinhole SPECT imaging have gained increasing attention in recent years for low cost high resolution emission tomography imaging of small laboratory animals. This work develops both the underlying theory and a practical methodology to calibrate the pinhole sensitivity and the pinhole acquisition geometry and it incorporates these results in the image reconstruction algorithm for optimal reconstruction accuracy. For single pinhole imaging, the methodology yields excellent results and it has successfully been applied in practice. The geometrical calibration was further successfully extended to multipinhole situations. This work also addresses the potential benefit of multipinhole SPECT over single pinhole imaging. The first results indicate that multipinhole imaging yields a superior and more uniform accuracy of image reconstruction in comparison to single pinhole imaging.

MicroSPECT Beeldvorming van Kleine Proefdieren

In de voorbije jaren hebben pinhole en ook multipinhole SPECT een steeds grotere aandacht gekregen voor de emissie tomografische beeldvorming van kleine proefdieren tegen een lage kostprijs. Dit werk ontwikkelt zowel de onderliggende theorie als een praktische methodologie voor de calibratie van de pinhole sensitiviteit en de pinhole acquisitiegeometrie en het brengt deze resultaten in rekening in de beeldreconstructie om een optimale beeldkwaliteit te bekomen. De voorgestelde methodologie levert zeer goede resultaten op voor pinhole beeldvorming en is reeds met succes toegepast in de praktijk. De geometrische calibratie werd ook met succes uitgebreid naar multipinhole situaties. Dit werk onderzoekt verder ook de potentiële voordelen van multipinhole beeldvorming in vergelijking met de traditionele pinhole SPECT beeldvorming. De eerste resultaten wijzen uit dat multipinhole SPECT leidt tot een superieure en meer uniforme kwaliteit van de gereconstrueerde beelden in vergelijking met pinhole SPECT.

MicroSPECT Beeldvorming van Kleine Proefdieren

Inleiding

Nucleaire Geneeskunde

Nucleaire geneeskunde is een hoofdzakelijk diagnostische discipline van de geneeskunde met als doel het in beeld brengen van het metabolisme en andere functionele processen in het menselijk lichaam. Hiervoor krijgen patiënten een radioactief gelabelde tracer toegediend en wordt de verdeling daarvan in het menselijk lichaam in beeld gebracht. Drie verschillende modaliteiten staan hiervoor ter beschikking: de planaire scintigrafie, SPECT (single photon emission computed tomography) en PET (positron emissie-tomografie). Planaire scintigrafie is de meest eenvoudige techniek en levert een 2-dimensioneel projectiebeeld van de activiteitsverdeling in het menselijk lichaam. De tomografische technieken SPECT en PET leveren daarentegen 3-dimensionale beelden van deze activiteitsverdeling en stellen de artsen in staat om de activiteitsverdeling in dwarse sneden van het menselijk lichaam te bekijken. SPECT is de oudste, maar over het algemeen ook de goedkoopste modaliteit, zowel wat de kost van de tracer betreft als ook de kost van de benodigde apparatuur (de gamma- of SPECT camera). PET is een meer recente techniek, die slechts gedurende het laatste decennium zijn intrede heeft gedaan in de klinische praktijk. Hoewel het voordelen biedt in vergelijking met SPECT omwille van de betere sensitiviteit en de tracers die voor de beeldvorming kunnen worden aangewend, is het doorgaans ook aanzienlijk duurder dan SPECT.

Beeldvorming van Proefdieren

SPECT en PET dragen niet alleen bij tot de klinische diagnostiek, het zijn ook waardevolle instrumenten in het fundamenteel onderzoek van humane aandoeningen en voor het testen van nieuwe geneesmiddelen. Het merendeel van dergelijk onderzoek wordt echter uitgevoerd op proefdieren en bij voorkeur op kleine proefdieren zoals muizen en ratten. Naast SPECT en PET bestaan er ook andere manieren om

proefdieren te onderzoeken, zoals autoradiografie, maar deze technieken zijn meestal invasief en vereisen zelfs vaak het opofferen van de proefdieren. Dit maakt het bijzonder moeilijk om de dieren gedurende langere tijd op te volgen en vaak zijn daardoor meer proefdieren vereist om eenzelfde graad van statistische significantie te bereiken in de resultaten van het onderzoek.

De toepassing van SPECT en PET op kleine proefdieren wordt echter gehinderd door de beperkte spatiale resolutie van deze technieken, en verder is de sensitiviteit bij dergelijke toepassingen ook suboptimaal. Om deze problemen te verhelpen, zijn in de afgelopen jaren speciale varianten van SPECT en PET ontwikkeld, respectievelijk microSPECT en microPET genaamd. Het algemene principe achter microSPECT, is het overschakelen van parallel hole naar pinhole collimatie, waardoor een automatische vergroting van de projectiebeelden wordt bekomen. Dit principe wordt verder soms gecombineerd met een verkleining van het volledige systeem en het gebruik van detectoren met een betere spatiale resolutie. Zeer recent werd ten slotte multipinhole collimatie voorgesteld om ook de sensitiviteit verder op te drijven. MicroPET systemen zijn daarentegen altijd een neergeschaalde versie van de traditionele PET systemen. Net zoals bij hun klassieke varianten, biedt microPET een betere sensitiviteit dan microSPECT, maar is microPET doorgaans ook aanzienlijk duurder. Ten slotte dient vermeld te worden, dat de spatiale resolutie van microPET gelimiteerd is tot de positron range van de gebruikte isotopen, terwijl de spatiale resolutie van microSPECT, tenminste in theorie, ongelimiteerd is.

Doel van dit Werk

Het doel van dit werk is een fundamentele studie van de problemen die specifiek bij pinhole en multipinhole SPECT beeldvorming optreden. Specifieke aandachtspunten in dit werk zijn de bemonsterstrategie en de sensitiviteitscorrectie bij pinhole SPECT reconstructie (hoofdstuk 3), de geometrische calibratie van pinhole SPECT camera's (hoofdstuk 4, 5 en 7) en een preliminaire studie van de verschillen tussen pinhole en multipinhole beeldvorming (hoofdstuk 6). Uiteindelijk moet dit resulteren in de praktische realisatie van performante pinhole en multipinhole beeldvorming met een traditionele SPECT camera (hoofdstuk 8 geeft hiervan een voorbeeld).

Pinhole SPECT Beeldvorming

MicroSPECT heeft tot doel om metabole en functionele processen te bestuderen in kleine proefdieren. Deze proefdieren krijgen daartoe een welbepaalde radioactieve stof toegediend die zich door interactie met de bovenvermelde processen op een specifieke manier zal verdelen over het lichaam van het proefdier. Omwille van het radioactief verval van de toegediende stof zendt deze gammastraling uit, waarbij de intensiteit van de uitgezonden straling evenredig is met de concentratie van de radioactieve stof. De uitgezonden straling wordt vervolgens opgemeten met een

pinhole camera om later de 3-dimensionele activiteitsverdeling in het lichaam van het proefdier te kunnen reconstrueren.

De pinhole camera bestaat uit een vlakke scintillatiedetector voor gammafotonen uitgerust met een pinhole collimator. De collimator fungeert als lens voor het systeem en bestaat uit een afscherming van de detector voor de invallende straling met één enkele opening, de focus of het focale punt. Dit focale punt bevindt zich dichter bij het proefdier dan bij de detector en enkel de fotonen uitgezonden doorheen dit focale punt kunnen de detector bereiken. Hierdoor registreert de detector een uitvergrote spiegelprojectie van de oorspronkelijke activiteitsverdeling in het proefdier. Door de camera rond het proefdier te roteren en onder verschillende hoeken projecties van het proefdier te verzamelen, ontstaat ten slotte een 3-dimensionele dataset die toelaat om de activiteitsverdeling in het proefdier bij benadering te reconstrueren. De reconstructie is enkel benaderend, omdat zelfs de bovenvermelde rotatie onvoldoende informatie oplevert voor een exacte reconstructie. Andere, meer complexe, acquisitiemethodes zijn mogelijk die wel voldoende informatie opleveren voor een exacte reconstructie, maar in de praktijk is de bovenstaande rotatie rond het proefdier verreweg de meest gebruikte acquisitiemethode. In dit werk beperken wij ons daarom tot de bovenstaande rotatie-acquisitie.

Multipinhole collimatie is een recente ontwikkeling in microSPECT. Het is een variant van pinhole collimatie, waarbij meerdere focale punten beschikbaar zijn voor de beeldvorming. Als gevolg daarvan registreert de detector gelijktijdig verschillende projecties van dezelfde activiteitsverdeling. De belangrijkste motivatie voor multipinhole collimatie is een potentieel verhoogde sensitiviteit voor de activiteitsverdeling in het proefdier, aangezien de uitgezonden fotonen hierbij door meerdere focale punten in beeld worden gebracht. Het grotere aantal focale punten kan verder ook een verbeterde bemonstering van de activiteitsverdeling opleveren, die beter tegemoet komt aan de voorwaarden voor een exacte beeldreconstructie. De verschillende projectiebeelden kunnen elkaar echter ook ten dele overlappen, waardoor de informatie-inhoud in de bekomen projecties daalt. Om al te veel overlap te vermijden, kunnen pinhole openingen met kleinere openingshoeken worden aangewend en op een grotere afstand van het proefdier. Dit gaat echter ten koste van de sensitiviteit en de bemonstering. Bijgevolg is het op dit moment nog onduidelijk of en in welke mate multipinhole SPECT superieur is aan traditionele pinhole SPECT.

Zoals vermeld, leveren zowel pinhole als multipinhole SPECT beeldvorming een set van 2-dimensionele projectiebeelden op van de activiteitsverdeling in het beschouwde proefdier. Het betreft hier een niet-orthogonale projectie die gewogen is met de niet-uniforme sensitiviteit eigen aan pinhole en multipinhole beeldvorming (zie verder). Voor de reconstructie van de 3-dimensionele activiteitsverdeling op basis van deze projectiebeelden, maken we in dit werk gebruik van de MLEM (maximum likelihood expectation maximization) reconstructiemethode [18–20]. Dit is een iteratieve reconstructiemethode die algemeen toepasbaar is in emissietomografie en die intrinsiek rekening houdt met de Poisson ruiskenmerken van emissietomografische metingen. De methode vertrekt van een initiële schatting λ_j^{oud} van de gemeten activiteitsverdeling en biedt een eenvoudig algoritme om op basis van

een vorige schatting λ_j^{oud} een verbeterde reconstructie λ_j^{nieuw} te bekomen

$$\lambda_j^{nieuw} = \frac{\lambda_j^{oud}}{\sum_i c_{ij}} \sum_i c_{ij} \frac{q_i}{\sum_k c_{ik} \lambda_k^{oud}} \quad \forall j = 1, ..., J. \tag{1}$$

In dit algoritme wordt de oude reconstructie λ_j^{oud} eerst geprojecteerd ($\sum_k c_{ik} \lambda_k^{oud}$) en vervolgens vergeleken met de gemeten projectiedata q_i door een deling van deze data met de bovenstaande projectie. Het resultaat van deze deling wordt daarna weer teruggeprojecteerd naar de reconstructieruimte en vermenigvuldigd met de oude reconstructie λ_j^{oud}. Na normalisatie door de deling door $\sum_i c_{ij}$ levert dit uiteindelijk de verbeterde reconstructie λ_j^{nieuw}. Het stelselmatig herhalen van deze procedure, met de substitutie van λ_j^{oud} door λ_j^{nieuw}, leidt tot steeds betere schattingen van de eigenlijke activiteitsverdeling in het proefdier en convergeert naar die reconstructie waarvan de projecties het best overeenkomen met de gemeten projectiedata q_i.

De kwaliteit van de reconstructie staat of valt met een correcte modellering van de coëfficiënten c_{ij} in de bovenstaande uitdrukking. Deze coëfficiënten modelleren de projectie van de activiteitsverdeling in het proefdier door de pinhole of multipinhole camera en brengen zowel de sensitiviteit als de geometrie van deze systemen in rekening. Aangezien zowel de gemeten projectiedata als de reconstructie enkel in digitale vorm beschikbaar zijn, speelt verder ook de bemonstering van de projectiedata en het reconstructiebeeld een belangrijke rol in het bepalen van de coëfficiënten c_{ij}. Een belangrijk deel van dit werk bestaat uit het bepalen van deze coëfficiënten.

Bemonstering & Sensitiviteitscorrectie

Twee verschillende manieren van bemonstering worden doorgaans gebruikt in de reconstructie van emissietomografische beelden: de voxel gebaseerde en de projectiestraal gebaseerde projectie. De voxel gebaseerde projectiemethode levert automatisch een uniforme bemonstering op van het reconstructiebeeld en vereist bijgevolg de modellering van de ware 3-dimensionele pinhole sensitiviteit in de reconstructie. Deze 3D sensitiviteit kan opgesplitst worden in een afstands- en een hoekafhankelijk deel. De correctie voor het afstandsafhankelijke deel kan enkel uitgevoerd worden in het 3D reconstructiebeeld, terwijl de correctie voor de hoekafhankelijke sensitiviteit ook kan worden uitgevoerd in de 2D projectiebeelden. De projectiestraal gebaseerde projectie leidt tot een niet-uniforme bemonstering van het reconstructiebeeld bij pinhole en multipinhole SPECT en vereist naast de sensitiviteitscorrectie bijgevolg nog een bijkomende correctie. Deze bijkomende correctie is echter de inverse van de afstandsafhankelijke sensitiviteitscorrectie, waardoor beide elkaar opheffen [23, 28]. Bijgevolg biedt de projectiestraal gebaseerde projectie het voordeel dat enkel voor de hoekafhankelijke pinhole sensitiviteit moet worden gecorrigeerd. Deze correctie kan verder uitgevoerd worden in de 2D projectiebeelden, wat aanzienlijk minder computergeheugen en/of rekentijd vereist. Dit vereenvoudigt de correctie voor de plaatsafhankelijke pinhole sensitiviteit aanzienlijk en is ook de methode waarvoor in dit werk wordt geopteerd.

Teneinde deze hoekafhankelijke sensitiviteit in de reconstructie te modelleren werd een beroep gedaan op een bestaand analytisch model van de 3D pinhole sensitiviteit [14] waaruit de hoekafhankelijke sensitiviteit kan worden afgeleid. Het model bevat echter een aantal parameters waarvan de waarde enkel via metingen kan worden bepaald. Hoewel het mogelijk is om deze parameters te bepalen uit de metingen van een puntbron op verschillende posities in het gezichtsveld van de camera [14], is het moeilijk om deze methode in de praktijk nauwkeurig uit te voeren zonder bijkomende gespecialiseerde instrumenten. Als alternatief hebben we echter afgeleid dat de benodigde parameters van de hoekafhankelijke pinhole sensitiviteit eveneens kunnen bekomen worden uit een veel eenvoudiger experiment met een uniforme vlakke bron. Een dergelijke bron is normaal gezien op elke dienst nucleaire geneeskunde beschikbaar of kan ook eenvoudig bekomen worden als een horizontale laag van een radioactieve vloeistof. Mits een kleine correctie kan de meting ook zelf gebruikt worden voor de sensitiviteitscorrectie, maar dit heeft het nadeel dat de Poisson ruis in de meting dan kan propageren naar het uiteindelijke reconstructiebeeld, waardoor dit een minder aantrekkelijke methode is.

Onze ervaring leert dat de bovenstaande methode zeer goed toepasbaar is voor traditionele pinhole toepassingen, waarbij de pinhole opening een relatief grote openingshoek heeft. Voor dergelijke toepassingen is deze methode reeds herhaaldelijk met succes toegepast. Voor multipinhole toepassingen, waarbij de pinhole openingen doorgaans een kleinere openingshoek hebben en een complexere geometrie, blijkt het gebruikte analytische sensitiviteitsmodel echter ontoereikend. Het blijkt noodzakelijk om de geometrie van deze pinhole openingen nauwgezet te modelleren. Een verbeterd analytisch model voor dergelijke multipinhole toepassingen werd ontwikkeld, maar verder onderzoek is nodig om een goede overeenkomst met de metingen te bereiken. Zoniet moet de meting zelf voor de sensitiviteitscorrectie worden gebruikt, met het bovenvermelde nadeel van de propagatie van ruis naar de gereconstrueerde beelden. De niet-analytische 'ray-tracing' techniek van Schramm *et al.* [2] biedt ten slotte een tweede alternatief om de multipinhole sensitiviteit te modelleren. Het analytische multipinhole sensitiviteitsmodel wordt wel reeds als voldoende nauwkeurig beschouwd voor de vergelijkende studie tussen pinhole en multipinhole beeldvorming, verderop in dit werk.

Geometrische Calibratie van Pinhole SPECT

Naast de bemonstering en sensitiviteit, modelleren de coëfficiënten c_{ij} uit (1) tevens de geometrie van de pinhole of multipinhole projectie. Voor een goede reconstructie, is het hierbij belangrijk dat de ware acquisitiegeometrie van de pinhole camera wordt gemodelleerd, zoniet kunnen een verlies aan spatiale resolutie en vervormingen van de gereconstrueerde beelden optreden [31]. De behoefte aan een nauwkeurige beschrijving van de ware acquisitiegeometrie tijdens de beeldreconstructie, beperkt zich niet tot pinhole en multipinhole SPECT, maar is terug te vinden bij alle tomografische systemen. De meeste tomografische systemen zijn echter specifiek ontworpen voor een welbepaalde beeldvormingsopdracht. Daardoor is hun ware acquisitiegeometrie vanzelf met voldoende nauwkeurigheid gekend en is geen verdere

calibratie vereist. Pinhole en multipinhole SPECT worden echter vaak uitgevoerd met traditionele SPECT camera's ontworpen voor parallel hole SPECT beeldvorming van het menselijk lichaam. Omwille van de intrinsieke beeldvergroting stellen pinhole en multipinhole beeldvorming zwaardere eisen aan het beeldvormingssysteem dan parallel hole beeldvorming en het is bijgevolg niet gegarandeerd dat deze traditionele SPECT camera's aan deze zwaardere eisen voldoen. Bijgevolg dient voor pinhole en multipinhole SPECT een calibratie van de acquisitiegeometrie van het systeem te worden uitgevoerd om die geometrie met voldoende nauwkeurigheid te kunnen bepalen. Op basis van een theoretische studie ontwikkelt deze sectie een praktische methodologie om de bovenstaande calibratie uit voeren aan de hand van een eenvoudige meting. De beoogde methodologie bestaat erin om onmiddellijk na de acquisitie van het proefdier een mogelijk kortere, maar verder identieke acquisitie van een calibratiefantoom uit te voeren. Deze bijkomende acquisitie moet het mogelijk maken om de acquisitiegeometrie van het pinhole systeem te bepalen. Die informatie kan dan worden gebruikt voor de reconstructie van de activiteitsverdeling in het proefdier.

Voor een traditionele pinhole camera met een vlakke detector die een circulaire beweging beschrijft rond het in beeld te brengen proefdier, kan de acquisitie geometrie volledig worden beschreven met 7 parameters [31]. Figuur 1 illustreert de geometrie van een dergelijke pinhole camera en de definitie van de bovenstaande 7 parameters. De focale lengte f en de elektrische shifts e_u en e_v vormen de intrinsieke pinhole parameters. Hun waarde is onafhankelijk van de positie van de detector ten opzichte van de as van rotatie. De focale lengte is de afstand tussen het focale punt van de collimator en het detectoroppervlak en de elektrische shifts beschrijven een collectieve translatie van de projectiebeelden, veroorzaakt door drift van de elektrische componenten van de detector. De extrinsieke parameters d, m, Φ and Ψ beschrijven verder de relatieve positie van de detector-collimator combinatie ten opzichte van de as van rotatie. Ze kunnen beschreven worden aan de hand van de centrale projectiestraal: de pinhole projectiestraal die loodrecht op het detectoroppervlak staat. De mechanische offset m is de afstand tussen deze centrale projectiestraal en de as van rotatie. De detectorafstand d is de afstand van de detector tot de rotatie-as langs de centrale projectiestraal als $m = 0$. Deze afstand bepaalt de straal waarop de detector rond de as van rotatie draait tijdens de acquisitie. De tilt Φ is de hoek tussen het oppervlak van de detector en de as van rotatie, of ook het complement van de hoek tussen de centrale projectiestraal en de rotatie-as. De twist Ψ beschrijft uiteindelijk de oriëntatie van de detector pixels ten opzichte van de rotatie-as. De hoek θ geeft de rotatie van de pinhole camera weer tijdens de acquisitie. In multipinhole toepassingen zijn verder 3 bijkomende parameters per bijkomende pinhole opening vereist. Met uitzondering van de projectiehoek θ, worden alle bovenstaande parameters constant verondersteld tijdens de beeldvorming.

In de literatuur zijn reeds verschillende methodes beschreven om de ware acquisitiegeometrie van een traditionele pinhole camera te bepalen [30–36]. De meeste methodes laten echter slechts toe om een subset van de 7 bovenvermelde parameters te schatten [31–34, 36]. Andere methodes [30, 35] vereisen dan weer verschillende

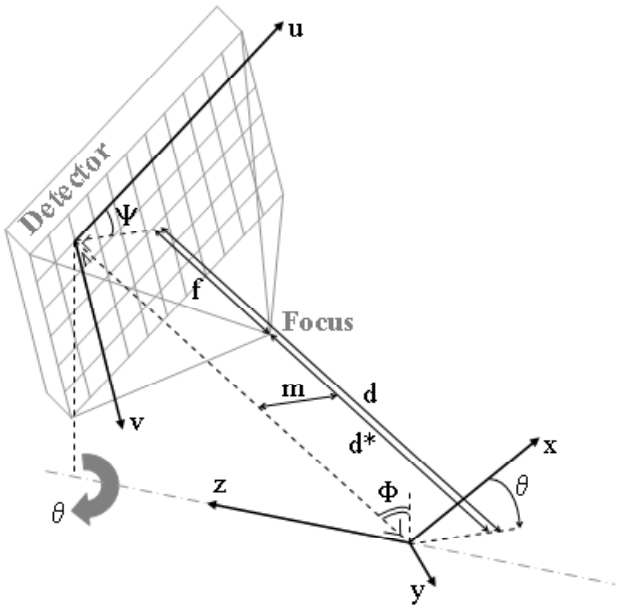

Figuur 1: Pinhole camera met focale lengte f en op projectiehoek θ. De z-as is de rotatieas van het systeem en de xyz-oorsprong is zodanig gekozen dat de centrale projectiestraal van het systeem de x-as snijdt bij $\theta = 0$. De focale lengte f en de detectorafstand d zijn aangeduid langsheen de centrale projectiestraal. De mechanische offset m is de afstand tussen de xyz-oorsprong en de centrale projectiestraal. De tilthoek Φ is het complement van de hoek tussen de centrale projectiestraal en de rotatieas. De twisthoek Ψ is tenslotte de hoek tussen de rijen van detectorpixels (u-as) en de orthogonale projectie van de x-as op de detector bij $\theta = 0$.

calibratiemetingen met ingewikkelde calibratiefantomen. In dit werk stellen wij een nieuwe calibratiemethode voor, die toelaat om de volledige pinhole of multipinhole acquisitiegeometrie te bepalen uit 1 enkele calibratiemeting met een eenvoudig fantoom bestaande uit 3 stationaire puntbronnen in het gezichtsveld van de camera. De methode is geïnspireerd op reeds bestaande methodes die een deel van de acquisitiegeometrie bepalen op basis van de SPECT acquisitie van 1 [32–34] of 2 [31] puntbronnen.

Allereerst werd een theorie ontwikkeld die toelaat om te bepalen hoeveel puntbronnen noodzakelijk zijn voor een bepaalde calibratiemethode en of er bijkomende voorwaarden aan de posities van de puntbronnen dienen te worden gesteld. De methode is zowel in pinhole als in multipinhole situaties toepasbaar en is verder in principe ook uitbreidbaar naar meer ingewikkelde acquisitiegeometrieën (zoals geïllustreerd in hoofdstuk 7). Voor de volledige calibratie van een traditionele pinhole camera toont de theorie aan dat 3 puntbronnen noodzakelijk zijn en dat er verder een beperkt aantal restricties bestaan betreffende de positie van deze bron-

nen. De theorie geeft verder ook aan dat ten minste 2 van de afstanden tussen de puntbronnen gekend moeten zijn en als een restrictie opgenomen dienen te worden in de calibratieberekeningen. In de praktijk worden alle 3 de afstanden tussen de puntbronnen gebruikt. De vereisten voor de traditionele pinhole calibratie blijken ten slotte ook voldoende voor de calibratie van de multipinhole situatie beschouwd in dit werk. Of deze voorwaarden ook noodzakelijk zijn in die multipinhole situatie werd niet onderzocht.

In de voorgestelde calibratiemethode worden eerst de projectielocaties van de 3 calibratiebronnen berekend voor elke projectiehoek θ als de massacentra van de intensiteit van hun projecties. Deze projectielocaties kunnen eveneens analytisch berekend worden uitgaande van een schatting van de 7 parameters f, d, m, e_u, e_v, Φ en Ψ (plus 3 bijkomende parameters per bijkomende pinhole opening in multipinhole situaties) en van de posities van de puntbronnen in het gezichtsveld van de camera. Dit laat toe om de waarden van de 7 pinhole parameters te bepalen door de analytisch berekende projectielocaties te fitten aan de gemeten locaties. Hierbij wordt niet alleen de waarde van de 7 acquisitie parameters bepaald, maar tevens de posities van de puntbronnen. Hoewel de posities van de calibratiepuntbronnen niet relevant zijn voor de reconstructie van pinhole SPECT beelden, levert deze aanpak toch voordelen op. De kennis van deze posities is immers noodzakelijk om de 7 acquisitieparameters te kunnen bepalen. Het fitten van de puntbronposities vermijdt dat deze via een bijkomende meting bepaald dienen te worden of dat de bronnen zeer nauwkeurig op vooraf bepaalde posities in het gezichtsveld van de camera moeten worden bevestigd. Beide alternatieven zouden het toepassen van de calibratiemethode in de praktijk immers aanzienlijk bemoeilijken. Merk hierbij op dat de afstanden tussen (ten minste 2 van) de puntbronnen wel steeds nauwkeurig gekend moeten zijn. Dit wordt bekomen door de drie puntbronnen op een plaat te fixeren.

Goede resultaten werden bekomen met de voorgestelde calibratiemethode, zowel in pinhole als multipinhole situaties en zowel voor simulaties als met werkelijke calibratiemetingen. Uit de simulaties blijkt verder dat sommige acquisitieparameters sterk met elkaar zijn gecorreleerd, waardoor hun exacte waarde moeilijk te bepalen is. Met uitzondering van de correlatie tussen de elektrische shift e_v en de tilt ϕ blijkt dit echter maar weinig effect te hebben op de kwaliteit van de reconstructie, zoals experimenteel werd aangetoond.

Optimalisatie van Pinhole SPECT Calibratie

Bij de toepassing van de bovenstaande calibratiemethode in de praktijk kunnen de projectielocaties van de puntbronnen slechts met een beperkte nauwkeurigheid worden berekend als gevolg van de Poisson ruis in de projectiebeelden. Deze bron van onnauwkeurigheden wordt in deze sectie verder aangeduid als dataruis. Verder vereist de methode ook de kennis van de afstanden tussen de 3 puntbronnen en ook deze zijn slechts met een beperkte nauwkeurigheid gekend. Deze onnauwkeurigheden omschrijven we verder als modelfouten, aangezien deze afstanden de vorm

van het calibratiefantoom bepalen. Tijdens de calibratie propageren deze fouten doorheen het algoritme naar de resultaten van de calibratie. De resulterende fouten op de acquisitiegeometrie zullen vervolgens verder propageren in de reconstructie en aanleiding geven tot een verlies aan spatiale resolutie en/of vervormingen van het reconstructiebeeld. De posities van de 3 puntbronnen in het gezichtsveld van de camera, beïnvloeden de mate waarin de dataruis en modelfouten aanleiding geven tot een verminderde nauwkeurigheid van de calibratie en beïnvloeden dus ook indirect de nauwkeurigheid van de pinhole reconstructie. Het doel van deze sectie is om de optimale posities van de drie puntbronnen te bepalen voor een zo nauwkeurig mogelijke reconstructie van pinhole SPECT beelden, ondanks dataruis en modelfouten.

Aangezien de bovenstaande calibratiemethode voorlopig de enige is die werkt op basis van drie puntbronnen, biedt de literatuur slechts weinig informatie over de optimale positie van de puntbronnen. Wang *et al.* [34] ontwikkelde een calibratiemethode op basis van 1 puntbron en zij vermelden dat de nauwkeurigheid van de resultaten van de calibratie verbetert naarmate die puntbron zich op een grotere afstand van de as van rotatie bevindt. Noo *et al.* [31] gebruiken twee puntbronnen voor calibratie en vermelden verder dat deze op een voldoende grote afstand van elkaar dienen te worden geplaatst en buiten het rotatievlak van het focale punt van de collimator. Een systematische studie van de invloed van de positie van een of meerdere calibratiepuntbronnen op de nauwkeurigheid van de reconstructie wordt voor zover wij weten echter nergens in de literatuur beschreven.

Eerst en vooral dient de invloed van de dataruis en modelfouten op de nauwkeurigheid van de calibratieresultaten te worden bepaald in functie van de posities van de puntbronnen. Zowel de dataruis als de modelfouten worden hiervoor gemodelleerd als ongecorreleerde Gaussiaanse ruis en de resulterende covariantiematrix wordt vervolgens doorheen een lineair systeem gepropageerd. Dit lineaire systeem modelleert bij benadering de werking van de calibratiemethode en brengt daarbij ook de posities van de puntbronnen in rekening. Dit leidt tot een covariantiematrix van de onzekerheden op de parameters van de pinhole acquisitiegeometrie, die in tegenstelling tot de invoer van het lineaire systeem niet langer ongecorreleerd is. Deze covariantiematrix wordt vervolgens ontbonden in een representatieve set van concrete fouten op de schatting van de verschillende acquisitieparameters die de input vormen van een tweede model dat de invloed hiervan op de reconstructie modelleert. Het model evalueert zowel het maximale verlies aan spatiale resolutie in het reconstructiebeeld als de maximale vervorming ervan, zonder daarbij kleine translaties of rotaties van dat beeld als een vervorming te beschouwen. De combinatie van de bovenstaande modellen vormt een snelle en efficiënte methode om het effect van dataruis en modelfouten op de reconstructie te evalueren.

Teneinde de invloed van de posities van de calibratiebronnen te bestuderen, wordt de bovenstaande evaluatiemethode toegepast op een set van vele tienduizenden realisaties van mogelijke posities van de 3 puntbronnen. Deze set wordt als representatief beschouwd voor het oneindige aantal realisaties dat in de praktijk met 3 puntbronnen kan worden bekomen. De resultaten van deze studie geven aan dat geen enkele realisatie gelijktijdig de nauwkeurigheid van zowel de reconstructie

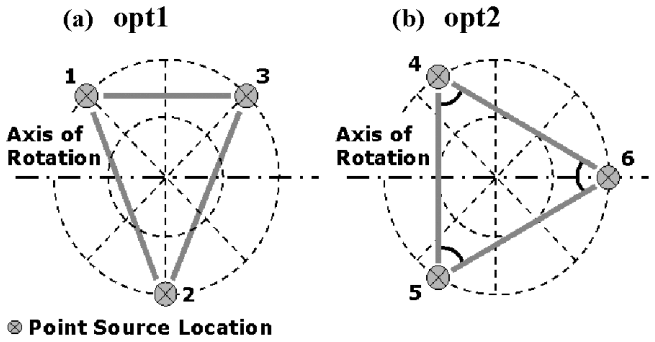

Figuur 2: Optimale posities van de calibratiepuntbronnen voor dataruis (a) en modelfouten (b). De grootste cirkel in stippellijn geeft de grens van het gezichtsveld van de pinhole camera weer.

als van de 7 acquisitieparameters optimaliseert, noch voor dataruis en noch voor modelfouten. Wel bestaat er een set van realisaties die in beide gevallen een quasi-optimale nauwkeurigheid van de reconstructie garanderen die zodanig hoog is dat het overblijvende verlies aan spatiale resolutie en de overblijvende vervormingen van het reconstructiebeeld ver onder de limiet van de haalbare spatiale resolutie blijven. Uit deze set van realisaties werden uiteindelijk de twee realisaties 'opt1' en 'opt2' van figuur 2 geselecteerd omwille van hun bijkomende optimale kenmerken betreffende de nauwkeurigheid van de 7 acquisitieparameters respectievelijk in het geval van dataruis en modelfouten. De realisatie 'opt1' geniet hierbij onze persoonlijke voorkeur omdat ruis in de calibratiedata naar onze mening moeilijker te vermijden is dan fouten op de afstanden tussen de puntbronnen van het calibratiefantoom. Bovendien wijst een verdere analyse van de resultaten uit dat modelfouten een vervorming in het reconstructiebeeld veroorzaken van dezelfde grootteorde, zodat de nauwkeurigheid waarmee de afstanden tussen de puntbronnen gekend dienen te zijn op voorhand kan worden bepaald.

Vergelijking tussen Pinhole en Multipinhole Beeldvorming

Zoals hoger reeds vermeld, is het op dit moment nog onduidelijk in welke mate en onder welke voorwaarden multipinhole SPECT superieur is aan traditionele pinhole SPECT met 1 enkel focaal punt. Multipinhole SPECT biedt mogelijk voordelen op het gebied van sensitiviteit en bemonstering omwille van het grotere aantal focale punten, maar geeft ook aanleiding tot overlappende projectiebeelden waardoor de informatie-inhoud van de bekomen projectiebeelden daalt. Deze overlap kan vermeden worden door het gebruik van pinhole openingen met kleinere openingshoeken op een grotere afstand van de in beeld te brengen activiteitsverdeling, maar in dat geval

nemen de ogenschijnlijke voordelen op het gebied van sensitiviteit en bemonstering weer af.

Om hierin meer inzicht te krijgen werd een vergelijkende studie opgezet tussen pinhole en multipinhole beeldvorming. De studie analyseert de pinhole en multipinhole reconstructie van een sfeer met uniforme activiteitsverdeling. Het multipinhole systeem bevat 7 pinhole openingen met kleine openingshoek die elk de volledige sfeer in beeld brengen met een minimale overlap van de projecties. Het traditionele pinhole systeem beschikt over een opening met veel grotere openingshoek op een zo kort mogelijke afstand van de sfeer om een optimale sensitiviteit te bekomen zonder truncatie van de sfeer in de projecties. De studie bestudeert daarmee hoofdzakelijk het verschil in bemonstering tussen pinhole en multipinhole SPECT gekoppeld aan een realistische sensitiviteit en niet zozeer de overlap van projecties.

De studie gebeurt aan de hand van de gelinearizeerde lokale impuls respons van de pinhole en multipinhole reconstructie van de sfeer met uniforme activiteitsverdeling. Deze gelinearizeerde lokale impuls respons is een veralgemening van de impuls respons van lineaire systemen naar het niet-lineaire reconstructieprobleem van emissietomografie [41, 42] en kan bij benadering op een zeer efficiënte manier worden berekend. Deze impuls respons is afhankelijk van de in beeld gebrachte activiteitsverdeling en van de plaats in het reconstructiebeeld. In het ideale geval leidt de perturbatie van de beschouwde activiteitsverdeling met een impuls op een specifieke locatie tot een reconstructiebeeld met een identieke impuls op dezelfde locatie. Een dergelijke ideale respons vereist een exacte inversie van de projectie van de beschouwde activiteitsverdeling. Omwille van de Poisson ruis in emissietomografische projectiebeelden is een dergelijke exacte inversie echter onmogelijk. In de beschouwde pinhole en multipinhole toepassingen is de situatie bovendien nog erger. De pinhole en multipinhole projectiebeelden bevatten immers zelfs in het ruisloze geval onvoldoende informatie voor de bovenstaande inversie. Om dit probleem te stabiliseren wordt daarom gebruik gemaakt van een maximum-a-postiori (of MAP) reconstructie met een kwadratische prior. Deze reconstructiemethode heeft de neiging om de reconstructie meer en meer te smoothen naarmate er minder informatie beschikbaar is voor de reconstructie. De mate waarin een gereconstrueerde impuls gelijkt op de oorspronkelijke perturbatie geeft bijgevolg de informatie-inhoud weer van de projectiebeelden over die welbepaalde locatie in de activiteitsverdeling.

Het toepassen van de bovenstaande procedure in de praktijk vereist de kwantificatie van de gelijkenis tussen de oorspronkelijke perturbatie (een Dirac impuls) en de resulterende respons. Qi *et al.* [43, 44] hebben voorgesteld om hiervoor de waarde van de respons op de plaats van de impuls te nemen, 'contrast recovery' genaamd, aangezien de respons naar verwachting een gesmoothe versie van de impuls is. Aan de hand van een eenvoudige parallel hole SPECT toepassing tonen we echter aan dat dit op zichzelf niet altijd een betrouwbare maat is, aangezien deze de specifieke vorm van de impuls respons niet mee in rekening brengt. Heel asymmetrische impulsen en impulsen met een sterk uitstralende intensiteit in bepaalde richtingen vormen daarbij de minst aantrekkelijke responsen. Daarom voeren we 4 bijkomende maten in die ook de vorm van de impuls respons mee in rekening brengen: na het afkappen van de impuls op een bepaald percentage van zijn contrast recovery, wor-

den ook het totaal aantal voxels van de impuls, de minimum en maximum afstand tot de rand van de impuls en het tweede orde moment van de intensiteit van de respons (ten opzichte van de plaats van de impuls) berekend.

De vergelijkende studie berekent de impuls respons van elke voxel van de bovenstaande sferische activiteitsverdeling en parameterizeert deze met de bovenvermelde 5 parameters: de contrast recovery en de 4 bijkomende maten. De multipinhole resultaten zijn quasi overal in het reconstructiebeeld beter dan die van de traditionele pinhole beeldvorming en ze zijn ook veel uniformer, waardoor multipinhole beeldvorming onze voorkeur krijgt. Deze betere uniformiteit is te danken aan de meer uniforme bemonstering van de activiteitsdistributie in de multipinhole situatie. De resultaten werden verder gevalideerd met daadwerkelijke MAP reconstructies van de sferische activiteitsverdeling met en zonder perturbatie voor 6 verschillende voxels uit het beeld en zowel voor de pinhole als de multipinhole situatie. De gelijkenis met de gesimuleerde resultaten is opmerkelijk en geeft aan dat de techniek van de gelinearizeerde lokale impuls respons zeer geschikt is om de verschillen tussen pinhole en multipinhole beeldvorming te bestuderen.

Praktische Toepassingen

Pinhole SPECT Calibratie met een Oscillerende Detector

De pinhole calibratiemethode ontwikkeld in dit werk is gebaseerd op een model van de pinhole acquisitie geometrie bestaande uit 7 parameters $f, d, m, e_u, e_v, \Phi, \Psi$ en veronderstelt dat deze parameters constant blijven gedurende de beeldvorming. In de praktijk is het echter bijna onvermijdbaar dat er kleine afwijkingen van dit model zullen optreden. Over het algemeen zullen dergelijke kleine afwijkingen weinig invloed hebben op de calibratiemeting en daardoor ook moeilijk detecteerbaar zijn. In dat geval is het echter ook weinig waarschijnlijk dat deze afwijkingen een grote invloed zullen hebben op de nauwkeurigheid van de reconstructie. Calibratiemetingen met een DSX camera (SMV) vertoonden echter grote afwijkingen van de verwachte metingen en konden onmogelijk met het bovenstaande model worden gecalibreerd. De oorzaak van deze afwijkende metingen kon uiteindelijk (met grote waarschijnlijkheid) worden bepaald als een sinusoidale oscillatie van de detector rond zijn draagas tijdens de acquisitie met een amplitude van slechts 0.3^o. Het acquisitiemodel van de calibratie en reconstructie werd daarom uitgebreid met twee extra parameters die de amplitude en fase van deze oscillatie definiëren. Met dit uitgebreide model was het mogelijk om de camera te calibreren en visuele inspectie van gereconstrueerde beelden met correctie voor de bovenstaande oscillatie toont een duidelijke verbetering in kwaliteit ten opzichte van beelden die zonder deze correctie werden gereconstrueerd.

MicroSPECT Beeldvorming van een Ratmodel voor de Ziekte van Parkinson

De bovenstaande calibratiemethode en de reconstructiemethode met sensitiviteitscorrectie werden toegepast bij de beeldvorming van een ratmodel voor de ziekte van Parkinson. De ratten ondergaan een unilaterale stereotactische injectie van lentivirale vectoren, gemanipuleerde stukjes viraal genetisch materiaal, in de Substantia Nigra. Het daaropvolgende ziektebeeld, dat sterk op de ziekte van Parkinson lijkt, zorgt voor een asymmetrische opname van de tracer ^{123}I-FP-CIT in het striatum van de rat. De hersenen van 5 'Parkinson' ratten en 5 controle ratten werden met pinhole SPECT in beeld gebracht en de resolutie van de gereconstrueerde beelden was voldoende om de asymmetrie in de intensiteit van het linker en rechter striatum te bepalen. Bij de controle ratten werd een lichte asymmetrie vastgesteld. Een simulatie toont echter aan dat dit het gevolg kan zijn van een uitwas van activiteit uit de hersenen tijdens de beeldvorming in combinatie met het feit dat het rechter striatum bij het begin van de acquisitie met de hoogste sensitiviteit en vergroting in beeld wordt gebracht, terwijl dat voor het linker striatum op het einde van de acquisitie gebeurt. De rechts-links asymmetrie in de Parkinson ratten was echter significant groter en in de tegengestelde richting, wat de goede werking van het ratmodel bevestigt.

Bijdrage van dit Werk

De belangrijkste bijdragen van dit werk in het domein van pinhole SPECT beeldvorming, zijn de theoretische studie van de geometrische calibratie van pinhole SPECT systemen en de daaropvolgende ontwikkeling en optimalisatie van een praktische calibratiemethode om de volledige acquisitiegeometrie van deze systemen te bepalen. De theorie bestudeert de voldoende en noodzakelijke voorwaarden om de acquisitiegeometrie te bepalen op basis van de projecties van een set van puntbronnen. Deze theorie was oorspronkelijk ontwikkeld voor traditionele pinhole systemen, maar werd later uitgebreid om ook multipinhole systemen te kunnen bestuderen. Een verdere uitbreiding van de theorie (zoals voor pinhole systemen met meerdere detectoren of pinhole systemen met afwijkende acquisitiegeometrieën) is in principe op gelijkaardige wijze mogelijk.

De theorie werd gebruikt om een nieuwe pinhole SPECT calibratiemethode te ontwikkelen, die bestaat uit de beeldvorming van drie puntbronnen in het gezichtsveld van de camera. Verder dienen ten minste twee van de afstanden tussen deze puntbronnen gekend te zijn. De massacentra van de puntbronprojecties worden aangewend in een kleinste kwadraten fitprocedure om de acquisitiegeometrie van het pinhole systeem te bepalen. De calibratiemethode is gemakkelijk uitvoerbaar en levert, in tegenstelling tot andere methodes [30–36], de volledige acquisitiegeometrie op basis van één enkele meting. De methode veronderstelt een star camera systeem, maar er werd aangetoond dat correcties voor minder starre camera systemen gemakkelijk kunnen worden geïmplementeerd.

De nauwkeurigheid van de calibratiemethode hangt af van de ruis in de calibratiemeting, de positie van de calibratiebronnen in het gezichtsveld van de camera en de nauwkeurigheid waarmee de afstanden tussen de calibratiebronnen gekend zijn. De fouten in de calibratieresultaten propageren naar de gereconstrueerde beelden, wat leidt tot een verlies aan spatiale resolutie en vervormingen van de gereconstrueerde beelden. Om deze propagatie van fouten tot een minimum te beperken, werden de posities van de calibratiebronnen in het gezichtsveld van de camera geoptimaliseerd voor de best mogelijke nauwkeurigheid van zowel de calibratie als de reconstructie. Deze optimalisatie vereiste de ontwikkeling van een efficiënte methode om de nauwkeurigheid van de calibratie en reconstructie te evalueren bij ruizige calibratiedata en fouten op de afstanden tussen de calibratiebronnen.

In het kader van de recente ontwikkeling van multipinhole SPECT beeldvorming, werd ten slotte een preliminaire studie gedaan naar de voordelen van multipinhole SPECT in vergelijking met de traditionele pinhole beeldvorming. De studie evalueert en vergelijkt de kenmerken van de gelineariseerde lokale impuls respons van de pinhole en multipinhole reconstructie. Hierbij werd aangetoond dat de contrast recovery op zichzelf niet altijd een betrouwbare maat is voor de kwaliteit van de reconstructie. De resultaten van de studie tonen een globaal betere en meer uniforme kwaliteit van de multipinhole reconstructie in vergelijking met de traditionele pinhole SPECT. Bovendien wijzen de resultaten uit dat de gelineariseerde lokale impuls respons een uitstekende methode is voor deze vergelijkende studie. Meer onderzoek is in dit domein echter noodzakelijk om optimale pinhole en multipinhole systemen te ontwikkelen en met elkaar te vergelijken.

De evaluatie van de bovenstaande calibratiemethode en de vergelijkende studie tussen pinhole en multipinhole SPECT vereisten de implementatie van de nodige calibratie- en reconstructiesoftware. Aangezien de correctie voor de pinhole sensitiviteit essentieel is voor nauwkeurige pinhole SPECT beeldvorming in de praktijk, werd ook de pinhole sensitiviteit bestudeerd en werd een praktische methode ontwikkeld om de ware sensitiviteit van pinhole systemen te bepalen. De methode is voldoende nauwkeurig voor traditionele pinhole toepassingen, maar vereist bijkomend onderzoek voor de praktische toepassing ervan op multipinhole systemen. Desondanks is het reeds mogelijk om multipinhole SPECT reconstructies te berekenen, maar met het nadeel dat daarbij de ruis van de sensitiviteitsmeting naar de reconstructiebeelden zal propageren. Dankzij de ontwikkelde software en de opgedane ervaring met pinhole SPECT beeldvorming, zijn we nu in staat om succesvolle pinhole SPECT studies op kleine proefdieren uit te voeren.

Suggesties voor Verder Onderzoek

Sensitiviteitscorrectie

Zoals reeds aangehaald, is het analytische model van de pinhole sensitiviteit, zoals gebruikt in dit werk, onvoldoende nauwkeurig voor multipinhole toepassingen met geïnclineerde pinhole openingen en met kleine openingshoeken. Voor zover wij we-

ten is er nog geen analytisch model van de sensitiviteit van dergelijke geïnclineerde pinhole openingen beschreven in de literatuur en blijft het een onderwerp voor toekomstig onderzoek. Een ander alternatief is het overschakelen naar het numerische sensitiviteitsmodel van Schramm *et al.* [2]. In combinatie met een dergelijk onderzoek dient in gedachte te worden gehouden dat sterke gradiënten in sensitiviteit moeten worden verwacht in de projectiebeelden en dat die gradiënten zich verplaatsen bij veranderingen in de mechanische offset en elektrische shifts. We anticiperen daarom dat een correct model van de sensitiviteit van geïnclineerde pinhole openingen enkel bruikbaar zal blijken in de praktijk, als dergelijke variaties in rekening kunnen worden gebracht.

Multipinhole SPECT

De theoretische studie van pinhole en multipinhole beeldvorming is enkel een eerste poging om de verschillen tussen pinhole en multipinhole SPECT beeldvorming grondig te begrijpen. De meeste van de huidige benaderingen van multipinhole beeldvorming [2–4] zijn op zijn minst gedeeltelijk gebaseerd op intuïtie met experimentele validatie, maar een fundamentele theorie over dit onderwerp dient nog steeds ontwikkeld te worden. Een dergelijke theorie zou aandacht moeten besteden aan de bemonstering, resolutie, sensitiviteit en ruis en aan de effecten van overlappende projecties. Uiteindelijk zou een dergelijke theorie het mogelijk moeten maken optimale configuraties van pinhole openingen te ontwerpen voor multipinhole beeldvorming.

Herstel van Spatiale Resolutie

Pinhole beeldvorming is altijd een afweging tussen resolutie en sensitiviteit: grotere pinhole openingen leiden tot een betere sensitiviteit maar met een lagere resolutie en omgekeerd. Met 'resolutie recovery' technieken, kan echter een deel van het ogenschijnlijke verlies aan spatiale resolutie worden herwonnen. Als gevolg daarvan is het mogelijk eenzelfde spatiale resolutie in de gereconstrueerde beelden te verkrijgen met een verhoogde sensitiviteit wanneer dergelijke technieken worden toegepast. Een 'resolutie recovery' techniek, gebaseerd op het evalueren van meerdere projectstralen door de pinhole opening, werd zeer recent ontwikkeld aan de Vrije Universiteit Brussel. Deze techniek is ook reeds beschikbaar in de huidige implementatie van onze pinhole en multipinhole reconstructiesoftware. De eerste resultaten tonen een duidelijke verbetering in de spatiale resolutie van de reconstructie en de techniek blijkt ook een ruisonderdrukkend effect te hebben. In zijn huidige implementatie leidt de techniek echter tot beduidend langere reconstructietijden (7 maal langer!) en verder onderzoek naar een efficiëntere implementatie van de techniek is wenselijk.

Multipinhole Calibratie

De pinhole acquisitie van 3 puntbronnen in combinatie met de kennis van 2 van de afstanden tussen deze puntbronnen vormt de strikte minimum vereiste voor de geometrische calibratie van een traditioneel pinhole systeem. Deze vereiste laat verder ook de calibratie van de beschouwde multipinhole systemen toe, maar is hiervoor misschien niet strikt noodzakelijk. In deze multipinhole toepassingen is het aanzienlijk moeilijker om de gemeten projectielocaties van de puntbronnen toe te wijzen aan de juiste puntbron en de juiste pinhole opening. Het is daarom interessant om de minimum vereisten voor de correcte calibratie van deze multipinhole systemen te bepalen om zo het aantal puntbronnen tot het strikte minimum te kunnen beperken.

Pinhole Reconstructie met Anatomische Informatie

Gelijktijdig aan dit werk, ontwikkelde K. Baete *et al.* [64–66] op onze dienst een maximum-a-posteriori algoritme dat toelaat om anatomische informatie uit MRI (magnetic resonance imaging) of CT (computed tomography) beelden aan te wenden bij de reconstructie van emissietomografische beelden. De methode is gebaseerd op voorkennis van de activiteitsverdeling in de structuren die zichtbaar en aflijnbaar zijn in die anatomische beelden. De veel hogere spatiale resolutie van de gebruikte anatomische informatie laat daarbij toe om partieel volume effecten in de emissietomografische reconstructie tot een minimum te beperken. Dit komt de kwaliteit van dergelijke reconstructies op het gebied van kwantificatie ten goede. Bovendien zou de techniek een geschikte regularisatie kunnen vormen voor het ondergedetermineerde reconstructieprobleem in pinhole en multipinhole toepassingen. Bijgevolg wordt verwacht dat de toepassing van deze techniek in pinhole en multipinhole reconstructie tot een significante verbetering van de kwaliteit van de gereconstrueerde beelden kan leiden.

Attenuatie & Scatter

Tot dusver worden attenuatie en scatter niet gemodelleerd in de huidige versie van onze pinhole en multipinhole reconstructiesoftware. De toepassing van correcties voor attenuatie en scatter zouden, tenminste in theorie, de nauwkeurigheid van de gereconstrueerde beelden verder ten goede moeten komen, voornamelijk voor absolute kwantificatie.

Symbols

f	focal length
d	detector distance
m	mechanical offset
n_u, n_v	detector shifts
e_u, e_v	electrical shifts
Φ	detector tilt
Ψ	detector twist
θ	projection angle
xyz	general cartesian coordinate system in the pinhole field of view
$r\alpha z$	general cylindrical coordinate system in the pinhole field of view
uv	general cartesian coordinate system in the projection image
$x_p y_p z_p$	aperture specific cartesian coordinate system in the pinhole field of view
$u_p v_p$	aperture specific cartesian coordinate system in the projection image
$A(x, y, z)$	activity distribution in the pinhole field of view
$B(x, y, z)$	backprojection in the pinhole field of view
$S(x, y, z)$	pinhole sensitivity distribution in the pinhole field of view
$Q(u, v, \theta)$	projection (in the projection image)
$M((x, y, z) \mapsto (u, v, \theta))$	pinhole mapping function for projection
$M^T((u, v, \theta) \mapsto (x, y, z))$	pinhole mapping function for backprojection
$PSF(x, y, z, u, v, \theta)$	pinhole point spread function

$p(.)$	probability
$p(.\|.)$	conditional probability
L	log-likelihood objective function based on Poisson statistics or projection ray
Λ	reconstruction image
q_i	photon count in detector pixel i
λ_j	activity in image pixel j
c_{ij}	sensitivity of detector pixel i for activity in image pixel j
D	diameter of pinhole aperture
T	thickness of pinhole aperture plate
α	acceptance angle of pinhole aperture
η	inclination angle of pinhole aperture
τ	angle with respect to the pinhole central ray
κ	angle with respect to the system central ray
ζ_p	rotation angle of the aperture specific coordinate system $u_p v_p$ with respect to the general coordinate system uv
μ	linear attenuation coefficient [cm^{-1}]
I	total number of detector pixels
i	detector pixel index
J	total number of image pixels
j	image pixel index
P	total number of pinhole apertures
p	pinhole aperture index
δ	Dirac impulse

Contents

Chapter 1

General Introduction

1.1 Nuclear Medicine

Nuclear medicine is a mainly diagnostic discipline of medicine, aiming at imaging metabolism and other functional processes of the human body. For this purpose, the patient is administered a radioactive tracer and the distribution of this tracer in the body is imaged. Three types of imaging are available: planar scintigraphy, SPECT (single photon emission computed tomography) and PET (positron emission tomography). Planar scintigraphy can be considered the most simple way of imaging, since only a 2D image of the 3D tracer distribution is obtained. SPECT and PET produce 3D images of the patient, which allow the physicians to look at slices through the body of the patient. SPECT is the oldest, but generally also the least expensive technique both in terms of the tracer and the equipment (SPECT camera) needed. PET is a more recent technique that has only been applied in clinical practice over the last decade. Although it offers advantages over SPECT by the increased sensitivity and the different tracers that can be used, it is usually also far more expensive than SPECT.

1.2 Small Animal Imaging

Apart from being diagnostic tools in clinical practice, SPECT and PET are also valuable research tools for studying human disease or for testing new drugs and radiopharmaceuticals. Most of such research, especially in the preliminary stages, is however conducted on animals and preferably on small laboratory animals. Other techniques exist as well for studying laboratory animals, but they are usually invasive and often even require sacrificing the animals, like in autoradiography. This makes follow-up studies difficult or impossible and requires more animals to achieve the same level of statistical significance of the results.

The application of SPECT and PET to small laboratory animals is however

hampered by the limited spatial resolution of these systems and the sensitivity is likely to be suboptimal as well in these applications. To relieve these problems, dedicated small animal imagers have been developed over the past years, called microSPECT and microPET respectively. In microSPECT, the general principle is to change from the traditional parallel hole collimation to pinhole collimation, possibly combined with scaling down the system and using higher resolution detectors. Recently, multipinhole SPECT has further been proposed as a variant of regular single pinhole SPECT. (Single and multipinhole SPECT imaging are explained in chapter 2 of this work.) MicroPET systems on the other hand are always scaled versions of a conventional PET system. Like for the conventional systems, microPET offers better sensitivity, but it is generally more expensive than microSPECT. In microPET the attainable spatial resolution is also limited by the positron range of the tracer isotopes, while for microSPECT it is, at least in principle, unlimited.

1.3 Purpose of this Work

Accurate artifact free reconstruction of SPECT images requires correction for several physical effects which influence the imaging results. First of all, the SPECT data will inevitably be corrupted by Poisson noise. Secondly, the human or animal body will attenuate part of the radiation that is emitted from inside the body, decreasing the amount of radiation measured by the camera. Attenuation in both the body and the camera itself also yields scattered photons corrupting the measurement even further. The relative orientation of the camera with respect to the human or animal body (acquisition geometry) further determines how the activity distribution is being imaged. Finally, the sensitivity of the camera for the activity distribution is not necessarily uniform and the camera can only image this distribution with limited spatial resolution.

All of the above problems have been well studied for parallel hole SPECT imaging and various correction approaches for these different effects have been proposed. Not all of those approaches are applicable however to pinhole and multipinhole imaging. The aim of this work is a fundamental study of those aspects which are specifically different in pinhole and multipinhole SPECT imaging and to propose appropriate solutions for these problems. Eventually this should result in the practical implementation of high performance pinhole and multipinhole SPECT imaging on a conventional SPECT camera.

The effects addressed in this work are therefore the pinhole SPECT acquisition geometry and the pinhole sensitivity. These effects are fundamentally different in parallel hole and pinhole imaging. The pinhole spatial resolution is also very specific for pinhole imaging and some attention is paid to this topic, but an efficient solution to take this effect into account is considered beyond the scope of this work. Poisson noise and photon attenuation do not depend on the type of collimation and are not specifically addressed in this work. Nevertheless, the MLEM reconstruction algorithm used in this work will take the noise characteristics of the data into account. Given the small size of laboratory animals, attenuation is further not

expected to have a major influence in pinhole applications. The animal size will also limit the amount of animal induced scattered photons, but part of the scatter originates from the collimator itself and is thereby specific to pinhole or multipinhole imaging. Nevertheless, scatter is ignored in this work, assuming that it is either negligible or that it is estimated (and corrected) in a way that does not involve knowledge of the collimator, like with the dual energy window scatter correction technique [1].

1.4 Overview

In chapter 2 the principle of pinhole SPECT image formation is discussed, with specific attention for the pinhole acquisition geometry, pinhole sensitivity and the pinhole spatial resolution. In chapter 3 the problem of pinhole reconstruction is addressed, with particular emphasis on the combination of pinhole sampling and pinhole sensitivity correction during reconstruction. Further, a practical method to measure the true pinhole sensitivity is derived from theory. The method is successful for most single pinhole applications, but requires further research for multipinhole applications. Chapter 4 is about the measurement of the pinhole acquisition geometry, which is needed for accurate image reconstruction. At the start of our research, no efficient and easy to perform method for such calibration was described in the literature. First a new theory is developed about the necessary and sufficient requirements to measure this geometry, which resulted in a practical calibration method for pinhole cameras. The calibration method is evaluated by simulations and measurements. A theoretical argument shows that the calibration method can be applied as well in many multipinhole situations and a practical multipinhole calibration is designed and performed. In chapter 5, we develop a fast approximative procedure to evaluate the accuracy of pinhole SPECT image reconstruction in function of the accuracy of the calibration. This allowed us to further optimize the above calibration procedure for optimal calibration and reconstruction accuracy. Chapter 6 addresses, from a theoretical point of view, the question about the benefit of multipinhole SPECT in comparison with single pinhole SPECT imaging by studying the linearized local impulse responses of single and multipinhole reconstruction. The concept of the linearized local impulse response proofs to be very valuable for this purpose and the first results indicate that the accuracy of reconstruction is more uniform for multipinhole SPECT in comparison with single pinhole imaging. More research is however needed on this topic. Chapter 7 demonstrates with a practical example how the calibration method of chapter 4 can be extended to more complicated acquisition geometries. At the same time it also demonstrates how critical small variations of the pinhole detector tilt are for accurate pinhole SPECT imaging. Chapter 8 finally illustrates the successful application of single pinhole SPECT for imaging a new animal model for Parkinson's disease.

Chapter 2

Pinhole SPECT Imaging

2.1 Introduction

This chapter provides an introduction to image acquisition in single and multipinhole SPECT imaging. Only image acquisition is discussed; the problem of image reconstruction is deferred to chapter 3. Section 2.2 provides a general overview of the biological, physical and mathematical principles behind SPECT imaging, with particular emphasis on pinhole SPECT where necessary. Section 2.3 explains in detail the image acquisition geometry of single and multipinhole SPECT imaging, resulting in explicit mathematical expressions for the projection and backprojection of pinhole SPECT systems. Section 2.4 further elaborates on the spatial dependency of the sensitivity of pinhole collimation. Again, mathematical expressions for the pinhole sensitivity are derived. Section 2.5 eventually explains the point spread function of pinhole imaging and its effect on spatial resolution.

2.2 Single Photon Emission Computed Tomography

2.2.1 Radionuclide Tracers

Each investigation in *Single Photon Emission Computed Tomography* or *SPECT*, starts with the administration of a radiolabelled tracer to the patient or laboratory animal. The tracer consists of a vector, usually a particular molecule, to which a radioactive isotope is attached. The vector is designed to participate with specific metabolic or other functional processes in the human or animal body, but it is administered in sufficiently small amounts in order not to disturb these natural processes. During these vector interactions, the radioactive isotopes will decay, in which process they emit γ-rays which can be measured from outside the body. This

allows us to measure the distribution of the tracer concentration in the body as a function of position and time.

The isotopes used in SPECT are isotopes for which the relative number of neutrons and protons in the nucleus is out of balance, causing the isotopes to be unstable. As a result, the isotopes only have a limited average life span of typically a few hours and will eventually decay into a more stable isotope by either electron capture or β^- emission. In the case of electron capture, the nucleus has a relative excess of protons and captures an orbital electron to combine it with a proton into a neutron. In the case of β^- emission the nucleus has a relative excess of neutrons and a neutron is transformed into a proton and an electron. The proton stays in the nucleus, while the electron is emitted. Regardless of the exact type of decay, the daughter product is in an excited energy state and proceeds virtually instantaneously to a more stable energy state. In this process, it emits a single photon or γ-ray to get rid of its excess energy. The isotope will continue to return to even more stable states until it eventually reaches the ground state of the isotope. For the isotopes used in SPECT, there is usually only one or a few dominating ways in which the isotopes proceed from their excited to ground state, yielding a limited number of prevailing photon energies. The isotope ^{123}I is an example of this way of producing γ-rays. It has a half-life of 13 hours and decays by electron capture into ^{123}Te, which mainly emits γ-rays of 159 keV.

In some cases the energy state of the above daughter product is an isomeric or metastable state. This means that the isotope is in an excited, but relatively stable energy state. Because of this relative stability, it takes the isotope generally much longer to make the first transition to a regular excited energy state. As a result, not the parent, but the daughter product itself can be used in the tracer. A good example is ^{99m}Tc, which is by far the most important single photon isotope. It has a half-life of 6 hours and has a photon energy of 140 keV. It is the daughter product of ^{99}Mo, which decays by β^- emission with a half life of 66 hours.

2.2.2 Interaction of Photons with Matter

At the photon energies typically encountered in SPECT imaging (60 keV to 600 keV) the dominating types of interaction with matter are the photo-electric effect and Compton scatter.

Photo-electric Effect The photo-electric effect dominates in high density materials like in the typical collimation materials Lead and Tungsten. In the photo-electric effect, an incoming photon hits an electron in the material, which absorbs all of its energy. If the energy is higher than the binding energy of the electron, the electron will escape from the atom with a kinetic energy, equal to the difference between the energy of the incoming photon and the binding energy of the electron. The departed electron will leave an electron vacancy in the atom, that can be filled up by a higher energy electron. In that process it will emit a photon with the energy of the difference between its original energy state and that of the vacancy. If the energy of the incoming photon

is insufficient for the targeted electron to escape, the energy can alternatively be used by the electrons in higher energy states to escape from the atom. In both cases the original photon has completely disappeared and all secondary photons have lower energies.

Compton Scatter Compton scatter dominates in low density materials like virtually all tissues in the human and animal body. It can be regarded as an elastic collision between the incoming photon and the target electron, which means that the kinetic energy is conserved during the collision. The collision deflects the incoming photon from its original path with lower probabilities for larger deflections and knocks the electron away. The entire process is governed by the laws of preservation of momentum and energy, resulting in lower energies of the outgoing photon for larger deflection angles. The same laws also determine the speed and direction of the outgoing electron.

Both types of interaction result in the disappearance of photons with the original energy and direction when travelling through matter. This process is called attenuation and the chance for a photon to get attenuated is described by the linear attenuation coefficient μ of the material it is travelling through. The linear attenuation coefficient μ is the probability for attenuation per unit length travelled and is independent of the distance already travelled through the material so far. This results in the exponential law of attenuation that yields the number of photons $N(d)$ after travelling over a distance d through a material with attenuation coefficient $\mu(s)$ at position s, when $N(0)$ photons started at position 0

$$N(d) = N(0)\,\exp\left(-\int_0^d \mu(s)\,\mathrm{d}s\right). \tag{2.1}$$

In the remainder of this work, we will often use the assumption that an animal body has zero attenuation ($\mu_{\text{body}} = 0$), yielding $N(d) = N(0)\,\forall\, d$. Although this assumption is only a moderately accurate representation of reality, the animal attenuation is not believed to have a major influence on the results of this work. We will further often assume as well that collimator material (see 2.2.4) has infinite attenuation ($\mu_{\text{collimator}} = \infty$), yielding $N(d) = 0$ for $d > 0$. Given the very high attenuation coefficients of typical collimation materials for typical SPECT photon energies, this assumption is highly accurate, except for very thin layers of collimator material. Thus, it is assumed that the animal body does not attenuate any photons, while collimator material immediately stops all incoming photons.

2.2.3 Photon Detection

In virtually all current SPECT systems, detection and registration of the photons emitted by the radionuclide tracer distribution in the human or animal body is done by a scintillation crystal of about a centimeter thick, with a series of Photo Multiplier Tubes (PMTs) coupled to its backside.

Scintillation Crystal The scintillation crystal, typically a NaI crystal in SPECT, stops the majority of the incoming photons by photo-electric absorption or by multiple Compton scattering events (see section 2.2.2). The free electrons generated in this way, will travel through the crystal and distribute their energy over thousands of other electrons by knocking them in an excited energy state. These excited electrons then get rid again of this excess energy by emitting a low energy photon of typically a few eV. The exact energy of these secondary photons depends on the type of scintillation crystal (e.g. NaI), while the number of secondary photons is proportional to the energy of the incoming photon. Normally these secondary photons will immediately be reabsorbed by the NaI crystal, since they have exactly the right energy to knock another electron into the excited state again. By doping the NaI crystal with Tl, additional energy levels are introduced into the crystal by which the excited electrons can return to their original state. The tertiary photons created by this path cannot be reabsorbed by the crystal. Eventually, part of the scintillation photons will reach the photo multiplier tubes at the backside of the crystal.

Photo Multiplier Tubes When a scintillation photon hits the base of a Photo Multiplier Tube or PMT, it will knock an electron from that base (a cathode) into the PMT, which consists of series of dynodes at sequentially higher voltages. The electrons are attracted by the next dynode and build up speed while travelling to it. When hitting the dynode they release even more electrons which are again attracted to the next dynode. This process is repeated until a sufficient amount of electrons is obtained for electronic readout.

Eventually the readout of the different PMTs is combined to obtain information about the energy of the original photon incident on the scintillation crystal and the place where that scintillation occurred. The energy of the original photon is proportional to the combined electrical output of the PMTs. It is used to discriminate between photons originating directly from the animal activity distribution and others, that might for example have undergone Compton scattering and need to be rejected. The place of scintillation, the mass center of the PMTs output, is further used to allocate the measured photon to a particular location in the projection image. Note that neither the energy nor position measurement will be entirely accurate. Instead there is an uncertainty with approximately Gaussian distribution about both energy and position. These uncertainties are called the energy resolution and the intrinsic spatial resolution of the detector respectively. The intrinsic spatial resolution results in a blurring of the projection image, the finite energy resolution in the imperfect rejection of scattered photons.

2.2.4 Collimation

By itself, the photon detection capability described in the previous section 2.2.3 is not sufficient to produce useful images of the radionuclide distribution in the patient or animal body. The problem is that the detection mechanism of the previous

section does not yield any information about the direction the incident photon was coming from before hitting the scintillation crystal. Consequently, the detected photon could have come from anywhere within that body. The situation is similar to taking a photograph without the use of a lens. Unfortunately, present knowledge does not allow us to construct lenses for the high energy photons encountered in SPECT imaging. Thereby, we are forced to use a more crude approach to the problem: collimation. The principle of collimation is to make sure that a photon incident on the scintillation crystal could only have come from a specific direction, because all other directions are excluded. To achieve this, collimation makes use of the attenuation characteristics of high density materials (see section 2.2.2). The basic idea is to put a device, the collimator, in front of the scintillation crystal that stops all photons by attenuating them, except when they are travelling in a specific direction. The downside of this technique is that only a small fraction of the photons emitted from within the body are accepted, while the majority of them is simply rejected. The fraction of the photons that are detected by the system is called the sensitivity of the system and for SPECT imaging this sensitivity is unfortunately always quite low. (Nevertheless, the diagnostic sensitivity of SPECT is usually very high!) Various types of collimation exist, but we limit ourselves to parallel hole, single pinhole and multipinhole collimation. These types of collimation are illustrated in figure 2.1.

Parallel Hole Collimation Parallel hole collimation is the type of collimation most often used in clinical practice to image the human body. It consists of a plate of high density material like Lead or Tungsten to yield high attenuation over small distances. The plate is perforated by narrow channels, separated by thin septa of the collimator material. The channels are all orthogonal to the detector surface and consequently, only photons travelling in directions orthogonal (or almost orthogonal) to the detector can reach the detector surface. All photons travelling at inclined directions towards the collimator will be stopped by the septa between the channels. As illustrated in figure 2.1(a), parallel hole collimation is not very suitable for small animal imaging, where the entire activity distribution is concentrated in a small part of the field of view. Because of parallel hole collimation, the small disk representing the laboratory animal, projects on a small part of the detector, while the rest of the scintillation crystal is not used at all.

Single Pinhole Collimation Single pinhole collimation is the type of collimation that is currently most often used for imaging small laboratory animals. The basic idea is to provide a focal point in front of the detector, through which all photons that are to be detected must pass. The detector is shielded for all other photons by a layer of dense collimator material, usually in the shape of a large cone, as illustrated in figure 2.1(b). In practice, the focal point is simply a small aperture at the vertex of the collimation cone. This type of collimation offers two major advantages over parallel hole collimation for small animal imaging. First of all, a much larger part of the scintillation crystal is used for imaging a concentrated activity distribution in comparison with parallel hole imaging, reflecting a potentially higher sensitivity for

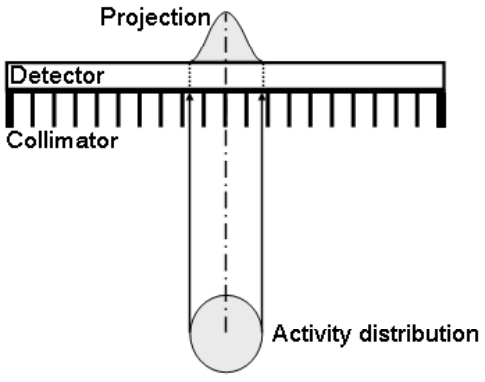

(a)

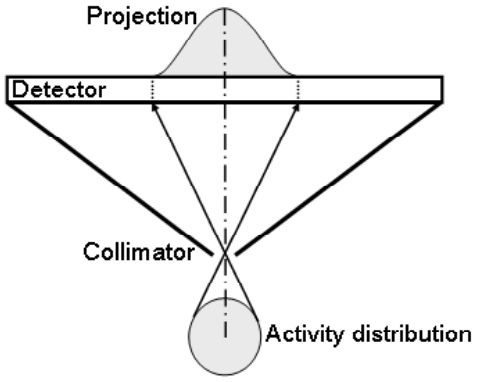

(b)

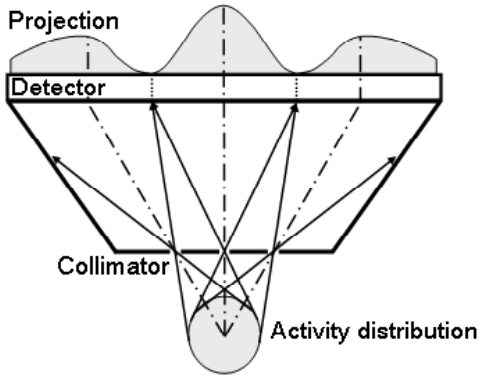

(c)

Figure 2.1: Different types of collimation: (a) parallel hole collimation, (b) single pinhole collimation and (c) multipinhole collimation. In each case, a small activity distribution is projected by the collimator onto the detector, yielding the gray distribution of photon counts.

such concentrated activity distributions. The second advantage comes from the intrinsic magnification effect of pinhole collimation: the accuracy of the magnified projection image is less susceptible to the blurring effect of the intrinsic resolution of the detector, allowing for better overall spatial resolution. The downside of the improved sensitivity and resolution is the smaller field of view, but this poses no problem in small animal imaging.

Multipinhole Collimation Even with single pinhole collimation, still only a limited part of the crystal is usually illuminated by the concentrated activity distribution. In recent years the idea arose that single pinhole sensitivity could be further enhanced by filling up the empty spots of the crystal with additional pinhole projections [2–4], as illustrated in figure 2.1(c). The effect of the increased sensitivity seems evident because the additional pinhole apertures accept photons that where previously rejected. Because of the additional pinhole apertures, the different projections may also overlap each other however (not illustrated). In such overlapping regions, a photon can have come from more than one direction. With each such additional direction of incidence, the information content of the detected photons about the activity distribution under study drops, since the uncertainty about the correct direction of incidence increases. This will make image reconstruction more difficult (see chapter 2), since image reconstruction tries to allocate photon counts not just back to their direction of incidence, but to their origin (along this direction) in the activity distribution. Also note that the sensitivity of a single pinhole collimator can be enhanced by moving the pinhole aperture further away from the detector and closer to the activity distribution. Whatever option is better, is still a topic of ongoing research and it will be addressed in chapter 6.

2.2.5 Pinhole Image Formation

Like parallel hole collimation, single pinhole collimation performs a mapping operation between each point in the field of view of the pinhole collimator and the location on the detector where photons emitted from that point can be detected. Consider the pinhole projection $Q_p(u_p, v_p)$ of an activity distribution $A(x_p, y_p, z_p)$ by a single pinhole aperture p with focal length f_p, as illustrated in figure 2.2. The origin of the $x_p y_p z_p$ coordinate system is located in the pinhole focal point, with the $x_p y_p$ plane parallel to the detector surface. The origin of the $u_p v_p$ detector coordinate system is further located at the orthogonal projection of the pinhole focal point on the detector, and the u_p and v_p axes are parallel to the x_p and y_p axes respectively. The subscripts p indicate that the definition of the $x_p y_p z_p$ and $u_p v_p$ coordinate systems is specific for pinhole aperture p and independent of its position in space. In the remainder of this work, we will frequently use these aperture specific coordinate systems, without explicitly redefining them.

The pinhole projection $Q_p(u_p, v_p)$ of the distribution $A(x_p, y_p, z_p)$ by the pinhole

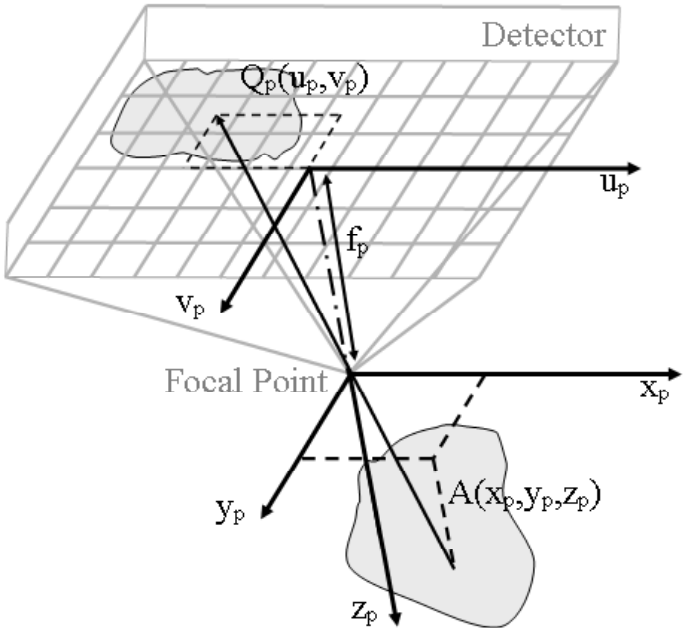

Figure 2.2: Pinhole image formation: a 3D activity distribution $A(x_p, y_p, z_p)$ is projected through the focal point of a pinhole collimator onto the detector, yielding the 2D projection image $Q_p(u_p, v_p)$. The pinhole focal point is located at the origin of the $x_p y_p z_p$ coordinate system and at a distance f_p from the detector surface.

aperture p can be described as

$$Q_p(u_p, v_p) =$$

$$\iiint A(x_p, y_p, z_p)\, S_p(x_p, y_p, z_p)\, M_p((x_p, y_p, z_p) \mapsto (u_p, v_p))\, \mathrm{d}x_p\, \mathrm{d}y_p\, \mathrm{d}z_p \qquad (2.2)$$

in which $M_p((x_p, y_p, z_p) \mapsto (u_p, v_p))$ represents the mapping operation of pinhole aperture p and $S_p(x_p, y_p, z_p)$ represents the sensitivity of the pinhole aperture for activity at position (x_p, y_p, z_p) in its field of view. The sensitivity $S_p(x_p, y_p, z_p)$ is discussed in detail in section 2.4. Here it is sufficient to note that it expresses the fraction of the photons emitted at (x_p, y_p, z_p) that are accepted by the pinhole aperture. The mapping operation $M_p((x_p, y_p, z_p) \mapsto (u_p, v_p))$ can further be expressed as

$$M_p((x_p, y_p, z_p) \mapsto (u_p, v_p)) = \delta\left(-\frac{f_p x_p}{z_p} - u_p\right) \delta\left(-\frac{f_p y_p}{z_p} - v_p\right) \qquad (2.3)$$

in which δ represents a Dirac impulse. Equation (2.2) is easily understood as follows: the number of photons emitted at (x_p, y_p, z_p) is $A(x_p, y_p, z_p)$, but only the fraction $S_p(x_p, y_p, z_p)$ of them will be accepted by pinhole aperture p. The accepted number of photons $A(x_p, y_p, z_p)\, S_p(x_p, y_p, z_p)$ will be detected at detector

position $(-f_p\, x_p/z_p, -f_p\, y_p/z_p)$; this is taken care off by the mapping operation $M_p((x_p, y_p, z_p) \mapsto (u_p, v_p))$. To obtain the complete projection image $Q_p(u_p, v_p)$ this procedure is finally repeated for each point of the activity distribution $A(x_p, y_p, z_p)$ by the integration.

In a multipinhole situation with P focal points $p = 1, ..., P$, the projection image $Q_p(u_p, v_p)$ of each focal point p individually is obtained with equation (2.2). By converting the different aperture specific coordinate systems $u_p v_p$ into a common coordinate system uv, the complete multipinhole projection image $Q(u, v)$ is easily obtained as

$$Q(u, v) = \sum_{p=1}^{P} Q_p(u, v). \tag{2.4}$$

In the aperture specific coordinate systems, the above pinhole mapping operations $M_p((x_p, y_p, z_p) \mapsto (u_p, v_p))$ yield the relatively simple relations (2.3), but these coordinate systems are inadequate in both multipinhole and tomography situations, just because of their aperture specific and position independent nature. Section 2.3 will derive the same mapping operations in the non-aperture specific coordinate systems xyz and uv, which are more convenient for multipinhole and tomography purposes. For convenience, we defer the exact definitions of the xyz and uv systems to that section. To proceed, it is sufficient to know that these systems exist and that the xyz system is fixed in space, while the uv system is fixed to the detector and thereby moves along with it.

2.2.6 Tomography

So far, our discussion was mostly limited to a singe projection $Q_p(u, v)$ of the activity distribution $A(x, y, z)$ by a single pinhole aperture p. Tomography consists in measuring and recovering the complete 3D information of the activity distribution $A(x, y, z)$. From (2.2), it is clear that a single projection $Q_p(u, v)$ of $A(x, y, z)$ is obtained by a sensitivity weighted mapping and integration procedure. From the mapping equation (2.3) it is further clear that this integration occurs along the lines $L_p(u_p, v_p)$

$$\begin{aligned} f_p x_p + u_p z_p &= 0 \\ f_p y_p + v_p z_p &= 0. \end{aligned} \tag{2.5}$$

These lines $L_p(u_p, v_p)$, or $L_p(u, v)$ when expressed in the general xyz and uv coordinate systems, are called projection lines and the above observation indicates that in the projection image $Q_p(u, v)$ all depth information along these projection lines is lost. Consequently, a single projection image $Q_p(u, v)$ does not contain sufficient information to reconstruct the 3D activity distribution $A(x, y, z)$. The lost depth information can be recovered however by combining different projections $Q_{Tp}(u, v)$ obtained by moving the pinhole system over a trajectory $T(x, y, z)$ "around"the activity distribution $A(x, y, z)$.

From integral theory, data sufficiency conditions have been derived to determine which sets of projection images $Q_{Tp}(u, v)$ are sufficient to completely recover this

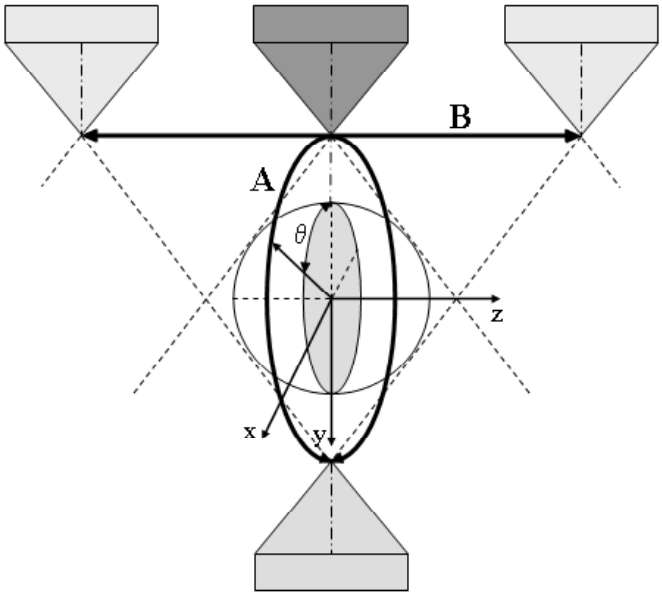

Figure 2.3: Pinhole SPECT acquisition of a spherical field of view centered about the xyz origin, which satisfies the Tuy data sufficiency criterium. The acquisition consists of a rotation of the detector (trajectory A) around the field of view and a translation (trajectory B) orthogonal to trajectory A. When the acquisition is restricted to just the rotation, the data sufficiency criterium is only satisfied in the central gray plane of the field of view.

depth information. For single pinhole collimation, the data sufficiency criteria of Tuy *et al.* [5], Smith *et al.* [6] or Metzler *et al.* [7] can be used. The Tuy condition states for example that each plane through the activity distribution $A(x, y, z)$ must intersect the pinhole focal point trajectory T at least once. Figure 2.3 shows a pinhole trajectory satisfying this condition for a spherical activity distribution [8]. The trajectory consists of a circular rotation of the focal point around the activity distribution (trajectory A) combined with a translational trajectory orthogonal to the circular trajectory (trajectory B). Other trajectories exist, which also satisfy the above mentioned conditions [5–11].

It is common practice however, to use only the circular part A of the complete trajectory (A+B) of figure 2.3, since pinhole SPECT is often performed with regular SPECT cameras. These cameras are designed for parallel hole imaging and orbit A satisfies the parallel hole data sufficiency criterium [12]. Implementing a 'complete' pinhole trajectory on a regular SPECT camera may be possible, but it is not straightforward [9, 11]. As a result of the circular orbit A, only sufficient depth information is recovered to exactly reconstruct the central plane of the activity distribution $A(x, y, z)$ [7], shown as the shaded surface in figure 2.3. For the noncentral parts of the activity distribution $A(x, y, z)$, the required depth information is not

completely absent, but it is only partially available. This explains why the circular pinhole trajectory A, nevertheless allows to obtain very useful reconstructions of the non-central parts as well. The image quality is often considered sufficiently high and no attempts are made to implement the more difficult pinhole trajectories satisfying the pinhole data sufficiency criteria. Throughout this work, only the traditional pinhole trajectory A will be considered. It is conveniently parameterized by the projection angle θ, also indicated in figure 2.3. To our knowledge no data sufficiency conditions are available for multipinhole imaging with overlapping pinhole projections. This problem will be addressed in chapter 6 of this work. In the multipinhole SPECT situations considered in this work, the detector performs the same circular rotation about the activity distribution as in figure 2.3. Of course, each pinhole aperture p then describes its own circular orbit.

In conclusion, the general single ($P = 1$) or multipinhole ($P > 1$) image acquisitions considered in this work can be described as

$$Q(u, v, \theta) = \sum_{p=1}^{P} Q_p(u, v, \theta) \tag{2.6}$$

in which $Q_p(u, v, \theta)$ represents the projection data obtained through pinhole aperture p and the projection angle θ describes the rotation of the detector about the activity distribution under investigation.

2.3 Pinhole SPECT Geometry

2.3.1 Parameters

Before starting the rigorous description of the pinhole SPECT geometry in section 2.3.2 and 2.3.3, it is instructive to start with a brief overview of the different parameters involved. The description is restricted to a single pinhole system performing the traditional circular trajectory A of figure 2.3. For such system, 10 different geometrical parameters can be identified. These parameters are often divided into intrinsic and extrinsic parameters. Extrinsic parameters explicitly define the position and/or orientation of the detector and collimator with respect to the axis of rotation, while the intrinsic parameters do not. To define these parameters, it is further convenient to introduce the concept of the central ray of the pinhole system. It is the line through the pinhole focal point (the center of the pinhole aperture) and orthogonal to the detector surface. In the remainder of this work, we will refer to it as the 'system central ray', to distinguish it from the 'pinhole central ray' introduced in section 2.4.

The starting point for this section is the ideal or perfectly aligned pinhole system, illustrated in figure 2.4 (a) to (c). In this perfectly aligned system, the system central ray connects the center of the detector with the pinhole focal point and the origin of the axis of rotation. The detector is further parallel to the axis of rotation. Only three parameters are required to describe this system.

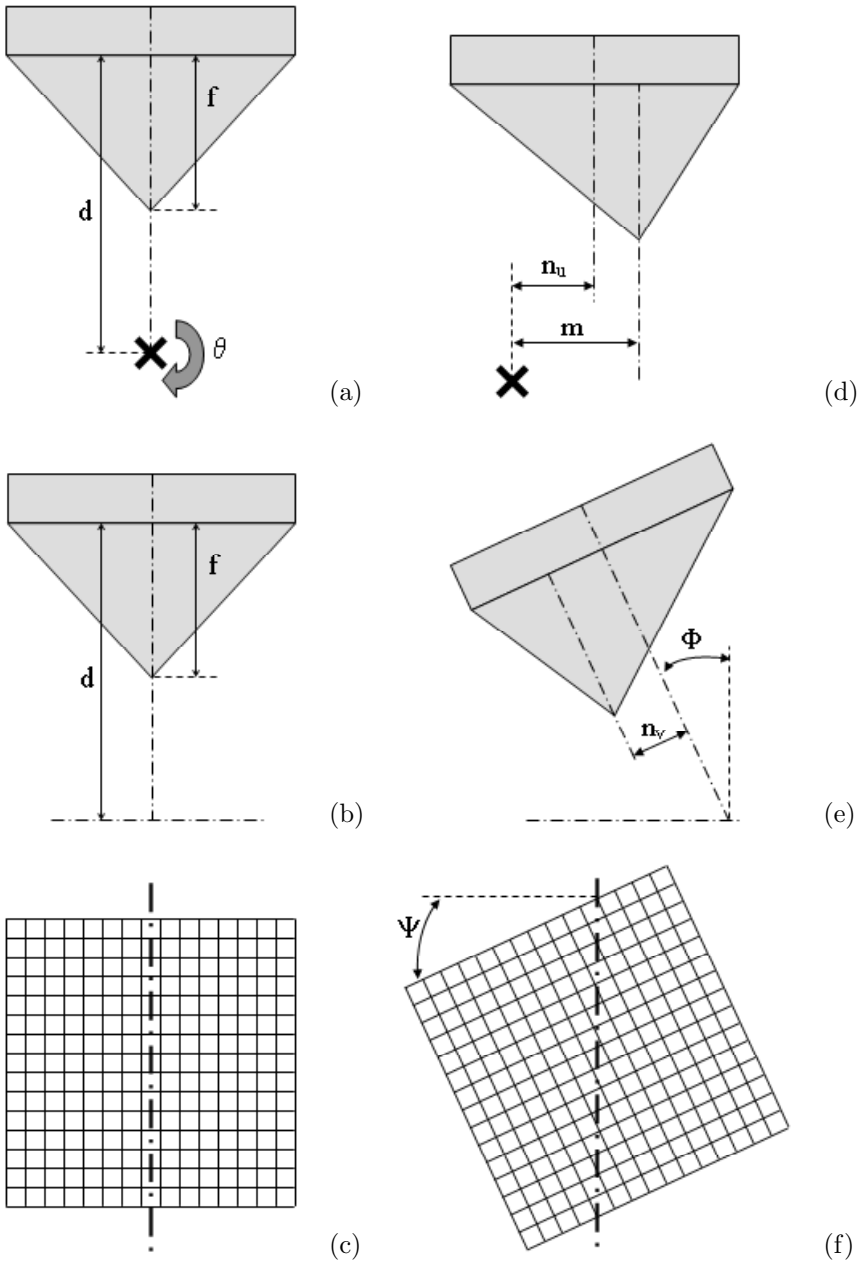

Figure 2.4: Pinhole SPECT geometry: the left side shows a frontal (a), side (b) and top (c) view of a perfectly aligned pinhole SPECT system, with the focal length f and the detector distance d indicated. The right side shows possible misalignments of the ideal left side systems. (d) Mechanical offset m and detector offset n_u. (e) Detector offset n_v and tilt angle Φ. (f) Twist angle Ψ.

Focal length f The focal length f of the pinhole system is the distance between the focal point and the detector. By definition, it is an intrinsic parameter which is measured along the system central ray.

Detector distance d The detector distance d is the distance between the detector and the origin of the axis of rotation. By definition, it is an extrinsic parameter. It can only be measured along the system central ray in absence of a mechanical offset (see below).

Projection angle θ The projection angle θ describes the rotation of the detector around the axis of rotation during image acquisition. It is the only parameter that varies during image acquisition; all other parameters are assumed to remain constant.

The 7 remaining parameters can all be considered to be practical deviations from the above ideal pinhole system. Each deviation is treated here separately, but in reality they may all occur simultaneously, which complicates their correct definition. The descriptions provided below are only valid if the deviation considered is the only deviation from the above ideal case. For more complicated cases, we refer to section 2.3.2 and 2.3.3.

Mechanical offset m The mechanical offset m represents an offset of the pinhole focal point orthogonal to the axis of rotation. It is an extrinsic parameter that can be measured as the distance between the axis of rotation and the system central ray. The mechanical offset is illustrated in figure 2.4 (d).

Detector offsets n_u **and** n_v The detector offsets n_u and n_v are extrinsic parameters representing offsets of the center of the detector in the directions orthogonal (n_u) and parallel (n_v) to the axis of rotation. The detector offsets n_u and n_v are illustrated in figure 2.4 (d) and 2.4 (e) respectively, although the displacement n_v in figure 2.4 (e) is no longer parallel to the axis of rotation due the nonzero tilt angle Φ.

Electrical shifts e_u **and** e_v Ideally, the detection of a photon in the center of the detector should be allocated to the center of the projection image. In reality the allocation of all photon detections is offset by the electrical shifts e_u and e_v in the directions orthogonal (e_u) and parallel (e_v) to the axis of rotation, due to offsets of the electrical components of the detector. The electrical shifts are intrinsic parameters.

Tilt angle Φ The tilt angle Φ is an extrinsic parameter, indicating the inclination of the detector with respect to the axis of rotation. It is measured as the complement of the angle between the central ray of the system and the rotation axis. The tilt angle is illustrated in figure 2.4 (e).

Twist angle Ψ The twist angle Ψ is an extrinsic parameter indicating a rotation of the detector in its own plane. For a nonzero twist angle, the column and row directions of the projection image pixels are no longer orthogonal and

Table 2.1: Pinhole parameters.

Symbol	Name	Type	Figure
f	Focal length	Intrinsic	2.4 (a) and (b), 2.5
d	Detector distance	Extrinsic	2.4 (a) and (b), 2.5
m	Mechanical offset	Extrinsic	2.4 (d), 2.5
n_u n_v	Detector offset	Extrinsic	2.4 (d) 2.4 (e)
e_u e_v	Electrical shift	Intrinsic	
Φ	Tilt	Extrinsic	2.4 (e), 2.5
Ψ	Twist	Extrinsic	2.4 (f), 2.5

parallel respectively to the axis of rotation. The twist angle is illustrated in figure 2.4 (f).

Throughout this work, all pinhole parameters except the rotation angle θ are assumed to remain constant during image acquisition. Only chapter 7 will study a situation in which the above assumption is violated and this violation will there be mentioned explicitly. Table 2.1 summarizes the above descriptions.

2.3.2 Camera-Image Geometry

Consider a pinhole system consisting of a flat detector and a single pinhole collimator with an infinitely small aperture. During image acquisition, the detector rotates on a circular orbit around the 3D activity distribution $A(x, y, z)$, describing the traditional circular pinhole orbit A of figure 2.3. The activity distribution $A(x, y, z)$ is projected through the pinhole focus onto the detector, yielding the projection image $Q(u, v, \theta)$ at projection angle θ. The distribution $A(x, y, z)$ is defined in the right handed Cartesian coordinate system xyz, with the z axis along the rotation axis of the pinhole system, like in figure 2.5. At zero projection angle θ, the x axis is further by definition parallel to the detector. The projection image $Q(u, v, \theta)$ is defined in the uv Cartesian coordinate system with the axes fixed along the column and row directions in the detector element grid. The origin of the uv coordinate system is the orthogonal projection of the xyz origin on the detector. The projection angle θ is finally defined as the angle between the detector surface and the x axis, measured in the xy plane.

At every detector position θ, the relative orientation of the activity distribution $A(x, y, z)$ and the detector is different. By correcting for this rotation θ, the same distribution can be expressed in a new coordinate system $x'y'z'$ rotating with the uv system around its own z' axis and keeping the x' axis parallel to the detector surface.

$$\begin{bmatrix} x' \\ y' \\ z' \end{bmatrix} = \begin{bmatrix} cos\theta & sin\theta & 0 \\ -sin\theta & cos\theta & 0 \\ 0 & 0 & 1 \end{bmatrix} \begin{bmatrix} x \\ y \\ z \end{bmatrix} \tag{2.7}$$

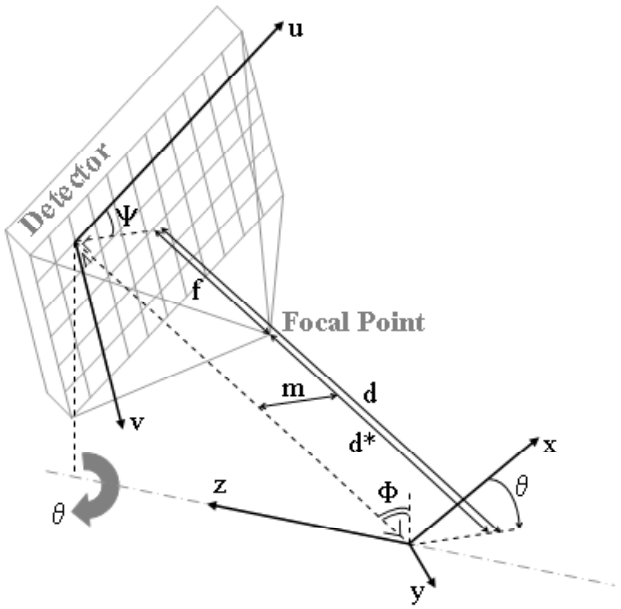

Figure 2.5: Camera-Image geometry. Pinhole camera with focal length f at projection angle θ. The z axis is the rotation axis of the system and the xyz origin is chosen such that the system central ray intersects the x axis for $\theta = 0$. The focal length f and the detector distance d are indicated along the system central ray. The mechanical offset m is the distance between the xyz origin and the system central ray. The tilt angle Φ is the complement of the angle between the system central ray and the axis of rotation. The twist angle Ψ is the angle between the rows of detector pixels (u axis) and the orthogonal projection of the x axis on the detector for $\theta = 0$.

The angle θ only expresses the relative orientation of the detector and the image $A(x, y, z)$ with respect to each other. Their absolute orientations are of no importance for image reconstruction purposes.

The orientation of the uv system (detector) with respect to the $x'y'z'$ system can further be specified by two additional angles, namely the tilt Φ and the twist Ψ (See figures 2.5, 2.4 (e) and 2.4 (f)). The tilt Φ represents the angle between the detector and the rotation axis. A pinhole camera may be tilted deliberately to bring the focal point close to a target organ, but in a way that allows the camera to clear other parts of the body [13]. The tilt can be taken into account by rotating the $x'y'z'$ system over the tilt angle Φ to obtain the $x''y''z''$ coordinate system. This rotation is performed about the x' axis and as a result, both the x'' and z'' axes are

parallel to the detector surface.

$$\begin{bmatrix} x'' \\ y'' \\ z'' \end{bmatrix} = \begin{bmatrix} 1 & 0 & 0 \\ 0 & cos\Phi & -sin\Phi \\ 0 & sin\Phi & cos\Phi \end{bmatrix} \begin{bmatrix} x' \\ y' \\ z' \end{bmatrix} \tag{2.8}$$

The twist Ψ represents the angle between the u axis and the direction on the detector surface perpendicular to the rotation axis. It is the orientation angle of the pixels on the detector surface. Since the x'' axis is still parallel to the detector surface and orthogonal to the rotation axis, the twist angle Ψ is also the angle between the u and x'' axis. Rotating the $x''y''z''$ system over this angle Ψ, finally yields the $x'''y'''z'''$ coordinate system, with the x''' and z''' axes parallel to the u and v axis respectively.

$$\begin{bmatrix} x''' \\ y''' \\ z''' \end{bmatrix} = \begin{bmatrix} cos\Psi & 0 & -sin\Psi \\ 0 & 1 & 0 \\ sin\Psi & 0 & cos\Psi \end{bmatrix} \begin{bmatrix} x'' \\ y'' \\ z'' \end{bmatrix} \tag{2.9}$$

After application of the above rotations, the camera-image geometry can further be described by the distances f, d, n_u, n_v and m as illustrated in figure 2.4 and 2.5. The distances f and d are measured along the central ray and represent respectively the focal length and the distance between the detector and the plane parallel to the detector and through the xyz origin. The detector offsets n_u and n_v represent the offsets of the uv origin from the center of the detector in the u and v direction respectively. The mechanical offset m is the distance between the central ray and the rotation axis. By definition this distance is measured in the direction orthogonal to the rotation axis and parallel to the detector surface, like the x' axis (x'' axis). Thereby, it forms the angle Ψ with the u axis and the length m can be decomposed into its uv components (m_u, m_v).

$$\begin{aligned} m_u &= m\cos\Psi, \\ m_v &= m\sin\Psi. \end{aligned} \tag{2.10}$$

The origin of the xyz system on the axis of rotation is chosen such that the central ray intersects the x' axis (x'' axis). Thereby, the mechanical offset m can be measured as the distance between the xyz origin and the system central ray. Since the uv origin was defined as the orthogonal projection of the xyz origin, the offset m can equivalently be measured as the distance between the uv origin and the central ray. Please note that the xyz origin has been defined with respect to the focal point and detector positions, instead of defining their absolute positions in space. Once again, this absolute reference is of no importance for image reconstruction.

2.3.3 Point Source Projection

Using the parameters and coordinate systems of section 2.3.2, the pinhole projection of a point source (x, y, z) can be calculated. The projection is defined by its

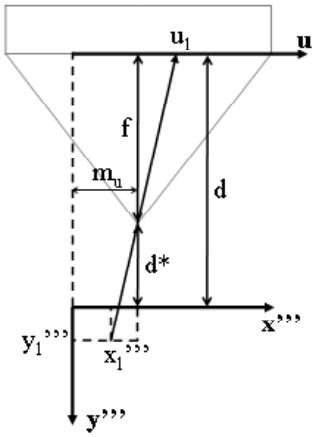

Figure 2.6: Projection of a point source (x_1''',y_1''',z_1''') by a pinhole camera, seen in the direction of the axis of rotation, being the z''' axis.

coordinates (u_θ, v_θ) in the uv coordinate system of the detector. The mathematics of congruent triangles, illustrated in figure 2.6, justifies the relations

$$\frac{x''' - m_u}{d - f + y'''} = \frac{m_u - u_\theta}{f}, \tag{2.11}$$

$$\frac{z''' - m_v}{d - f + y'''} = \frac{m_v - v_\theta}{f}. \tag{2.12}$$

Rearranging them and inserting (2.10) yields

$$u_\theta = f\frac{m\,\cos\Psi - x'''}{d - f + y'''} + m\,\cos\Psi, \tag{2.13}$$

$$v_\theta = f\frac{m\,\sin\Psi - z'''}{d - f + y'''} + m\,\sin\Psi. \tag{2.14}$$

The projections (u_θ, v_θ) are defined in the uv coordinate system of the detector, but the origin of this system in the projection image $Q(u^{img}, v^{img}, \theta)$ is still unknown. The assumption that the center of the projection image corresponds with the center of the detector, would yield the relations

$$u_\theta^{img} = u_\theta - n_u, \tag{2.15}$$

$$v_\theta^{img} = v_\theta - n_v, \tag{2.16}$$

which take into account the offsets n_u and n_v of the uv origin with respect to the center of the detector. The above assumption does not take into account however the electrical shifts e_u and e_v which represent a collective translation of the projection image, caused by offsets of the internal electrical components of the detector. Taking

these electrical shifts also into account yields

$$u_\theta^{img} = u_\theta + e_u - n_u, \tag{2.17}$$

$$v_\theta^{img} = v_\theta + e_v - n_v. \tag{2.18}$$

These relations reveal that the electrical shifts e_u and e_v interact with the detector offsets n_u and n_v. For reconstruction purposes, only the combined effect of the electrical shifts and the detector offsets is important. For historical reasons, we deal with this by lumping the detector offsets n_u and n_v into the electrical shifts e_u and e_v respectively, yielding

$$u_\theta^{img} = u_\theta + e_u^*, \tag{2.19}$$

$$v_\theta^{img} = v_\theta + e_v^*. \tag{2.20}$$

These relations remain fully general, but it should be kept in mind that the electrical shifts e_u^* and e_v^* in the relations (2.19) and (2.20) now have a mixed intrinsic and extrinsic character. For the remainder of this work, this will have no effect on future results and we will drop the superscripts '*' again.

The substitution of (2.19) and (2.20) into (2.13) and (2.14) and dropping the superscripts '*' eventually yields

$$u_\theta^{img} = f\frac{m\,\cos\Psi - x'''(\theta,\Phi,\Psi)}{d - f + y'''(\theta,\Phi,\Psi)} + m\,\cos\Psi + e_u, \tag{2.21}$$

$$v_\theta^{img} = f\frac{m\,\sin\Psi - z'''(\theta,\Phi,\Psi)}{d - f + y'''(\theta,\Phi,\Psi)} + m\,\sin\Psi + e_v. \tag{2.22}$$

These relations yield the projection location $(u_\theta^{img}, v_\theta^{img})$ of a point source at position (x, y, z) in the field of view. They thereby express the mapping operation $M_p((x_p, y_p, z_p) \mapsto (u_p, v_p))$ of (2.3) in the general xyz and uv coordinate systems.

2.3.4 Multipinhole Geometry

In multipinhole imaging, different pinhole apertures project (parts of) the same activity distribution on the same detector. The description of the acquisition geometry of the single pinhole system of the previous section can easily be extended to such multipinhole situations. Consider the general case of P pinhole apertures all projecting on the same detector. The orientation and position of the detector is of course identical for all pinhole apertures, and consequently the parameters θ, d, e_u, e_v, Φ and Ψ are identical for each pinhole aperture. Each pinhole aperture further has its own focal length f_p for $p = 1, ..., P$ and introduces its own system central ray. In the single pinhole case, the mechanical offset m was introduced as the distance from the only system central ray to the axis of rotation. The specific choice of the origin of the xyz and uv coordinate systems in function of this central ray, eventually lead to the definition of m_u and m_v by relation (2.10). The point (m_u, m_v) defines the position of the intersection of the central ray with the detector

in the uv detector coordinate system. Each of the P pinhole apertures p of the multipinhole case introduce their own system central ray with its own intersection point (m_{up}, m_{vp}). As a result, each pinhole aperture can generally be described by 3 parameters f_p, m_{up} and m_{vp}. The origin of the xyz and uv coordinate systems, can only be chosen once however and relation (2.10) is only valid for a single aperture. In the remainder of this work we will choose this aperture to be aperture $p = 1$. With this definition we can now restate the projection locations (u_p^{img}, v_p^{img}) of a point source (x, y, z) by the pinhole apertures $p = 1, ..., P$ as

$$u_{\theta p}^{img} = f_p \frac{m_{up} - x'''(\theta, \Phi, \Psi)}{d - f_p + y'''(\theta, \Phi, \Psi)} + m_{up} + e_u \quad \text{for } p = 1, ..., P \tag{2.23}$$

$$v_{\theta p}^{img} = f_p \frac{m_{vp} - z'''(\theta, \Phi, \Psi)}{d - f_p + y'''(\theta, \Phi, \Psi)} + m_{vp} + e_v. \quad \text{for } p = 1, ..., P \tag{2.24}$$

and

$$m_{v1} = m_{u1} \tan \Psi. \tag{2.25}$$

These equations again express a mapping operation similar to the mapping operation $M_p((x_p, y_p, z_p) \mapsto (u_p, v_p))$ of (2.3) in the general xyz and uv coordinate systems.

2.3.5 Projection and Backprojection

By combining the results of this chapter up till here, the image acquisition process of multipinhole SPECT imaging can be expressed as

$$Q(u, v, \theta) = \sum_{p=1}^{P} Q_p(u, v, \theta) \tag{2.26}$$

with

$$Q_p(u, v, \theta) = \iiint A(x, y, z)\, S_{\theta p}(x, y, z)\, M_p((x, y, z) \mapsto (u, v, \theta))\, \mathrm{d}x\, \mathrm{d}y\, \mathrm{d}z \tag{2.27}$$

and

$$M_p((x, y, z) \mapsto (u, v, \theta)) = \delta(u - u_{\theta p}^{img})\, \delta(v - v_{\theta p}^{img}) \tag{2.28}$$

and with $u_{\theta p}^{img}$ and $v_{\theta p}^{img}$ as in (2.23) and (2.24) respectively. In terms of projection rays, each point (u, v, θ) in the projection data now relates to P projection rays $L_{\theta p}(u, v)$ for $p = 1, ..., P$

$$\begin{aligned} x'''f_p + y'''(u^{img} - m_{up} - e_u) + (d - f_p)(u^{img} - e_u) - d\, m_{up} = 0 \\ z'''f_p + y'''(v^{img} - m_{vp} - e_v) + (d - f_p)(v^{img} - e_v) - d\, m_{vp} = 0. \end{aligned} \tag{2.29}$$

The above relations define the *projection* of the activity distribution $A(x, y, z)$ by a multipinhole SPECT camera. The projection establishes a transition from the xyz image domain to the $uv\theta$ projection domain. Closely related to the projection

operation is the *backprojection* operation. This operation establishes a transition in the opposite direction, i.e. from the $uv\theta$ projection space to the xyz image space. The backprojection $B(x, y, z)$ of a projection $Q(u, v, \theta)$ for the above multipinhole SPECT camera is defined as

$$B(x, y, z) = \sum_{p=1}^{P} B_p(x, y, z) \tag{2.30}$$

with

$$B_p(x, y, z) = \iiint Q(u, v, \theta)\, M_p^T((u, v, \theta) \mapsto (x, y, z))\, S_{\theta p}(x, y, z)\, \mathrm{d}u\, \mathrm{d}v\, \mathrm{d}\theta \tag{2.31}$$

and

$$\begin{aligned} M_p^T((u, v, \theta) \mapsto (x, y, z)) \quad &= 1 \quad \text{for} \quad (x, y, z) \in L_{\theta p}(u, v) \\ &= 0 \quad \text{for} \quad (x, y, z) \notin L_{\theta p}(u, v). \end{aligned} \tag{2.32}$$

The backprojection performs very similar operations as the projection, but in reversed order. First the observed photon counts $Q(u, v, \theta)$ (not $Q_p(u, v, \theta)$!) are 'projected back' into the image space along the same projection rays $L_{\theta p}(u, v)$. However, instead of allocating every count back to its exact origin, the counts are smeared out over the entire projection ray by the mapping operation $M_p^T((u, v, \theta) \mapsto (x, y, z))$. Allocating each count back to its origin is simply impossible, since this kind of 'depth information' was lost during projection. Next, the result is multiplied with the pinhole sensitivity $S_{\theta p}(x, y, z)$ and eventually the contributions of the different projection rays are added together by the integration. Like for the projection operation, the results $B_p(x, y, z)$ for the individual pinhole apertures p may simply be added together.

The backprojection operation is the transpose of the projection operation, not its inverse. Therefore, $B(x, y, z)$ is not equal to $A(x, y, z)$. Nevertheless $B(x, y, z)$ looks like a blurred version of $A(x, y, z)$, since adding the contributions of different projection lines together already partially recovers the depth information that was lost during projection for the individual projection lines. The projection and backprojection operations will form the heart of the MLEM image reconstruction algorithm of the next chapter.

Now the sensitivity $S_{\theta p}(x, y, z)$ still needs to be expressed.

2.4 Pinhole Sensitivity

2.4.1 Ideal Pinhole Sensitivity

To study the sensitivity of pinhole collimation, we return to the aperture specific $x_p y_p z_p$ and $u_p v_p$ coordinate systems. Now, consider a point source of activity A and at position (x_p, y_p, z_p) in the field of view of the pinhole camera, as illustrated in figure 2.7. The point source isotropically emits photons in all directions. For the moment, the pinhole collimator is modelled as an infinitely thin plate parallel

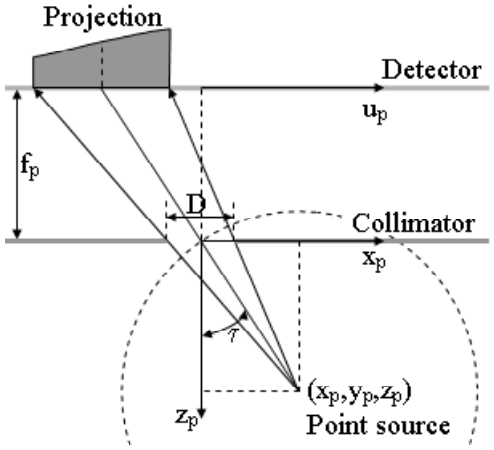

Figure 2.7: Projection of a point source (x_p, y_p, z_p) through an ideal pinhole aperture with diameter D on a detector at a distance f_p (focal length) behind the collimator. The pinhole aperture is located at the origin of the $x_p y_p z_p$ coordinate system. The intrinsic spatial resolution of the detector is not taken into account.

to the detector with a circular opening with diameter D representing the pinhole aperture. The collimator plate consists of a material with infinitely high attenuating capabilities, such that no photons emitted by the point source can reach the detector, unless they travel through the pinhole aperture.

The sensitivity $S_p(x_p, y_p, z_p)$ for the point source (x_p, y_p, z_p) is defined as the fraction of the photons emitted by the point source that reach the detector. Since the point source emits those photons isotropically, the fraction of those photons emitted in a specific solid angle ω equals $\frac{\omega}{4\pi}$. Now construct a sphere around the point source (x_p, y_p, z_p) through the center of the pinhole aperture $(0, 0, 0)$. For a point source (x_p, y_p, z_p) at a sufficiently large distance from a sufficiently small pinhole aperture ($\sqrt{x_p^2 + y_p^2 + z_p^2} \gg D$), the solid angle ω occupied by the pinhole aperture can be well approximated by

$$\omega = 4\pi \frac{\pi \frac{D^2}{4} \cos\tau}{4\pi \left(\frac{z_p}{\cos\tau}\right)^2} = \frac{\pi D^2 \cos^3\tau}{4 z_p^2} \tag{2.33}$$

in which the numerator and the denominator of the first equation represent the area of the aperture as seen from the point source and the surface area of the sphere respectively. The angle τ further represents the angle between the z axis and a projection ray through the center of the pinhole aperture

$$\tau = \arctan\left(\frac{\sqrt{x_p^2 + y_p^2}}{z_p}\right). \tag{2.34}$$

Dividing this expression by the 4π cone angle of the sphere eventually yields the desired sensitivity $S_p(x_p, y_p, z_p)$

$$S_p(x_p, y_p, z_p) = \frac{D^2 \cos^3\tau}{16 z_p^2} \tag{2.35}$$

with τ as in (2.34).

Equation (2.35) states that the pinhole sensitivity varies proportional to the area of the pinhole aperture D^2, as expected. It further varies inversely quadratic with the distance from the point source to the pinhole aperture $z_p^2/\cos^2\tau$. Note that this dependency introduces a singularity for $z_p = 0$, which arises from the approximation used to calculate ω in (2.33). The accuracy of the approximation in (2.33) rapidly improves at larger values of z_p and the remaining part of this section will only consider situations in which the above approximation is sufficiently accurate for the entire non-zero part of the activity distribution under study. This situation is usually satisfied in practice, where the activity distributions are concentrated around the axis of rotation, which is at a sufficient distance $d - f$ from the pinhole aperture. Finally, the sensitivity also depends on the angle τ in a sinusoidal way $\cos\tau$.

2.4.2 Pinhole Aperture Design

The design of pinhole apertures in practice differs from the ideal pinhole aperture model of section 2.4.1. Figure 2.8 (a) illustrates the practical design of a typical knife edge aperture, which is by far the most common pinhole aperture design and the only one considered in this work. The design consists essentially of a plate of a high density material like Lead or Tungsten, offering a high attenuation coefficient μ. The thickness T of the plate is chosen such that the penetration of photons incident on the plate is negligible, even for an angle of incidence of 90^o

$$\exp\left(-\int_0^T \mu \, \mathrm{d}s\right) \approx 0. \tag{2.36}$$

The aperture itself is obtained by two coaxial conical resections of the collimation material, yielding a circular opening of diameter D flanked by collimation material of increasing thickness t until the full thickness T of the plate is reached. The vertex angle α of the cones determines how fast the thickness t of the flanking material increases. This is important, because close to the actual aperture, the thickness of the collimation material t is significantly smaller than T and photon penetration will not be negligible until t reaches a sufficiently large value. On the other hand, α also approximates the maximum angle by which a photon can travel through the pinhole aperture without penetrating the collimation material and the approximation becomes exact for an infinitely small pinhole diameter D or an infinitely large plate thickness T. It is therefore called the acceptance angle of the pinhole aperture and it determines the part of space in front of the aperture that is visible for the detector through the pinhole aperture.

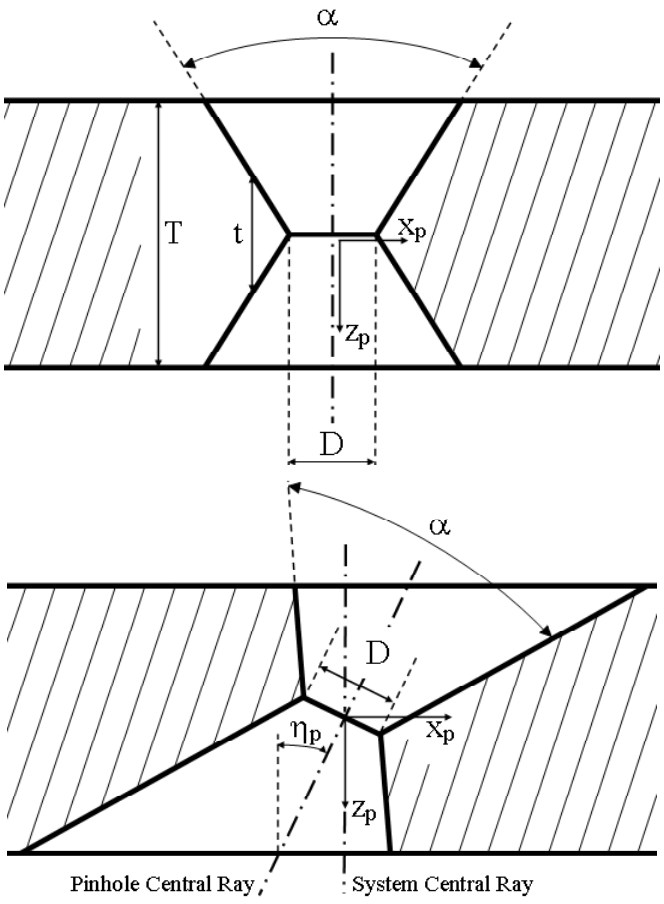

Figure 2.8: Knife edge pinhole aperture design: (a) non-inclined and (b) inclined pinhole central ray. Cross-sections of the pinhole aperture plate with indication of the pinhole diameter D, the acceptance angle α, the aperture plate thickness T and the inclination angle η. In (a) $\eta = 0$.

In single pinhole collimation, the axes of the resecting cones are generally orthogonal to the collimation plate as illustrated in figure 2.8 (a), with the plate parallel to the detector. In multipinhole imaging, it can be interesting however to have several pinhole apertures observe the same field of view, as illustrated in figure 2.1 (c). This can be realized by inclining these cone axes with respect to the system central ray by an angle η_p, like in figure 2.8 (b). (Please note that, also in this situation, we keep the $x_p y_p$ plane of the $x_p y_p z_p$ coordinate system parallel to the detector and that we define the angle η_p about the y_p axis.) The axis of the coaxial cones will proof to be particularly useful in describing the sensitivity of the corresponding pinhole aperture. In the remainder of this work, we will refer to this axis as the pinhole

central ray. In the situation of figure 2.8 (a), this pinhole central ray coincides with the system central ray of section 2.3.1, but in the more general situation of figure 2.8 (b), they intersect in the pinhole focal point. From figure 2.8 (b) it is further clear that large inclination angles η_p can only be realized in practice for sufficiently small acceptance angles α. In the remainder of this work, we therefore assume that large acceptance apertures always have small to zero inclination angles η_p.

2.4.3 Realistic Pinhole Sensitivity

Looking back to the ideal pinhole aperture model of section 2.4.1, it is now clear that this is actually a knife edge aperture with an acceptance angle α approaching 180^o and with an inclination angle η_p of the pinhole central ray of 0^o. Due to the 180^o acceptance angle, the flanking material of the aperture never reaches full thickness T and remains infinitely thin. The resulting photon penetration problem could however be neglected by the infinite attenuation assumption of the collimator material ($\mu = \infty$). Since $\eta_p = 0$, the z_p axis of figure 2.7 is further also the pinhole central ray and the angle τ actually represents the angle between the projection ray of a point source (x_p, y_p, z_p) and this pinhole central ray.

A realistic pinhole aperture has an acceptance angle α of less than 180^o, but the collimation material also has a finite attenuation coefficient μ. As explained in the previous section 2.4.2, photons can then penetrate through the low thickness flanking material of the actual aperture with the amount of penetration dropping from 100% at the physical edge of the aperture to almost 0% once the flanking material reaches a sufficient thickness t. The situation is worse for larger acceptance angles α, since the thickness t increases more slowly in those situations. Apparently, a realistic pinhole aperture does not have a sharp edge for photon penetration, but a more fuzzy edge and the physical diameter D only represents a lower limit for the diameter. Due to this penetration, the sensitivity of the pinhole aperture is larger than expected and the sensitivity does not drop immediately to zero outside the cone. To express this higher sensitivity, the physical diameter D in (2.35) can be replaced by a larger effective diameter D_e [14].

$$S_p(x_p, y_p, z_p) = \frac{D_e^2 \cos^3\tau}{16(x_p \sin\eta_p + z_p \cos\eta_p)^2}. \tag{2.37}$$

To keep expression (2.37) fully general, the factor z_p^2 in the denominator of (2.35) has also been replaced by $(x_p \sin\eta_p + z_p \cos\eta_p)^2$. In this way it is also valid for nonzero inclination angles η_p. To maintain this generality, the angle τ must further be redefined as

$$\tau = \arctan\left(\frac{\sqrt{(x_p \cos\eta_p - z_p \sin\eta_p)^2 + y_p^2}}{x_p \sin\eta_p + z_p \cos\eta_p}\right). \tag{2.38}$$

The replacement of D by D_e only corrects for the general increase in sensitivity, it neglects the possibility that this increase in sensitivity also depends on the position

in the part of space visible through the pinhole aperture. There is however good reason to believe that this increase in sensitivity also depends on the angle τ, since the penetration path lengths and hence the chance for successful penetration depend on it. Smith *et al.* [14] demonstrated that for $\eta_p = 0$ this is indeed not generally the case and that the true sensitivity of a realistic knife edge pinhole aperture can be more accurately described by replacing $\cos^3\tau$ in (2.37) by $\cos^{n_p}\tau$

$$S_p(x_p, y_p, z_p) = \frac{D_e^2 \cos^{n_p}\tau}{16(x_p \sin\eta_p + z_p \cos\eta_p)^2} \tag{2.39}$$

in which n_p is a real number usually slightly larger than 3. The fact that $n_p \geq 3$ indicates that the increase in sensitivity by photon penetration is most prominent for $\tau = 0$ and that this effect decreases for larger values of τ. The exact values of n_p and D_e depend on the design of the pinhole aperture and will be determined experimentally later on (for pinhole apertures with sufficiently large acceptance angles α). In (2.39) we consider the findings of Smith *et al.* to be valid as well for $\eta_p \neq 0$. Although this has never been reported in literature, it will at least be a reasonable approximation for low values of η_p, since the approximation is known to be good at $\eta_p = 0$.

For the typical knife-edge aperture of figure 2.8 (a) and (b), the acceptance angle α limits the visible part of space in front of the aperture approximately to a cone with vertex angle α. Outside this cone, i.e. at $\tau > \alpha/2$, the sensitivity drops to zero, but not instantaneously since the finite diameter D (or D_e) and the finite plate thickness T still allow photons travelling at slightly higher angles of τ to pass. For pinhole apertures with large acceptance angles α and zero inclination η_p, this observation does not have serious implications, since at high values of $\tau > \alpha/2$ the sensitivity would be very low anyway, due to the factor $\cos^{n_p}\tau$ in the numerator of (2.39). For small acceptance angles α however, with potentially nonzero inclination angles η_p, the drop in sensitivity needs to be addressed.

To do so, consider the general case of a knife-edge aperture with (small) acceptance angle α and inclination angle η_p, as illustrated in figure 2.9. Besides the circular pinhole aperture opening E_c, the conical resections of the collimator material yield two elliptical intersections E_f and E_b with the front and back plane of the collimator plate respectively. Ignoring the possibility of penetration, the straight trajectory of a photon must pass through all three ellipses E_c, E_f and E_b for the photon to pass through the collimator. For point sources at sufficiently large distances from the pinhole aperture, all photons emitted by the point source through the circular area E_c can further be assumed to travel all parallel to each other. The area available for those photons to pass through the collimator can thereby be calculated as the common area E of the orthogonal projections of E_c, E_f and E_b on a plane perpendicular to the photon paths, as illustrated in figure 2.9. In general, the area $E(\alpha, D, T, \eta_p, x_p, y_p, \tau)$ depends on the aperture parameters α, D, T, η_p and the point source position $\arccos(x_p/y_p), \tau$. For $\eta_p = 0$, the dependency reduces to $E(\alpha, D, T, \tau)$. For point sources within the expected conical field of view $\tau \leq \alpha/2$, this area E is exactly the area of the pinhole aperture ($E_c \cos\tau$) or ($\pi D^2 \cos\tau/4$) as seen by the point source. For point sources just outside this cone $\tau > \alpha/2$, the

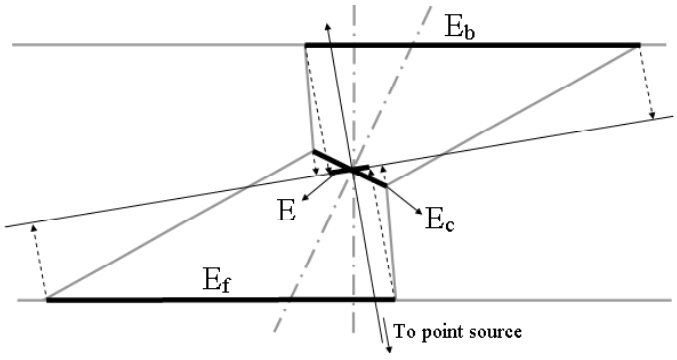

Figure 2.9: Sensitivity model of a small acceptance angle knife edge pinhole aperture. Without penetration, the sensitivity of the aperture for photons from a specific direction is proportional to the area available for the photons to pass. This area is calculated as the area of overlap E of the orthogonal projection of the ellipses E_f, E_b and E_c defined by the aperture design on a common plane orthogonal to the photon paths.

projections of the ellipses E_f and E_b will only partially overlap with the projection of the actual aperture opening E_c, yielding lower sensitivities for increasing values of τ until zero sensitivity is reached. Appendix A.1 elaborates on how the overlap E is calculated.

To correct for the different behavior of the sensitivity $S_p(x_p, y_p, z_p)$ at the edge of its field of view, the effective aperture area $\pi D_e^2 \cos\tau/4$ in (2.39) is substituted by an equivalent effective area E_e, yielding

$$S_p(x_p, y_p, z_p) = \frac{E_e \cos^{(n_p-1)}\tau}{4\pi(x_p \sin\eta_p + z_p \cos\eta_p)^2}. \tag{2.40}$$

Please note however that the 'effective' area E_e is only introduced to keep the above expression general for both large and small acceptance angles. For small acceptance angles, photon penetration is actually ignored. Other models of pinhole sensitivity, taking penetration into account, have been developed as well [15–17], but only for zero inclination angles η_p.

The description of the pinhole sensitivity at the end of section 2.4.1 in terms of the distance $z_p^2/\cos^2\tau_p$ and the additional factor $\cos\tau$ was inspired by the geometrical meaning of these factors in the derivation of (2.35). In practice however, it is more convenient to use the factors $1/(x_p \sin\eta_p + z_p \cos\eta_p)^2$ and $E_e(\tau)\cos^{(n_p-1)}\tau$, which we will call (somewhat erroneously) the 'distance dependency' and the 'angular dependency' respectively. The advantage of this description is the separation of the parameters z_p and τ which will become particularly convenient, since the parameter τ is related by a simple geometrical relation to a specific position on the detector, while this detector position bears no unique relation to a specific value of z_p. As a consequence, a pinhole projection image contains direct information about

the angle τ, but provides no information about the parameter z_p. As a result, an individual pinhole projection can be corrected for the angular pinhole sensitivity, but it can never be corrected for the distance dependent sensitivity. This will play a crucial role when discussing sensitivity correction in pinhole reconstruction.

2.5 Pinhole Spatial Resolution

2.5.1 Pinhole Point Spread Function

The single pinhole mapping function $M_p((x, y, z) \mapsto (u, v, \theta))$ of (2.28) and its related mapping function $M_p^T((u, v, \theta) \mapsto (x, y, z))$ of (2.32) assume that each arbitrary point source (x, y, z) projects on a single point (u, v) in each projection image. This assumption would only be true if both the effective pinhole aperture area as well as the intrinsic spatial resolution of the detector were infinitely small. In reality this assumption will never be satisfied and as a result the projection of a point source always yields a distribution of photon counts around the point predicted by the mapping function $M_p((x, y, z) \mapsto (u, v, \theta))$. See for example figure 2.7 as an illustration. The number of photons in this distribution depends on the activity A of the point source and the pinhole sensitivity $S(x, y, z)$, which have been studied in the previous section. This section studies the shape of the above distribution and its position in the uv projection image. The combination of shape and location defines the pinhole point spread function $PSF(x, y, z, u, v, \theta)$, which is a natural extension of the above mapping function M_p. This point spread function PSF does not depend on the total number of photon counts and it satisfies by definition

$$\iint_{-\infty}^{\infty} PSF(x, y, z, u, v, \theta)\,\mathrm{d}u\,\mathrm{d}v = 1 \quad \forall x, y, z, \theta. \tag{2.41}$$

Taking this non-ideal point spread function into account during projection and backprojection, in theory, simply requires the substitution of the mapping function M_p and its transpose in (2.28) and (2.32) respectively, by the appropriate point spread function $PSF(x, y, z, u, v, \theta)$ and its transpose. In image reconstruction, this approach is called resolution recovery and it yields reconstructed images with optimal spatial resolution. This spatial resolution is a measure of how well fine details of the original activity distribution are still visible in the reconstructed image. It is usually expressed as the full width at half maximum (FWHM) of the reconstruction of a point source (Dirac impulse). In practice, the efficient implementation of resolution recovery for pinhole image reconstruction is difficult however and it is only addressed briefly in section 9.2.3 about future research. As a result the spatial resolution of the reconstructed images in this work will be suboptimal. This section only provides a small overview of the pinhole point spread function and its effect on the spatial resolution.

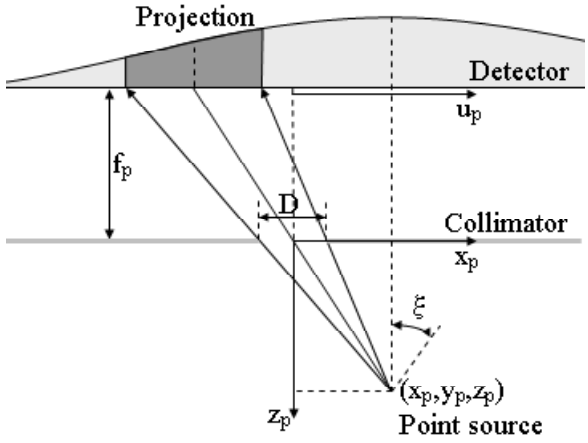

Figure 2.10: Projection (dark gray distribution) of a point source (x_p, y_p, z_p) through an ideal pinhole aperture with diameter D on a detector at a distance f_p behind the collimator. The pinhole aperture is located at the origin of the $x_p y_p z_p$ coordinate system. The light gray distribution is the projection of the point source onto the detector in absence of the pinhole collimator. The intrinsic spatial resolution of the detector is not taken into account.

2.5.2 Ideal Pinhole Point Spread Function

To study the pinhole point spread function $PSF(x, y, z, u, v, \theta)$, we return, like we did for the sensitivity, to the aperture specific $x_p y_p z_p$ and $u_p v_p$ coordinate systems. Consider again a point source of activity A at position (x_p, y_p, z_p) in the field of view of an ideal pinhole camera, as illustrated in figure 2.10. For the moment, we further assume an infinitely small intrinsic spatial resolution of the detector. In absence of the pinhole collimator, the point source would illuminate the entire scintillation crystal. For each infinitely small area $\mathrm{d}u_p\,\mathrm{d}v_p$ at position (u_p, v_p) of the detector, the photon flux would then depend on the solid angle occupied by that area with respect to the point source, yielding a photon flux of

$$A\frac{\cos^3\xi}{4\pi(f_p+z_p)^2}\,\mathrm{d}u_p\,\mathrm{d}v_p \tag{2.42}$$

with

$$\xi = \arctan\left(\frac{\sqrt{(u_p-x_p)^2+(v_p-y_p)^2}}{f_p+z_p}\right). \tag{2.43}$$

Normalization of (2.42), such that relation (2.41) is satisfied, yields the point spread function $PSF_0(u_p, v_p, x_p, y_p, z_p)$ for the projection of a point source (x_p, y_p, z_p) on an uncollimated detector with perfect intrinsic spatial resolution

$$PSF_0(u_p, v_p, x_p, y_p, z_p) = \frac{1}{N_0}\cos^3\xi. \tag{2.44}$$

In this expression N_0 is a simple normalization constant

$$N_0 = \iint_{-\infty}^{\infty} \cos^3 \xi \, \mathrm{d}u_p \, \mathrm{d}v_p. \tag{2.45}$$

As illustrated in figure 2.10, pinhole collimation blocks all photons not travelling through the circular pinhole aperture area with radius D, denoted E_c in section 2.4.3

$$\begin{array}{ccc} x_p^2 + y_p^2 & \leq & \frac{D^2}{4} \\ z_p & = & 0 \end{array} . \tag{2.46}$$

This pinhole aperture area E_c is projected by the point source (x_p, y_p, z_p) on the circular area C in the projection image

$$\left(u_p + \frac{f_p x_p}{z_p}\right)^2 + \left(v_p + \frac{f_p y_p}{z_p}\right)^2 \leq \frac{D^2}{4} \frac{(f_p + z_p)^2}{z_p^2}. \tag{2.47}$$

The restriction of the original point spread function $PSF_0(u_p, v_p, x_p, y_p, z_p)$ to the circular area C yields, after normalization to satisfy (2.41), the new point spread function $PSF_1(u_p, v_p, x_p, y_p, z_p)$

$$\begin{array}{lll} PSF_1(u_p, v_p, x_p, y_p, z_p) & = \frac{1}{N_1} \cos^3 \xi & (u_p, v_p) \in C \\ & = 0 & (u_p, v_p) \notin C \end{array} \tag{2.48}$$

with

$$N_1 = \iint_C \cos^3 \xi \, \mathrm{d}u_p \, \mathrm{d}v_p \tag{2.49}$$

and ξ like in (2.43). In this point spread function $PSF_1(u_p, v_p, x_p, y_p, z_p)$, the contribution of the finite pinhole aperture area E_c is modelled. For future purposes, please note that the function $\cos^3 \xi$ will generally not vary significantly over the circular area C (provided that the pinhole diameter D is sufficiently small in comparison with the z_p coordinate of the point source). In that case, the function $\cos^3 \xi$ can by approximation be considered constant over the circular area C, yielding

$$\begin{array}{lll} PSF_1(u_p, v_p, x_p, y_p, z_p) & = \frac{1}{N_1} & (u_p, v_p) \in C \\ & = 0 & (u_p, v_p) \notin C \end{array} \tag{2.50}$$

with

$$N_1 = \iint_C \mathrm{d}u_p \, \mathrm{d}v_p. \tag{2.51}$$

Besides the finite pinhole aperture area E_c, the limited intrinsic spatial resolution of the scintillation detector also contributes to the actual pinhole point spread function $PSF(u_p, v_p, x_p, y_p, z_p)$. This intrinsic spatial resolution results in a blurring of the projection image. In reality, this blurring is usually to a good approximation shift invariant and can be well modelled by a 2D Gaussian blurring with a FWHM of approximately 4.0 mm for current scintillation detectors. As a result, the actual ideal pinhole point spread $PSF(u_p, v_p, x_p, y_p, z_p)$ can be expressed as

$$PSF(u_p, v_p, x_p, y_p, z_p) = PSF_1(u_p, v_p, x_p, y_p, z_p) \otimes PSF_2(u_p, v_p) \tag{2.52}$$

in which $\otimes$ denotes a 2D convolution in the $u_p v_p$ projection space and $PSF_2(u_p, v_p)$ denotes a 2D Gaussian blurring kernel with the appropriate FWHM

$$PSF_2(u_p, v_p) = \frac{4 \ln 2}{\pi \, \mathrm{FWHM}^2} \exp\left(-\frac{4 \ln 2 \, (u_p^2 + v_p^2)}{\mathrm{FWHM}^2} \right). \tag{2.53}$$

In contrast to the aperture contribution PSF_1, the blurring effect of the intrinsic spatial resolution PSF_2 can easily be modelled during reconstruction by a simple convolution of the projection image after projection and before backprojection with the smoothing kernel PSF_2. Given the simplicity of this operation, this part of resolution recovery is performed during image reconstruction in this work, yielding a partial resolution recovery. The aperture contribution PSF_1 is much more difficult to model efficiently in projection and backprojection and forms the real challenge of pinhole SPECT resolution recovery.

2.5.3 Realistic Pinhole Point Spread Function

As explained in section 2.4.2, the design of real knife-edge pinhole apertures differs considerably from the ideal pinhole collimator model of the previous section. Just like for the pinhole sensitivity $S(x, y, z)$, this difference in design has its implications for the point spread function $PSF(x, y, z, u, v, \theta)$, or more specifically for the aperture contribution $PSF_1(x, y, z, u, v, \theta)$. Although the derivation of a more realistic pinhole point spread function is beyond the scope of this work, a couple of simple observations allow to get some intuitive appreciation of the expected changes to the above ideal point spread function.

First of all, the photon penetration through the flanking material of the actual pinhole aperture will widen the nonzero part of above point spread function, since photons will also be detected outside the circular area C of (2.47). Furthermore, the approximate point spread function of (2.52) and (2.50) is circularly symmetrical about the theoretically predicted point source projection. As already discussed in section 2.4.2, the photon penetration for point sources off the pinhole central ray is asymmetrical. As a result, the realistic pinhole point spread function for point sources off the pinhole central ray will become asymmetrical as well. Since this penetration effect is most prominent for large acceptance angles α, the widening of the pinhole point spread function and the degree of asymmetry, can be expected to become more pronounced at larger acceptance angles α.

At the edge of the field of view, i.e. where $\tau \simeq \alpha/2$, another and probably more severe effect will emerge, caused by the combination of the nonzero pinhole aperture diameter D and the limited thickness T of the pinhole aperture plate. At this edge of the field of view, the contribution of the finite pinhole aperture area can be expected to reduce significantly in the direction orthogonal to the edge, as is illustrated in figure 2.11. This is the result of the fact that the width of the overlap between the projected ellipses E_f, E_b and E_c (see section 2.4.2) reduces significantly in the direction orthogonal to the edge when τ passes $\alpha/2$.

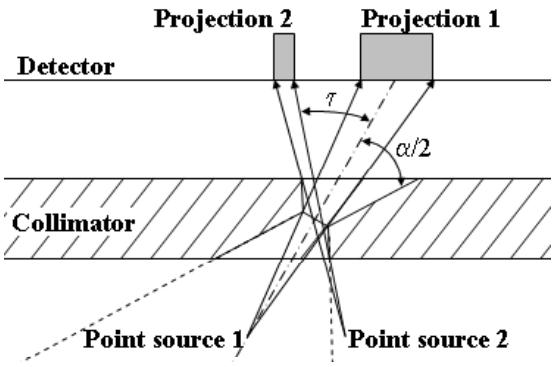

Figure 2.11: Projection of a point source in the center (1) and at the edge (2) of the pinhole field of view. In situation (2) the width of the point spread function is considerably reduced with respect to the width in situation (1). The intrinsic spatial resolution of the detector is not taken into account.

2.5.4 Pinhole Spatial Resolution

The fact that a point source (x, y, z) is not projected as a single point in the uv projection image, but as the distribution $PSF(x, y, z, u, v, \theta)$ with nonzero extent in uv space, indicates that spatial information is irretrievably lost during projection. The distribution $PSF(x, y, z, u, v, \theta)$ can in this respect (by approximation) be considered as a spatial (low-pass) filter acting locally on the ideal projection data. The loss in spatial information is directly related to the spatial frequencies lost in this filtering step. During reconstruction, even when performing resolution recovery, this will eventually result in a loss of spatial resolution in the reconstructed image, since the highest spatial frequencies of the original activity distribution can not be reconstructed by a lack of information. It is very difficult to predict how the spatial resolution of the reconstructed images will exactly be affected, especially for the non-linear MLEM reconstruction algorithm used throughout this work (see chapter 3). The notion that the point spread function can be considered as a locally acting spatial filter nevertheless allows us to get an appreciation of its effect.

For this appreciation, we study the smoothing effect in a one-dimensional cross-section $PSF_c(u_p, z_p)$ of the ideal point spread function $PSF(u_p, v_p, x_p, y_p, z_p)$ (2.52) with approximation (2.50) applied. (Please note that we only study this cross section as a filter, of which the shape is independent from x_p and y_p by approximation (2.50), so PSF_c does not need to depend on x_p or y_p.) We assume that the smoothing effect of the 2D point spread function $PSF(u_p, v_p, x_p, y_p, z_p)$ is sufficiently similar. Under these approximations, the resulting 1D smoothing function $PSF_c(u_p, z_p)$ can be written as the convolution

$$PSF_c(u_p, z_p) = PSF_{c1}(u_p, z_p) \otimes PSF_{c2}(u_p) \tag{2.54}$$

with $PSF_{c1}(u_p, z_p)$ being a block function representing the contribution of the pin-

hole aperture

$$\begin{aligned} PSF_{c1}(u_p, z_p) &= \tfrac{1}{D}\tfrac{z_p}{f_p+z_p} & u_p &\in \left[-D\tfrac{f_p+z_p}{2z_p}, D\tfrac{f_p+z_p}{2z_p}\right] \\ &= 0 & u_p &\notin \left[-D\tfrac{f_p+z_p}{2z_p}, D\tfrac{f_p+z_p}{2z_p}\right] \end{aligned} \tag{2.55}$$

and $PSF_{c2}(u_p)$ being a 1D Gaussian smoothing kernel representing the contribution of the intrinsic spatial resolution of the detector

$$PSF_{2c}(u_p) = \frac{\sqrt{4\ln 2}}{\sqrt{\pi}\,\mathrm{FWHM}} \exp\left(-\frac{(4\ln 2)\,u_p^2}{\mathrm{FWHM}^2}\right). \tag{2.56}$$

The frequency response of the above filter $PSF_c(u_p, z_p)$, its fourier transform $\mathcal{F}_u$, is easily calculated, yielding

$$\mathcal{F}_u\{PSF_c\}(k_u, z_p) = \mathcal{F}_u\{PSF_{c1}\}(k_u, z_p)\,\mathcal{F}_u\{PSF_{c2}\}(k_u) \tag{2.57}$$

with

$$\mathcal{F}_u\{PSF_{c1}\}(k_u, z_p) = \mathrm{sinc}\left(\pi D\frac{f_p + z_p}{z_p}\,k_u\right) \tag{2.58}$$

and

$$\mathcal{F}_u\{PSF_{c2}\}(k_u) = \exp\left(\frac{-\pi^2\mathrm{FWHM}^2}{4\ln 2}\,k_u^2\right). \tag{2.59}$$

This frequency response consists of the product of a sinc function (2.58) and a Gaussian (2.59). This is also illustrated in figure 2.12 for a pinhole system with 170 mm focal length f, a pinhole diameter D of 2.0 mm, an intrinsic spatial resolution of 3.8 mm FWHM and for $z_p = 50.0$ mm. The sinc function models the contribution of the pinhole aperture to the pinhole point spread function, while the Gaussian models the contribution of the limited spatial resolution of the detector. Combined together, these contributions yield the solid line in figure 2.12. The frequency response shows that low spatial frequencies are reasonably well preserved, while higher spatial frequencies get increasingly suppressed. Please note that the spatial frequencies k_u have been corrected for the magnification effect of pinhole projection. In this way these spatial frequencies can be considered to be spatial frequencies in the reconstruction domain, instead of in the projection domain.

For optimal image reconstruction accuracy, resolution recovery tries to recover the original power of all spatial frequencies during image reconstruction. However, the lower the response of these spatial frequencies, the more difficult it is to recover them. To proceed, we somewhat arbitrarily assume that no spatial frequencies with a frequency response of less than 10% (see threshold in figure 2.12) can be recovered due to noise, while all other frequencies can be completely recovered. This situation would result in the spatial frequency response, called 'recovered' in figure 2.12 and represented by the dashed line (long dashes). In a more realistic approach, a Wiener filter could be applied to take the actual power spectrum of the noise into account. In order to express this frequency response of the reconstruction in terms of a FWHM, it is finally transferred back into image space by an inverse fourier

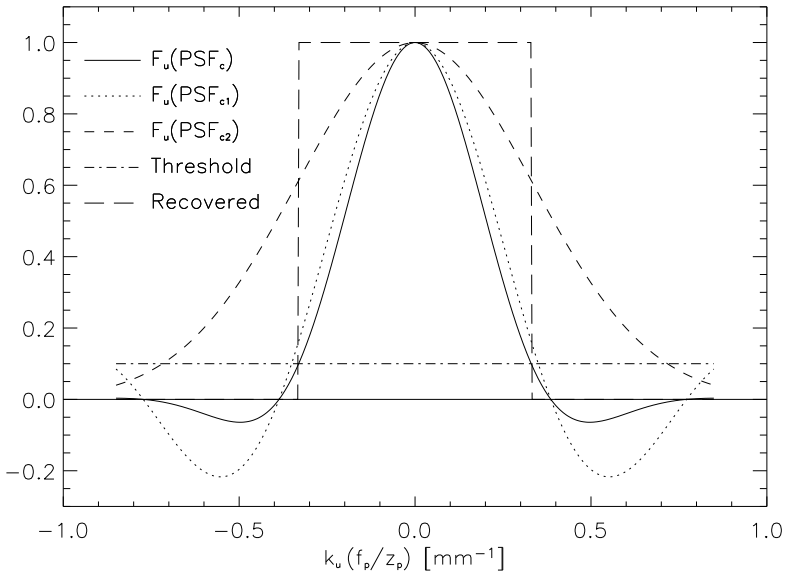

Figure 2.12: 1D ideal pinhole point spread function (solid line), with the contributions of the pinhole aperture (dotted line) and the intrinsic spatial resolution of the detector (dashed line). The block function (long dashed line) shows which spatial frequencies have a response above (1) or below (0) the threshold indicated by the dash-dotted line. The spatial frequencies k_u have been corrected for the magnification effect of pinhole projection.

transform. The result is shown in figure 2.13. This distribution can be considered to be the response of the reconstruction process to the pinhole projection of a point source. The FWHM of the resulting point source reconstruction can eventually be calculated, yielding a FWHM of 1.82 mm in this particular situation. Without resolution recovery, the spatial resolution of the reconstructed point source would be worse.

2.6 Conclusion

In this chapter, we have described the basics for understanding the image acquisition process in single and multipinhole SPECT imaging. In combination with the discussion of the pinhole SPECT acquisition geometry, it is essential knowledge to tackle the image reconstruction problem of the next chapter. The acquisition geometry will also serve as a basis for appreciating and understanding the pinhole calibration problem encountered in chapters 4, 5 and 7. The description of the pinhole sensitivity will proof to be of interest for the sensitivity correction in pinhole

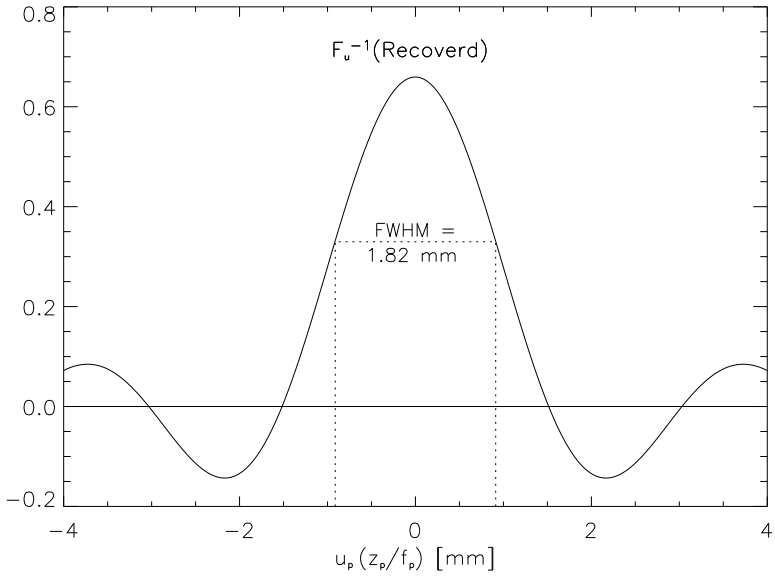

Figure 2.13: Reconstruction of the pinhole projection of a point source.

SPECT image reconstruction, also encountered in the next chapter. The description of the pinhole point spread function was mainly added for completeness, although it does have some implications on the measurement of the pinhole sensitivity in the next chapter.

Chapter 3

Pinhole SPECT Reconstruction

3.1 Introduction

This chapter explains the iterative MLEM algorithm, used throughout this work for single and multipinhole image reconstruction. Section 3.2 provides a general derivation of the MLEM algorithm, applicable to all image reconstruction in nuclear medicine. Section 3.3 elaborates on the incorporation of pinhole sensitivity correction in the MLEM algorithm and its relation with the sampling strategy of the practical implementation of the MLEM algorithm. Section 3.4 then proposes a method to measure the pinhole sensitivity in practice and demonstrates it by two real sensitivity measurements. Section 3.5 eventually comments on the effects of the spatial resolution of pinhole collimation on pinhole SPECT image reconstruction.

3.2 MLEM Image Reconstruction

This section provides a general introduction to the *Maximum Likelihood Expectation Maximization* or *MLEM* algorithm [18–20], which is by far the most popular iterative image reconstruction algorithm in nuclear medicine. Various non-iterative image reconstruction algorithms for pinhole SPECT tomography exist as well, and they are generally faster than the iterative ones [6, 21–27]. Nevertheless we choose the iterative MLEM algorithm for 3 reasons.

1. MLEM only needs a forward projection model and not the inverse model. This makes MLEM easy to derive and implement and also facilitates modifications and corrections, like sensitivity correction.
2. MLEM takes the Poisson nature of the noise of the pinhole projection images into account, thereby reducing noise artifacts in the reconstructed images.

3. MLEM is known to be robust in tomography applications where insufficient information is available about the image to be reconstructed, as is the case in traditional single pinhole imaging (circular orbit).

The MLEM algorithm implicitly assumes that the activity distribution $A(x, y, z)$, its projection data $Q(u, v, \theta)$ and its reconstruction $\Lambda(x, y, z)$ all exist in a digital form. In practice, this is true for the projection data Q and the reconstruction Λ, but the activity distribution $A(x, y, z)$ is actually a continuous distribution. By performing MLEM reconstruction, we assume nevertheless that the distribution A can to a good approximation be represented in a digital way.

3.2.1 Maximum Likelihood

The MLEM algorithm aims at maximizing the likelihood $p(\Lambda|Q)$ that the reconstruction Λ would yield the projection data Q. By Bayes' rule, this likelihood $p(\Lambda|Q)$ can be further expressed as

$$p(\Lambda|Q) = \frac{p(Q|\Lambda)p(\Lambda)}{p(Q)} \tag{3.1}$$

in which $p(Q|\Lambda)$ expresses the likelihood to obtain the projection data Q from the reconstruction Λ and $p(\Lambda)$ expresses the likelihood of the reconstruction image itself. The denominator $p(Q)$ finally expresses the likelihood of the projection data, which is constant, since the projection data Q have already been obtained previous to reconstruction. In the regular MLEM case, no assumptions are made about the reconstruction Λ, so $p(\Lambda)$ is a constant as well. Consequently, optimizing $p(\Lambda|Q)$ is equivalent to optimizing $p(Q|\Lambda)$, which is much easier to calculate.

To do so, we first have to calculate the projection data that we expect to obtain from the reconstruction Λ. This was already done in (2.26) to (2.28), but here we need a digital version

$$r_i = \sum_{j=1}^{J} c_{ij}\lambda_j, \quad i = 1, ..., I. \tag{3.2}$$

In this expression, $r_i \in R$ is the number of photon counts in pixel i of the expected projection data R (i combines the parameters u, v, θ), $\lambda_j \in \Lambda$ is voxel j of the reconstruction Λ (j combines the coordinates x, y, z) and c_{ij} represents the sensitivity of projection pixel i for activity in reconstruction voxel j. Referring to (2.26) to (2.28), c_{ij} takes the sensitivity $S_{\theta p}$ and the mapping $M_{\theta p}$ into account and this simultaneously for all pinhole apertures $p = 1, ..., P$. The digital summation further takes the continuous integration into account.

By the nature of nuclear medicine imaging, the measured data q_i are Poisson realizations of the expected data r_i, calculated in (3.2), and different measurements q_i and q_{i^*} ($i \neq i^*$) are independent from one another. From Poisson statistics, the likelihood $p(q_i|r_i)$ of measuring q_i counts in pixel i, when r_i counts are actually expected is given by

$$p(q_i|r_i) = \frac{r_i^{q_i}\exp(-r_i)}{q_i!}. \tag{3.3}$$

Since the measurements q_i with $i = 1, ..., I$ are all independent, the likelihood $p(Q|\Lambda)$ of measuring the projection data Q from the activity distribution Λ is simply the product of the individual likelihoods $p(q_i|r_i)$ over $i = 1, ..., I$

$$p(Q|\Lambda) = \prod_i \frac{r_i^{q_i} \exp(-r_i)}{q_i!}. \tag{3.4}$$

Relation (3.4) expresses the likelihood $p(Q|\Lambda)$ to be optimized with respect to the reconstruction Λ in the ML approach. Since the natural logarithm is a monotonically increasing function, optimizing the likelihood $p(Q|\Lambda)$ is further equivalent to optimizing the log-likelihood $L(Q|\Lambda) = \ln(p(Q|\Lambda))$. By substituting (3.2) into (3.4), taking the natural logarithm of (3.4) and omitting the terms independent of the Λ we obtain

$$L(Q|\Lambda) = \sum_i q_i \ln(r_i) - r_i \tag{3.5}$$

$$= \sum_i q_i \ln(\sum_j c_{ij}\lambda_j) - \sum_j c_{ij}\lambda_j. \tag{3.6}$$

It has been shown that the Hessian of $L(Q|\Lambda)$ is negative definite when the matrix $C = \{c_{ij}\}$ is of full rank [18,19]. This means that in that case, the likelihood $L(Q|\Lambda)$ has a single maximum with respect to Λ and so the ML reconstruction has a unique solution Λ. In conventional parallel hole imaging, the matrix C will generally be of full rank, when a sufficient number of projection angles θ is used during image acquisition. For the traditional pinhole SPECT acquisition trajectory A of figure 2.3, the matrix C (which performs the mapping operation M) will never be of full rank, regardless of the number of projection angles θ, since the trajectory does not satisfy the data sufficiency criteria of [5–7]. As discussed before, we simply proceed anyway, assuming that the ML approach will nevertheless yield a useful solution Λ.

3.2.2 Expectation Maximization

The conventional approach for optimizing any function $f(x)$, is to set its first derivative to 0 and solve for x. Applying this approach to the likelihood $L(Q|\Lambda)$ results in a nonlinear system of equations in the unknowns λ_j

$$\frac{\partial L}{\partial \lambda_j} = \sum_i c_{ij} \left(\frac{q_i}{\sum_k c_{ik}\lambda_k} - 1 \right) = 0 \quad \forall j = 1, ..., J. \tag{3.7}$$

The *Expectation Maximization* or *EM* approach provides an iterative solution to this inversion problem, yielding a very simple expression for emission tomography. Because of the complexity of the mathematical theory behind the *EM* approach, we limit ourselves to a simple illustration of the EM algorithm and refer to the literature for a more detailed explanation [18, 19].

The EM algorithm starts from the complete variables $X = \{x_{ij}\}$, which represent the number of photons emitted from the reconstruction voxel j to the detector

pixel i and which are assumed to be Poisson distributed. Of course, the complete variables X cannot be measured directly, but they relate to the projection data Q in a simple way

$$q_i = \sum_{j=1}^{J} x_{ij}. \tag{3.8}$$

Similar to the projection data q_i ($r_i = E(q_i|\Lambda)$), the expectation $E(x_{ij}|\Lambda)$ of the complete variables x_{ij} given the reconstruction image $\Lambda = \{\lambda_j\}$ can be calculated as

$$E(x_{ij}|\Lambda) = c_{ij}\lambda_j \tag{3.9}$$

and the log-likelihood L_x of the complete variables can be calculated as

$$L_x(X|\Lambda) = \sum_i \sum_j x_{ij} \ln(c_{ij}\lambda_j) - c_{ij}\lambda_j. \tag{3.10}$$

Since the complete variables x_{ij} cannot be measured, it is impossible to evaluate the likelihood L_x in practice, but we can evaluate its expected value $E(L_x(X|\Lambda)|Q, \Lambda^{old})$ when the projection data Q and an old estimate Λ^{old} of the reconstruction Λ are available

$$E(L_x(X|\Lambda)|Q, \Lambda^{old}) = \sum_i \sum_j n_{ij} \ln(c_{ij}\lambda_j) - c_{ij}\lambda_j \tag{3.11}$$

with

$$n_{ij} = E(x_{ij}|Q, \Lambda^{old}) = c_{ij}\lambda_j^{old} \frac{q_i}{\sum_k c_{ik}\lambda_k^{old}}. \tag{3.12}$$

In these expressions, n_{ij} represents the expected value of x_{ij} when both the projection data Q and the old reconstruction Λ^{old} are available. This expected value combines the expected value $E(x_{ij}|\Lambda)$ of (3.9) with the restriction derived from (3.8) that

$$q_i = \sum_{j=1}^{J} E(x_{ij}|Q). \tag{3.13}$$

The EM theory shows that *maximizing* (3.11) with respect to Λ, also *improves* L_x and L. The optimization of (3.11) is straightforward. Setting the first derivative equal to 0 yields

$$\frac{\partial E(L_x(X|\Lambda)|Q, \Lambda^{old})}{\partial \lambda_j} = \sum_i \left(\frac{n_{ij}}{\lambda_j} - c_{ij} \right) = 0 \quad \forall j = 1, ..., J \tag{3.14}$$

yielding

$$\lambda_j^{new} = \lambda_j = \frac{\sum_i n_{ij}}{\sum_i c_{ij}} \quad \forall j = 1, ..., J. \tag{3.15}$$

Note that $\Lambda_j^{new} = \{\lambda_j^{new}\}$ maximizes $E(L_x(X|\Lambda)|Q, \Lambda^{old})$, but it only improves L_x and L. The EM theory proves however that repeating the above process, continuously improves L until the maximum of L is reached. The substitution of (3.12) into

(3.15) eventually yields a simple update step to iteratively improve the likelihood L

$$\lambda_j^{new} = \frac{\lambda_j^{old}}{\sum_i c_{ij}} \sum_i c_{ij} \frac{q_i}{\sum_k c_{ik}\lambda_k^{old}} \quad \forall j = 1, ..., J. \tag{3.16}$$

This equation describes the MLEM algorithm. It is continuously repeated until convergence, starting from an arbitrary initial image $\Lambda^{init} = \{\lambda^{init} > 0\}$. Although the above derivation is strongly based on Poisson statistics, an alternative non-statistical derivation can be found in the work of De Pierro *et al.* [20].

3.2.3 Projection and Backprojection

The MLEM algorithm mainly consists of two operations: the projection $\sum_k c_{ik}\lambda_k^{old}$ in the second denominator and the backprojection $\sum_i c_{ij}t_i$ with $t_i = q_i / \sum_k c_{ik}\lambda_k^{old}$. The digital version of the projection operation was already defined in expression (3.2). In general, the digital projection operation $C = \{c_{ij}\}$ is a linear transformation of an image $\Lambda = \{\lambda_j\}$ in the image space j into the projection image $Q = \{q_i\}$ in the projection space i

$$q_i = \sum_{j=1}^{J} c_{ij}\lambda_j \quad \forall i = 1, ..., I. \tag{3.17}$$

Knowing that the coefficients c_{ij} model the projection lines created by the collimation of the detector, the projection operation can basically be considered as the integration of the activity along those lines, as can be seen by the summation sign in (3.17).

The backprojection operation C^T is defined as the transpose of the projection operation C and thereby performs a transformation from the projection space i back to the image space j. The backprojection of a projection image $Q = \{q_i\}$ yields the backprojection image $B = \{b_j\}$

$$b_j = \sum_{i=1}^{I} c_{ij}q_j \quad \forall j = 1, ..., J. \tag{3.18}$$

The backprojection reintroduces integrated activity of the projection back into the image space by distributing it uniformly along the projection lines. In each image voxel j, the contributions of all the projection lines intersecting that voxel are added together by the summation sign in (3.18). The continuous versions of the projection and backprojection operations were already defined in (2.26) to (2.32).

The observation that the MLEM algorithm consists of a sequential projection and backprojection operation yields some intuitive insight into how it actually works. First the current reconstruction estimate Λ^{old} is projected, yielding the expected projection data $\sum_k c_{ik}\lambda_k^{old}$ for the current reconstruction Λ^{old}. These estimated projection data are then compared with the measured projection data in the ratio $t_i = q_i / \sum_k c_{ik}\lambda_k^{old}$. This ratio is larger (smaller) than 1 for all projection

lines i for which the measured projection data are larger (smaller) than the expected data. In other words, the ratio t_i provides information about the excess or deficit of observed counts along the projection rays i. This information is backprojected back into the image space and multiplied with Λ^{old} to obtain a better reconstruction estimate Λ^{new}. The first denominator $\sum_i c_{ij}$ is only there for normalization.

3.3 Sampling & Sensitivity Correction

In the MLEM algorithm (3.16), the coefficients c_{ij} represent the sensitivity of projection pixel i for activity in reconstruction voxel j. It was already mentioned that these coefficients take both the pinhole sensitivities $S_{\theta p}(x, y, z)$ and the pinhole mapping functions $M_p((x, y, z) \mapsto (u, v, \theta))$ or $M_p^T((x, y, z) \mapsto (u, v, \theta))$ into account. The MLEM algorithm is thereby intrinsically capable of performing sensitivity correction during image reconstruction. The question remains however how these coefficients c_{ij} can be efficiently modelled in the projection and backprojection operations of a practical implementation of the MLEM algorithm and how the sensitivities $S_{\theta p}(x, y, z)$ can be measured in practice. The measurement of the actual pinhole sensitivity is deferred to section 3.4, this section deals with the modelling of the coefficients c_{ij} in the practical implementation of the projection and backprojection operation.

3.3.1 Projection Models

The projection operation performs a transition from the image domain of the 3D activity distribution A and its reconstruction Λ, to the projection domain of the set of 2D projection images Q, with one image for each projection angle θ. The activity distribution and its reconstruction are represented digitally by a 3D grid of voxels j, while each digital projection image is represented by a 2D grid of pixels i.

Two different implementations of the projection operation are commonly used in nuclear medicine imaging: voxel driven projection and ray driven projection. The voxel driven projection starts from the image domain and allocates the contribution of each reconstruction voxel j to the projection domain. These contributions can generally not be allocated to a specific projection pixel i however and this implementation thereby requires interpolation in the projection domain. Ray driven projection on the other hand starts from the projection domain and integrates the activity in the image domain along the projection ray L_i associated with each projection pixel i. The integration requires interpolation in the projection domain, since the projection rays L_i generally do not nicely intersect the grid of reconstruction pixels j. These differences in interpolation, cause some differences in terms of small interpolation artifacts, but these are not considered here.

In pinhole applications, the above models of the projection operation also yield a different sampling of the image domain however. In voxel driven projection, each image voxel is considered exactly once, yielding a homogeneous sampling pattern throughout the image domain. In ray driven projection, the sampling is typically

performed at equidistant locations along the projection rays. Because of the diverging beam geometry of the pinhole projection rays, this yields an inhomogeneous sampling of the image domain. These differences in sampling and their interaction with the pinhole sensitivity correction are studied in the next sections.

3.3.2 Voxel Driven Projection

To start, we return to the continuous version of the projection operation as derived in 2.2.5 for pinhole aperture p.

$$Q_p(u_p, v_p, \theta) = \iiint A(x_p, y_p, z_p, \theta)\, S_p(x_p, y_p, z_p)\, M_p \; \mathrm{d}x_p\, \mathrm{d}y_p\, \mathrm{d}z_p \tag{3.19}$$

with

$$M_p = M_p((x_p, y_p, z_p) \mapsto (u_p, v_p)) = \delta\left(-\frac{f_p x_p}{z_p} - u_p\right) \delta\left(-\frac{f_p y_p}{z_p} - v_p\right). \tag{3.20}$$

Note that the $x_p y_p z_p$ coordinate system is attached to the pinhole focal point and rotates over all projections angles θ. As a result the stationary activity distribution $A(x_p, y_p, z_p, \theta)$ depends on this projection angle θ. For the general case of a pinhole aperture with the pinhole central ray inclined by an angle η_p with respect to the system central ray, the sensitivity $S_p(x_p, y_p, z_p)$ was already derived in 2.4.3 (2.40).

$$S_p(x_p, y_p, z_p) = \frac{E_e(\tau, x_p, y_p) \cos^{(n_p-1)}\tau}{4\pi\,(x_p \sin\eta_p + z_p \cos\eta_p)^2} \tag{3.21}$$

with

$$\tau = \arctan\left(\frac{\sqrt{(x_p \cos\eta_p - z_p \sin\eta_p)^2 + y_p^2}}{x_p \sin\eta_p + z_p \cos\eta_p}\right). \tag{3.22}$$

The continuous projection model of (3.19) closely resembles the voxel-driven projection, since it samples the $x_p y_p z_p$ image domain in a homogeneous $\mathrm{d}x_p\, \mathrm{d}y_p\, \mathrm{d}z_p$ pattern, like the voxel-driven projection does by using the voxels of the image domain. In its current form, the above projection model (3.19) requires knowledge of the 3D sensitivity distribution $S_p(x_p, y_p, z_p)$ of (3.21). In the xyz coordinate system fixed in space, the sensitivity correction would even require a 4D function $S_p(x, y, z, \theta)$, while the activity distribution can then be expressed more conveniently as $A(x, y, z)$.

3.3.3 Ray Driven Projection

In the 'voxel driven projection' of the previous section, the pinhole projection image $Q_p(u_p, v_p, \theta)$ is obtained by simply integrating the contributions of each individual point (x_p, y_p, z_p) to $Q_p(u_p, v_p, \theta)$ over the field of view. The integration itself does not model the mapping from the $x_p y_p z_p$ space to the $u_p v_p \theta$ space of the

projection image and thereby requires the introduction of the mapping function $M_p((x_p, y_p, z_p) \mapsto (u_p, v_p))$. The explicit mapping of (3.19) can also be achieved implicitly by a simple change in integration

$$\begin{array}{rcl} x_{p1} = & -\frac{f_p x_p}{z_p} & \\ y_{p1} = & -\frac{f_p y_p}{z_p} & \text{with} \quad \mathrm{d}x\,\mathrm{d}y\,\mathrm{d}z = \frac{z_{p1}^2}{f_p^2}\,\mathrm{d}x_{p1}\,\mathrm{d}y_{p1}\,\mathrm{d}z_{p1}. \\ z_{p1} = & z_p & \end{array} \tag{3.23}$$

Substituting (3.23) and (3.20) in (3.19) yields

$$Q_p(u_p, v_p, \theta) = \int A_1(u_p, v_p, z_{p1}, \theta)\, S_{p1}(u_p, v_p, z_{p1})\, \frac{z_{p1}^2}{f_p^2}\, \mathrm{d}z_{p1} \tag{3.24}$$

in which $A_1(u_p, v_p, z_{p1}, \theta)$ and $S_{p1}(u_p, v_p, z_{p1})$ represent the original activity distribution $A(x_p, y_p, z_p, \theta)$ and the original pinhole sensitivity $S_p(x_p, y_p, z_p)$ in the new coordinate system $x_{p1}y_{p1}z_{p1}$ respectively.

$$A_1(u_p, v_p, z_{p1}, \theta) = A\left(-\frac{z_{p1}u_p}{f_p}, -\frac{z_{p1}v_p}{f_p}, z_{p1}, \theta\right) \tag{3.25}$$

$$S_{p1}(u_p, v_p, z_{p1}) = \frac{f_p^2}{z_{p1}^2}\, \frac{E_e(\tau, u_p, v_p)\cos^{n_p-1}\tau}{4\pi(f_p\cos\eta_p - u_p\sin\eta_p)^2} \tag{3.26}$$

with

$$\tau = \arctan\left(\frac{\sqrt{(f_p\sin\eta_p + u_p\cos\eta_p)^2 + v_p^2}}{f_p\cos\eta_p - u_p\sin\eta_p}\right). \tag{3.27}$$

The implicit mapping of this new way of integration is evident from the vanishing of the integrals over x_{p1} and y_{p1} and by the fact that x_{p1} and y_{p1} can be replaced by u_p and v_p respectively. As a result the angle τ can now be expressed in terms of u_p, v_p and f_p. Another important observation from (3.24) is that the Jacobian of the change in integration yields the factor z_{p1}^2, which will cancel out the distance dependency of the pinhole sensitivity $S_{p1}(u_p, v_p, z_{p1})$ like in [23, 28]. The substitution of (3.26) into (3.24) yields

$$Q_p(u_p, v_p, \theta) = S_{p1}^*(u_p, v_p) \int A_1(u_p, v_p, z_{p1})\, \mathrm{d}z_{p1} \tag{3.28}$$

with

$$S_{p1}^*(u_p, v_p) = \frac{E_e(\tau, u_p, v_p)\cos^{n_p-1}\tau}{4\pi(f_p\cos\eta_p - u_p\sin\eta_p)^2}. \tag{3.29}$$

In comparison with (3.19), expression (3.28) seems to offer the advantage that it only requires a single integration over $\mathrm{d}z_{p1}$ instead of the triple integral over $\mathrm{d}x_p\mathrm{d}y_p\mathrm{d}z_p$. This advantage is only apparent, since both ways of integration require an equal number of interpolations in practice. The true advantage of (3.28) comes from the fact that the correction function $S_{p1}^*(u_p, v_p)$ in front of the integral sign is only 2 dimensional, regardless whether it is expressed in the u_pv_p coordinate system or in

the uv coordinate system. As a result, this type of sensitivity correction requires less memory to store than the voxel driven sensitivity correction $S(x, y, z)$ and it also requires less computation time by a reduction in the number of computations.

Expression (3.28) already closely resembles a ray driven projection, in that the projection rays are implicitly modelled in the integration. However, in ray driven projection, the remaining integration would typically occur along the projection ray instead of in the direction $\mathrm{d}z_{p1}$, which is always orthogonal to the detector. This ray driven type of integration is easily obtained by a second change in integration

$$l_p = \frac{z_{p1}}{\cos\kappa} \quad \text{with } \mathrm{d}z_{p1} = \cos\kappa \,\mathrm{d}l_p \tag{3.30}$$

in which l_p is the coordinate along any projection ray (u_p, v_p) and κ is the angle between the projection ray (u_p, v_p) and the *system* central ray (τ is the angle between such projection ray and the *pinhole* central ray)

$$\kappa = \arctan\left(\frac{\sqrt{u_p^2 + v_p^2}}{f_p}\right). \tag{3.31}$$

Applying this change in integration to (3.29) eventually yields

$$Q_p(u_p, v_p, \theta) = S_{p2}(u_p, v_p) \int A_2(u_p, v_p, l_p, \theta)\ \mathrm{d}l_p \tag{3.32}$$

with

$$A_2(u_p, v_p, l_p, \theta) = A\left(-\frac{l_p u_p}{f_p}\cos\kappa, -\frac{l_p v_p}{f_p}\cos\kappa, l_p\cos\kappa, \theta\right) \tag{3.33}$$

and with

$$S_{p2}(u_p, v_p) = S^*_{p1}(u_p, v_p)\cos\kappa = \frac{E_e(\tau, u_p, v_p)\cos^{(n_p-1)}\tau\cos\kappa}{4\pi(f_p\cos\eta_p - u_p\sin\eta_p)^2}. \tag{3.34}$$

Note in (3.34) that the change in integration results in an additional factor $\cos\kappa$ in $S_{p2}(u_p, v_p)$ in comparison with the correction $S^*_{p1}(u_p, v_p)$ of (3.29).

Expression (3.32) is easily implemented in practice, since the integration is identical to a classical ray driven projector and the sensitivity correction is a simple multiplication of the resulting projection image with the 2D image $S_{p2}(u_p, v_p)$. The next step is to express the above relations in the xyz and uv coordinate systems, in which we can relate the sensitivity correction to the pinhole acquisition geometry and also provide an equivalent expression of the sensitivity corrected backprojection.

3.3.4 Projection and Backprojection

So far, the discussion of the pinhole sensitivity correction was limited to the sensitivity correction of projections. The MLEM algorithm requires this sensitivity correction to be performed both during projection and backprojection. To provide

a general expression for the continuous projection and backprojection, we need a change in coordinate system from the $x_p y_p z_p$ system attached to the pinhole focal point the xyz coordinate system fixed in space and an equivalent change from the $u_p v_p$ coordinate system to the uv system. Appendix A.2 provides the relations for this change of coordinate systems which requires the introduction of the angle ζ_p between the aperture specific $x_p y_p$ coordinate system and the non-aperture specific $x'''y'''$ coordinate system. With

$$u_p^* = u - m_{up} - e_u \tag{3.35}$$

$$v_p^* = v - m_{vp} - e_v \tag{3.36}$$

the substitution of (A.35) into (3.27), (3.29), (3.31) and (3.34) yields

$$S_{p1}^*(u,v) = \frac{E_e(\tau, u_p^*, v_p^*)\cos^{(n_p-1)}\tau}{4\pi(f_p\cos\eta_p - (u_p^*\cos\zeta_p + v_p^*\sin\zeta_p)\sin\eta_p)^2}, \tag{3.37}$$

$$S_{p2}(u,v) = \frac{E_e(\tau, u_p^*, v_p^*)\cos^{(n_p-1)}\tau\cos\kappa}{4\pi(f_p\cos\eta_p - (u_p^*\cos\zeta_p + v_p^*\sin\zeta_p)\sin\eta_p)^2}, \tag{3.38}$$

with

$$\tan\tau = \frac{\sqrt{(f_p\sin\eta_p + (u_p^*\cos\zeta_p + v_p^*\sin\zeta_p)\cos\eta_p)^2 + (u_p^*\sin\zeta_p - v_p^*\cos\zeta_p)^2}}{f_p\cos\eta_p - (u_p^*\cos\zeta_p + v_p^*\sin\zeta_p)\sin\eta_p} \tag{3.39}$$

and

$$\kappa = \arctan\left(\frac{\sqrt{u_p^{*2} + v_p^{*2}}}{f_p}\right). \tag{3.40}$$

With the above relations, the projection and backprojection can be rewritten as

$$Q_p(u,v,\theta) = S_{p2}(u,v)\int_{L_{\theta p}(u,v)} A(x,y,z)\ \mathrm{d}l_p. \tag{3.41}$$

$$B_p(x,y,z) = \int M_p^T((u,v,\theta)\mapsto(x,y,z))\, S_{p2}(u,v)\, Q_{\theta p}(u,v)\ \mathrm{d}\theta \tag{3.42}$$

with $M_p^T((u,v,\theta)\mapsto(x,y,z))$ as in (2.32).

Relation (3.38) and (3.39) may seem quite complicated, because of the nonzero angle η_p. For $\eta_p = 0$, as usual in single pinhole tomography, the above relations reduce to

$$S_{p2}(u_p,v_p) = \frac{E_e(\tau)\cos^{n_p}\tau}{4\pi\, f_p^2}, \tag{3.43}$$

$$\tau = \kappa = \frac{\sqrt{u_p^{*2} + v_p^{*2}}}{f_p}. \tag{3.44}$$

For a sufficiently large acceptance angle α of the pinhole aperture, (3.43) can be simplified even further (see section 2.4.3) to

$$S_{p2}(u_p, v_p) = \frac{D_e^2 \cos^{(n_p+1)}\tau}{16\, z_p^2}. \tag{3.45}$$

3.4 Measurement of Pinhole Sensitivity

3.4.1 Concept

The correction image $S_{p2}(u, v)$ of (3.38) provides a way to model the pinhole sensitivity in both projection and backprojection, which are the key operations in iterative reconstruction. Consequently, the correction image $S_{p2}(u, v)$ is all that is needed to perform sensitivity correction in iterative pinhole SPECT image reconstruction. This raises the question of how to measure this correction image in practice. The definition of pinhole sensitivity, immediately suggests that the true pinhole sensitivity $S(x, y, z)$ can be obtained by imaging a point source of known activity at various known positions in the field of view. Knowledge of the true pinhole sensitivity $S(x, y, z)$ should then in theory allow us to calculate the required correction image S_{p2}. Performing the above experiment in practice, is not only time consuming, but accurate positioning of the point source is also difficult to achieve unless additional dedicated equipment is available. This section shows how a flood source measurement, which is much easier to perform, can yield the same information. Such flood source, a thin plate of uniformly distributed activity, should be readily available at any nuclear medicine department and can also easily be created as a thin (horizontal) layer of a radioactive fluid.

Consider the measurement of a flood source of thickness T, by a pinhole camera. The flood source is positioned at a distance b in front of the pinhole aperture and parallel to the detector. To calculate the projection image $Q_p(u_p, v_p)$, obtained from this flood source measurement, we return to equation (3.28). In the $x_{p1}y_{p1}z_{p1}$ coordinate system, the activity distribution $A_{flood}(u_p, v_p, z_{p1}) = A_{flood}(z_{p1})$ is conveniently described as

$$A_{flood}(z_{p1}) = \begin{array}{lll} 0 & \text{for} & z_{p1} < b - T/2 \\ A & \text{for} & b - T/2 \le z_{p1} \le b + T/2. \\ 0 & \text{for} & z_{p1} > b + T/2 \end{array} \tag{3.46}$$

Substituting the activity distribution (3.46) in (3.28) yields

$$Q_p(u_p, v_p) = S^*_{p1}(u_p, v_p)AT. \tag{3.47}$$

Since $Q_p(u_p, v_p)$ is actually the result of the measurement of a pinhole camera, it is only known in the uv coordinate system. Applying the coordinate transformation (A.35) yields

$$Q_p(u, v) = S^*_{p1}(u, v)AT. \tag{3.48}$$

Equation (3.48) reveals that imaging a flood source immediately yields the correction image $S^*_{p1}(u,v)$ scaled by a constant factor AT. To obtain a scaled version of the required correction image $S_{p2}(u,v)$, the above image $S^*_{p1}(u,v)$ only needs to be multiplied with the image $\cos\kappa$, which is easily calculated from (3.40), provided that f_p, $(m_{up}+e_u)$ and $(m_{vp}+e_v)$ are known. The camera calibration method of the next chapter determines these parameters, so for the remainder of this chapter we can assume them to be known. The next sections demonstrate the application of the above concept in two different cases in practice.

3.4.2 Large Acceptance Angle

In single pinhole applications, the inclination angle η is usually equal to 0. The acceptance angle α is further often relatively large or can be assumed so, since only the high sensitivity part of the sensitivity correction image $S_2(u,v)$ at $\tau < \alpha/2$ can be used for imaging. As explained in section 2.4.3, the drop in sensitivity at the edge of the field of view $\tau \simeq \alpha/2$ can in this situation be neglected. The flood source measurement can now be expressed as

$$S^*_{p1}(u,v) = \frac{D_e^2 \cos^{n_p}\tau}{16\, f^2}. \tag{3.49}$$

Figure 3.1 (a) shows such a ^{57}Co flood source measurement performed on a GE Millennium MPR camera equipped with a single pinhole collimator of (approximately) 240 mm focal length f. The collimator has a pinhole aperture of 3 mm diameter D and a zero inclination angle η. The acceptance angle is approximately 75^o, but by the design of the collimator cone and the 1.85 cm thick collimator plate, only the central part of the detector at sufficiently low angles of τ can be used for imaging. Consequently, the measurement was collected in a 128x128 image matrix of 1.695x1.695 mm^2 pixels. A total of 15.3 million counts were collected overnight, yielding a maximum pixel count of 1242.

To calculate the sensitivity correction image S_2, the function

$$f(u,v) = \frac{B\cos^{n_p}\tau}{f^2}, \tag{3.50}$$

with $f = 240$ mm and

$$\tau = \arctan\left(\frac{\sqrt{(u-m_{up}-e_u)^2+(v-m_{vp}-e_v)^2}}{f}\right) \tag{3.51}$$

is fitted to the measurement, yielding the parameters B, n_p, $(m_{up}+e_u)$ and $(m_{vp}+e_v)$. The Poisson nature of the data is taken into account by performing weighted least square fitting. The fitted function $f(u,v)$ is shown in figure 3.1 (b) and is in excellent agreement with the measurement ($n_p = 3.09$). The parameters n_p, $(m_{up}+e_u)$ and $(m_{vp}+e_v)$ now allow us to calculate the sensitivity correction image

$$S_2(u,v) = \cos^{(n_p+1)}\tau \tag{3.52}$$

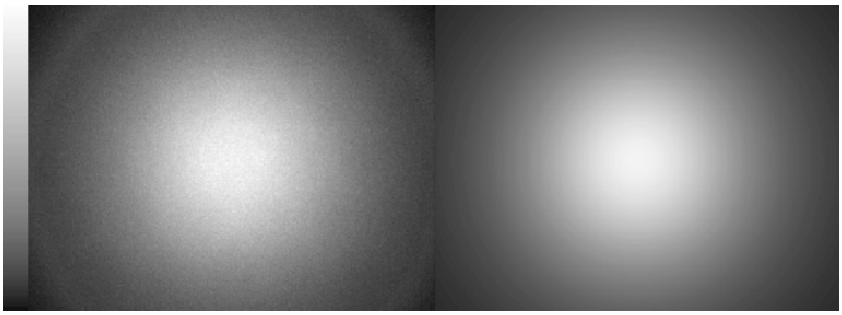

(a) (b)

Figure 3.1: Sensitivity measurement (a) and the function $f(u, v)$ of (3.50) fitted to it (b).

which is automatically scaled to unity at maximum sensitivity. This relative sensitivity correction image is sufficient for reconstruction purposes, since absolute quantification is generally not desired. This approach yields a simple scaling of the coefficients c_{ij} of the MLEM algorithm (3.16) by a constant factor B/f^2 and results in a scaled reconstruction image $B\Lambda/f^2$.

From (3.51), it is clear that the sensitivity correction image $S_2(u, v)$ of (3.52) depends on the mechanical offset m and the electrical shifts e_u and e_v. Theoretically, the correction image should be corrected for changes in these parameters, which results in a translation of the correction image $S_2(u, v)$ in uv space. Note however that $S_2(u, v)$ varies rather slow throughout the uv space, so small changes in m, e_u and e_v will not cause dramatic changes in any of the pixels of the sensitivity correction image $S_2(u, v)$. Such corrections were thereby neglected in practice.

The above and similar fitting procedures have the disadvantage that they can only be used when a good match between the measured and estimated flood source image can be obtained. Whether this is possible or not, depends on the accuracy of the pinhole sensitivity model used. They offer however the big advantage that the noise in the sensitivity measurement will not propagate into the reconstructed images, except for some small inaccuracies in the determination of the parameters n_p, $(m_{up} + e_u)$ and $(m_{vp} + e_v)$. Sensitivity correction images, obtained by the above procedure, have been successfully used in the single pinhole SPECT application of chapter 8.

3.4.3 Small Acceptance Angle

In multipinhole situations, pinhole apertures with small acceptance angles α and at inclined angles η can be encountered. We have developed a prototype multipinhole collimator intended for rat brain imaging on a Siemens ECAM camera. The design is inspired on the work of Schramm *et al.* [2] and the practical realization was done by Nuclear Fields International in the Netherlands. Figure 3.2 shows the collimator,

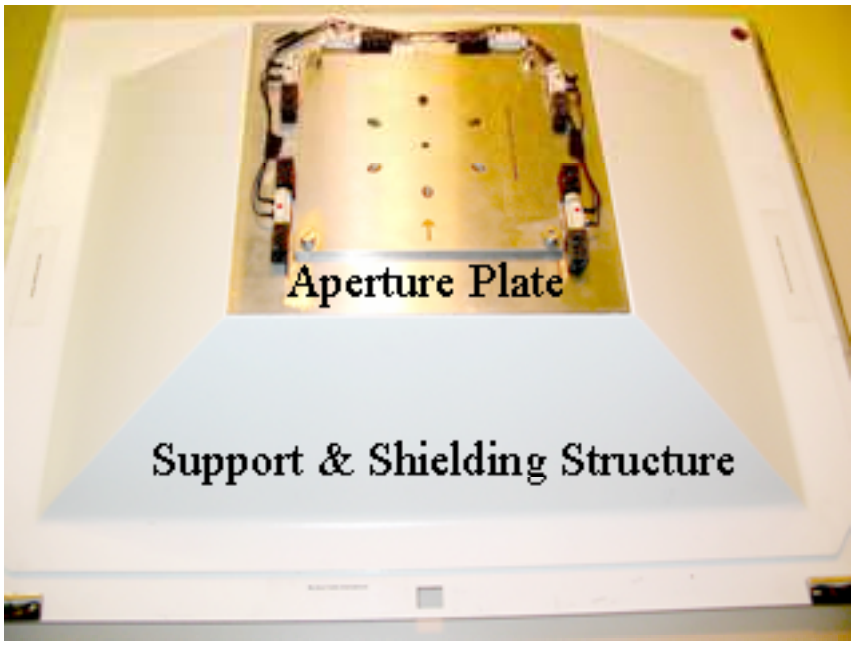

Figure 3.2: Prototype multipinhole collimator. The collimator consists of a lead supporting and shielding structure which holds a tungsten plate containing the pinhole apertures.The design of this aperture plate is illustrated in more detail in figure 3.3

which consists of a Lead supporting and shielding structure with a Tungsten plate containing the pinhole apertures on top of it. Figure 3.3 illustrates the aperture design in detail. The collimator has 7 pinhole apertures of 1.5 mm diameter D with a focal length f of 170 mm and an acceptance angle α of 60^o. The aperture configuration consists of 1 central aperture and 6 off-center apertures. The apertures are all inclined towards the same point at 50 mm below the collimator plate, yielding an inclination angle η of approximately 37.5^o for the noncentral pinhole apertures. The design is an attempt to get optimal sensitivity with minimal overlap for a spherical field of view of 50 mm in diameter, but such optimality remains to be investigated.

Figure 3.4 (a) shows a flood source measurement of one of the non-central pinhole apertures of this prototype collimator. The flood source was created as a horizontal layer of an aqueous solution of 37 MBq of ^{99m}Tc-pertechnetate in a small container at approximately 10 mm above the pinhole aperture to avoid overlapping projections from the other pinhole apertures. A total of 3.6 million photon counts were collected, yielding a maximum pixel count of 662. Some low intensity projections of the other pinhole apertures are visible in the measurement, but they do not overlap with the actual high intensity projection in the top right corner of the image. Figure 3.4

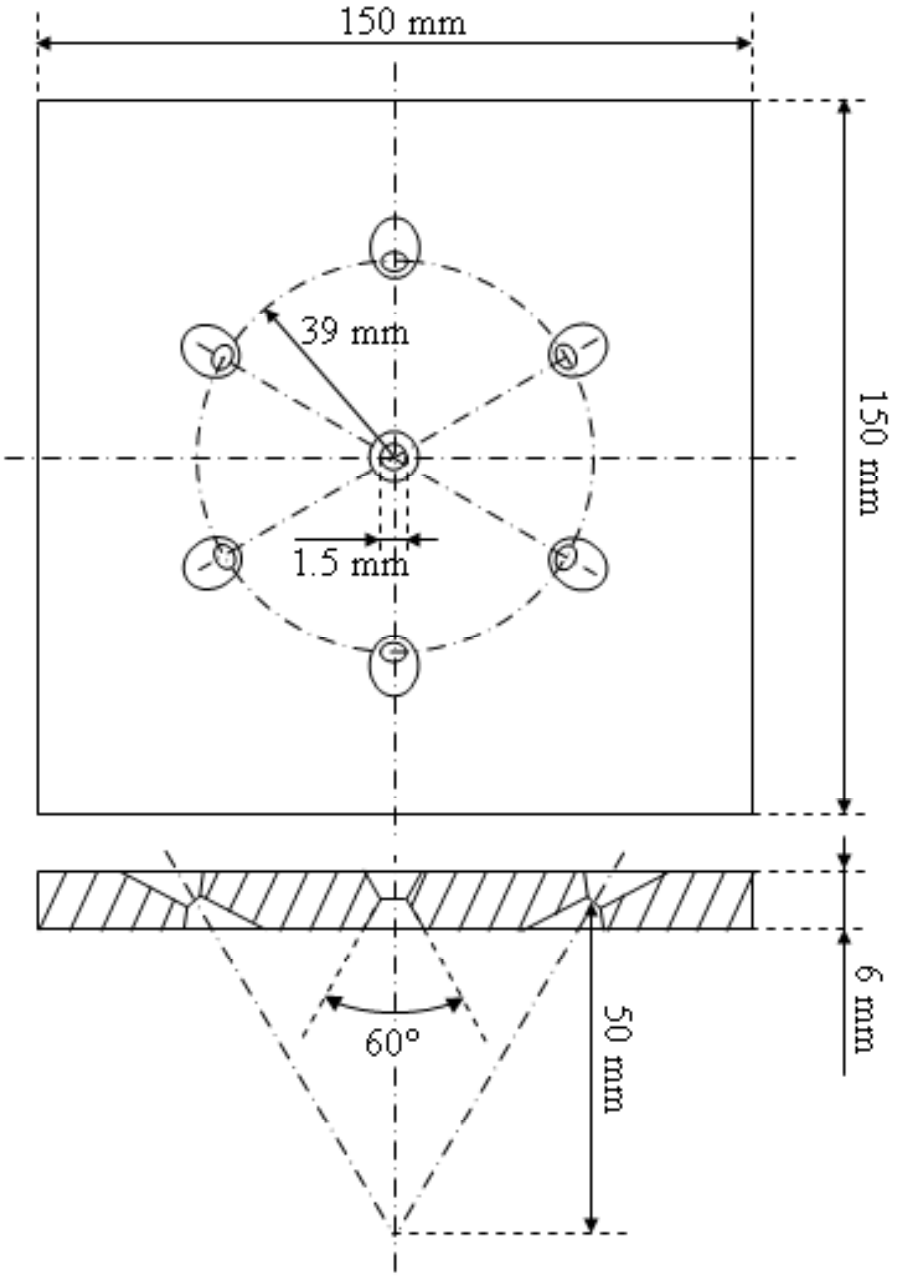

Figure 3.3: Multipinhole aperture design. The drawing is intended as an illustration and is therefore not to scale.

(b) shows a simulation (no fitting) of the same flood source measurement using (3.29) of section 3.3.3. (See the end of section 2.4.3 and appendix A.1 for an explanation of the small acceptance angle sensitivity model.) Both images have their maximum photon count at the same position in the image and both images also show a similar drop off in sensitivity at the edge of the field of view. In the central part of the images, the contours of the simulation are smoother than the contours of the measurement. This can be explained by the fact the 'ellipses' E_b and E_f in the practical realization of the inclined pinhole apertures are slightly pointed on one side. The nonzero part of the actual measurement is also somewhat wider than the nonzero part of the simulation and the isocontours of the measurement and the simulation show some slight discrepancies. Because of this, the proposed sensitivity model for inclined small acceptance angle pinhole apertures is not yet applicable in practical multipinhole situations. Either the model needs further improvements, or the flood source measurements themselves need to be used for sensitivity correction. The sensitivity model is considered sufficiently accurate however for the theoretical study of single and multipinhole imaging in chapter 6.

3.5 Pinhole Point Spread Function

3.5.1 Sensitivity Correction

Up till here, all results have been derived for the ideal pinhole mapping functions $M_p((x,y,z) \mapsto (u,v,\theta))$ and $M_p^T((u,v,\theta) \mapsto (x,y,z))$ of (2.28) and (2.32) respectively. As was illustrated in section 2.5, these mapping functions should actually be substituted by the real point spread function $PSF(u,v,x,y,z)$ of pinhole imaging. With this point spread function $PSF(u,v,x,y,z)$, the changes of integration (3.23) and (3.30) which led to (3.32) only yield

$$Q_p(u_p,v_p) = \iiint S_{p2}(x_{p1},y_{p1}) A_2\, PSF(u_p,v_p,x_{p1},y_{p1},l_p)\,\mathrm{d}x_{p1}\mathrm{d}y_{p1}\mathrm{d}l_p \tag{3.53}$$

with

$$S_{p2}(x_{p1},y_{p1}) = \frac{E_e(\tau,x_{p1},y_{p1})\cos^{(n_p-1)}\tau\cos\kappa}{4\pi(f_p\cos\eta_p - x_{p1}\sin\eta_p)^2} \tag{3.54}$$

and

$$\tau = \arctan\left(\frac{\sqrt{(f_p\sin\eta_p + x_{p1}\cos\eta_p)^2 + y_{p1}^2}}{f_p\cos\eta_p - x_{p1}\sin\eta_p}\right), \tag{3.55}$$

$$\kappa = \arctan\left(\frac{\sqrt{x_{p1}^2 + y_{p1}^2}}{f_p}\right). \tag{3.56}$$

Like for the ideal mapping functions, the change in coordinates has countered the distance dependency of the pinhole sensitivity, but the angular dependency of the pinhole sensitivity, expressed in $S_{p2}(x_{p1},y_{p1})$ can not be brought outside the

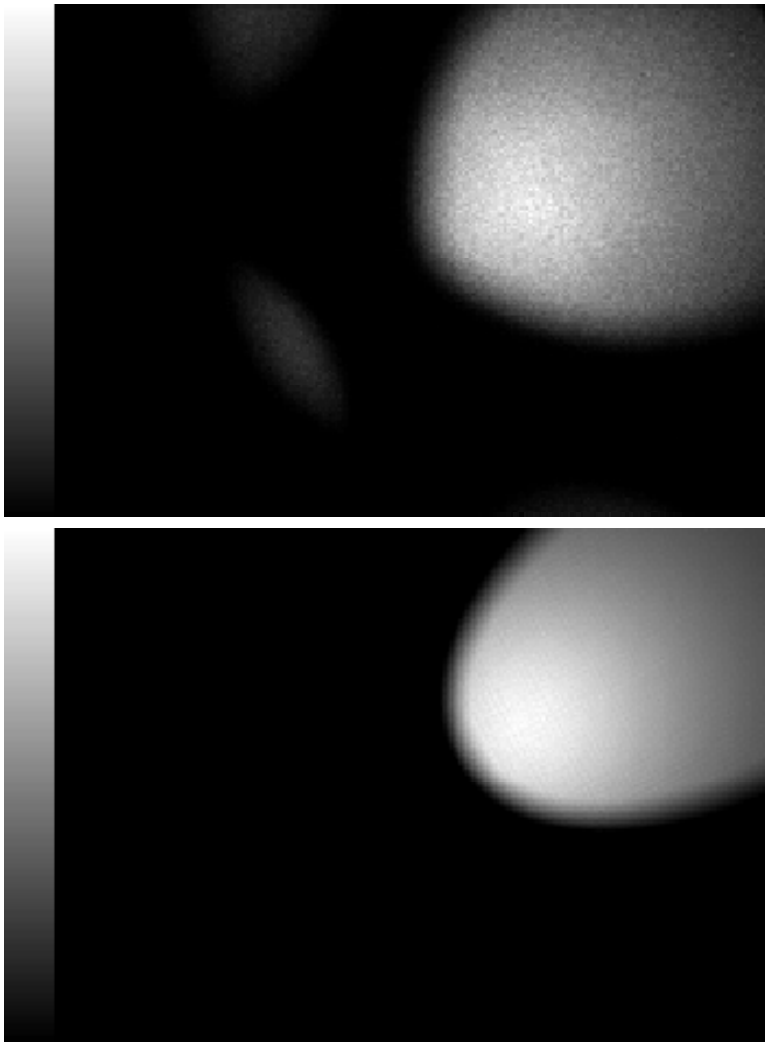

(a)

(b)

Figure 3.4: Sensitivity measurement (a) and simulation (b) for an inclined small acceptance aperture. The acceptance angle α is 60^o and the inclination angle η is approximately 37.5^o.

integral signs. Please notice however that $S_{p2}(u_p, v_p)$ would be a continuous function which varies relatively slowly in the $u_p v_p$ space, except near the edge of the field of view where $\tau \simeq \alpha/2$. The contribution of the intrinsic resolution PSF_2 is easily corrected for by smoothing the projection images after sensitivity correction during the reconstruction, as we do in practice. We can therefore neglect it here. Now only the contribution of the pinhole aperture PSF_1 still needs to be considered. As discussed in section 2.5, this contribution will be very small at the edge of the field of view (at least in the direction orthogonal to this edge), and larger for the central part of the field of view (see figure 2.11). As a result, the aperture contribution PSF_1 may be large where $S_{p2}(x_{p1}, y_{p1})$ varies slowly and it will be small where $S_{p2}(x_{p1}, y_{p1})$ varies rapidly. This observation may still justify the approximation

$$Q_p(u_p, v_p) \simeq S_{p2}(u_p, v_p) \iiint A_2 PSF(u_p, v_p, x_{p2}, y_{p2}, l_p)\, \mathrm{d}x_{p2}\mathrm{d}y_{p2}\mathrm{d}l_p \qquad (3.57)$$

with $S_{p2}(u_p, v_p)$ as in (3.34). As discussed before, we will ignore the effects of the pinhole aperture contribution to the realistic point spread function throughout this work and stay with equation (3.32). Relation (3.53) indicates that this approach is actually not entirely correct and we consider this a point of potential future improvement. A second reason to mention the realistic point spread function here, is to show that it will probably only have a limited impact on the accuracy of the measurement of the sensitivity correction image $S_{p2}(u_p, v_p)$ of section 3.4.

3.5.2 Measurement of Pinhole Sensitivity

The point spread function of pinhole imaging will probably only have a limited effect on the results of the measurement of the sensitivity correction image $S_{p1}(u_p, v_p)$. To clarify this, first remember that the activity distribution of the flood source has a very limited extent T in the z_{p1} direction. To calculate the projection image $Q_p(u_p, v_p)$ of the flood source, only the point spread function $PSF(u_p, v_p, x_{p1}, y_{p1}, b)$ in this plane $z_{p1} = b$ needs to be considered. This yields

$$Q_p(u_p, v_p) = AT \iint S_{p1}(x_{p1}, y_{p1}) PSF(u_p, v_p, x_{p1}, y_{p1}, b)\, \mathrm{d}x_{p1}\mathrm{d}y_{p1}. \qquad (3.58)$$

Within the plane $z_{p1} = b$, it is further reasonable to assume that the shape of the point spread function $PSF(u_p, v_p, x_{p1}, y_{p1}, b)$ will vary relatively slow. With the approximation (2.50), the shape of the ideal point spread function (2.52) of section 2.5 does not even vary at all as function of x_{p1} and y_{p1}. This assumption of slow variation is not valid however at the edge of the field of view, i.e. at $\tau \simeq \alpha/2$. Fortunately, the width of the point spread function decreases rapidly at this edge and can be considered to be small, as was illustrated in figure 2.11. In a first approximation, the shape of the point spread function is here considered piecewise independent of x_{p1} and y_{p1}, with a wide extent in the center and a small extent at the edge of the field of view. The shape itself can thereby be expressed in the $u_p v_p$ projection space as $PSF_{shape}(u_p, v_p)$, but its position within that space still

depends on the position (x_{p1}, y_{p1}), yielding $PSF_{shape}(u_p - x_{p1}, v_p - y_{p1})$. Equation (3.58) can now be written as

$$Q_p(u_p, v_p) \simeq AT \iint S_{p1}(x_{p1}, y_{p1}) PSF_{shape}(u_p - x_{p1}, v_p - y_{p1}) \mathrm{d}x_{p1} \mathrm{d}y_{p1} \quad (3.59)$$

which represents the convolution of the correction image $S_{p1}(x_{p1}, y_{p1})$ with the piecewise constant point spread function $PSF_{shape}(u_p, v_p)$. For both parts of the PSF, the convolution can in a first approximation be neglected, since the convolution kernel PSF is either small or the function to be convolved $S_{p1}(x_{p1}, y_{p1})$ is a very smooth function. Consequently, the result of the convolution will closely resemble the function $S_{p1}(x_{p1}, y_{p1})$ itself and equation (3.58) can further be approximated as

$$Q_p(u_p, v_p) \simeq ATS_{p1}(u_p, v_p). \quad (3.60)$$

This indicates that the spatial resolution of pinhole collimation is not expected to have a considerable impact on the measurement of the sensitivity correction image $S_{p1}(u_p, v_p)$ in practice.

3.6 Conclusion

In this chapter, we have provided the theoretical background on how to perform sensitivity corrected iterative image reconstruction in single and multipinhole SPECT imaging. By using ray driven projection and backprojection, the correction for the nonuniform spatial sampling cancels out the distance dependency of the pinhole sensitivity. As a result, only the angular pinhole sensitivity needs to be modelled during reconstruction, which is conveniently done in the projection space. We further demonstrated that the realistic angular pinhole sensitivity can be determined from a flood source measurement.

Chapter 4

Pinhole SPECT Calibration

4.1 Introduction

Section 2.3 described the geometry of pinhole SPECT systems and how this geometry relates to the pinhole SPECT image acquisition process. This resulted in the expressions (2.26) to (2.32) describing the projection and backprojection operations for single and multipinhole systems, which are the key operations for the MLEM image reconstruction algorithm of (3.16). In order to perform such image reconstructions in practice, knowledge of the acquisition geometry is required and this chapter describes how to obtain this information. Except for the extension to multipinhole collimation, this chapter is based on [29].

The need for accurate knowledge of the acquisition geometry is certainly not restricted to single and multipinhole SPECT imaging, but it extends to all tomography applications. In any application, the acquisition geometry is intrinsically involved in the data acquisition process and therefore it has to be taken into account during image reconstruction. Most tomography systems are specifically designed and build for a designated imaging application and require no further calibration when used for those purposes. Regular SPECT systems are usually designed for example for parallel hole imaging of the human body. For these applications, the predicted and actual acquisition geometries of the system are, by virtue of the system design, sufficiently similar not to cause any appreciable artifacts in the reconstructed images. Only a center of rotation correction needs to be applied. Although these systems are usually not designed for pinhole SPECT imaging, they are often used for this purpose anyway, like in this work. Changing from parallel hole to pinhole collimation changes the geometry of the system however and may change the behavior of the system as well. Differences between the actual and predicted acquisition geometry will further also be magnified in the pinhole projections and may therefore no longer be negligible. As a result, pinhole and multipinhole imaging poses stronger requirements to the system design and the systems used can not be expected to meet these requirements. Consequently, pinhole and multipinhole imaging require

a geometrical calibration of the imaging system, which is not necessary for parallel hole imaging.

To describe the acquisition geometry of a single pinhole camera with a circular detector orbit, seven parameters are required besides the rotation angle θ [30, 31]

1. the focal length f,
2. the detector distance d,
3. the mechanical offset m,
4. the electrical shift e_u,
5. the electrical shift e_v,
6. the detector tilt Φ and
7. the detector twist Ψ.

See figures 2.4 and 2.5 on page 16 and 19 respectively for illustration. In the multipinhole case, three additional parameters are further required for each additional pinhole aperture p, namely

1. the focal length f_p,
2. the mechanical offset m_{up} and
3. the mechanical offset m_{vp}.

Throughout this work, the above parameters are assumed to remain fixed during image acquisition, i.e. they do not vary as a function of the projection angle θ. Apart from the detector rotation θ, the system can therefore be considered as a rigid system during image acquisition. Only chapter 7 will study a situation in which the above assumption is violated and this violation will there be mentioned explicitely. Some of the above parameters may vary however for different scan setups, like the detector distance d and the tilt angle Φ. The electrical shifts e_u and e_v may further vary over time and remounting the same collimator has also been reported to cause changes of the mechanical offset m [32]. Since these changes call for frequent calibration of the pinhole camera, we aim for an easy calibration procedure that allows the determination of all the above geometrical parameters from a single calibration measurement. The idea is to perform a calibration immediately after each (series of) acquisition(s), with the camera left in the same acquisition geometry. The laboratory animal in the field of view is simply replaced by a calibration phantom and an additional possibly shorter, but otherwise identical acquisition is performed. The phantom used for calibration must be simple and easy to position under the camera. In addition, the simplicity of the phantom design should make it equally suited for cone beam SPECT and X-ray CT, which may encounter similar calibration problems.

Several methods have already been proposed to calculate or estimate the geometry of a (single) pinhole camera, cone beam camera or X-ray CT. First Gullberg *et al.* [33] proposed a very straightforward approach by fitting the calculated projections of a point source to the measured ones by a least squares minimization.

The method assumes an ideal camera geometry, except for the electrical shift. The method was later extended to include the mechanical offset [32] and for the calibration of astigmatic collimators [34]. The method has the advantage of using a very simple calibration phantom, applicable for SPECT as well as CT. Some calibration parameters prove however to be highly correlated and local minima in the cost function to be minimized are expected to exist [30–34]. This reduces the accuracy of the parameter estimates and makes them dependent on the initial estimates of the fitting procedure. To avoid this, Li *et al.* [32] and Wang *et al.* [34] incorporated a priori knowledge to confine the solutions to a region near the global minimum of the cost function.

Rizo *et al.* [30] take a different approach by performing a series of measurements to avoid the correlations in the simultaneous estimation of all parameters. The geometrical parameters are separated into the intrinsic and extrinsic parameters. The intrinsic parameters are measured using a grid of point sources, carefully placed with respect to the detector. The phantom is specifically designed to fit on the cone beam collimator. The extrinsic parameters are again estimated by non-linear fitting using the tomographic projection data of a single point source. The method estimates all seven geometrical parameters and also allows to measure the size of the detector pixels. Kyriakopoulos *et al.* [35] adopt the idea of separate measurements for the intrinsic and extrinsic parameters. The intrinsic parameters are measured in a similar way as in the method of Rizo *et al.*. The extrinsic parameters are estimated by nonlinear fitting, using the projection of a regular grid of point sources. The calibration is performed for every projection angle, so the detector rotation is not restricted to a circular orbit. The range of the projection angles is however limited.

Finally, Bronnikov [36] and Noo *et al.* [31] use algebraic approaches to avoid the difficult non-linear estimation problems of the above methods. Bronnikov makes strong assumptions about the camera geometry, but needs only two 180^o opposed projections to calculate it. Noo *et al.* calculate the complete camera geometry, except for the detector tilt, using the tomographic projection data of two point sources at a known distance from each other. The parameters are calculated from the mathematical description of the ellipses that the point source projections describe in the projection images during the acquisition.

Because of the parameter correlations, complex and system dependent calibration phantoms or multiple calibration measurements seem necessary for the accurate calculation of a complete pinhole geometry. Even small errors on one of the parameter estimates can cause visibly detrimental effects in the reconstructed image [31]. The question remains however whether this also applies for correlated errors. We propose a new calibration method to estimate all seven parameters with a single calibration measurement using non-linear fitting. The method is based on the tomographic projection data of three point sources at known distances from each other. The method incorporates some a priori knowledge, mainly to avoid local minima of the cost function. Its performance is not evaluated for the accuracy of the parameter estimates, but for image reconstruction accuracy. This approach tolerates correlated errors, as long as they do not influence the reconstructed image significantly.

This chapter mainly concentrates on the single pinhole calibration problem, which is the fundamental problem of camera calibration. Extension to multipinhole calibration depends on the specific design of the multipinhole configuration. We thereby limit ourselves to the multipinhole situation of section 3.4.3. Section 4.2 explains the theory behind the calibration method. Subsection 4.2.1 treats the estimation of the single pinhole geometry from point source projections. It determines the necessary number of point sources and the conditions on their locations in the field of view. Subsection 4.2.2 further illustrates how the fitting procedure is implemented in practice. Subsection 4.2.3 finally extends the calibration method to the above multipinhole situation. Section 4.3 presents the simulations and experiments performed to evaluate the methods performance, again focussing on the single pinhole situation. First the necessary number of point sources for calibration is studied experimentally in subsection 4.3.1. Further, in subsection 4.3.2, the accuracy of the estimated camera geometry is determined. The impact of the estimation errors on the accuracy of reconstruction are assessed in subsection 4.3.3 and section 4.3.4 evaluates the performance of the method in practice. Subsection 4.3.5 eventually performs a multipinhole calibration experiment. The results of the above experiments are presented in section 4.4 and discussed in section 4.5.

4.2 Theory

4.2.1 Projection Information

Consider again the relations (2.21) and (2.22), which express the projection coordinates (u_θ, v_θ) of a point source by a single pinhole system.

$$u_\theta = f\frac{m\,\cos\Psi - x'''(\theta,\Phi,\Psi)}{d^* + y'''(\theta,\Phi,\Psi)} + m\,\cos\Psi + e_u \tag{4.1}$$

$$v_\theta = f\frac{m\,\sin\Psi - z'''(\theta,\Phi,\Psi)}{d^* + y'''(\theta,\Phi,\Psi)} + m\,\sin\Psi + e_v \tag{4.2}$$

with

$$d^* = d - f. \tag{4.3}$$

The parameter d^* represents the distance between the pinhole aperture and the axis of rotation measured along the system central ray and will often be used in single pinhole situations in the remainder of this work. (In multipinhole situations d is the parameter of choice, since it does not depend on a specific pinhole aperture, while d^* does.) The above equations present the coordinates (u_θ, v_θ) as a function of the rotation angle θ, the point source coordinates (x, y, z) and the geometrical parameters $f, d^*, m, e_u, e_v, \Phi$ and Ψ. The calibration procedure under study poses the inverse problem of determining the values of $f, d^*, m, e_u, e_v, \Phi$ and Ψ from the measurement of a set of point sources $i = 1, ..., I$ with unknown positions (x_i, y_i, z_i) in the field of view. These positions are assumed unknown, because the calibration phantom would otherwise have to be positioned very carefully in the field of view or

additional measurements to determine them would be required. However, assuming a rigid calibration phantom, the distances s_{ii^*} between the different point sources i, i^* are fixed and known.

This section investigates how much information the projections of a point source provide about the camera geometry. It determines the minimum number of point sources yielding a unique solution of the calibration problem and the restrictions on the point source locations in the field of view. It does so by equating the relations (4.1) and (4.2) expressed in function of two different sets of parameters and coordinates

$$f, d^*, m, e_u, e_v, \Phi, \Psi \text{ and } (x_i, y_i, z_i) \quad \text{for } i = 1, ..., I \tag{4.4}$$

$$\widetilde{f}, \widetilde{d^*}, \widetilde{m}, \widetilde{e_u}, \widetilde{e_v}, \widetilde{\Phi}, \widetilde{\Psi} \text{ and } (\widetilde{x_i}, \widetilde{y_i}, \widetilde{z_i}) \quad \text{for } i = 1, ..., I \tag{4.5}$$

and for an increasing number of point sources I. The resulting set of relations is then solved for the first set of parameters and coordinates as a function of the second set. The calibration problem has a unique solution if the two sets of parameters are found to be identical. This means that no false set of parameters and point source locations can be found yielding the same projection locations $(u_{i\theta}, v_{i\theta})$ as the correct set.

Before starting, it is convenient to transform the Cartesian coordinates $x_i y_i z_i$ into cylindrical coordinates $r_i \alpha_i z_i$ with

$$x_i = r_i \cos \alpha_i, \tag{4.6}$$

$$y_i = r_i \sin \alpha_i, \tag{4.7}$$

$$z_i = z_i. \tag{4.8}$$

Using these coordinates, the right hand sides of equations (4.1) and (4.2) expressed in the different sets of parameters and coordinates are set equal to each other. The resulting relations must be satisfied for every projection angle θ. Assuming however a sufficiently large number of projections angles, this is equivalent to satisfying those relations for arbitrary projection angles θ. For point sources located off the axis of rotation, appendix A.3 demonstrates that this yields the set of equations

$$\widetilde{\Psi} = \Psi, \tag{4.9}$$

$$\widetilde{f} = f \frac{\cos \widetilde{\Phi}}{\cos \Phi}, \tag{4.10}$$

$$\widetilde{\alpha_i} = \alpha_i \quad i = 0, 1, ..., I \ , \tag{4.11}$$

$$\frac{\widetilde{z_i}}{\widetilde{r_i}} = a \frac{z_i}{r_i} + b \frac{d^*}{r_i} \quad i = 0, 1, ..., I \ , \tag{4.12}$$

$$\frac{\widetilde{d^*}}{\widetilde{r_i}} = b \frac{z_i}{r_i} + a \frac{d^*}{r_i} \quad i = 0, 1, ..., I \ , \tag{4.13}$$

$$\frac{\widetilde{m}}{\widetilde{r_i}} = \frac{m}{r_i} \quad i = 0, 1, ..., I \ , \tag{4.14}$$

$$(\widetilde{m} - m)\cos\Psi + (\widetilde{e_u} - e_u) = f\frac{\sin\Psi}{\cos\Phi}(\sin\Phi - \sin\widetilde{\Phi}), \tag{4.15}$$

$$(\widetilde{m} - m)\sin\Psi + (\widetilde{e_v} - e_v) = -f\frac{\cos\Psi}{\cos\Phi}(\sin\Phi - \sin\widetilde{\Phi}) \tag{4.16}$$

with

$$a = \frac{1 - \sin\Phi\sin\widetilde{\Phi}}{\cos\Phi\cos\widetilde{\Phi}}, \tag{4.17}$$

$$b = \frac{\sin\widetilde{\Phi} - \sin\Phi}{\cos\Phi\cos\widetilde{\Phi}}. \tag{4.18}$$

First consider equation (4.13). Since both $\widetilde{d^*} > 0$ and $\widetilde{r_i} > 0$, the right hand side of equation (4.13) must be strictly positive as well. Since $\Phi \in \left]-\frac{\pi}{2}, \frac{\pi}{2}\right[$, it can easily be shown that this is always true for $|z_i| < d^*$, which will normally be satisfied because of the limited field of view of a pinhole camera. Furthermore, for $|z_i| \geq d$, it can still be shown that there is always a range of values of $\widetilde{\Phi}$ for which the above remark is satisfied. This range narrows with larger values of $|\Phi|$ and $|z_i|$, but is still approximately equal to $\left]-\frac{\pi}{2}, \frac{\pi}{2}\right[$ for any practical values of $|\Phi|$ and $|z_i|$. Therefore, we can neglect this constraint in the rest of the calculations.

With $I = 1$, the relations (4.9) to (4.16) show that different sets of parameters can describe the same tomographic projection of a single point source. The parameters Ψ and α_i always have to be identical, as shown by equations (4.9) and (4.11). But, equation (4.10) and (4.12) to (4.14), allow to calculate the values of $\widetilde{f}$, $\widetilde{z}$, $\widetilde{d^*}$ and $\widetilde{m}$ respectively as a function of arbitrary values of $\widetilde{\Phi}$, $\widetilde{r}$ and the true geometrical parameters. Equations (4.15) and (4.16) finally determine the values $\widetilde{e}_u$ and $\widetilde{e}_v$ respectively.

Now consider the projection of two point sources at location $r_1\alpha_1 z_1$ and $r_2\alpha_2 z_2$, with $z_1 \neq z_2$, by a pinhole camera. The equations (4.9) to (4.16) still hold, but now for $I = 2$. With $m \neq 0$ and $\widetilde{m} \neq 0$, it is easy to prove that these relations can only hold for $\widetilde{\Phi} = \Phi$ and that

$$\frac{z_1}{\widetilde{z_1}} = \frac{z_2}{\widetilde{z_2}} = \frac{r_1}{\widetilde{r_1}} = \frac{r_2}{\widetilde{r_2}} = \frac{d^*}{\widetilde{d^*}} = \frac{m}{\widetilde{m}}. \tag{4.19}$$

The above relation only allows a scaling of the r- and z- coordinates of the point source locations. The distance between the two point sources will be scaled as well. However, the knowledge of the distance between the two point sources can be used to constrain the solution to the ones with the correct distances, leaving only the trivial solution possible. Thereby, two point sources provide sufficient information for the complete calibration of a pinhole camera, if the mechanical offset m of the camera is non-zero. However, for a normal pinhole camera, the mechanical offset may be assumed to be small and so a normal pinhole camera agrees reasonably well with the special case of $m = 0$. In that case the equations (4.9) to (4.16) can be satisfied for an arbitrary value of $\widetilde{\Phi}$ and this with an arbitrary number of point sources I.

As mentioned before, the distances between different point sources yield additional relations, that can be used to constrain the solutions. For two different point sources i and k, the conservation of the distance s_{ik} between them yields the relation

$$\begin{aligned}(z_i - z_k)^2 + r_i^2 + r_k^2 - 2r_i r_k \cos(\alpha_i - \alpha_k) = \\ (\widetilde{z}_i - \widetilde{z}_k)^2 + \widetilde{r}_i^2 + \widetilde{r}_k^2 - 2\widetilde{r}_i \widetilde{r}_k \cos(\alpha_i - \alpha_k)\end{aligned} \tag{4.20}$$

The parameters $\widetilde{z}_i$, $\widetilde{z}_k$, $\widetilde{r}_i$ and $\widetilde{r}_k$ can be written as a function of $\widetilde{d^*}$ using the equations (4.12) and (4.13). Substituting them in equation (4.20) and solving for $\widetilde{d^*}$ yields

$$\widetilde{d^*} = g_i g_k \sqrt{\frac{(z_i - z_k)^2 + r_i^2 + r_k^2 - 2r_i r_k \cos(\alpha_i - \alpha_k)}{(z_i - z_k)^2 d^{*2} + r_i^2 g_k^2 + r_k^2 g_i^2 - 2r_i r_k g_i g_k \cos(\alpha_i - \alpha_k)}} \tag{4.21}$$

with

$$g_i = b\, z_i + a\, d^* \tag{4.22}$$

and a and b as defined by equations (4.17) and (4.18). It is easy to show that $\widetilde{d^*}$ has always a real solution for an arbitrary value of $\widetilde{\Phi}$. Thereby, with $m = 0$, it is possible to calculate a false set of parameters to describe the tomographic projection data of two point sources, even if the distance between the points is fixed at the correct value.

Finally consider the three point sources case. The distances between these point sources yield three different equations (like equation (4.21)) to calculate the value of $\widetilde{d^*}$. Of course, only those solutions that yield the same solution of $\widetilde{d^*}$ by all three equations are acceptable. Equation (4.21) shows that this depends on d^* and on the point source locations r_i, α_i, z_i for $i = 1, 2, 3$. It is easy to prove that a common value of $\widetilde{d^*}$ is always found if

$$z_1 = z_2 = z_3. \tag{4.23}$$

So three point sources located at the same z location form an inappropriate phantom to calibrate a pinhole camera. Assuming three different z locations, it is unclear whether point source configurations exist yielding a common value of $\widetilde{d^*}$ for arbitrary values of $\widetilde{\Phi}$. However, there are certainly point source configurations, that yield nearly the same value of $\widetilde{d^*}$ for a broad range of $\widetilde{\Phi}$-values. From a calibration perspective, these geometries are equally unfavorable. This can be checked prior to calibration by plotting the right hand side $\widetilde{d^*}_{ik}$ of equation (4.21) as a function of $\widetilde{\Phi}$ for the different point source combinations ik. At $\widetilde{\Phi} = \Phi$ the different curves cross or touch each other at exactly the same point. For a configuration of point sources to be suitable for calibration, at least two of the curves should cross each other at a sufficiently large angle. Figure 4.1 shows two examples of such curves for the point source configurations of table 4.1. The point source configuration of figure 4.1 (a) yields large variances for the parameters Φ and e_v, while the configuration of figure 4.1 (b) yields good results.

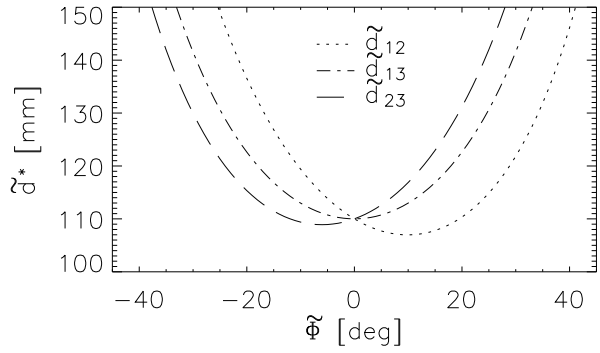

(a)

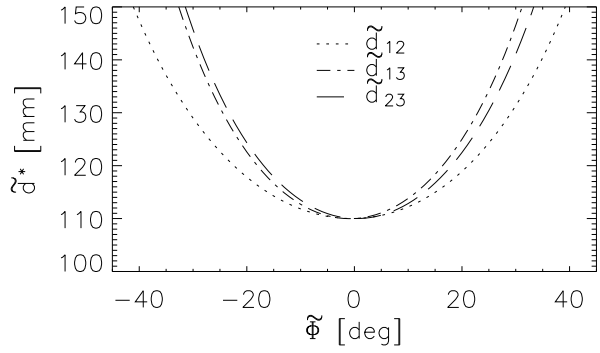

(b)

Figure 4.1: Parameter $\widetilde{d}^*$ as a function of $\widetilde{\Phi}$ for an unfavorable (a) and a favorable (b) point source configuration.

Table 4.1: Point Source Configurations used in Figure 4.1.

Fig nr.	Point nr.	x [mm]	y [mm]	z [mm]
4.1 (a)	1	-30.0	0.0	-10.8
	2	-35.0	0.0	0.0
	3	-30.0	0.0	13.9
4.1 (b)	1	-30.0	0.0	-33.5
	2	-35.0	0.0	-8.5
	3	-30.0	0.0	33.5
$d^* = 110\,\text{mm},\ \Phi = 0.0\,\text{deg}$				

4.2.2 Parameter Estimation

To estimate the geometry of a pinhole camera, we select an appropriate point source configuration, as described above. In principle, this requires knowledge of the point source locations, the distance d^* and the tilt Φ. We assume however that estimates of these parameter values with limited accuracy provide sufficient information for this purpose. The resulting configuration serves as the calibration phantom and a tomographic set of projections is obtained from it over J projection angles θ_j ($j = 1, ..., J$). Since the above equations (2.21) and (2.22) provide very good approximations for the relation between the mass center of a physical point source and that of its pinhole projection [34], a set of projection data (u_{ij}, v_{ij}) is obtained as the projection mass centers of each point i at each angle j. To these data, we fit analytically calculated data $(u_{ij}^{est}, v_{ij}^{est})$ based on estimates of the point source locations and the geometrical pinhole parameters. The quality of the fit is evaluated by the least square cost function F. This cost function sums the squared distances between the estimated and measured point source projection locations. Better estimates lead to smaller distances, eventually leading to $F = 0$ for a perfect fit.

$$F = \sum_i \sum_j \left[\left(u_{ij} - u_{ij}^{est}\right)^2 + \left(v_{ij} - v_{ij}^{est}\right)^2 \right]. \tag{4.24}$$

The minimization of F is performed with Powell's method. This is a direction set method for the multidimensional minimization of functions. The minimization of an N-variable function is performed by repeated cycles of N successive one-dimensional line minimizations along conjugate directions [37].

The choice of the calibration phantom assures that only the correct pinhole and point source geometry can be found as a valid solution that minimizes the above function F. Therefore, the correct distances between the different point sources are imposed on the solution. This is done by expressing the point source coordinates x_i, y_i, z_i with $i = 1, 2, 3$ as a function of the distances s_{12}, s_{13}, s_{23} between the point sources. To do so, consider the calibration phantom as a triangle with the three point sources located in the vertices. The known distances s_{12}, s_{13}, s_{23} define the shape of the triangle. The triangle can be placed at an arbitrary position in the xyz space by three translations t_x, t_y, t_z and three rotations ρ_1, ρ_2, ρ_3 as shown in appendix A.4. Only the translations t_x, t_y, t_z and the rotations ρ_1, ρ_2, ρ_3 have to be fitted, while the distances s_{12}, s_{13}, s_{23} need to be known in advance.

Finally, the parameters f, d, Φ and Ψ can be measured up to some reasonable accuracy. They are used to constrain the result by specifying intervals in which the parameter estimate is acceptable. For a parameter estimate outside such interval, the cost function is evaluated in the closest acceptable value of the parameter and a penalty proportional to the squared difference between the estimate and the acceptable value is added to the result. This drives the algorithm back into the acceptable parameter range.

4.2.3 Multipinhole Extension

In a multipinhole situation, the above considerations can of course be repeated for each pinhole $p = 1, ..., P$ individually. As explained in the introduction however, each additional pinhole aperture $p > 1$ only introduces three additional parameters f_p, m_{up} and m_{vp}, while the parameters d, e_u, e_v, Φ and Ψ are common for all pinhole apertures. This observation can be exploited in designing multipinhole calibration methods. Here, the idea is illustrated for the multipinhole situation of section 3.4.3 in which all pinhole apertures observe an activity distribution in a common field of view. The 7 pinhole collimator design of section 3.4.3 satisfies this assumption. In this case, all pinhole apertures observe the same three calibration point sources encountered before. So each pinhole aperture $p > 1$ yields an additional set of projection coordinates $(u_{pi}(\theta), v_{pi}(\theta))$ for each of the point sources $i = 1, 2, 3$. The coordinates (x_i, y_i, z_i) of these point sources i are of course identical for all pinhole apertures. Consequently, the three point sources provide sufficient information to calibrate the multipinhole acquisition geometry, if the additional projection data $(u_{pi}(\theta), v_{pi}(\theta))$ of pinhole aperture $p > 1$ allow to calculate the parameters f_p, m_{up} and m_{vp}.

Section 4.2.1 showed that the parameters d, e_u, e_v, Φ and Ψ and the point source coordinates (x_i, y_i, z_i) for $i = 1, 2, 3$ are uniquely determined by the projection data $(u_{1i}(\theta), v_{1i}(\theta))$ of pinhole $p = 1$. Now the substitutions of $f_p = f$, $m_{up} = m \cos\Phi$ and $m_{vp} = m \sin\Phi$ in (A.50) and (A.51) of appendix A.3 immediately yield for each additional pinhole aperture $p > 1$

$$\widetilde{f_p} = f_p, \tag{4.25}$$

$$\widetilde{m_{up}} = m_{up}, \tag{4.26}$$

$$\widetilde{m_{vp}} = m_{vp}. \tag{4.27}$$

As a result, the three calibration point sources provide sufficient information to calibrate the multipinhole situation considered. By noting that the equations (A.50) to (A.54) are obtained for a single point source off the axis of rotation, it further appears only necessary that each of the additional pinhole apertures $p > 1$ has one such point source in its common field of view with the aperture $p = 1$.

To perform the above multipinhole calibration in practice, the single pinhole parameters $f, d, m, e_u, e_v, \Phi, \Psi$ and the phantom translations t_x, t_y, t_z and rotations ρ_1, ρ_2, ρ_3 are simply fitted simultaneously with the additional parameters f_p, m_{up}, m_{vp} for $p = 2, ..., P$ to all the available projection data $(u_{pi}(\theta), v_{pi}(\theta))$.

4.3 Experiments

4.3.1 Calibration Phantom

The tomographic projection data of the calibration phantom must contain sufficient information to enable the correct determination of the complete acquisition geometry. Noo *et al.* [31] already observed that for this purpose more than two point

sources are necessary. This observation was confirmed by the calculations in the previous section. The first experiment illustrates that at least three point sources are necessary. For that purpose, the ideal projection data of two point sources are simulated and used to perform a camera calibration, while fixing one parameter at a wrong value. A configuration of point sources provides sufficient information if no false set of parameter values can be found that yields exactly the same projection data set $(u_{i\theta}, v_{i\theta})$, as discussed in the theory. The experiment shows that such false data sets can easily be found for the two point source case, as predicted in the previous chapter. The results obtained from the above fitting procedure are compared with results from an analytical procedure. The latter method calculates the pinhole parameters using the equations (4.9) to (4.16) and (4.21) with $m = 0$.

The experiment is performed for a pinhole camera with a focal length f of 240 mm and a detector distance d of 350 mm ($d^* = 110$ mm). The other pinhole parameters, including the mechanical offset m, are all equal to zero. The two point sources are located at $x = -33.0$ mm, $y = 0.0$ mm and at $z = -33.5$ mm or $z = 33.5$ mm. The simulation is performed for 64 equidistant projection angles over 360^o.

4.3.2 Estimation Accuracy

In combination with noise, the correlations between the geometric parameters can affect the estimation accuracy. The mass centers of the projected point sources can however be accurately measured, except for any systematic errors [33], yielding low uncertainties about the projection locations. To evaluate the parameter estimation accuracy, the second experiment calculates the means, standard deviations and cross-correlations of the parameter estimates from 100 simulations of calibration data sets. For two sample populations $(x_0, x_1, ..., x_N)$ and $(y_0, y_1, ..., y_N)$, with means $\bar{x}$ and $\bar{y}$ respectively, the cross-correlation P_{xy} is defined as

$$P_{xy} = \frac{\sum_{k=0}^{N} (x_k - \bar{x})(y_k - \bar{y})}{\sqrt{\left[\sum_{k=0}^{N} (x_k - \bar{x})^2\right]\left[\sum_{k=0}^{N} (y_k - \bar{y})^2\right]}}. \tag{4.28}$$

The data sets are obtained by adding Gaussian noise with 0.2 mm or 0.3 mm standard deviation, to the exact point source projection coordinates, calculated with equations (2.21) and (2.22) for 64 equidistant projection angles. These standard deviations were chosen approximately 2 and 3 times larger then the statistical errors obtained by Gullberg *et al.* [33]. For still larger standard deviations, the shape of the 'elliptical' paths of the point source projections in the projection image is visually more disturbed than the shape of a measured path. The camera- and phantom geometries used, are similar to those used for the real phantom measurements of section 4.3.4 and are listed in table 4.2. Figure 4.2 further illustrates the positions of the calibration point sources in the field of view. Note that the curves of figure 4.1 (b) have been generated for this geometry. Table 4.2 also contains the initial values with which the estimation process is started and the constraints for the parameters f, d^*, Φ and Ψ.

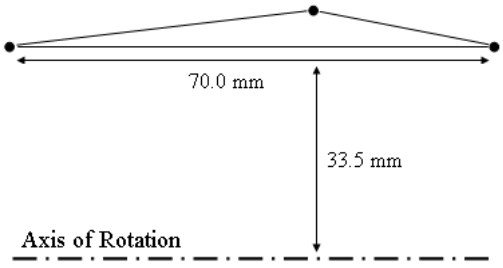

Figure 4.2: Shape of the calibration phantom and its relative position with respect to the axis of rotation.

The variances and covariances of the parameter estimates can also be approximated analytically. For that purpose, the equations (2.21) and (2.22) are approximated by a linear Taylor series expansion about the true parameter values and point source coordinates, taking into account that the distances between the point sources are fixed. This yields a linear system

$$U = U_0 + M\,\Delta P \tag{4.29}$$

where U_0 is a vector with the u_{ij} and v_{ij} measurements obtained at the expansion point. The matrix M contains the first derivatives of the equations (2.21) and (2.22) evaluated at the expansion point and the vector ΔP contains the deviation of the parameters from the expansion point. Such deviation yields the measurement U instead of U_0. The substitution of equation (4.29) into equation (4.24) yields a linear estimator minimizing the function F. The covariances of the parameters $\mathrm{cov}(P)$ can be approximated by propagating the covariances of the data $\mathrm{cov}(U)$ through this linear estimator, yielding

$$\mathrm{cov}(P) = (M^T M)^{-1} M^T \mathrm{cov}(U)\, M (M^T M)^{-1}. \tag{4.30}$$

The parameter cross-correlations are easily obtained by dividing each column and each row of $\mathrm{cov}(P)$ by the square root of its diagonal element. The approximated standard deviations and cross-correlations are compared with those obtained from the fitting procedure.

4.3.3 Reconstruction Accuracy

This third experiment relates estimation errors to the estimation residue and the image reconstruction accuracy. For this purpose a software phantom is created. The phantom consists of a sphere, containing background activity, with a cubic grid of point sources (pixels with high activity) inside. The contrast (highest activity level divided by lowest activity level) between the point source and background activity equals 10. The sphere has a diameter of 72.8 mm and the distance between neighboring point sources is 15.4 mm. The sphere is discretized into pixels of 1.4 mm.

In total the sphere contains 57 point sources. Figure 4.3 (a) shows the central slice of this phantom.

Using the camera- and calibration phantom geometries already listed in table 4.2, the tomographic data of the sphere and the calibration phantom are simulated for 64 equidistant projections of 128x128 pixels of 1.695 mm, using a ray driven projector. With one parameter held at a wrong value and using the initial values and constraints of table 4.2 for the other parameters, an estimate of the camera geometry is calculated. Using this estimate, an OS-EM reconstruction [18,38,39] of the sphere phantom is made and compared to the original image. The reconstruction used an iteration scheme with a decreasing number of subsets: 10x8, 8x4 and 5x1, where the first figure denotes the number of OS iterations and the second one the number of subsets. The reconstructed image is registered to the original image by translation and rotation, by a least squares minimization of the distances between the original and reconstructed point sources. In this experiment, the average distance between the original and reconstructed point sources provides a measure of the reconstruction accuracy, while the errors of the fixed parameter values relate to the estimation accuracy. Both measures are compared to the calibration residue, which is the only measure available in practice.

4.3.4 Phantom Measurement

To evaluate the performance of the calibration method with real data, a phantom was developed consisting of a grid of 16 point sources. The grid can be divided into three slices of 5 point sources. The point sources are approximately located in the vertices and the center of a 5 cm by 5 cm square. The distance between the different slices is approximately 2.5 cm. One extra point source is added to allow the unique identification of every point source in the reconstructed images.

Using our GE Millennium MPR camera with approximately the camera- and calibration phantom geometries listed in table 4.2 and a tungsten knife-edge [14] pinhole aperture of 3 mm, a tomographic acquisition of the phantom was performed with 64 equidistant 60 s projections of 128x128 pixels of 1.695 mm. The phantom point sources contain approximately 1.85 MBq ^{99m}Tc in 2.5 μL water. Without repositioning the camera, an identical acquisition, but with 25 s projections, is performed of the calibration phantom, which contains three 3.7 MBq ^{99m}Tc point sources in 5.0 μL water. The data of the second acquisition are used to calibrate the camera. This allows to reconstruct the grid phantom from the data of the first acquisition. The reconstruction is performed with an OS-EM algorithm with compensation for the pinhole sensitivity [14] as discussed in section 3.4.2. The reconstruction used an iteration scheme with a decreasing number of subsets: 10x8, 10x4 and 5x1, where the first figure denotes the number of OS iterations and the second one the number of subsets. The reconstruction pixel size is 1.4 mm. The calibration is performed using the initial values and constraints of table 4.2. The distances between the different point sources of the original phantom and of its reconstruction are measured and compared distance by distance. The differences between the measured and reconstructed distances provide a measure of the re-

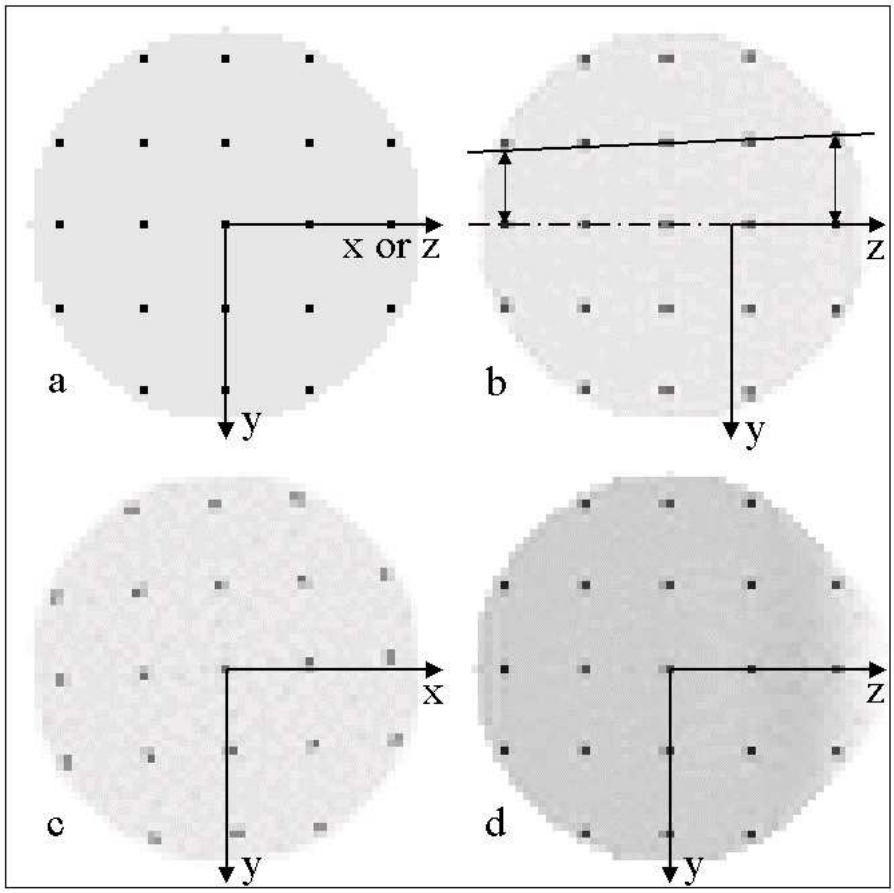

Figure 4.3: Reconstruction Accuracy. (a) Central slice of the software phantom. (b) Reconstruction of the yz plane of the phantom, with the calibration estimate of Φ fixed at -6.0^o instead of 0.0^o. The radial scaling along the rotation axis is indicated by the double arrows in the upper part of the image. The translation along the rotation axis is visible by the displaced yz-origin. (c) Reconstruction of the xy plane of the phantom, with the calibration estimate of m fixed at -7.5 mm instead of 0.0 mm ($\Phi = 0.0^o$). (d) Reconstruction of the yz plane of the phantom, with the calibration estimate for f fixed at 223.3 mm instead of 240.0 mm ($\Phi = -25.0^o$). The background has been set to twice the normal value for better visualization of the under sampling artifact.

construction accuracy. The resolution of the reconstructed point sources is also investigated.

4.3.5 Multipinhole Calibration

To illustrate the application of the calibration method in a multipinhole situation, a calibration measurement was performed on a Siemens ECAM camera, equipped with the 7 pinhole collimator illustrated in section 3.4.3. The calibration measurement was acquired over 64 equidistant projection angles over 360^o using the entire scintillation crystal for photon detection. This resulted in a projection image matrix of 220x160 square pixels of 2.40x2.40 mm^2. The detector distance d was approximately 220 mm and the tilt angle Φ was close to zero. The position of the calibration point sources closely resembled the optimal calibration setup 'opt1' of chapter 5 (see figure 5.3 (a)), with the distances between the point sources s_{12}, s_{13} and s_{23} equal to 25.89 mm, 19.00 mm and 26.43 mm respectively. The plane trough the point sources was horizontal and at zero projection angle θ the detector is parallel to it. The initial values of the point source locations were chosen close to their actual positions. The collimator design and the approximate camera setup provided the initial values for the calibration procedure and they are listed in table 4.6.

4.4 Results

4.4.1 Calibration Phantom

Consider the ideal pinhole camera with f and d^* equal to 240.0 mm and 110.0 mm respectively. For the case of two point sources, the calibration with e_v fixed at a wrong value results nevertheless in a perfect fit. For a linear variation of e_v from -10.0 mm to 10.0 mm, in steps of 2.5 mm, the detector tilt varies linearly from -2.4^o to 2.4^o. The parameters f and d^* show some sub-millimeter variation as well. Similar results are obtained by fixing Φ at a wrong value and allowing the parameter e_v to be fitted. These results are confirmed by the analytical calculations, based on equations (4.9) to (4.16) and (4.21). The above variations clearly indicate that the tomographic projection data of two point sources contain insufficient information for the complete calibration of a pinhole camera with circular detector orbit. Using the projection data of three point sources, the experiment was repeated both for 0.0^o and -25.0^o tilt. Consecutively, every parameter was fixed to four different values, with increasing error, but none of the attempts resulted a perfect fit using the incorrect parameter estimate, as predicted by the theory. The three point source case is discussed in more detail in section 4.4.3.

Table 4.2: Estimation Accuracy.
True stands for the real camera and calibration phantom geometry, init for the initial estimates, and constraint for the parameter estimate bounding limits. Upper standard deviations are based on simulations; lower standard deviations are based on the analytic approximation.

Calibration Point Source Locations									
	x_1 [mm]	y_1 [mm]	z_1 [mm]	x_2 [mm]	y_2 [mm]	z_2 [mm]	x_3 [mm]	y_3 [mm]	z_3 [mm]
true	-30.0	0.0	-33.5	-35.0	0.0	-8.5	-30.0	0.0	33.5
init	0.0	0.0	0.0	0.0	0.0	25.5	0.0	13.2	65.7

Camera Geometry									
	f [mm]	d^* [mm]	m [mm]	e_u [mm]	e_v [mm]		Φ [deg]		Ψ [deg]
true	240.0	110.0	0.0	0.0	0.0	0.0	or	-25.0	0.0
init &	250.0	120.0	1.8	-0.4	0.8	-1.6	or	-26.6	0.3
constraint	±50.0	±50.0				±10.0		±10.0	±5.0

Calibration Residue CR			**Parameter Estimate Standard Deviations**						
Tilt & Noise level	μ_{CR} [mm]	σ_{CR} [mm]	f [mm]	d^* [mm]	m [mm]	e_u [mm]	e_v [mm]	Φ [deg]	Ψ [deg]
$\Phi = 0.0^o$	0.25	0.01	0.2	0.1	0.1	0.3	0.4	0.10	0.01
$\sigma = 0.2$ mm			0.3	0.1	0.1	0.4	0.4	0.10	0.01
$\Phi = 0.0^o$	0.37	0.01	0.3	0.2	0.2	0.5	0.6	0.16	0.02
$\sigma = 0.3$ mm			0.4	0.2	0.2	0.5	0.6	0.14	0.02
Φ = -25.0^o	0.25	0.01	0.3	0.1	0.1	0.4	0.4	0.10	0.03
$\sigma = 0.2$ mm			0.3	0.1	0.1	0.4	0.4	0.10	0.03
Φ = -25.0^o	0.37	0.01	0.4	0.2	0.2	0.5	0.7	0.16	0.04
$\sigma = 0.3$ mm			0.4	0.2	0.2	0.5	0.7	0.14	0.04

[h]

Table 4.3: Parameter Estimate Cross-correlations

Parameter Estimate Cross-correlation ($\sigma = 0.3\,\mathrm{mm}$)								
Fitting		f	d^*	m	e_u	e_v	Φ	Ψ
$\Phi = 0.0^o$	f	**1.00**	**0.97**	-0.01	0.02	0.08	0.09	0.00
	d^*		**1.00**	0.01	-0.01	0.10	0.11	0.02
	m			**1.00**	**-1.00**	-0.11	-0.12	-0.14
	e_u				**1.00**	0.11	0.12	0.14
	e_v					**1.00**	**0.99**	-0.02
	Φ						**1.00**	-0.02
	Ψ							**1.00**
Analytical		f	d^*	m	e_u	e_v	Φ	Ψ
$\Phi = 0.0^o$	f	**1.00**	**0.97**	0.00	0.00	0.00	0.02	0.00
	d^*		**1.00**	0.00	0.00	-0.03	-0.05	0.00
	m			**1.00**	**-1.00**	0.00	0.00	-0.06
	e_u				**1.00**	0.00	0.00	0.06
	e_v					**1.00**	**0.98**	0.00
	Φ						**1.00**	0.00
	Ψ							**1.00**
Fitting		f	d^*	m	e_u	e_v	Φ	Ψ
$\Phi = -25.0^o$	f	**1.00**	**0.70**	0.00	0.00	0.23	0.29	0.11
	d^*		**1.00**	-0.11	0.10	**-0.51**	**-0.44**	-0.08
	m			**1.00**	**-1.00**	0.14	0.15	**0.88**
	e_u				**1.00**	-0.14	-0.15	**-0.88**
	e_v					**1.00**	**0.99**	0.24
	Φ						**1.00**	0.25
	Ψ							**1.00**
Analytical		f	d^*	m	e_u	e_v	Φ	Ψ
$\Phi = -25.0^o$	f	**1.00**	**0.69**	0.00	0.00	0.18	0.24	0.00
	d^*		**1.00**	0.00	0.00	**-0.54**	**-0.46**	0.00
	m			**1.00**	**-1.00**	0.00	0.00	**0.90**
	e_u				**1.00**	-0.00	-0.00	**-0.90**
	e_v					**1.00**	**0.95**	0.00
	Φ						**1.00**	0.00
	Ψ							**1.00**

4.4.2 Estimation Accuracy

Table 4.2 presents the mean μ_{CR} and standard deviation σ_{CR} of the calibration residue CR. This calibration residue CR is expressed as the average distance between the simulated and estimated point source projections after calibration. The residue is very closely centered around its mean value. It does not change with the detector tilt, but differs for different noise levels. The table also presents the standard deviations of the parameter estimates. Those are calculated both using the series of noisy simulations (upper values in table 4.2) and by the analytical approximation of equation (4.30) (lower values in table 4.2). All estimates are centered around the correct solution, but the spread differs for the different parameters. The largest errors are found for the distances e_u and e_v, and for the tilt angle Φ. The simulated and approximated standard deviations are in very good agreement. A close inspection of the analytically approximated standard deviations indicates slightly larger values of the estimates of tilted geometries than of non-tilted geometries. The largest differences are found for the parameters d^* and e_v, but remain nevertheless under 0.04 mm for 0.3 mm noise.

Table 4.3 presents the cross-correlations of the parameter estimates, calculated for both 0.0^o and -25.0^o tilt and 0.3 mm noise. The results for the 0.2 mm noise cases are nearly identical. The cross-correlations from the analytical and fitting procedures are in good agreement with each other. The parameters m and e_u, and e_v and Φ are highly correlated. The parameters f and d^* are highly correlated for 0.0^o tilt, but to a lesser extent for the -25.0^o tilt case. In the latter case, there is an additional correlation between the distance d^* and the parameters e_v and Φ. Finally, the twist Ψ shows no clear correlations with any other parameter for the 0.0^o tilt case. For $\Phi = -25.0^o$ however, there is strong correlation with the parameters m and e_u. The above mentioned correlations are indicated in bold in table 4.3.

4.4.3 Reconstruction Accuracy

Figure 4.4 shows the reconstruction error RE as a function of the calibration residue CR, for calibrations performed with one parameter estimate fixed at a wrong value. The calibration residue CR is again defined as the average distance between the estimated and measured projections of the calibration point sources. The reconstruction error RE is defined as the average distance between the original and reconstructed point sources in the software phantom. The different symbols in the figure indicate the different parameters, of which the estimate is fixed at 4 different values, with increasing errors with respect to the correct value. These errors are given in the table included in figure 4.4 and were chosen to yield calibration residues of approximately 1 mm and less, since real calibration measurements indicated this limit to be easily obtainable. For all parameters, the calibration residues increase with increasing errors. The residues show no large differences between the 0.0^o and -25.0^o tilt case, except for the parameter Ψ. The estimate errors only cause subpixel reconstruction errors which are less than the calibration residue. Table 4.4

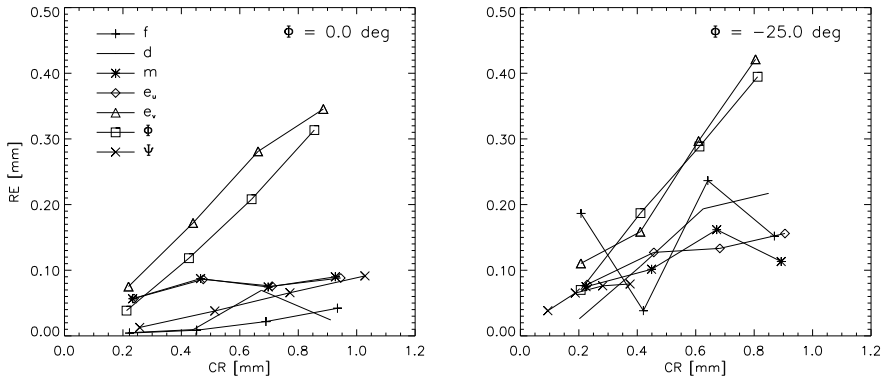

Parameter Estimate Errors

Δf [mm]	Δd^* [mm]	Δm [mm]	Δe_u [mm]	Δe_v [mm]	$\Delta\Phi$ [deg]	$\Delta\Psi$ [deg]
-4.18	-5.75	-1.88	-6.25	-6.88	-1.50	-0.20
-8.35	-11.50	-3.75	-12.50	-13.75	-3.00	-0.40
-12.53	-17.25	-5.63	-18.75	-20.63	-4.50	-0.60
-16.70	-23.00	-7.50	-25.00	-27.50	-6.00	-0.80

Figure 4.4: RE versus CR for the listed Parameter Estimate Errors

shows that this also holds for estimate errors of the twist Ψ larger than -1.6^o in the -25.0^o tilt case. Fixing the parameter estimates of e_v or Φ to a wrong value results in the largest reconstruction errors. The reconstruction errors must be interpreted carefully, since the error on these sub-pixel values can be of the same magnitude as the reconstruction errors themselves.

Visual inspection of the reconstructed images shows that errors on the parameters e_v and Φ cause the reconstructed image to be translated along the axis of rotation with respect to the original image. Additionally, the reconstructed image is slightly scaled in radial direction according to the position along the axis of rotation, as shown in figure 4.3 (b). Inspection of the parameter estimates again shows these parameters to be strongly correlated. Another prominent correlation exists between the parameters m and e_u and errors on them cause the reconstructed images to be rotated around the axis of rotation. There is however no sign of a real image distortion. A reconstruction of the central slice of the phantom is shown in figure 4.3 (c). Errors on the other parameters visually have a less prominent influence on the reconstructed images. Besides the effects of estimate errors, all reconstructions of the -25.0^o tilt case show an artifact due to the insufficient sampling of the back region of the phantom. The artifact is clearly visible in the right side of figure 4.3 (d).

Table 4.4: Calibration Residues and Reconstruction Errors in function of the Estimate Error of Ψ (Φ = -25.0^o).

$\Delta\Psi$ [deg]	CR [mm]	RE [mm]
-0.20	0.09	0.04
-0.40	0.19	0.07
-0.60	0.28	0.08
-0.80	0.38	0.08
-1.00	0.47	0.08
-1.20	0.56	0.07
-1.40	0.66	0.10
-1.60	0.75	0.12
-1.80	0.84	0.13
-2.00	0.93	0.11

Table 4.5: Camera Calibration Results.

	CR	**Parameter Estimates**						
	CR [mm]	f [mm]	d^* [mm]	m [mm]	e_u [mm]	e_v [mm]	Φ [deg]	Ψ [deg]
$\Phi \cong 0.0^o$	0.52	252.9	117.4	0.3	4.1	5.9	0.97	-0.13
	0.53	253.0	117.5	0.2	4.3	6.2	1.04	-0.12
$\Phi \cong$ -25.0^o	0.46	253.9	128.4	2.2	-2.2	7.7	-23.23	0.19
	0.48	253.9	128.3	2.5	-3.0	8.2	-23.15	0.22

4.4.4 Phantom Measurement

For each acquisition of the grid of point sources (Φ = 0.0^o and Φ = -25.0^o), two calibration measurements, with intermediate repositioning of the calibration phantom, were performed. The repositioning of the calibration phantom provides two independent calibration measurements of the same camera geometry and with the calibration point sources at approximately the same location. The results of the camera calibrations are listed in table 4.5. The calibration residue is approximately 0.5 mm in all four cases. The parameter estimates for the same camera geometries show some little differences, as expected due to the parameter correlations. The distances between the point sources in the different reconstructions (based on different calibration measurements) of the same projection data, are however identical up to 0.1 mm for both tilt cases. When comparing the distances with those measured on the actual phantom, the largest difference found was 1.0 mm for -25.0^o tilt and 1.3 mm for 0.0^o tilt. Most differences are however much smaller. The distances between the point sources of the real phantom have been measured with an accuracy of approximately 0.3 mm.

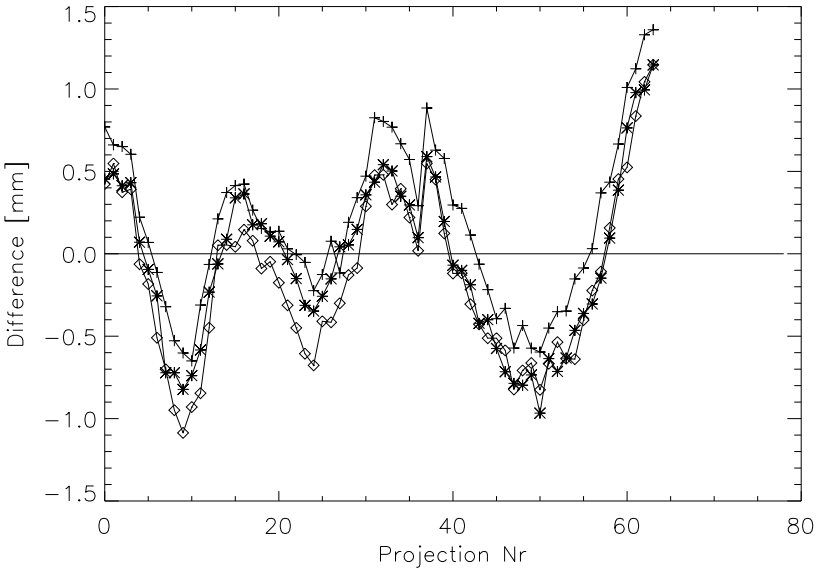

Figure 4.5: The difference in u coordinates of the measured (u^{meas}) and estimated (u^{est}) calibration point source projections: ($u^{meas} - u^{est}$).

The difference in coordinates of the estimated and measured point source projections after calibration, is not entirely random and shows similarities for the three calibration point sources. This is illustrated in figure 4.5 by the differences for the u coordinates of the projections of the three calibration point sources from the first calibration measurement with $\Phi = 0.0^o$.

The FWHM of the reconstructed point sources ranges from 4.0 to 5.0 mm.

4.4.5 Multipinhole Calibration

Table 4.6 lists the results of the multipinhole calibration and figure 4.6 shows the estimated and measured point source locations. Like for the single pinhole calibration measurements, the estimated and measured projection locations generally match well, although some systematic deviations between the estimated and measured locations do exist like for the small ellipse at the bottom of figure 4.6. The calibration residue CR, expressed as the average distance between the estimated and measured projection locations, is 0.49 mm. The estimated geometry of the camera generally corresponds very well with the anticipated initial values, although the electrical shift e_u is larger than expected.

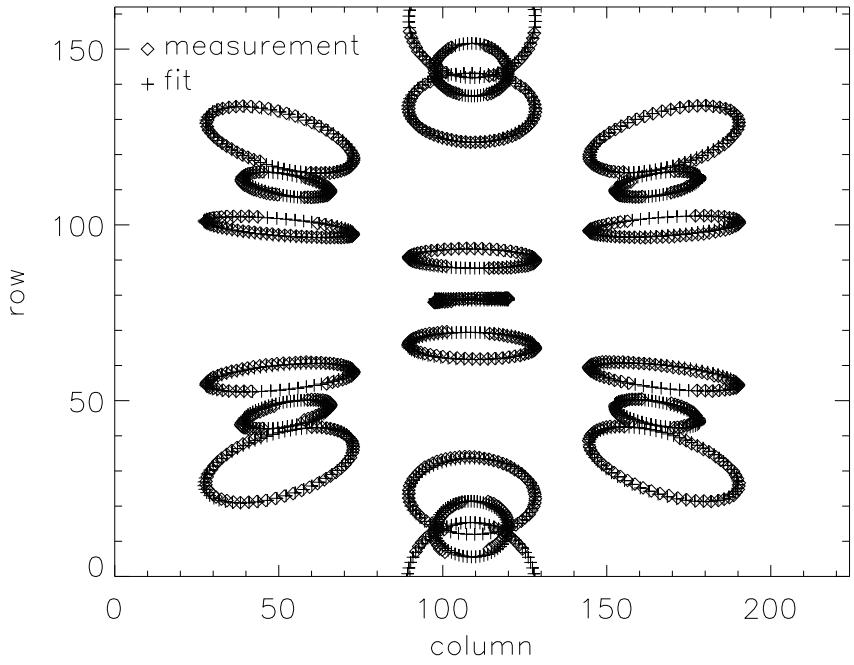

Figure 4.6: Estimated and measured point source projection locations of the multipinhole calibration measurement.

4.5 Discussion

Like Noo *et al.* [31], we find that two calibration point sources provide insufficient information for the complete calibration of a pinhole camera. The addition of a third point source overcomes this problem, if the point sources are sufficiently well located, as shown in the theory. For the experiments, the three point sources are located on a slightly broken line, but approximately parallel to the rotation axis. This proved to be more stable than the use of a straight line, exactly parallel to the rotation axis. The last, rather theoretic, method occasionally yielded an outlier with respect to the results in table 4.2. The point sources are located as far as possible from the axis of rotation and the two outermost sources are also located as far as possible from each other along the z-axis (axis of rotation). The third point source was finally located in between, but avoiding the plane of the focal point. In this arrangement, the outermost point sources satisfy the description of Noo *et al.* [31] about the ideal point source locations in his method. The location of the middle point source seems a logical extension of this for three point sources. However, placing the middle point source in the plane of the pinhole focus does not

Table 4.6: Multipinhole Calibration.
Init stands for the initial values of the calibration derived from the collimator design, while fit stands for the results of the actual calibration procedure.

	CR	d	e_u	e_v	Φ	Ψ
	[mm]	[mm]	[mm]	[mm]	[deg]	[deg]
init		220.0	0.0	0.0	0.00	0.00
fit	0.49	226.8	-7.2	-1.21	-0.04	-0.54

	f_p [mm]		m_{up} [mm]		m_{vp} [mm]	
p	init	fit	init	fit	init	fit
1	170.0	168.9	0.0	0.2	0.0	0.0
2	170.0	168.8	33.8	34.2	-19.5	-19.5
3	170.0	169.2	0.0	0.1	-39.0	-39.0
4	170.0	169.0	-33.8	-33.8	-19.5	-19.6
5	170.0	168.9	-33.8	-33.9	19.5	19.6
6	170.0	169.0	0.0	0.2	39.0	39.2
7	170.0	168.9	33.8	34.2	19.5	19.7

seem to cause any problems. Further, since a large number of projection angles over 360^o are used in the calibration, the orientation of the point sources around the rotation axis was not assumed critical and the simplest geometry of a broken line was chosen. However, later experiments show standard deviations of the e_v and Φ estimates of almost half the original values for the middle point source rotated 180^o around the rotation axis. The standard deviations of the other parameters seem unaffected by this rotation. Keeping in mind the results of figure 4.4, this should seriously reduce the reconstruction error. Surprisingly, this geometry shows a slightly worse intersection of the curves of $\widetilde{d}^*$ than the original geometry of figure 4.1 (b). Finding the optimal calibration phantom geometry is the topic of the next chapter.

As expected, some parameters are highly correlated. The correlated parameters e_v and Φ are clearly the most critical. The second experiment shows that noisy data cause the largest spread for the estimates of these parameters. Further, for the same calibration residue CR, the reconstruction errors RE are the largest for e_v and Φ, as shown in the third experiment. This causes these parameters to be the most difficult to estimate and it also causes the largest distortions of reconstructed images, when they are poorly estimated. From the image reconstruction point of view, not all correlations cause trouble however. Although noisy data also yield the largest standard deviation of the estimates of e_u, the reconstruction errors RE caused by e_u and m are only small.

The cross-correlations and their dependence on the tilt angle Φ can intuitively be explained from a number of geometrical considerations. First of all, for $m = 0$, the twist Ψ causes a rotation of the detector around the system central ray. During

acquisition, this rotation axis constantly changes, which explains why the twist can easily be estimated, yielding a small standard deviation of its estimate. A correlated error between m and e_u results in a rotation of the reconstructed image around the axis of rotation. For $\Phi = 0$, the system central ray is always orthogonal to the rotation axis and no correlation between m, e_u and Φ exists. For a tilted detector however, the central ray is inclined towards the rotation axis, yielding a component of the rotation Φ along the rotation axis. This component along a common axis establishes the correlation between m, e_u and Φ. Secondly, the ratio of the focal length f and the distance d^* determines the magnification of the object in the field of view. This explains the correlation between f and d^*. The magnification is larger for parts of the object closer to the focal point. Because of the rotation of the focal point during acquisition, the magnification of parts of the object away from the rotation axis varies with the rotation angle θ. For larger tilt angles Φ this variation is less prominent, explaining the smaller correlation of f and d^* for such tilt angles. Finally, a correlated error between e_v and Φ, causes a translation of the reconstructed image along the z-axis. This changes the distance between the object and the focal point. For a tilted detector this also changes the magnification of the object, which is normally determined by the ratio of f and d^*. Thereby, additional correlations between the parameters f, d, e_v and Φ emerge.

For the simulation studies, the calibration method performs well and the calibration residue CR provides a conservative measure of the reconstruction accuracy that may be expected. For all badly estimated parameters, including e_v, the reconstruction error is always smaller than the calibration residue and in most cases even much smaller. Further, for the largest reconstruction errors, caused by e_v and Φ, the errors vary slowly throughout the reconstructed image, indicating a gentle deformation of the original distribution. Finally, because of sensitivity considerations, the geometries simulated in the experiments normally require a pinhole aperture of approximately 3 mm. The reconstruction errors presented in figure 4.4, are small with respect to this aperture size, which determines the resolution of the system.

For the real camera calibrations, the residue is approximately 0.5 mm, both for the single and multipinhole calibrations. Figure 4.5 and 4.6 illustrate that the individual distances between measured and calculated point source projections are not totally random however. From figure 4.5 it is further clear that these differences are also not independent for different point sources. This suggests systematic deviations of the camera geometry from the model presented in section 4.2. For the GE Millennium MPR camera, we observed a sudden, sub-millimeter displacement of the collimator during every acquisition. The effect of this displacement is small, but noticeable in the projection data set. However, it does not provide a complete explanation for figure 4.5. The remaining systematic differences also suggest that with even more accurate models of the camera geometry, potentially tailored for a specific camera, the estimation and reconstruction accuracy can be increased even further, as illustrated in chapter 7 of this work.

The effect of the imperfect calibration match was studied on reconstructions of real tomographic data of the grid of point sources. The small differences in parameter estimates for the same camera geometry, only result in negligible dif-

ferences in the reconstructed images. The geometries in the reconstructed images were also compared to the real phantom geometry. Despite the measurement uncertainty, even the largest differences (1.0 mm for -25.0^o tilt and 1.3 mm for 0.0^o tilt) are small with respect to the pinhole aperture of 3 mm, which determines the resolution. The FWHM of the reconstructed point sources ranges between 4 mm and 5 mm and gives an indication of the system resolution. Because of the larger resolution, the errors will not cause any serious and noticeable degradation of the reconstructed image accuracy.

As mentioned in the theory, the values of the parameter estimates of f, d^*, Φ and Ψ were bounded during the experiments. This was done to guide the procedure to a useful solution. When starting with very poor initial estimates, the unbounded procedure sometimes leads to unrealistic solutions with very high calibration residues. The ranges of acceptable values were however sufficiently large to avoid any interference with the effects of the parameter correlations. Narrow parameter ranges, imposing strong a priori knowledge, are not always beneficial, since they may influence the convergence trajectory of the calibration procedure. For one of the real -25.0^o tilt measurements, constraining the parameter Φ within $\pm 5^o$ forced the procedure to stop before convergence with the estimate of Φ pinned at the limit of the acceptable values. The constraining of the same calibration within $\pm 10^o$ converged without any problem.

The results presented above are specific for the acquisition geometries used. The difference in standard deviation of the estimate of Ψ between the 0.0^o and -25.0^o tilt case, provides a clear example of this. Due to the difference in tilt angle, there is a clear difference in the correlations between the parameters m, e_u and Ψ. The difference in correlation affects the standard deviation of the estimate. Fortunately, it has almost no effect on the reconstruction accuracy. The acquisition geometries studied (for the single pinhole case) are those of a perfect pinhole camera with a non-tilted or severely tilted detector. The variation of the tilt was chosen to cover the expected useful range of tilt values. Further, non-ideal cameras have nonzero parameters m, e_u, e_v and Ψ. Deviations from this ideal case may however be expected to be small and the deviations of the calibration results are expected to be small as well. Finally, our experience with a different magnification f/d^* in the next chapter does not reveal markedly different behavior either.

4.6 Conclusion

In this chapter we have developed a new theory about the calibration of pinhole cameras, which gives insight into the necessary and sufficient conditions for solving the calibration problem. The theory resulted in a new and convenient method for the complete calibration of a single pinhole camera. The usefulness of the theory for designing calibration methods for multipinhole situations was demonstrated as well, by the development of a calibration method for the multipinhole imaging situation considered in this work. Both the accuracy of the geometry estimate of the single pinhole calibration and its effect on the accuracy of image reconstruction were

studied in simulations and real calibration experiments. In both cases, it could be concluded that the observed estimation accuracy only has a sub-resolution impact on the accuracy of the reconstructed images. The application of the calibration method in a multipinhole situation was further illustrated by a practical multipinhole calibration measurement. Because of the simplicity of the calibration phantom, the calibration method is also applicable to cone-beam SPECT and X-ray CT.

Chapter 5

Optimization of Pinhole SPECT Calibration

5.1 Introduction

In the previous chapter, we developed a calibration method to determine the pinhole SPECT acquisition geometry from the SPECT acquisition of a calibration phantom consisting of three point sources [29]. The method first acquires a pinhole SPECT scan of the three point sources and calculates the mass centers of their projections. The acquisition geometry is then determined by a least squares fit of estimated point source projection locations to the measured mass centers. Besides the 7 parameters of the acquisition geometry, the positions of the point sources are estimated as well, but not the distances between them. This is accomplished by specifying the point source coordinates by the 3 distances s_{12}, s_{13}, s_{23} between the point sources, 3 rotations ρ_1, ρ_2, ρ_3 and 3 translations t_x, t_y, t_z. The distances s_{12}, s_{13}, s_{23} define the shape or configuration of the calibration phantom and remain fixed during the calibration. This rigid phantom is then correctly positioned in the field of view by the 3 rotations ρ_1, ρ_2, ρ_3 and the 3 translations t_x, t_y, t_z, and these rotations and translations have to be estimated by the calibration procedure.

With noisy calibration data, the acquisition geometry can only be estimated with limited accuracy. Both the configuration of the calibration phantom s_{12}, s_{13}, s_{23} and its position in the field of view $t_x, t_y, t_z, \rho_1, \rho_2, \rho_3$ influence this accuracy. In the remainder of this work, this combination of phantom configuration and phantom position will be referred to as 'calibration setup'. Additionally, the use of an incorrect phantom model $s'_{12}, s'_{13}, s'_{23}$ (instead of s_{12}, s_{13}, s_{23}) in the calibration calculations can degrade this accuracy even further. During reconstruction, the resulting errors on the acquisition geometry propagate into the reconstructed images, causing loss of spatial resolution and/or image deformation. The aim of this study is to determine an optimal calibration setup for accurate image reconstruction with a single pinhole system in practice, despite noise on the calibration data and phantom model errors.

Table 5.1: Calibration Entities.

Name	# Parameters	Parameters
Acquisition geometry	7	$f, d, m, e_u, e_v, \Phi, \Psi$
Description: geometry of the pinhole system.		
Phantom configuration	3	s_{12}, s_{13}, s_{23}
Description: actual distances between the 3 calibration point sources.		
Phantom model	3	$s'_{12}, s'_{13}, s'_{23}$
Description: values of the distances between the 3 point sources used in the calibration calculations.		
Phantom position	6	$t_x, t_y, t_z, \rho_1, \rho_2, \rho_3$
Description: actual position & orientation of the phantom in the field of view.		
Calibration setup	9	$s_{12}, s_{13}, s_{23}, t_x, t_y, t_z, \rho_1, \rho_2, \rho_3$ or $x_1, y_1, z_1, x_2, y_2, z_2, x_3, y_3, z_3$
Description: phantom configuration + phantom position.		

For clarity, table 5.1 provides an overview of the different entities involved in the calibration process.

This chapter is entirely based on [40]. Section 5.2 first describes an efficient mathematical procedure to evaluate the effects of noisy calibration data or phantom model errors on the estimation accuracy of the calibration method and the resulting accuracy of subsequent image reconstruction. With the above procedure, section 5.3.1 then evaluates the accuracy of a large and representative set of possible calibration setups of three point sources. From these results section 5.4.1 selects two calibration setups yielding the best overall accuracy. The sections 5.3.2, 5.4.2 and 5.3.3, 5.4.3 further provide two experiments to verify or support the results of section 5.4.1. These results are finally discussed in section 5.5.

5.2 Method

This section studies two sources of errors: noise on the calibration data and the use of an incorrect phantom model in the calibration calculations. Both sources of error result in errors on the calibration results, which, in turn, degrade the accuracy of image reconstruction by loss of spatial resolution and/or image deformation. First, the analytical expressions for the projection of the calibration phantom are repeated. Next, these expressions are used to calculate linear systems, which allow us to evaluate the estimation accuracy as a function of the noise on the calibration data and/or the errors on the phantom model. Finally, the reconstruction

accuracy is derived from this estimation accuracy by simulating and evaluating the reconstruction of a grid of point sources. For that purpose, however, the estimation accuracy results first have to be transformed into a more suitable representation.

5.2.1 Estimation Accuracy

The relations (2.21) and (2.22), repeated here for convenience,

$$u_i(\theta) = f\frac{m\,\cos\Psi - x_i'''(\theta,\Phi,\Psi)}{d^* + y_i'''(\theta,\Phi,\Psi)} + m\,\cos\Psi + e_u \tag{5.1}$$

$$v_i(\theta) = f\frac{m\,\sin\Psi - z_i'''(\theta,\Phi,\Psi)}{d^* + y_i'''(\theta,\Phi,\Psi)} + m\,\sin\Psi + e_v \tag{5.2}$$

define the projections of the calibration point sources $U = (u_i(\theta), v_i(\theta))\ i = 1,2,3$ as a function of the unknown calibration parameters P, which consist of both the pinhole acquisition geometry $f, d^*, m, e_u, e_v, \Phi, \Psi$ and the phantom position $t_x, t_y, t_z, \rho_1, \rho_2, \rho_3$. Like in section 4.3.2, we assume again that for small variations ΔP of these calibration parameters, the resulting projection coordinates U can also be approximated from the original projections U_0 by the linear system (4.29)

$$U = U_0 + M\,\Delta P. \tag{5.3}$$

Here, M is a matrix containing the first order derivatives of the projection coordinates U, specified in (5.1) and (5.2), to each of the 13 parameters of P. The derivatives are evaluated for the original acquisition geometry and phantom position, yielding the projections U_0. Similar to the real calibration method, calibration of this linear system can be performed by solving (5.3) for the least square solution of ΔP. With $\Delta U = U - U_0$, this yields

$$\Delta P = (M^T M)^{-1} M^T \Delta U. \tag{5.4}$$

Expressed in this way, (5.4) allows us to calculate differences in the parameter estimates ΔP, due to specific changes of the projection coordinates ΔU. Noise on the projection coordinates, being the first source of error studied in this section, causes such differences ΔU. The noise is however better characterized by its covariance matrix $\mathrm{cov}(U)$ than by a single noise realization ΔU. This covariance matrix $\mathrm{cov}(U)$ is propagated through the linear estimator of (5.4), yielding the covariance matrix $\mathrm{cov}(P)$ of the estimated parameters P (4.30)

$$\mathrm{cov}(P) = (M^T M)^{-1} M^T \mathrm{cov}(U)\, M (M^T M)^{-1}. \tag{5.5}$$

The effect of phantom model errors on the estimation accuracy, the second source of error, is studied in a two-step procedure. First the effect of small differences ΔX in the calibration setup $(x_i, y_i, z_i)\ i = 1,2,3$ (which change the phantom model s_{12}, s_{13}, s_{23} into $s'_{12}, s'_{13}, s'_{23}$) on the resulting point source projections U is simulated by the linear system

$$U = U_0 + N\,\Delta X \tag{5.6}$$

in which N is the matrix of the first order derivatives of the projection coordinates U, given in (5.1) and (5.2), to the Cartesian coordinates X of the calibration point sources. This system allows us to calculate the covariance matrix $\mathrm{cov}(U)$ due to random variations $\mathrm{cov}(X)$ of the calibration setup

$$\mathrm{cov}(U) = N\mathrm{cov}(X)\, N^T. \tag{5.7}$$

By substituting (5.7) now into (5.5), with M evaluated for the original phantom configuration s_{12}, s_{13}, s_{23}, the effects of the random variations of the phantom model $\mathrm{cov}(X)$ on the estimation accuracy $\mathrm{cov}(P)$ are eventually obtained.

Finally, the combined effects of noise on the calibration data and errors on the phantom model can easily be obtained by simply summing the covariance matrices $\mathrm{cov}(P)$ of the individual effects together.

5.2.2 Toward Reconstruction Accuracy

The covariance matrix $\mathrm{cov}(P)$ provides an excellent measure of the errors on the estimated parameters. In the next section however, the reconstruction accuracy will be evaluated and that evaluation starts from specific differences ΔP instead of a covariance matrix $\mathrm{cov}(P)$. If the errors on the different parameters of P were all independent (zero covariances), the effects of each parameter error $\Delta P_j = [0, ..., 0, 2\sigma_j, 0, ..., 0]^T \;\; j = 1, ..., 13$ could be evaluated individually. In this expression, σ_j represents the standard deviation of parameter j and a value of 2 standard deviations is chosen as a conservative, but realistic parameter error. A similar approach will be followed here. As shown in appendix A.5, the covariance matrix $\mathrm{cov}(P)$ can be decomposed as

$$\mathrm{cov}(P) = \Gamma\, \mathrm{cov}(Q)\, \Gamma^T = \Gamma\, I\, \Gamma^T = \Gamma\Gamma^T \tag{5.8}$$

in which I is the 13x13 identity matrix. (Note that this decomposition resembles an eigenvalue decomposition, but the columns of Γ do not have to form a set of normalized and orthogonal (eigen)vectors.) Consequently, there exists a set of errors ΔQ, which are independent of one another and which can be translated into the parameter errors ΔP by a linear transformation $\Delta P = \Gamma \Delta Q$. Each individual error $\Delta Q_j = [0, ..., 0, 2, 0, ..., 0]^T \;\; j = 1, ..., 13$ is now first transformed $\Delta P_j = \Gamma \Delta Q_j$ to the parameter errors ΔP and is then further processed as explained in the next section. Appendix A.5 provides a recursive method to calculate Γ.

Finally note that the phantom position parameters $t_x, t_y, t_z, \rho_1, \rho_2, \rho_3$ are estimated during the calibration, but that they are not used in the reconstruction process. Consequently, they can be ignored in the evaluation of the reconstruction accuracy and the above decomposition can be restricted to the block of $\mathrm{cov}(P)$ of the parameters $f, d^*, m, e_u, e_v, \Phi, \Psi$, yielding only 7 sets of independent parameter errors $\Delta P_1, \Delta P_2, ..., \Delta P_7$.

5.2.3 Reconstruction Accuracy

The reconstruction accuracy is evaluated for both loss of spatial resolution and deformation of the reconstructed images by simulating the reconstruction of a grid of point sources. Relatively simple grids can be used, since the circular orbit of the pinhole camera causes circular symmetry of the reconstruction properties, with respect to the axis of rotation. (In practice, the grid of 11 coplanar point sources, shown in figure 5.2, will be used.)

Consider the reconstruction of a point source (x_k, y_k, z_k) from its pinhole projections $(u_k(\theta), v_k(\theta))$ at the projection angles θ. If it is reconstructed using the correct acquisition geometry $f, d^*, m, e_u, e_v, \Phi, \Psi$, all projection rays (2.29)

$$\begin{aligned} fx''' + (u_k(\theta) - m\cos\Psi - e_u)y''' + d^*(u_k(\theta) - m\cos\Psi - e_u) - fm\cos\Psi = 0 \\ fz''' + (v_k(\theta) - m\sin\Psi - e_v)y''' + d^*(v_k(\theta) - m\sin\Psi - e_v) - fm\sin\Psi = 0 \end{aligned} \tag{5.9}$$

intersect at the correct point (x_k, y_k, z_k) in the field of view. Mathematically, the above projection rays yield a set of linear equations

$$\begin{aligned} a_{uk}(\theta)x + b_{uk}(\theta)y + c_{uk}(\theta)z + d_{uk}(\theta) = 0 \quad \forall\theta \\ a_{vk}(\theta)x + b_{vk}(\theta)y + c_{vk}(\theta)z + d_{vk}(\theta) = 0 \quad \forall\theta \end{aligned}$$

or

$$A_k X + B_k = 0 \tag{5.10}$$

with the unique solution $X_k = [x_k, y_k, z_k]^T$. For an incorrect acquisition geometry $f', d^{*'}, m', e'_u, e'_v, \Phi', \Psi'$, a similar set of equations exists, but the system will generally be overdetermined. We assume that in this case, the point source will be reconstructed at the least squares solution

$$X_k^R = -\left(A_k^T A_k\right)^{-1} A_k^T B_k \tag{5.11}$$

of this linear system.

The distances $S_k(\theta)$ from the 'reconstructed' point source $X_k^R = [x_k^R, y_k^R, z_k^R]^T$ to its different projection rays, provide a measure of the loss in spatial resolution due to the incorrect calibration results. These distances can be specified as vectors $S_k = [s_{xk}, s_{yk}, s_{zk}]^T$ in the xyz coordinate system with a specific length and direction. The loss in spatial resolution is specified in turn as the length of the largest vector for all point sources and projection angles, regardless of its direction

$$\text{res. loss} = \max_{\theta}(\max_{k}(\|S_k(\theta)\|)) \tag{5.12}$$

in which $\|.\|$ denotes the L_2 norm of a vector.

The image deformation due to the incorrect acquisition geometry is further evaluated by considering the displacement vectors $L_k = [l_{xk}, l_{yk}, l_{zk}]^T = [|x_k^R - x_k|, |y_k^R - y_k|, |z_k^R - z_k|]^T$ of the reconstructed point sources with respect to their original locations. These vectors are first corrected for a global translation and a

global rotation of all 11 point sources along and around the axis of rotation. The remaining displacements reflect the deformation of the reconstructed image with respect to the original phantom. This image deformation will be specified as the largest displacement of all the point sources, regardless of its direction

$$\text{img. deform.} = \max_k(\|L_k\|). \tag{5.13}$$

The decomposition of a covariance matrix $\text{cov}(P) = \Gamma\Gamma^T$, explained in the previous section, yields seven sets of independent parameter estimate errors $\Delta P_1, \Delta P_2, ..., \Delta P_7$. In such a case, the distances $\|S_{kPj}(\theta)\|$ and $\|L_{kPj}\|$, obtained with those 7 sets ($j = 1, ..., 7$), are first quadratically added together, before evaluating (5.12) and (5.13).

$$\|S_k(\theta)\| = \sqrt{\sum_j \|S_{kPj}(\theta)\|^2} \tag{5.14}$$

$$\|L_k\| = \sqrt{\sum_j \|L_{kPj}\|^2} \tag{5.15}$$

This approach is based on the assumption that the 7 sets of errors each have an independent effect on the image reconstruction accuracy.

5.3 Experiments

5.3.1 Optimal Calibration Setup

The first experiment evaluates the effect of the calibration setup on the estimation and reconstruction accuracy, both in the case of noisy calibration data and the case of phantom model errors. The aim is to find a calibration setup for optimal reconstruction accuracy, and possibly also optimal estimation accuracy, in practice. For this purpose, the estimation and reconstruction accuracy are calculated, as described in section 5.2, for a large set of calibration setups. The setups are generated by systematically varying the positions of the 3 calibration point sources over a spherical grid of possible point source locations in the pinhole field of view. A cross-section of the grid is shown in figure 5.1, and the complete grid is obtained by rotating this cross-section over 0^o, 45^o, 90^o and 135^o about the axis of rotation. We assume that the set of calibration setups obtained in this way, is sufficiently representative for the actual (infinite) set of possible calibration setups. Appendix A.6 further demonstrates that the spherical volume of the point source grid covers almost the entire field of view for pinhole cameras with small to moderate acceptance angles. The pinhole field of view is here defined as that part of space which is seen by the camera at all projection angles. The results are inspected for the smallest possible image deformations and resolution losses, and also for the lowest standard deviations of the parameter estimates.

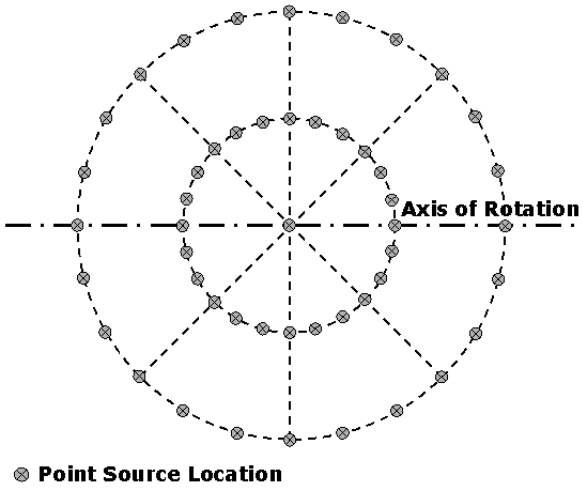

Figure 5.1: Cross-section of the spherical grid of possible point source locations in the field of view of the pinhole camera. The complete grid is obtained by rotating the displayed grid over 0^o, 45^o, 90^o and 135^o about the axis of rotation.

The experiment is performed for a pinhole camera with 24 cm focal length f. The focal point is rotating at 4 cm distance d^* around the rotation axis and the pinhole collimator has a 60^o acceptance angle α. The parameters m, e_u, e_v, Φ and Ψ are all equal to zero, simulating an 'ideal' pinhole system. This acquisition geometry yields a field of view of 4 cm in diameter and 64 equidistant projections over 360^o are simulated. The noise on the calibration data U is modelled by a diagonal covariance matrix $\text{cov}(U)$ in (5.5) with (independent) variances of 0.09 mm^2 (0.3 mm standard deviation) for each coordinate of U. This noise is visually worse than the noise of real calibration measurements with the above acquisition geometry. The phantom model errors are also represented by a diagonal covariance matrix $\text{cov}(X)$ (5.7), with (independent) variances of 0.01 mm^2 (0.1 mm standard deviation) for each Cartesian coordinate of X. Finally, the point source grid, used to evaluate the reconstruction accuracy is shown in figure 5.2.

5.3.2 Linear System Verification

In this experiment, the validity of the linear systems (5.4) and (5.6) are evaluated for the optimal calibration setups of the first experiment. This is done by applying the calibration method to a series of simulated calibration measurements. First, the noiseless projection locations U_0 of the calibration point sources are calculated with (5.1) and (5.2) for the correct calibration setup X. Next, 250 random noise realizations of either the projection data U_0 (Gaussian noise, 0.3 mm standard deviation) or the calibration setup X (Gaussian noise, 0.1 mm standard deviation) are generated. To evaluate the case of noisy calibration data, the calibration method

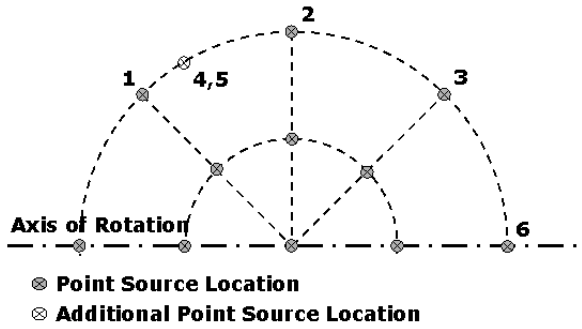

Figure 5.2: Grid of point sources to evaluate the deformation of reconstructed images. The numbers 1,2,3 and 4,5,6 indicate a relationship with the calibration point sources in Figure 5.3. The additional point source 4,5 is only used in experiment 5.3.3 for the optimal calibration setup 'opt2'.

is directly applied to each of the 250 noise realizations of U_0. For the phantom errors case, the noise realizations of X are used to calculate incorrect phantom models $s'_{12}, s'_{13}, s'_{23}$, which are then used in calibration calculations with the noiseless calibration data U_0. In the combined case, 250 different noise realizations of both U_0 and X are finally generated to simulate 250 calibrations with noise on the data and phantom model errors. In each of the cases, mean values, variances and covariances of the parameter estimates are calculated and compared with the corresponding results of the linear system approaches.

The experiment is conducted for the same pinhole and acquisition characteristics as in the first experiment.

5.3.3 Image Deformation

In the previous experiment, random modifications ΔX of the optimal calibration setups were generated by modifying the Cartesian coordinates X of the calibration point sources $i = 1, 2, 3$. For each calibration point source i individually, this modification causes a displacement of the point source, represented by the vector ΔX_i. In the evaluation of the reconstruction accuracy, the displacements L_k of the point sources k of the point source grid of figure 5.2 are studied. Keeping in mind the circular symmetry of the reconstruction properties, each of the calibration point sources i can be thought to be located at a specific location in the grid of point sources k, as indicated in the figures 5.2 and 5.3 (see further) by the corresponding numbers. With the displacements ΔX_i already calculated in the previous experiment, this additional experiment studies their relation with the resulting displacements $L_{k=i}$ of the corresponding point sources after reconstruction. It does so for both optimal calibration setups and is performed for the situation in which only phantom model errors are present. The results ΔP of each of the 250 calibrations of the previous experiment are used to evaluate the reconstruction accuracy as de-

scribed in section 5.2.3 and the resulting displacements $\|L_{k=i}\|$ are compared with the original displacements $\|\Delta X_i\|$ of the corresponding point sources. Note that, for calibration setup 'opt2', an additional point source '$4, 5$' was added to the grid of figure 5.2 to enable this experiment.

The experiment is again conducted for the same pinhole and acquisition characteristics as in the first experiment.

5.4 Results

5.4.1 Optimal Calibration Setup

With the standard deviations of the 7 acquisition parameters $f, d^*, m, e_u, e_v, \Phi, \Psi$ expressing the estimation accuracy, and with the resolution loss (5.12) and image deformation (5.13) expressing the reconstruction accuracy, a total of 9 parameters $p_i \quad i = 1, 9$ express the accuracy of the entire calibration-reconstruction process. For the same calibration setup, the accuracies p_i generally differ in the different situations of noisy data, phantom model errors and the combination of both. In each situation, different calibration setups further minimize different parameters p_i, yielding p_i^{min}. No solution was found minimizing all 9 parameters p_i simultaneously in either a single or all 3 cases.

For the case of noisy calibration data, a large number of setups can be found, yielding maximum image deformation and maximum loss of spatial resolution of less than 0.05 mm, while the attainable image resolution is expected to be 0.5 mm or worse. As these errors are much smaller than the attainable resolution, each of these setups can be considered to be equally favorable. In the phantom model errors case, also a large number of setups can be found yielding losses in spatial resolution of less than 0.05 mm, but image deformation is 0.20 mm or higher for all possible calibration setups. Nevertheless, a relatively large number of setups can be found with image deformations of less than 0.25 mm. Finally, roughly the same amount of setups satisfy these criteria in both cases

$$\begin{aligned} \text{res. loss} &\leq 0.05 \text{ mm} && \text{for noisy data} && (5.16)\\ \text{img. deform.} &\leq 0.05 \text{ mm} && && (5.17)\\ \text{res. loss} &\leq 0.05 \text{ mm} && \text{for model errors.} && (5.18)\\ \text{img. deform.} &\leq 0.25 \text{ mm} && && (5.19) \end{aligned}$$

This indicates that the optimality of the calibration setups in terms of the reconstruction accuracy is not very clearly defined and many calibration setups can in this respect be found to be optimal. This relative abundance of calibration setups with excellent reconstruction accuracy in any situation, is exploited to find solutions which also yield good estimation accuracy. The calibration setups 'opt1' and 'opt2' nearly minimize all 9 parameters p_i simultaneously in the noisy data and the

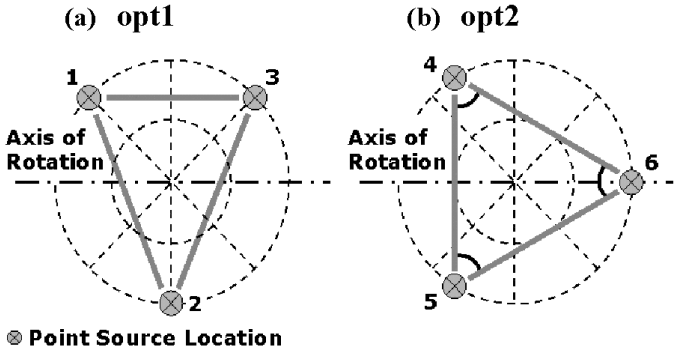

Figure 5.3: Optimal Calibration Setups: (a) 'opt1' and (b) 'opt2'. The numbers 1,2,3 and 4,5,6 indicate a relationship of the calibration point sources with specific point sources of the point source grid of figure 5.2.

phantom model errors case respectively. More precisely, they minimize the objective

$$\sqrt{\sum_{i=1}^{9} (p_i - p_i^{min})^2} \tag{5.20}$$

in those respective cases (with the parameters p_i expressed in millimeters or degrees), while also satisfying the reconstruction accuracy conditions (5.16) to (5.19). The setups are shown in figure 5.3 and table 5.2 lists the parameters p_i together with the minimum values p_i^{min} for each case. Note that the minimum values p_i^{min} are generally obtained with different calibration setups. Both optimal setups consist of a triangular phantom configuration with the axis of rotation in the plane of the triangle and all 3 point sources on the edge of the (spherical) field of view. In 'opt1' the triangle is isosceles, with the third side parallel to the axis of rotation. In 'opt2' the triangle is equilateral and one point source is located on the axis of rotation.

Figure 5.4 and 5.5 illustrate the 6 calibration setups with the best performance in terms of the objective (5.20) for the noisy data and phantom model errors case respectively and satisfying the restrictions (5.16) to (5.19) (in both cases). In comparison with the calibration setups (a), the setups (b) to (f) yield only a marginal increase in the value of the objective (5.20), indicating that this cost is relatively flat and that multiple effective optima are actually available.

Regardless of the situation in which they were tested, the optimal calibration setups 'opt1' and 'opt2' only show small deviations from the optimal accuracy. In terms of reconstruction accuracy, the differences are so small that they will not be noticeable in practice. In the phantom model errors and combined cases, the calibration setup 'opt1' shows a marked increase in the standard deviation of the focal length f and small increases in the standard deviations of e_v and Φ. The calibration setup 'opt2' on the other hand, shows small increases in the standard

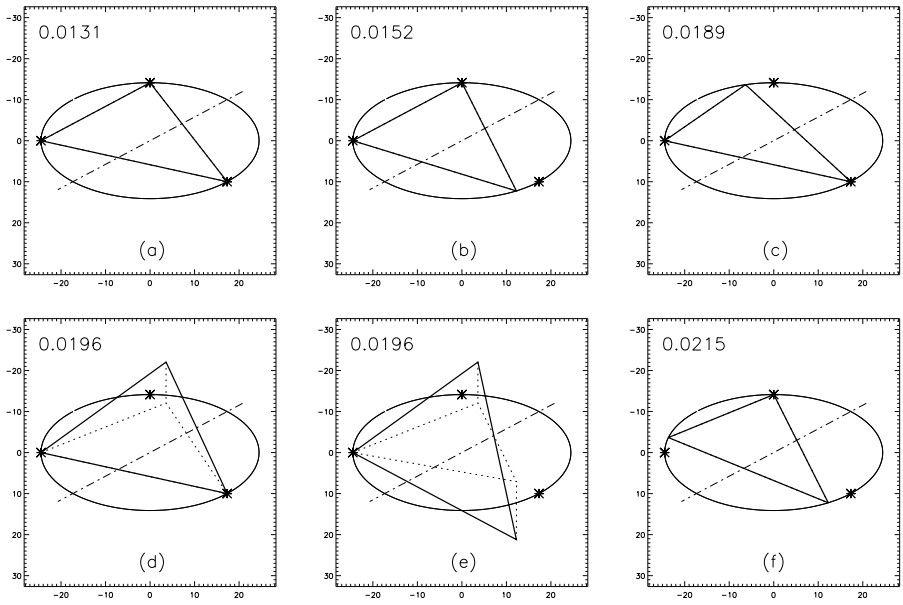

Figure 5.4: The 6 calibration setups with the best performance in terms of the objective (5.20) for noisy calibration data. The value of objective (5.20) is indicated in the figure. The circle represents the intersection of the horizontal plane containing the axis of rotation (the dash-dotted line) with the pinhole field of view. Asterisks indicate the position of the point sources of 'opt1'. The solid triangles show the calibration setups in 3D, while the dotted triangles are the orthogonal projections of these calibration setups on the horizontal plane.

deviations of f, d^*, e_v and Φ in the case of noisy calibration data and in the combined case.

The image deformations (0.215 mm and 0.202 mm) of the optimal setups in the phantom error case are clearly smaller than the 0.346 mm root mean square value of the displacements $2||\Delta X_i||$ causing them. (Twice the value of $||\Delta X_i||$ is selected, since the errors ΔP were calculated from two standard deviations of the geometric parameter estimates.) The image deformation due to an incorrect phantom model will thereby generally be of the same magnitude or less than the deformation of the phantom model itself.

5.4.2 Linear System Verification

The results of the calibration simulations are indicated by 'sim1' and 'sim2' for the calibration setups 'opt1' and 'opt2' respectively. The standard deviations of the parameter estimates, presented in table 5.2, show excellent agreement between the linear system and simulation approaches. The correlations between the estimates of

Table 5.2: Reconstruction & Estimation Accuracy.

		Reconstruction Accuracy		**Estimation Accuracy (Standard deviation)**						
		img. deform.	res. loss	f	d^*	m	e_u	e_v	Φ	Ψ
		[mm]	[mm]	[mm]	[mm]	[mm]	[mm]	[mm]	[deg]	[deg]
Data Noise	min	0.013	0.024	0.20	0.03	0.03	0.22	0.19	0.04	0.01
	opt1	0.014	0.025	0.21	0.03	0.03	0.23	0.19	0.04	0.01
	sim1			0.22	0.03	0.03	0.23	0.20	0.04	0.01
	opt2	0.018	0.034	0.35	0.05	0.03	0.23	0.29	0.05	0.01
	sim2			0.35	0.05	0.03	0.23	0.31	0.05	0.01
Model Errors	min	0.201	0.002	0.00	0.12	0.00	0.00	2.77	0.66	0.00
	opt1	0.215	0.027	0.54	0.13	0.00	0.00	2.95	0.71	0.00
	sim1			0.53	0.13	0.00	0.02	2.93	0.70	0.00
	opt2	0.202	0.002	0.00	0.12	0.00	0.00	2.77	0.66	0.00
	sim2			0.05	0.11	0.00	0.01	2.63	0.63	0.00
Combi	min	0.202	0.025	0.20	0.12	0.03	0.22	2.78	0.66	0.01
	opt1	0.215	0.037	0.58	0.13	0.03	0.23	2.95	0.71	0.01
	sim1			0.58	0.13	0.03	0.23	2.95	0.71	0.01
	opt2	0.203	0.034	0.35	0.13	0.03	0.23	2.79	0.66	0.01
	sim2			0.33	0.13	0.03	0.24	2.76	0.66	0.01

Table 5.3: Parameter Estimate Cross Correlations

Data		f	d^*	m	e_u	e_v	Φ	Ψ
Noise	f	**1.00**	**0.97**	0.00	0.00	0.00	0.00	0.00
	d^*		**1.00**	0.00	0.00	0.00	0.00	0.00
	m			**1.00**	**-1.00**	0.00	0.00	0.00
	e_u				**1.00**	0.00	0.00	0.00
	e_v		**opt1**			**1.00**	**0.92**	0.00
	Φ						**1.00**	0.00
	Ψ							**1.00**
		f	d^*	m	e_u	e_v	Φ	Ψ
	f	**1.00**	**0.97**	-0.06	0.06	-0.08	-0.12	-0.06
	d^*		**1.00**	-0.04	0.05	-0.08	-0.13	-0.07
	m			**1.00**	**-1.00**	0.02	-0.01	-0.09
	e_u				**1.00**	-0.03	0.00	-0.09
	e_v		**sim1**			**1.00**	**0.91**	0.00
	Φ						**1.00**	0.06
	Ψ							**1.00**
Model		f	d^*	m	e_u	e_v	Φ	Ψ
Errors	f	**1.00**	0.43			0.00	0.00	
	d^*		**1.00**			0.00	0.00	
	m			**1.00**				
	e_u				**1.00**			
	e_v		**opt1**			**1.00**	**1.00**	
	Φ						**1.00**	
	Ψ							**1.00**
		f	d^*	m	e_u	e_v	Φ	Ψ
	f	**1.00**	0.43			-0.08	-0.08	
	d^*		**1.00**			-0.09	-0.09	
	m			**1.00**				
	e_u				**1.00**			
	e_v		**sim1**			**1.00**	**1.00**	
	Φ						**1.00**	
	Ψ							**1.00**
Combi		f	d^*	m	e_u	e_v	Φ	Ψ
	f	**1.00**	**0.47**	0.00	0.00	0.00	0.00	0.00
	d^*		**1.00**	0.00	0.00	0.00	0.00	0.00
	m			**1.00**	**-1.00**	0.00	0.00	0.00
	e_u				**1.00**	0.00	0.00	0.00
	e_v		**opt1**			**1.00**	**1.00**	0.00
	Φ						**1.00**	0.00
	Ψ							**1.00**
		f	d^*	m	e_u	e_v	Φ	Ψ
	f	**1.00**	**0.49**	-0.06	0.05	0.00	0.00	0.05
	d^*		**1.00**	-0.08	0.09	0.03	0.03	0.03
	m			**1.00**	**-1.00**	0.05	0.05	0.00
	e_u				**1.00**	-0.05	-0.06	0.01
	e_v		**sim1**			**1.00**	**1.00**	-0.12
	Φ						**1.00**	-0.13
	Ψ							**1.00**

Cross correlations for parameters with zero standard deviation are omitted.

Table 5.4: Parameter Estimate Cross Correlations

Data		f	d^*	m	e_u	e_v	Φ	Ψ
Noise	f	**1.00**	**0.99**	0.00	0.00	**0.70**	**0.52**	0.00
	d^*		**1.00**	0.00	0.00	**0.71**	**0.51**	0.00
	m			**1.00**	**-1.00**	0.00	0.00	0.03
	e_u				**1.00**	0.00	0.00	0.03
	e_v		**opt2**			**1.00**	**0.92**	0.00
	Φ						**1.00**	0.00
	Ψ							**1.00**
		f	d^*	m	e_u	e_v	Φ	Ψ
	f	**1.00**	**0.99**	-0.07	0.07	**0.69**	**0.52**	-0.18
	d^*		**1.00**	-0.07	0.07	**0.70**	**0.51**	-0.17
	m			**1.00**	**-1.00**	-0.03	-0.05	-0.07
	e_u				**1.00**	0.03	0.05	0.08
	e_v		**sim2**			**1.00**	**0.93**	-0.02
	Φ						**1.00**	0.00
	Ψ							**1.00**
Model		f	d^*	m	e_u	e_v	Φ	Ψ
Errors	f	**1.00**						
	d^*		**1.00**			0.00	0.00	
	m			**1.00**				
	e_u				**1.00**			
	e_v		**opt2**			**1.00**	**1.00**	
	Φ						**1.00**	
	Ψ							**1.00**
		f	d^*	m	e_u	e_v	Φ	Ψ
	f	**1.00**						
	d^*		**1.00**			0.14	0.14	
	m			**1.00**				
	e_u				**1.00**			
	e_v		**sim2**			**1.00**	**1.00**	
	Φ						**1.00**	
	Ψ							**1.00**
Combi		f	d^*	m	e_u	e_v	Φ	Ψ
	f	**1.00**	**0.41**	0.00	0.00	0.07	0.04	0.00
	d^*		**1.00**	0.00	0.00	0.03	0.02	0.00
	m			**1.00**	**-1.00**	0.00	0.00	0.03
	e_u				**1.00**	0.00	0.00	-0.03
	e_v		**opt2**			**1.00**	**1.00**	0.00
	Φ						**1.00**	0.00
	Ψ							**1.00**
		f	d^*	m	e_u	e_v	Φ	Ψ
	f	**1.00**	**0.42**	0.05	-0.05	0.07	0.04	0.09
	d^*		**1.00**	0.06	-0.06	0.07	0.06	-0.01
	m			**1.00**	**-1.00**	-0.01	-0.01	-0.04
	e_u				**1.00**	0.02	0.02	0.04
	e_v		**sim2**			**1.00**	**1.00**	-0.01
	Φ						**1.00**	-0.01
	Ψ							**1.00**

Cross correlations for parameters with zero standard deviation are omitted.

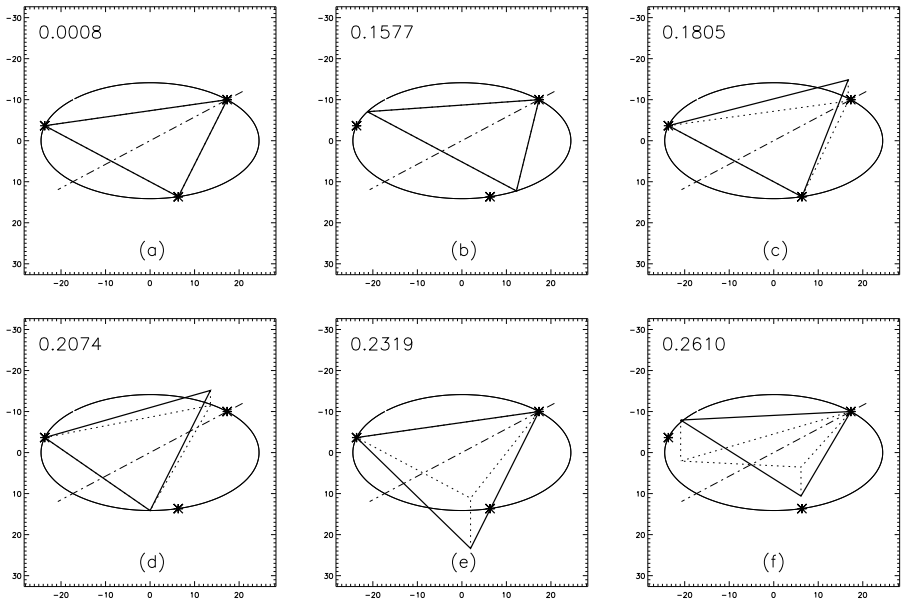

Figure 5.5: The 6 calibration setups with the best performance in terms of the objective (5.20) for phantom model errors. The value of objective (5.20) is indicated in the figure. The circle represents the intersection of the horizontal plane containing the axis of rotation (the dash-dotted line) with the pinhole field of view. Asterisks indicate the position of the point sources of 'opt2'. The solid triangles show the calibration setups in 3D, while the dotted triangles are the orthogonal projections of these calibration setups on the horizontal plane.

the different parameters, shown in table 5.3 and 5.4, further show good agreement as well between the different approaches. (Note that the cross correlations for parameters with zero variance are omitted in table 5.3 and 5.4). Finally, the linear system approaches assume zero bias on the parameter estimate results. Table 5.5 lists the mean values of the different parameter estimates. Considering the standard deviations for these parameter estimates, the mean values are always very close to the correct values, confirming the validity of the zero bias implicit assumption of the linear systems.

5.4.3 Image Deformation

In figure 5.6, the displacements $\|L_i\|$ of the reconstructed point sources $1, 2, 3$ and $4, 5, 6$ of figure 5.2 are plotted against the initial displacements ΔX_i of the corresponding point sources of the calibration setups 'opt1' and 'opt2' respectively. The reconstruction image deformations $\|L_i\|$ are generally smaller than the modelling errors $\|\Delta X_i\|$ for both calibration setups and for each of its point sources. The

Table 5.5: Parameter Estimate Mean Value

		Estimation Accuracy (Mean value)						
		f [mm]	d^* [mm]	m [mm]	e_u [mm]	e_v [mm]	Φ [deg]	Ψ [deg]
Exact	opt	240.00	40.00	0.00	0.00	0.00	0.00	0.00
Data Noise	sim1	239.99	40.00	0.00	0.01	0.00	0.00	0.00
	sim2	240.01	40.00	0.00	0.03	0.03	0.01	0.00
Model Errors	sim1	239.96	40.01	0.00	0.00	-0.13	-0.03	0.00
	sim2	240.01	40.01	0.00	0.00	0.32	0.07	0.00
Combination	sim1	239.96	40.00	0.00	-0.02	0.32	0.08	0.00
	sim2	240.03	40.01	0.00	-0.01	0.14	0.03	0.00

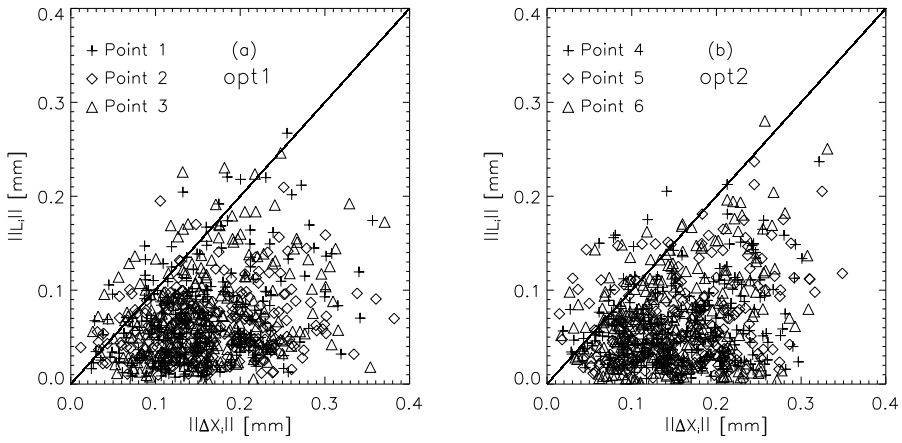

Figure 5.6: Displacements $\|L_i\|$ of the reconstructed point sources versus the displacements $\|\Delta X_i\|$ of the calibration model with respect to the phantom configuration. (a) results for 'opt1' and (b) results for 'opt2'.

sum of the displacements $\|L_i\|$ of the point source reconstructions $1, 2, 3$ or $4, 5, 6$ is further always less than the sum of the corresponding modelling errors $\|\Delta X_i\|$. These data again support the earlier observation that the reconstruction image deformation due to an incorrect phantom model is of the same magnitude or less than the deformation of the phantom model itself.

5.5 Discussion

The method we developed to determine the acquisition geometry of a pinhole camera [29], is based on the assumption that the calibration phantom is the representation of

an image, which can be thought of as an infinite collection of point sources. Stated in this way, the best calibration phantom, is the one best representing the entire image. From this point of view, the best way to improve the phantom probably consists in adding additional point sources to it. It also suggests that the point sources should be distributed to cover the entire field of view, although not necessarily in a uniform way. Our results indicate that the theoretically minimal number of point sources [29], placed at well chosen locations in the field of view, is already sufficient for practical purposes. The above concept also explains how the use of an incorrect phantom model, results in an equivalent deformation of the reconstructed image. The calibration minimizes the inconsistency between the fixed, but incorrect phantom model and the measured projections by modifying the projector. During reconstruction, the same projector is then used to generate an image, which is consistent with its projections.

The optimal calibration setups seem to agree with earlier findings of Wang *et al.* [34] and Noo *et al.* [31] about optimal setups for their calibration methods. Wang *et al.* [34] used a single calibration point source and reported that the estimation accuracy improved with larger distances between the point source and the axis of rotation. On the other hand, Noo *et al.* [31] used two point sources and reported that these point sources should be placed well apart from each other and from the focal plane, with the focal plane being the plane in which the focal point is rotating during image acquisition. In both optimal calibration setups, the point sources are all located on the edge of the field of view, yielding the best compromise in distance to the axis of rotation and distance to the focal plane for a spherical field of view. In calibration setup 'opt1', point source 2 is located exactly in the focal plane, but at the largest possible distance from the rotation axis. The point sources 1 and 3 on the other hand, are located at a considerable distance from the focal plane, but without sacrificing too much of their distance to the rotation axis. In the calibration setup 'opt2', point source 6 is placed as far as possible from the focal plane and therefore on the axis of rotation. Point sources 4 and 5 are placed at a considerable distance from the axis of rotation, but now closer to the focal plane. Some types of calibration setups are also specifically prohibited by theory [29]. The 3 point sources each must have a different position, they may not all 3 have the same z coordinate and at least one point source must be located off the axis of rotation. As expected, the optimal calibration setups are clearly different from these forbidden setups.

In practice, noise on the calibration data and errors on the phantom model will always be present in calibration experiments. In theory, the optimal setup for each particular calibration may depend on the relative magnitude of the noise and the model errors. The calibration setups we propose, are however nearly optimal for both noise and model errors, which suggests that their performance is rather independent of this relative magnitude. Further, for the realistic noise level of the experiments, the small phantom model errors (0.1 mm standard deviation) clearly dominate the reconstruction accuracy. Note however, that for a fixed phantom configuration, the phantom model (distances between the point sources) only needs to be measured once. Consequently, this should be done with care to keep the

errors below the maximum tolerable deformations of reconstructed images. The inaccuracies due to noise, on the other hand, only have a very limited impact on the reconstruction accuracy with the proposed calibration setups and further noise reduction does not seem necessary.

Apart from being quite simple and ignoring the difference between millimeters and degrees, one can argue that the objective (5.20) used to find the optimal calibration setups 'opt1' and 'opt2' is rather arbitrary. The main conclusion of section 5.4.1 is however that the geometrically attractive setups 'opt1' and 'opt2' yield nearly the best possible accuracies of all parameters p_i, especially with respect to the reconstruction accuracy, and they do so in all situations studied. Although the objective (5.20) may be simple, it will penalize calibration setups with a markedly different behavior. Further, other setups closely resembling 'opt1' and 'opt2' yield very similar accuracies in terms of the above objective (see figure 5.4 and 5.5), suggesting that the overall accuracy related to the proposed setups is stable as well.

The approach of the first experiment to start with a linear system to calculate the calibration covariance matrix $\mathrm{cov}(P)$ and then decompose it into a set of independent errors $\Delta P_1, ..., \Delta P_7$ to evaluate the reconstruction accuracy, may seem cumbersome. Two possible solutions have been considered. A first solution might be to perform a series of calibration simulations with noisy data sets (ΔU) to calculate the estimation accuracy. The result ΔP of each simulation individually can then be used to evaluate the reconstruction accuracy for that particular noise realization ΔU, while the calibration covariance matrix $\mathrm{cov}(P)$ can still be calculated from a sufficiently large number of simulations, like in the second and third experiment. Unfortunately, this procedure has to be repeated for each calibration setup and is far too slow for such purposes. A second possibility is the use of some linear system to evaluate the reconstruction accuracy directly from the covariance matrix $\mathrm{cov}(P)$, avoiding its decomposition. However, the reconstruction accuracy must be evaluated for both image deformation and spatial resolution. Further, a global rotation and translation of the reconstructed image should not be considered as image deformations. No linear system has been found that satisfies these requirements.

5.6 Conclusion

In this chapter, we have developed an efficient method to estimate the effect of noise and phantom model errors on the accuracy of pinhole SPECT calibration and the subsequent effect on the accuracy of image reconstruction. The method allowed us to optimize the calibration method of chapter 4 for optimal calibration and reconstruction accuracy. Two specific configurations of three point sources with a specific position and orientation in the field of view have been proposed as optimal pinhole SPECT calibration setups in practice. The setups yield optimal reconstruction accuracy, while the accuracy of the estimated pinhole acquisition geometry is nearly optimal as well. With the proposed calibration setups, errors in the phantom model will cause image deformations of the same magnitude or less.

Chapter 6

Preliminary Comparison of Single and Multipinhole SPECT Imaging

6.1 Introduction

Recently, multipinhole SPECT imaging has been proposed as an alternative to single pinhole SPECT for emission tomography imaging of small laboratory animals [2–4] and has been applied successfully for this purpose. Because of the additional pinhole apertures available for imaging, multipinhole SPECT imaging has the potential for providing a better sensitivity for the activity distribution under study. The additional pinhole apertures may also yield a better sampling of this activity distribution, thereby getting closer to satisfying the data sufficiency conditions [5–7] for pinhole imaging with a circular orbit of the detector. However, multipinhole imaging most often also leads to overlapping projections and the effect of such overlap on data sufficiency and on the accuracy of subsequent image reconstruction remains yet to be understood more thoroughly. To avoid overlap, multipinhole collimation can be applied with pinhole apertures with sufficiently small acceptance angles and at a sufficiently large distance from the activity distribution under study. However this has a negative effect on the overall sensitivity and the sampling of the activity distribution will also become more sparse, because of the converging-diverging beam geometry of pinhole SPECT imaging. In conclusion, multipinhole SPECT imaging shows potential for improved emission tomography of small laboratory animals over single pinhole SPECT, but the exact conditions under which this becomes reality remain yet to be determined.

This chapter conducts a comparative simulation study of the reconstruction problem in pinhole and multipinhole SPECT imaging. The multipinhole situation studied is the situation already explained in section 3.4.3. It is a 7 pinhole config-

uration with all pinholes focusing on the same spherical field of view, aiming for optimal sensitivity with minimal overlap of the pinhole projections. The situation is compared with a single pinhole situation with a much larger acceptance angle pinhole aperture at the minimum distance from the spherical field of view to avoid truncation. In this way, the single pinhole situation has optimal sensitivity for the activity in the field of view, but a significantly different way of sampling it in comparison with the multipinhole situation. We thereby mainly study the effects of differences in sampling, while keeping the corresponding sensitivities at realistic levels.

The idea of this chapter is to study how well each voxel of the above spherical field of view can be reconstructed in practice. From a data sufficiency point of view, most of these voxels can not be reconstructed exactly, but these sufficiency conditions do not reveal 'how bad' the reconstruction of those voxels will be. We therefore revert to the ideas of Fessler *et al.* [41, 42] and Qi *et al.* [43, 44] to study the characteristics of local impulse responses after convergence of a maximum-a-posteriori (or MAP) reconstruction with the quadratic prior. These local impulse responses allow us to evaluate the quality of reconstruction in each voxel of the reconstructed image. We select the contrast recovery coefficient from the work of Qi *et al.* [43, 44] as a measure of the quality of reconstruction, but we back it up with some additional measures, since we will show that the contrast recovery is not always a reliable measure.

6.2 Theory

6.2.1 MAP Reconstruction

In section 3.2.1 it was shown how the application of Bayes' rule to the problem of reconstructing an image Λ from emission tomography data Q with Poisson noise leads to the log-likelihood $L(Q|\Lambda)$

$$L(Q|\Lambda) = \sum_i q_i \ln(\sum_j c_{ij}\lambda_j) - \sum_j c_{ij}\lambda_j. \tag{6.1}$$

Optimization of this likelihood with respect to the reconstruction image Λ eventually yielded the MLEM algorithm (3.16) for image reconstruction in emission tomography. This algorithm was obtained by the assumption that each reconstruction image Λ is equally likely, such that $p(\Lambda)$ was constant. In maximum-a-posteriori or MAP reconstruction, some expectation $p(\Lambda)$ about the reconstruction image Λ is available prior to reconstruction and this expectation is taken into account during image reconstruction. This can be done by incorporating a mathematical expression of $p(\Lambda)$ in the derivation of the reconstruction algorithm, or equivalently by adding a penalty term $U(\Lambda)$ to the above log-likelihood $L(Q|\Lambda)$, yielding the posterior likelihood $G(\Lambda|Q)$,

$$G(\Lambda|Q) = \sum_i q_i \ln(\sum_j c_{ij}\lambda_j) - \sum_j c_{ij}\lambda_j - \beta U(\Lambda) \tag{6.2}$$

which penalizes solutions Λ not satisfying the expectation $p(\Lambda)$. The expectation $p(\Lambda)$ and the penalty term $U(\Lambda)$ in the above posterior likelihood are related by

$$\ln\left(p(\Lambda)\right) = -\beta U(\Lambda) \tag{6.3}$$

The parameter β controls the relative importance of the penalty term $U(\Lambda)$ with respect to the original log-likelihood. The choice of

$$U(\Lambda) = \sum_j \sum_k w_{jk} \frac{(\lambda_j - \lambda_k)^2}{2\sigma^2} \tag{6.4}$$

yields the posterior likelihood $G(\Lambda|Q)$ for image reconstruction with the quadratic prior. This quadratic prior favors smoothness in the reconstructed image Λ by penalizing differences in neighboring voxels in a quadratic way. The parameter σ allows you to tune the severity of the prior (although σ equals 1 throughout this chapter). The weights w_{jk} define the space invariant neighborhood of each voxel with $w_{jk} = w_{kj}$ and $w_{jk} = w_{j-k}$. The addition of the quadratic prior has a regularizing effect on image reconstruction: its smoothing effect is small for a strong likelihood $L(q_i|\Lambda)$ (i.e. when good quality information for the reconstruction is available), but large for a weak likelihood $L(q_i|\Lambda)$.

6.2.2 Linearized Local Impulse Response

In this section we explicitly assume that the activity distribution $\Lambda = \{\lambda_j : j = 1, ..., J\}$ and its projection $Q = \{q_i : i = 1, ..., I\}$ are expressed as column matrices, while $C = \{c_{ij}\}$ is the system matrix for projection. The reconstruction $\hat{\Lambda}$ from the projection data Q of an unknown activity distribution Λ, with $\bar{Q}(\Lambda) = C\,\Lambda$, by the above MAP algorithm can be considered as an optimization problem in which the estimator $\hat{\Lambda}$ is implicitly defined as

$$\hat{\Lambda} = \arg\max_{\lambda_j \geq 0} G(\Lambda|Q). \tag{6.5}$$

Because this estimator $\hat{\Lambda}$ is non-linear in the data Q, space-variant and object-dependent, it can not be studied using the regular impulse response theory for linear, space-invariant systems. However, Fessler [41] has proposed a generalization of the impulse response for emission tomography, called the linearized local impulse response l_j

$$l_j(\Lambda) = \frac{\partial}{\partial \lambda_j} \hat{\Lambda}(\bar{Q}(\Lambda)). \tag{6.6}$$

This linearized local impulse response measures the change in the mean reconstructed image due to a perturbation in one of the voxels of the activity distribution Λ. The impulse response is local, since it depends on the particular voxel being considered (voxel j) and also because it depends on the particular point Λ in the space of all possible realizations $\Lambda = \{\lambda_j \geq 0\}$. It is further linear because it is based on the assumption that the estimator $\hat{\Lambda}$ is locally linear about the expansion point

$\bar{Q}(\Lambda)$ (i.e. the ensemble mean of reconstructions from noisy data Q is approximately equal to the reconstruction from noiseless data [41]).

Now consider the perturbation of the unknown activity distribution Λ with a very small fraction δ of an impulse e_j, which is 1 in voxel j and 0 in each voxel $k \neq j$, yielding the new activity distribution Λ_e

$$\Lambda_e = \Lambda + \delta e_j. \tag{6.7}$$

Because of the linearity of the projection operation C, the projection of this modified activity distribution Λ_e further yields the projection data $\bar{Q}_e$ instead of $\bar{Q}$, with

$$\bar{Q}_e(\Lambda_e) = \bar{Q}(\Lambda) + C\delta e_j. \tag{6.8}$$

Reconstruction from the projection data $\bar{Q}_e$ will eventually yield the reconstruction $\hat{\Lambda}_e$

$$\hat{\Lambda}_e = \hat{\Lambda} + \delta l_j(\Lambda) \tag{6.9}$$

in which $l_j(\Lambda)$ (or l_j for convenience) represents the local impulse response of the reconstruction algorithm for the perturbation δe_j of the original activity distribution Λ.

Applying the chain rule of differentiation to the linearized local impulse response (6.6) yields

$$l_j(\Lambda) = \frac{\partial \hat{\Lambda}(\bar{Q})}{\partial \bar{Q}} \frac{\partial \bar{Q}(\Lambda)}{\partial \lambda_j}. \tag{6.10}$$

From (6.8) it is now clear that the second differentiation in (6.10) actually represents the projection of a perturbation e_j of the original activity distribution Λ [41], yielding

$$l_j(\Lambda) = \frac{\partial \hat{\Lambda}(\bar{Q})}{\partial \bar{Q}} Ce_j. \tag{6.11}$$

To evaluate the derivative of the reconstruction $\hat{\Lambda}$ in the above expression (6.11), note that reconstruction $\hat{\Lambda}(Q)$ from projection Q maximizes the posterior likelihood $G(\Lambda|Q)$ and thus it thereby satisfies

$$\left.\frac{\partial L(Q|\Lambda)}{\partial \lambda_j}\right|_{\Lambda=\hat{\Lambda}(Q)} - \beta \left.\frac{\partial U(\Lambda)}{\partial \lambda_j}\right|_{\Lambda=\hat{\Lambda}(Q)} = 0 \quad \forall j. \tag{6.12}$$

Performing a differentiation of (6.12) with respect to Q using the chain rule yields

$$\left(\left[\frac{\partial^2 L(Q|\hat{\Lambda})}{\partial \lambda_j \partial \lambda_k} \right] - \beta \left[\frac{\partial^2 U(\hat{\Lambda})}{\partial \lambda_j \partial \lambda_k} \right] \right) \frac{\partial \hat{\Lambda}(Q)}{\partial Q} = - \left[\frac{\partial^2 L(Q|\hat{\Lambda})}{\partial \lambda_j \partial q_i} \right] \tag{6.13}$$

in which the square brackets explicitly indicate that the derivatives of the likelihood L and the prior penalty U are the elements of a matrix. With the assumption that $\bar{Q}(\hat{\Lambda}) = \bar{Q}(\Lambda)$ (i.e. the projections of the reconstructed and original activity distribution are equal) the evaluation of (6.13) for $Q = \bar{Q}$ yields [41]

$$\left(C^T D \left(\frac{1}{\bar{q}_i} \right) C + \beta R \right) \frac{\partial \hat{\Lambda}(Q)}{\partial Q} = C^T D \left(\frac{1}{\bar{q}_i} \right) \tag{6.14}$$

in which $D(1/\bar{q}_i)$ represents a diagonal matrix with diagonal elements $(1/\bar{q}_i)$. The matrix R is further the matrix of the second derivatives of the prior energy function U with elements R_{jk}

$$R_{jk} = \sum_{l \neq j} w_{jl} \quad k = j \tag{6.15}$$

$$= -w_{jk} \quad k \neq j. \tag{6.16}$$

By assuming that $(C^T D(1/\bar{q}_i)C + \beta R)$ is invertible, the substitution of (6.14) into (6.11) with $Q = \bar{Q}$ eventually yields

$$l_j(\Lambda) = \left(C^T D\left(\frac{1}{\bar{q}_i}\right) C + \beta R \right)^{-1} C^T D\left(\frac{1}{\bar{q}_i}\right) C e_j \tag{6.17}$$

or

$$l_j(\Lambda) = [F + \beta R]^{-1} F e_j \tag{6.18}$$

in which $F = C^T D(1/\bar{q}_i)C$ represents the Fisher information matrix. The matrix inversion in (6.17) and (6.18) illustrates the importance of the quadratic prior for regularization in this application. Without the complicating scaling by the variance $D(1/\bar{q}_i)$, the Fisher information matrix F would yield $F = C^T C$, in which C is the system matrix of the pinhole or multipinhole projection. Both for pinhole and multipinhole imaging, with a circular detector orbit, this matrix is not of full rank (cfr. section 3.2.1) and as a result, F is not invertible. The smoothing prior R helps to regularize the inversion, although it excludes at the same time the ideal system response $l_j = e_j$.

6.2.3 Efficient Calculation of the Linearized Local Impulse Response

The calculation of the linearized local impulse response l_j from (6.18) requires the inversion of the JxJ matrix $F+\beta R$, in which J represents the total number of image voxels. Given the relatively high number of image voxels in emission tomography, this solution is not feasible in practice. Note however that R is a circulant matrix and so a multiplication with R is a space-invariant operation. If F were to be space-invariant as well, then (6.18) would reduce to the subsequent convolution of the perturbation e_j with the convolution masks defined by F and $[F + \beta R]^{-1}$ respectively. Generally, the pinhole and multipinhole SPECT projections are not space invariant and as a result F will not be space invariant either. However, for two neighboring voxels j and k, the projections Ce_j and Ce_k are expected to be very similar. Since the difference in count rates q_i in neighboring detector bins i (voxels j and k will project to neighboring detector bins) can generally be expected to be quite similar as well, the results of Fe_j and Fe_k are also expected to be very similar, except for the small shift of the result from voxel j to voxel k. Furthermore, the local impulse response l_j is typically concentrated around voxel j. These observations motivate the assumption of a locally space-invariant Fisher information matrix [41–44].

To calculate the linear local impulse response l_j for voxel j we exploit this local space-invariance by replacing the rows (or columns) of the Fisher information matrix by shifted versions of the row (or column) of voxel j. This results in a modified Fisher information matrix that is space-invariant, but well adapted to calculate the linearized local impulse response for voxel j. The resulting convolutions can now be performed in Fourier space, yielding an approximate, but efficient way of calculating linearized local impulse responses.

6.2.4 Linearized Local Impulse Response Analysis

Qi *et al.* [43, 44] proposed the contrast recovery as a measure of the accuracy with which a voxel can be reconstructed. This contrast recovery is the change of voxel j, termed l_j^j, for a perturbation e_j in that voxel j. The idea is that the more information there is available for the reconstruction of voxel j, the better the linearized local impulse response l_j will resemble the original perturbation e_j, since the quadratic prior will only cause very moderate smoothing of the response in such situations. With less information for reconstruction available, the prior will gain in relative strength and cause more smoothing of the response. As a result, a higher contrast recovery l_j^j reflects a better reconstruction for the voxel considered.

Although Qi *et al.* obtained very good results for regular PET imaging [43, 44], we believe that the contrast recovery by itself is not always an ideal measure of how well a voxel can be reconstructed from projections. The problem is that it does not take the shape of the linearized local impulse response into account, only the value of its central pixel. In our opinion, impulse responses which are symmetrical and closely centered about their origin are preferable over responses with activity radiating out in various directions. To evaluate such behavior, we introduce some additional measures. First the linearized local impulse response is thresholded to a fraction of its contrast recovery and only the central part of the response is selected by region growing. Then 4 additional measures of how well a voxel can be reconstructed are derived:

1. The minimum distance d_{min} from voxel j to the edge of the thresholded impulse response l_j.
2. The maximum distance d_{max} from voxel j to the edge of the thresholded impulse response l_j.
3. The second order moment of the intensities of the thresholded impulse l_j with respect to voxel j (d_{int}).
4. The total number of voxels $\sharp v$ in the thresholded impulse response l_j.

For a symmetrical and well centered local impulse response, all 4 measures should be as low as possible, and the ratio of d_{min}/d_{max} should be as high as possible.

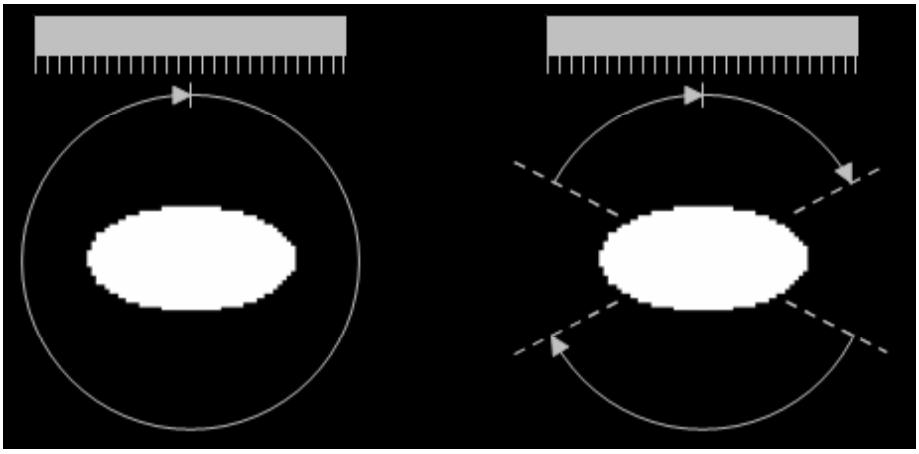

(a) (b)

Figure 6.1: Contrast Recovery Experiment: (a) regular circular parallel hole acquisition of a uniform elliptical activity distribution with 160 equidistant projections over 360^o, (b) similar acquisition of equal length, but skipping the 30% most horizontal projection angles.

6.3 Experiments

6.3.1 Contrast Recovery

To illustrate that the contrast recovery is not always an appropriate measure of how well an image can be reconstructed, we simulate 2 different parallel hole SPECT acquisitions (2D) of a uniformly attenuating ellipse of uniform activity, as illustrated in figure 6.1 (a) and (b). The ellipse has a long axis length of 54 cm, a short axis length of 27 cm and a linear attenuation coefficient of 0.15 cm^{-1}. The first acquisition (figure 6.1 (a)) is a regular circular acquisition over 360^o consisting of 160 equidistant projections. The second acquisition skips the 30% most horizontal projections as indicated in figure 6.1 (b), but the remaining projections are acquired over a longer time interval to keep the total acquisition time identical. For this second acquisition, the Orlov data sufficiency criterium [12] is not satisfied, and as a result the contrast recovery coefficients in the second scenario should be lower than in the first scenario, if the contrast recovery coefficient is to be a reliable predictor of how well the pixels of an image can be reconstructed. The contrast recoveries are calculated for a prior strength β of 0.1 and the neighborweights w_{jk} are 1/6 for horizontally and vertically neighboring pixels, 1/12 for diagonally neighboring pixels and 0.0 otherwise.

6.3.2 Single versus Multipinhole SPECT

To evaluate the difference between single and multipinhole SPECT imaging, the concept of the linearized local impulse response is applied to the reconstruction of a non-attenuating sphere of uniform activity (activity of 1 in each voxel) in the center of the field of view of a single and a multipinhole system. The sphere has a radius of 50 mm and is simulated in a 60x60x60 image matrix of 1.2 mm cubic voxels. Both the single and multipinhole systems perform a circular acquisition over 360^o with 64 equidistant projections. For both systems, the detector has 256x196 detector pixels of 1.95 mm, yielding the dimensions of the scintillation crystal of a Siemens ECAM system.

The multipinhole system is the system already discussed in section 3.4.3. It consists of 1 central and 6 non-central knife-edge pinhole apertures of 1.5 mm diameter D and 60^o acceptance angle α, which all focus on the same field of view. The focal length f equals 170 mm and the detector distance d equals 220 mm, such that the central pinhole aperture rotates on a distance d^* of 50 mm around the axis of rotation. Figure 6.2 shows a projection image of the above uniform sphere to illustrate the limited amount of overlap in these projections. The single pinhole system also has a knife-edge aperture of 1.5 mm diameter D and a focal length f of 170 mm, but it has an acceptance angle of 120^o which allows to reduce the distance d^* to 35 mm for better sensitivity without truncation of the spherical activity distribution. Like the multipinhole collimator, this collimator is available for future experimental evaluation. For both systems, the parameters $m_{1u}, m_{1v}, e_u, e_v, \Phi$ and Ψ are equal to zero, simulating the ideal single and multipinhole systems. The sensitivity of both the single and multipinhole systems is modelled with (2.40). This sensitivity model was assumed sufficiently accurate for this purpose.

Linearized local impulse responses are generated for a quarter plane, as illustrated in figure 6.3. Because of the circular symmetry of the reconstruction properties and the symmetry with respect to the central transaxial plane, this quarter plane provides all information about the reconstruction of the entire sphere. Besides the contrast recovery coefficient (for a perturbation e_j of 1), the additional measures $d_{min}, d_{max}, d_{int}$ and $\sharp v$ are calculated after thresholding the impulse responses to 1/15 of their contrast recovery. The quadratic prior has a strength β of 250 and the neighborweights w_{jk} are 1/12 for voxels with a touching plane, 1/24 for voxels with a common rib and 0.0 otherwise. For the six voxels indicated in figure 6.3 the results of the above calculations were also verified by MAP reconstruction of the above spherical activity distribution with and without a perturbation e_j. The reconstructions were performed with an iteration scheme with a decreasing number of subsets: 10x16, 10x12, 10x8, 10x4, 10x2, 10x1 in which the first figure denotes the number of iterations and the second figure the number of subsets.

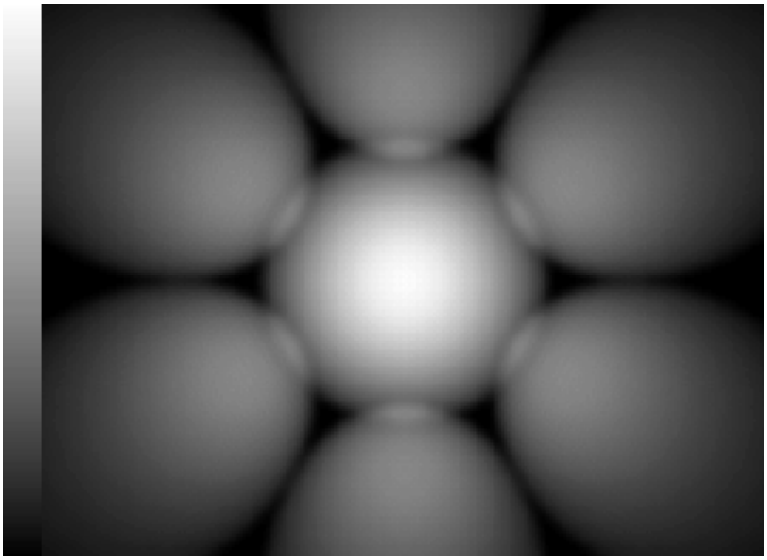

Figure 6.2: Projection of the sphere with uniform activity by the multipinhole system.

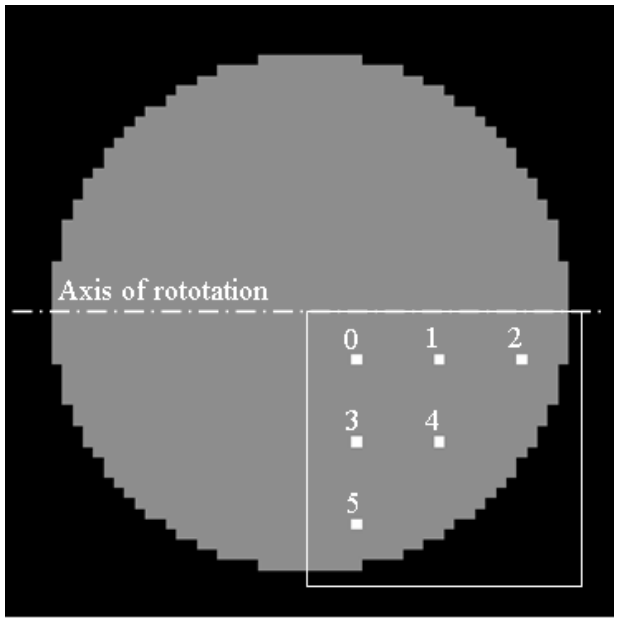

Figure 6.3: Comparison of single and multipinhole imaging: axial plane through the uniform activity distribution. The quarter plane studied, as well as the six control voxels are indicated.

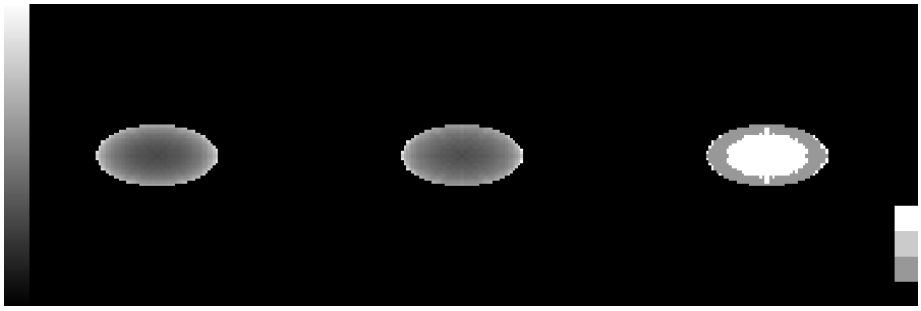

(a) (b) (c)

Figure 6.4: Contrast Recovery Experiment: the contrast recovery of the acquisitions (a) and (b) of figure 6.1, (c) indicates where the contrast recovery of acquisition (b) is better (white), equal (light gray) or inferior (dark gray) with respect to acquisition (a).

6.4 Results

6.4.1 Contrast Recovery

Figure 6.4 (a) and (b) show the contrast recovery results for the acquisitions illustrated in figure 6.1 (a) and (b) respectively. Figure 6.4 (c) further indicates where the contrast recovery of acquisition (b) is better (white), equal (light gray) or inferior (dark gray) with respect to acquisition (a). Despite the fact that acquisition (b) does not satisfy the Orlov data sufficiency condition for parallel hole imaging [12], yielding a very low quality image reconstruction as shown in figure 6.5 (b), the contrast recovery in the central part of the ellipse is higher for acquisition (b) than for acquisition (a).

The complete linearized local impulse responses for the central pixel of the ellipse are illustrated in figure 6.6 (a) and (b) respectively. Despite the higher contrast recovery for acquisition (b), the complete local impulse response of acquisition (a) is much more radially symmetric than the one of acquisition (b) and we therefore prefer acquisition (a). The higher contrast recovery of acquisition (b) for the central part of the ellipse is attributed to the fact that this acquisition always measures this part of the image with the highest sensitivity (low attenuation) and with lower interference of neighboring activity. This type of acquisition predominantly measures information however about the horizontal spread of the activity distribution, while the vertical spread is largely ignored. This explains the asymmetry of the local impulse response, with a large spread in the vertical direction and a relatively narrow spread in the opposite direction. The local impulse response of acquisition (a) is more symmetrical, since it measures the information about the spread of the activity distribution more uniformly over all possible directions.

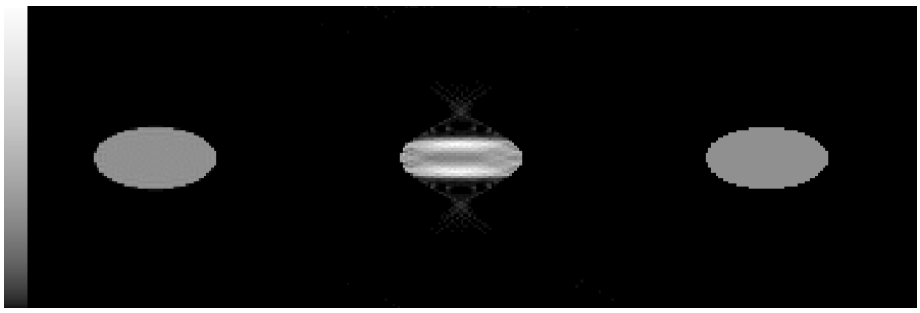

(a) (b) (c)

Figure 6.5: Contrast Recovery Experiment: MLEM reconstructions of the acquisitions (a) and (b) of figure 6.1 in comparison with the actual uniform activity distribution (c). The reconstructions are performed with an iteration scheme of 10x16, 10x12, 10x8, 10x4, 10x2, 10x1 in which the first figure indicates the number of iterations and the second figure the number of subsets.

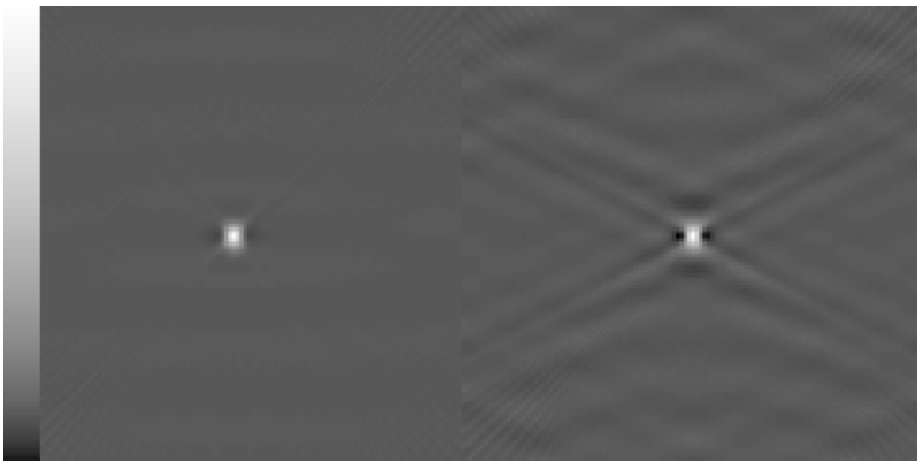

(a) (b)

Figure 6.6: Contrast Recovery Experiment: linearized local impulse responses for the central pixel of the elliptical activity distribution for acquisition (a) and (b) of figure 6.1.

6.4.2 Single versus Multipinhole SPECT

The figures 6.7 to 6.11 show the results of the contrast recovery l_j^j, the minimum distance d_{min}, the maximum distance d_{max}, the intensity weighted distance d_{int} and the total number of voxels $\sharp v$ respectively for both the single (a) and multipinhole case (b) for the quarter plane of the spherical activity distribution shown in figure 6.3. The images (c) further indicate for each parameter where in the image multipinhole shows better (white), equal (light gray) or inferior (dark gray) results with respect to single pinhole imaging. One pixel in the single pinhole simulation, yielded very unrealistic results, except for the contrast recovery, and is omitted in the above images. The cause for these errors is attributed to the convolution and inversion calculations in the Fourier domain, but the exact cause remains unknown for the moment. The results for the multipinhole situation are generally more uniform than in the single pinhole case. Multipinhole generally outperforms single pinhole imaging at larger distances from the central plane and also in the vicinity of the axis of rotation. This can easily be explained by the fact the multipinhole sampling of this region must be superior to the single pinhole sampling. Single pinhole imaging outperforms multipinhole however close to the single pinhole aperture orbit. This can be explained by the fact that here the sensitivity of the single pinhole aperture is higher than the combined sensitivity of the multipinhole apertures. Further, the sampling of the single pinhole in terms of data sufficiency is quite good as well for this region.

The performance of single and multipinhole imaging at the very edge of the spherical activity distribution is variable, but it is not considered here, since the assumption of the local space-invariance of the Fisher information is not correct at this edge. In the interior of the sphere, where this local invariance assumption is not violated, the above results appear to be very accurate, as supported by the results presented in figure 6.12. This figure compares the above results in the 6 voxels indicated in figure 6.3 with the results obtained from true MAP reconstructions of the sphere with and without the perturbations and for both the single and multipinhole situation. The results are in excellent agreement.

6.5 Discussion

In the theory section 6.2, 4 additional measures besides the contrast recovery l_j^j, were introduced to evaluate the shape of the linearized local impulse responses of MAP reconstructions. These measures are not claimed to be optimal, but the results of the first experiment indicate that the contrast recovery coefficient by itself is not always a reliable measure to study the reconstruction of emission tomography images. In this respect, we have to mention that, besides the contrast recovery coefficient, Qi *et al.* [43, 44] also study the noise properties of the reconstruction, by analyzing the variance of the reconstructed images. In this chapter we have not conducted such variance analysis, since our primary interest is a better understanding of the impact of the differences between single and multipinhole collimation on image reconstruction. In this first attempt, we chose to do so in the absence of noise,

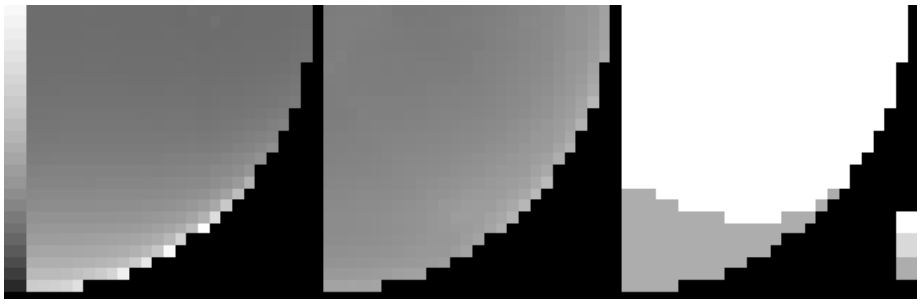

(a) (b) (c)

Figure 6.7: Contrast Recovery for single pinhole (a) and multipinhole (b) imaging in identical gray scale. Image (c) illustrates where multipinhole imaging performs better (white), equal (light gray) or inferior (dark gray) with respect to single pinhole imaging.

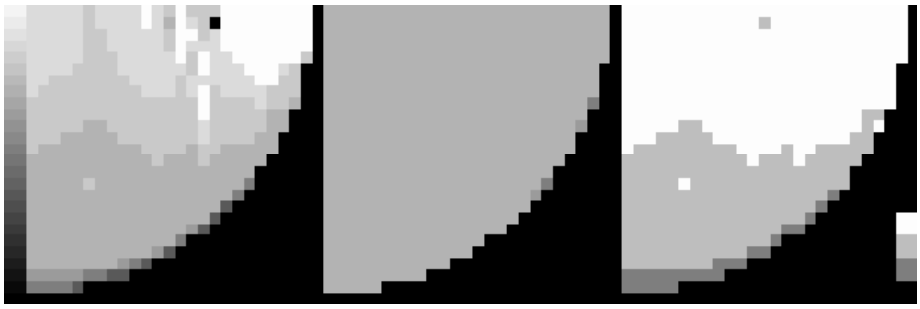

(a) (b) (c)

Figure 6.8: The minimum distance d_{min} for single pinhole (a) and multipinhole (b) imaging in identical gray scale. Image (c) illustrates where multipinhole imaging performs better (white), equal (light gray) or inferior (dark gray) with respect to single pinhole imaging.

although it should be included in later stages of the investigation. However, the above observation about the variance does not take away our concern that in terms of resolution, the contrast recovery coefficient is not always a reliable measure for reconstruction accuracy when sufficiently uniform resolution is desirable.

Multipinhole SPECT outperforms single pinhole SPECT in almost the entire field of view. Only in the most remote parts of the field of view with respect to the axis of rotation does single pinhole SPECT outperform multipinhole imaging. Furthermore, multipinhole SPECT yields also more uniform results over the entire sphere of interest in comparison with single pinhole imaging. We attribute this uniformity to a more uniform sampling of the activity distribution by the multipin-

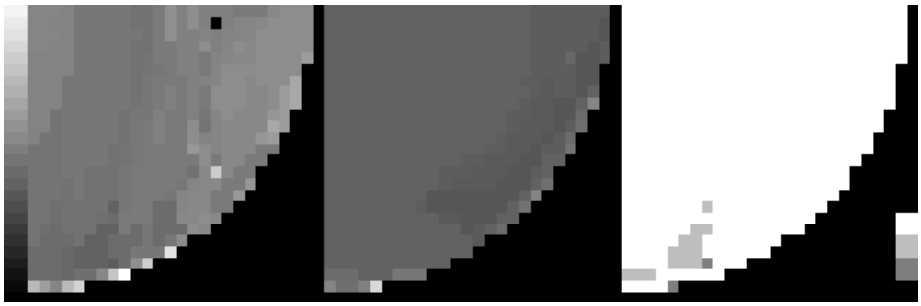

(a) (b) (c)

Figure 6.9: The maximum distance d_{max} for single pinhole (a) and multipinhole (b) imaging in identical gray scale. Image (c) illustrates where multipinhole imaging performs better (white), equal (light gray) or inferior (dark gray) with respect to single pinhole imaging.

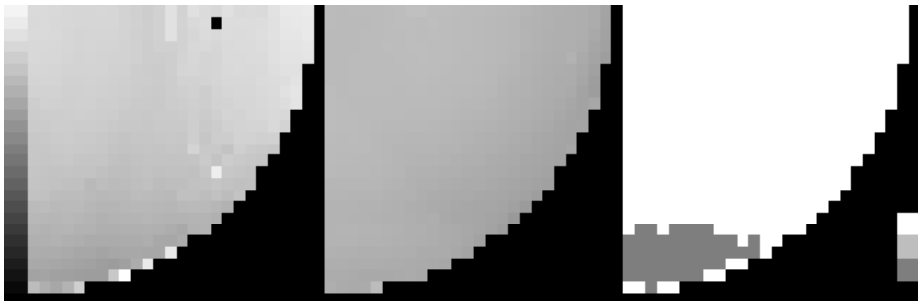

(a) (b) (c)

Figure 6.10: The intensity weighted distance d_{int} for single pinhole (a) and multipinhole (b) imaging in identical gray scale. Image (c) illustrates where multipinhole imaging performs better (white), equal (light gray) or inferior (dark gray) with respect to single pinhole imaging.

hole approach. This does not exclude however that for particular imaging purposes single pinhole SPECT might be the method of choice. For both the single and multipinhole case, it should also be noted that neither the collimator design or the distances d^* of the acquisition orbit were optimized for the given task, although we believe that the choices made do not specifically yield disadvantages for either of the imaging approaches. The spatial resolution of pinhole or multipinhole SPECT imaging was not taken into account.

The uniform sphere used as a phantom in this study is a poor representation of any real activity distribution that might be encountered in practice. It was nevertheless chosen, since it allows for an easy interpretation of the results.

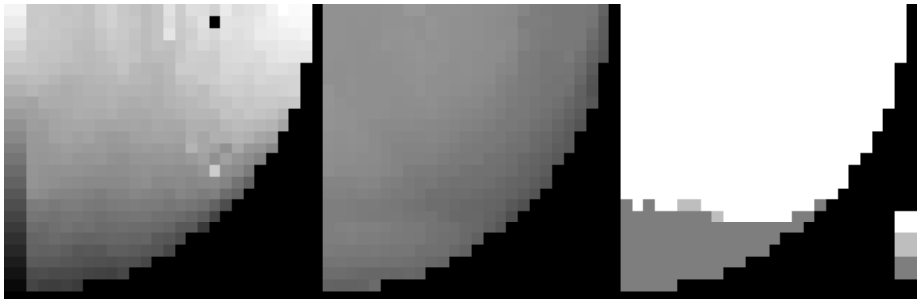

(a) (b) (c)

Figure 6.11: The number of voxels $\sharp v$ for single pinhole (a) and multipinhole (b) imaging in identical gray scale. Image (c) illustrates where multipinhole imaging performs better (white), equal (light gray) or inferior (dark gray) with respect to single pinhole imaging.

Finally, the close agreement between the simulated results and those obtained from MAP reconstructions with and without a perturbation show a remarkably good agreement. We thereby believe that the analysis of the linearized local impulse responses is a good approach for studying the differences between single and multipinhole imaging. In this context it should also be mentioned that the above results are expected to be equally valid for regular MLEM reconstruction, since the primary task of the quadratic prior is only to stabilize the matrix inversion in (6.18). The prior strength β of 250 required for sufficient regularization was surprisingly large. We do not have an explanation for this high value at this moment, but the actual validation MAP reconstructions used the same value and yielded excellent agreement.

6.6 Conclusion

In this chapter, we have demonstrated that the contrast recovery coefficient is not under all circumstances a reliable measure to study the quality of reconstruction in emission tomography. With an extended set of quality measures, the difference in reconstruction accuracy of single and multipinhole imaging was studied, revealing that multipinhole yields a generally better and more uniform image quality in comparison with single pinhole imaging. The study was performed by analyzing the linearized local impulse responses of MAP reconstructions and this technique has proven to be an excellent predictor of the reconstruction accuracy in single and multipinhole SPECT.

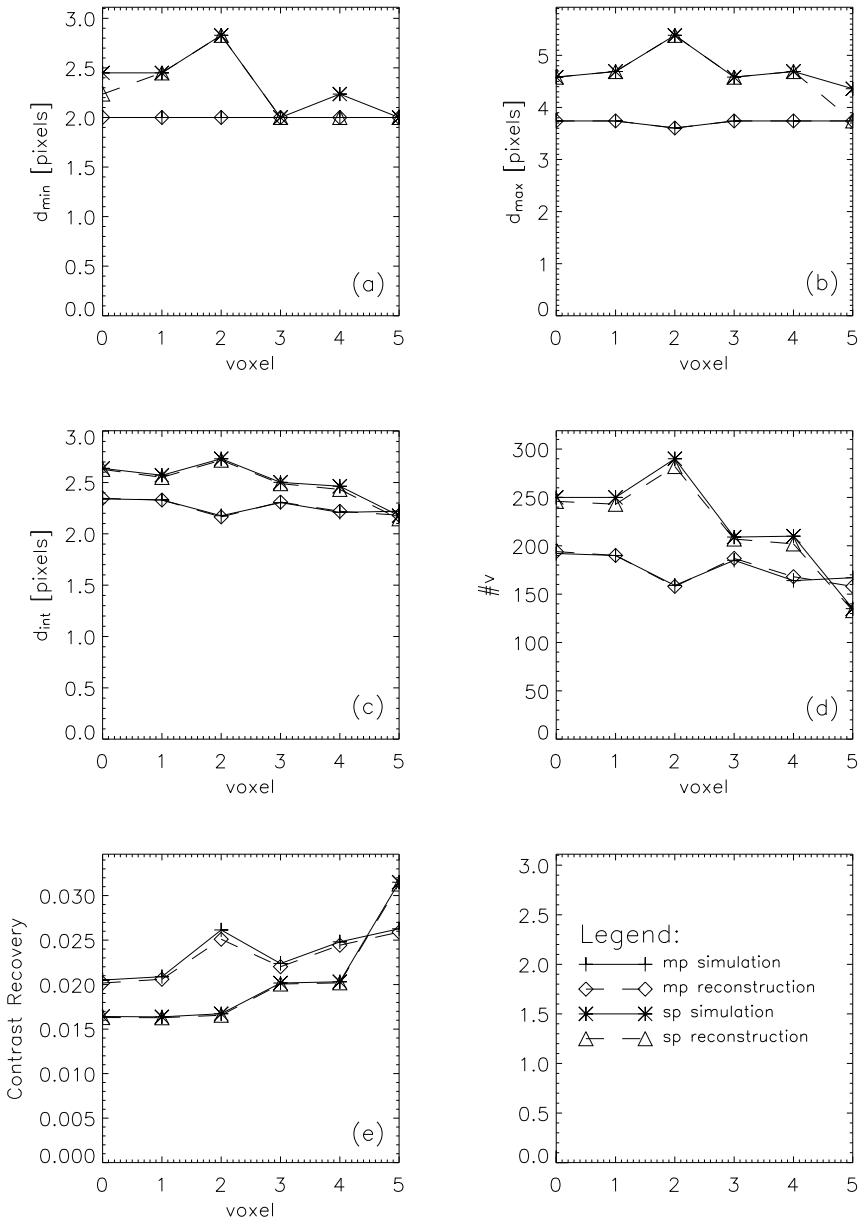

Figure 6.12: Validation of the simulation results in figure 6.7 to 6.11 for the 6 voxels indicated in figure 6.3. The numbering of the voxels is identical to 6.3.

Chapter 7

Extension: Pinhole SPECT Calibration with Oscillating Detector Tilt

7.1 Introduction

In chapter 4, a method was developed to determine the acquisition geometry of a pinhole camera. To do so, a model of the pinhole camera acquisition geometry was developed, yielding 7 parameters f, d, m, e_u, e_v, Φ and Ψ in the single pinhole case. The model assumed that all 7 parameters remain constant during image acquisition, yielding a rigid camera-collimator assembly that rotates on a circular orbit around a fixed axis during data acquisition. As discussed in section 4.5, the above assumption will often not be entirely accurate in practice. This chapter illustrates how the calibration method of chapter 4 can be extended to more complex acquisition geometries in order to increase the calibration and subsequent reconstruction accuracy in such situations. The chapter concentrates on a particular case, in which the tilt angle Φ oscillates slightly during image acquisition, but the idea of extension is potentially applicable to other situations as well. This chapter is based on [45].

7.2 Materials & Methods

Figure 7.1 (a) shows the mass centers of the projections of three point sources measured on a single head DSX camera (SMV) and the estimated projection locations which best fit these measurements under the assumption that the parameters f, d, m, e_u, e_v, Φ and Ψ remain constant during acquisition. A total of 4 of such calibration measurements were performed on the DSX camera with a 1.5 mm (2 measurements with identical acquisition geometry) and a 3.0 mm (2 measurements

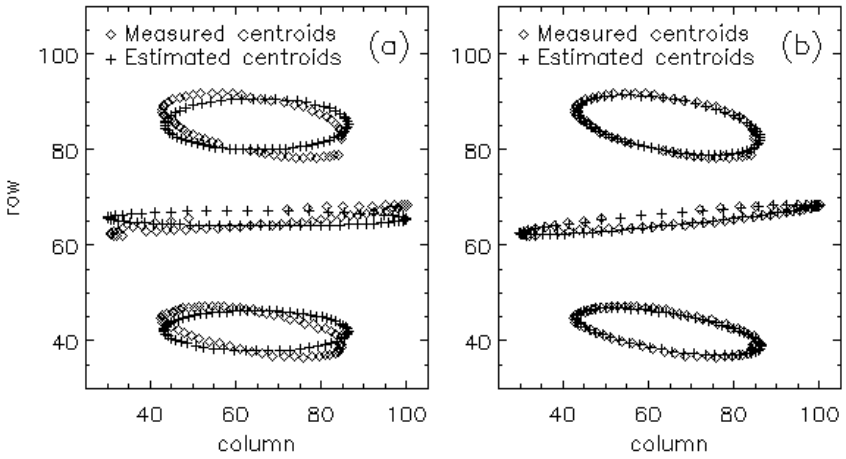

Figure 7.1: Measured and estimated mass centers of the projections of the 3 calibration point sources, (a) when neglecting the oscillating tilt angle and (b) when incorporating the oscillating tilt angle.

with identical acquisition geometry) pinhole aperture. The measurements consisted of 64 equidistant projection angles over 360^o with a focal length f of approximately 200 mm, a detector distance d of approximately 240 mm and an approximately zero tilt angle Φ. The calibration setup was very similar to the optimal calibration setup 'opt1' of chapter 5, with the distances between the point sources s_{12}, s_{13} and s_{23} equal to 25.89 mm, 19.00 mm and 26.43 mm respectively. The plane trough the point sources was horizontal and at zero projection angle θ the detector is parallel to it. A similar measurement was also obtained with an ECAM camera (Siemens). Clearly, the fixed 7 parameter model of chapter 4 results in a significant mismatch between the measured and estimated projection locations. This unsuccessful calibration is expected in turn to affect the accuracy of image reconstruction.

The most plausible explanation for the failing calibration is that the detector performs a slight oscillation around its supporting arm during the rotation of the camera, as illustrated in figure 7.2. We found that this oscillation is well modelled by a sinusoidal variation of the tilt angle around an axis inside the crystal and as a function of the projection angle θ, yielding

$$\Phi_\theta = \Phi + \Delta\Phi \cos(\theta + \beta) \tag{7.1}$$

in which Φ represents the average tilt angle, $\Delta\Phi$ represents the amplitude of the oscillation and β represents its phase. The variable tilt angle Φ_θ still indicates the inclination of the detector plane with respect to the axis of rotation, but because of its variable nature, the origin of the xyz coordinate system, as defined in section 2.3, is no longer uniquely defined. Instead, the location of the origin along the axis of rotation depends on the projection angle θ and as a result, both the detector distance d and the z coordinates of the point source locations now depend on the

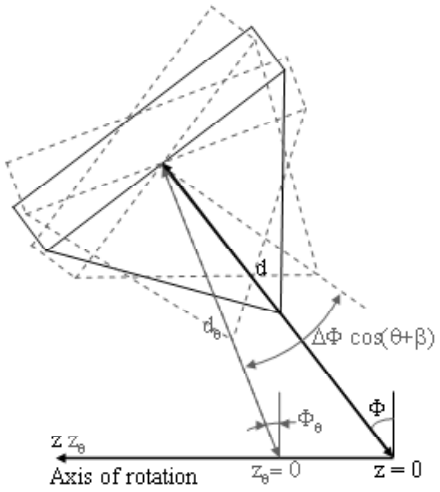

Figure 7.2: Model of the oscillating detector tilt. The solid lines show the average detector position, while the dashed lines show the most extreme positions of the detector during the oscillation.

angle θ as well, yielding d_θ and z_θ. Simple trigoniometry yields

$$d_\theta = d\,\frac{\cos\Phi}{\cos\Phi_\theta} \tag{7.2}$$

and

$$z_\theta = z - (d\sin\Phi - d_\theta\cos\Phi_\theta) \tag{7.3}$$

in which d and z now represent the detector distance and z coordinates respectively at the average tilt angle Φ. The substitution of the parameters Φ, d and z (not z''') of (4.1) and (4.2) by the parameters Φ_θ, d_θ and z_θ respectively, yields a new (extended) pinhole acquisition model which takes the oscillating tilt angle Φ_θ into account. With this extended model, containing two additional parameters $\Delta\Phi$ and β, a much closer match between the measured and estimated point source projection locations is obtained, as shown in figure 7.1(b).

7.3 Results and Discussion

For all four calibration measurements the extended calibrations consistently indicated an oscillation of the tilt with amplitude $\Delta\Phi = 0.3^o$ and a phase β ranging from 0.0^o to -0.6^o. Table 7.1 lists the results of these calibration measurements. Only the calibrations with oscillating tilt yield close matches between the estimated and measured point source projections like in figure 7.2 (b). The reconstructions of the three calibration point sources with compensation for this variable tilt are superior to reconstructions without compensation, as shown in figure 7.3 for one of the

measurements with the 1.5 mm pinhole aperture. With compensation, the reconstructed point sources resemble much closer the expected symmetrical blob-shaped activity distribution than without compensation.

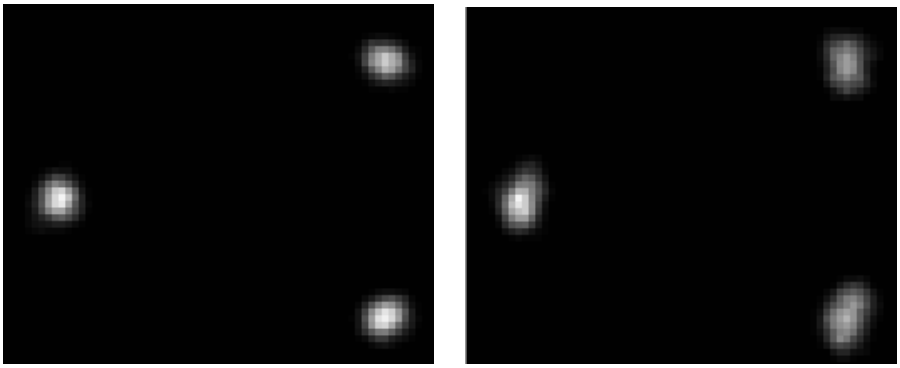

Figure 7.3: Reconstructed calibration sources with 1.5 mm pinhole, with (left) and without (right) variable tilt. Reconstruction from 64 128x128 projections by 8 subsets and 4 iterations of OSEM in a 128x128x128 image of 0.5 mm cubic voxels. A longitudinal slice is shown with the vertical axis along the axis of rotation. Each image is scaled to its own maximum. (Courtesy of M. Defrise).

Despite the small amplitude $\Delta\Phi$ of the tilt angle oscillation of just 0.3^o, the effect of the oscillation on image acquisition is surprisingly large, as can be clearly seen in figure 7.1 (a) by the inclination of the estimated set of ellipses with respect to the measured ones. As expected, this effect propagates into the accuracy of the reconstructed images and compensation for the variable tilt results in improved reconstruction accuracy, which is appreciable by simple visual inspection of figure 7.3. These observations indicate that even small variations of the tilt angle Φ proof to be critical for accurate pinhole SPECT imaging.

The small magnitude of the oscillation amplitude $\Delta\Phi$ makes it also a very plausible explanation for the unexpected results of the calibration measurements (the orientation of the measured ellipses), since relatively large deviations from the rigid acquisition model of chapter 4 are not expected for regular SPECT cameras and should be easy to determine. The same effect can for example also be explained by an oscillation of the electrical shift e_v as a function of the projection angle θ, but then the amplitude of the oscillation should be in the order of several millimeters, which is in our opinion very unlikely. A second observation motivating the oscillating tilt assumption is that most cameras, like the DSX and ECAM camera, have a supporting axis close to the scintillation crystal and the tilt of the detector can usually also be adjusted by a rotation around this axis. We hypothesize that if the mass distribution of the detector-collimator combination is not balanced with respect to this axis, gravity can cause small oscillations around this axis. This hypothesis is supported by the fact that the largest deviations from the average tilt angle Φ occurred when the above axis is in a horizontal position, since β is approx-

Table 7.1: Calibration results of the DSX calibration measurements. Measurements 1 and 2 were performed with the 1.5 mm pinhole aperture and an identical acquisition geometry. Measurements 3 and 4 were performed with the 3mm pinhole aperture and an identical acquisition geometry.

#	f [mm]	d [mm]	m [mm]	e_u [mm]	e_v [mm]	Φ [deg]	$\Delta\Phi$ [deg]	β [deg]	Ψ [deg]
Without oscillating tilt									
1	198.3	241.8	1.4	-6.0	2.3	2.04	0.00	0.00	-0.34
2	199.8	243.5	0.9	-2.2	-0.6	1.28	0.00	0.00	-0.20
3	193.5	242.3	1.9	-6.6	4.9	2.81	0.00	0.00	-0.58
4	191.2	240.4	1.2	-3.0	5.5	2.91	0.00	0.00	-0.59
With oscillating tilt									
1	200.6	244.7	0.2	0.8	3.2	1.11	0.31	-0.09	-0.19
2	201.6	245.7	0.1	2.3	3.3	1.36	0.31	-0.01	-0.12
3	196.7	246.2	0.1	2.8	4.2	1.45	0.31	-0.63	-0.17
4	195.0	244.1	0.2	2.2	4.9	1.62	0.31	-0.40	-0.19

imately zero. From this point of view, the problem of variable tilt angles, which to our knowledge has never been reported in the literature so far, may even be a more common problem than expected up till now.

The calibration procedure of this chapter estimated two additional parameters $\Delta\Phi$ and β when compared with the original calibration procedure of chapter 4. Nevertheless, it did so using the projections from just three point sources, which is also the minimal number of point sources required to estimate only the parameters f, d, m, e_u, e_v, Φ and Ψ. This can be explained by the fact that the measured ellipses contain more information about the acquisition geometry than just about the above 7 parameters. If not, it should have been possible to obtain a good match between the measured and estimated point source projections, using only the rigid acquisition model of chapter 4. The uniqueness of the solution of the calibration method of this chapter can in principle be analyzed analytically, as was done for the original calibration method of chapter 4 in section 4.2. We consider such analysis however beyond the scope of this chapter. In practice no problems with the uniqueness of the solution were encountered.

Finally, the oscillating tilt is certainly not the only deviation of the DSX acquisition geometry from the rigid acquisition model of chapter 4. The measured 'ellipses' of figure 7.1 are for instance not closed (even if all point source projections could have been used in the data). Consequently, further improvement may be obtained with even better models of this acquisition geometry.

7.4 Conclusion

Based on a practical example, this chapter illustrated how the original calibration method of chapter 4 can be extended to more complex acquisition geometries than the original rigid acquisition model. The chapter also illustrated how slight variations of the detector tilt during image acquisition have a clear impact and result in degraded accuracy of the reconstructed images if not corrected for.

Chapter 8

Application: MicroSPECT Imaging of a Rodent Model for Parkinson's Disease

8.1 Introduction

In recent years several studies using pinhole SPECT have been reported in literature [13, 17, 46–61]. This chapter illustrates the application of single pinhole SPECT imaging to a rodent model for Parkinson's disease. This model was developed at this university by Dr. E. Lauwers and Prof. Dr. V. Baekelandt of the Center for Experimental Surgery and Anaesthesiology, in corporation with Prof. Dr. Z. Debyser of the Subfaculty of Medicine KULAK and Prof. Dr. B. Nuttin of the Laboratory of Experimental Neurosurgery and Neuroanatomy.

8.2 Materials & Methods

Rodent Model Lentiviral vectors, manipulated strings of viral genetic material, are promising tools for gene transfer into the central nervous system. The stereotactic injection of lentiviral vectors encoding human α-synuclein in the substantia nigra of rats causes overexpression of α-synuclein. This results in a rat model with Lewy-like neuropathology and neurodegeneration similar to Parkinson's disease [62, 63]. This α-synuclein model offers advantages as a realistic and slowly-progressing neurodegenerative pathology as compared to acute lesional models, like the stereotactic injection of 6-OH-dopamine into the substantia nigra [59, 61].

Study Design Five unilateral lentiviral vector-transduced Wistar rats, 9 months after vector delivery, and 5 normal age-matched rats were injected with 300

MBq of the high affinity presynaptic dopamine transporter ligand ^{123}I-FP-CIT to evaluate the dopamine transporter in the rat striatum. In three lentiviral vector-transduced rats, contralateral control (sham) injections of green fluorescent protein vectors or saline were performed. For comparative evaluation, the 6-OH-dopamine lesion-model was used on a single rat.

Pinhole SPECT Imaging All rats were imaged, 1.5 hour after injection with ^{123}I-FP-CIT, using a single-head GE Millennium MPR camera with a single pinhole collimator of (approximately) 240 mm focal length f. The collimator has a pinhole aperture of 3 mm diameter D, zero inclination angle η and an acceptance angle α of approximately 75^o. The scan consists of 64 equidistant 1 min projections over 360^o in 128x128 projection images of 1.695x1.695 mm^2 pixels. The distance d^* between the focal point and the axis of rotation was approximately 50 mm. After each acquisition, a calibration scan was performed to estimate the acquisition geometry of the pinhole system with a calibration phantom similar to the optimal calibration phantom 'opt1' of chapter 5. The distances between the point sources s_{12}, s_{13} and s_{23} equal 25.89 mm, 19.00 mm and 26.43 mm respectively. The plane trough the point sources was horizontal and at zero projection angle θ the detector is parallel to it.

Iterative OS-EM image reconstruction [18, 38], taking the results of the camera calibration into account, was performed in a 50x50x80 image with a voxel size of 1.2 mm. The reconstruction used an iteration scheme with a decreasing number of subsets: 10x16, 10x8, 10x4, 10x2 and 10x1, where the first figure denotes the number of OS iterations and the second one the number of subsets. The pinhole sensitivity was modelled as explained in section 3.4.2 and resolution recovery was partially performed by a Gaussian smoothing of 12.0 mm FWHM during projection and backprojection. No corrections were made for attenuation or scatter.

Data Analysis The reconstructed images were registered manually to a rat brain atlas to determine the volumes of the right and left striatum in the reconstructed images. For quantification, the right-to-left asymmetry ratios of these volumes of interest were used. Both the average and maximum pixel values in the volumes of interest were considered.

8.3 Results and Discussion

Figure 8.1 shows the reconstructions of a normal rat, a lentiviral transduced rat and the 6-OH-dopamine rat. Figure 8.2 further shows the asymmetry ratios, obtained from the reconstructions, for the different groups of rats. The asymmetry ratios are shown for both the maximum pixel value and the average pixel values of the volume of interest. For the normal rats, the left and right striatum are both clearly visible and the resolution is sufficient to discriminate them from each other. The uptake in the left and right striatum is approximately equal, although the uptake

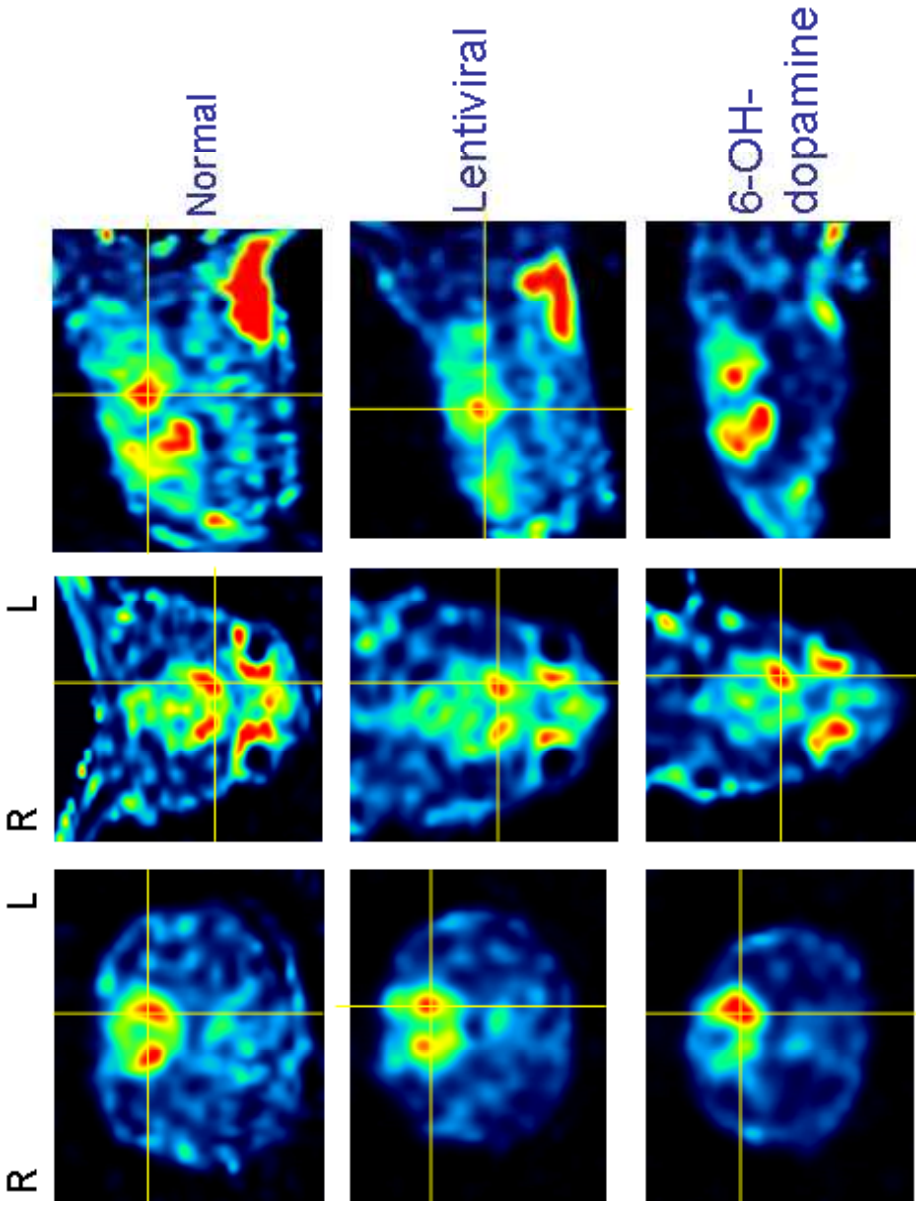

Figure 8.1: Examples of reconstructed images. The cursor is positioned in the left striatum. L and R indicate the left and right side of the animal respectively.

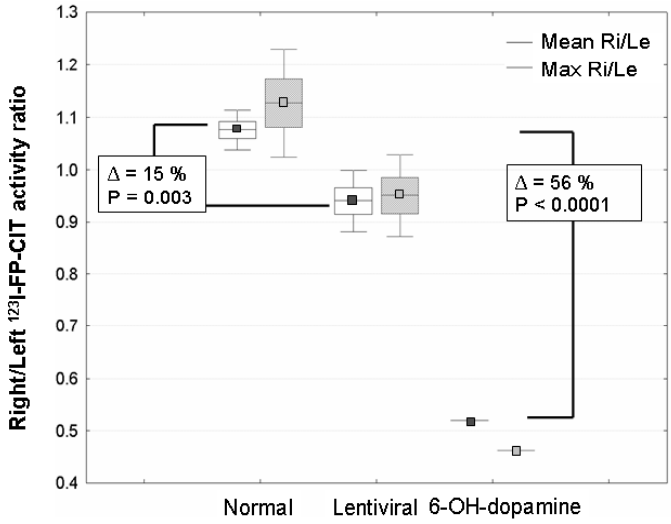

Figure 8.2: Right-to-left asymmetry ratios of the reconstructed activity in the right and left striatum. The boxplots show median value, 25% and 75% percentile, and minimum and maximum value. The left and right boxes show the results for the mean and maximum activity in the region of interest respectively.

in the right striatum always appears slightly larger than in the left striatum. This phenomenon can be explained by the washout of activity from the rat brain during image acquisition (approximately 1 hour) in combination with the fact that the right striatum is imaged with the highest sensitivity and magnification at the beginning of the acquisition (pinhole focus is closest to the right striatum), while the left striatum is imaged with the highest sensitivity and magnification at the end of the acquisition.

The above explanation for the unexpected right-to-left asymmetry ratio for the control rats was validated by a simulation experiment. A software phantom was created consisting of two small spheres with high activity, representing the left and right striatum, in a larger sphere of 3.5 cm diameter with uniform background activity. The ratio of the striatum to background activity equals 5. Figure 8.3 shows the central slice of the phantom. With this phantom, the above pinhole acquisition is simulated with a linear 30% washout of activity from the striatum and a linear 10% washout of activity from the background during the acquisition. The projections take a realistic model of the pinhole resolution (obtained from a point source measurement) and the pinhole sensitivity into account and also model uniform attenuation of 0.15 cm^{-1} within the sphere. The reconstruction is performed as explained in section 8.2, without attenuation correction and with only partial resolution recovery. The reconstruction (iteration scheme: 10x16, 10x12, 10x8, 10x4, 10x2, 10x1 with the first figure indicating the number of iterations and the second figure the number of subsets) shows a right-to-left asymmetry of 1.074

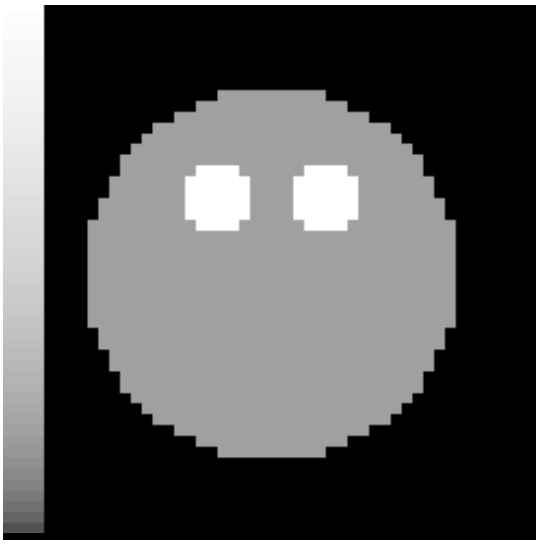

Figure 8.3: Central slice of the striatum phantom.

in terms of the maximum intensity in the right and left striatum and 1.051 in terms of the mean intensity, similar to the rat brain reconstructions. Although we don't know the actual washout of activity during the pinhole acquisition, the experiment demonstrates at least that right-to-left asymmetries in the reconstruction of the striatum can be expected.

For the lentiviral transduced rats, the right striatum is still visible, but shows a moderately reduced uptake in comparison with the left striatum, which is assumed unaffected by the unilateral transduction. The average asymmetry ratio is decreased by 15% in comparison with the normal rats. For the 6-OH-dopamine rat, the decrease in uptake of the right striatum is clearly appreciable from the reconstruction image. The asymmetry ratio is down by 56% in comparison with the normal rat population. This decrease is highly significant. Please note that the asymmetry ratios also take any aspecific tracer uptake into account and that the asymmetry ratios for just the specific tracer uptake will be even better than the above values. The above results also confirm the expectations raised by the results of motor behavioral tests.

8.4 Conclusion

The lentiviral vector-mediated rat model with α-synuclein overexpression in the substantia nigra results in a moderate regional reduction of dopamine transporter activity and single pinhole SPECT imaging is able to provide sufficient spatial resolution and sensitivity to detect this reduction in practice.

Chapter 9

General Conclusion

9.1 Main Contributions

The major contribution of this work to the field of pinhole SPECT imaging, is the theoretical study of the geometrical calibration of pinhole SPECT systems and the subsequent development and optimization of a convenient calibration method to determine the complete acquisition geometry of these systems in practice. The theory studies the necessary and sufficient conditions to uniquely determine the acquisition geometry from the projections of a set of point sources. The theory was originally developed to study single pinhole systems, but was later extended to multipinhole situations as well and any further extensions (like pinhole SPECT with multiple detectors or the calibration of pinhole SPECT systems with deviating detector orbits) are in principle straightforward.

The results of the theory were used to develop a new pinhole SPECT calibration method, which consists of imaging three point sources in the field of view, with at least two of the distances between the point sources being known. The mass centers of the point source projections are processed by least square fitting to determine the desired acquisition geometry. The calibration method is easy to perform in practice and yields, in contrast to previously developed methods [30–36], the entire acquisition geometry from this single measurement. The calibration method assumes a rigid camera system, but it has been demonstrated that corrections for less rigid camera systems can easily be implemented as well.

The accuracy of the calibration method depends on the noise in the calibration measurement, the position of the calibration point sources in the field of view and the accuracy with which the distances between these point sources are known. The errors on the calibration results propagate in turn into the reconstructed images, causing loss of spatial resolution and image deformations. In order to minimize this propagation of errors, the position of the point sources in the field of view (the calibration setup) was optimized for both the best possible calibration and reconstruction accuracy. This optimization required the development of an efficient

method to evaluate the calibration and reconstruction accuracy in case of noisy calibration data and errors on the distances between the point sources.

Finally, with the recent development of multipinhole SPECT imaging, a preliminary study has been performed to evaluate the benefit of multipinhole SPECT imaging over single pinhole SPECT. The study evaluates the characteristics of the linearized local impulse responses of single and multipinhole SPECT reconstruction. It has been demonstrated that the contrast recovery coefficient of these responses [43, 44] is by itself not always a reliable measure of the quality of image reconstruction. To verify the results of the comparative study, some additional measures of image quality were therefore used as well. The study shows a generally better and more uniform accuracy of multipinhole reconstruction in comparison with single pinhole imaging. Furthermore, validation of the results indicates that the linearized local impulse responses are excellent tools for this type of study. More research is however needed on this topic to develop and compare optimal pinhole and multipinhole systems.

The evaluation of the above calibration method and the comparison between single and multipinhole SPECT required the implementation of the necessary pinhole SPECT calibration and reconstruction software. Since the correction for the pinhole sensitivity is essential for performing accurate pinhole SPECT imaging in practice, pinhole SPECT sensitivity was studied as well and a practical method to determine the true angular pinhole sensitivity from a flood source measurement was developed. This method is sufficiently accurate for single pinhole SPECT imaging with relatively large acceptance angles, but the sensitivity model needs further refinement to accurately predict the angular sensitivity of inclined pinhole apertures with small acceptance angles, which are typically encountered in multipinhole SPECT imaging. Nevertheless, multipinhole reconstruction with sensitivity correction is already possible, but only by using measurements of the angular pinhole sensitivity. These measurements inevitably contain noise which will propagate into the reconstructed images. Thanks to the software and the experience gained with pinhole SPECT imaging, we are now able to successfully perform small animal pinhole SPECT studies, as was illustrated in chapter 8.

9.2 Suggestions for Future Work

9.2.1 Pinhole Sensitivity

As discussed in the previous section, the analytical model of pinhole sensitivity used in this work is not sufficiently accurate for inclined pinhole apertures with small acceptance angles. Up to our knowledge, analytical expressions of the sensitivity of such inclined pinhole apertures have not been discussed in the literature either and remain a topic for future research. A possible alternative is the numerical sensitivity calculation of Schramm *et al.* In combination with such research, it should be kept in mind that large gradients in sensitivity will be present in the projection images and that these gradients will shift with variations in the mechanical offsets and

electrical shifts. We therefore anticipate that an accurate model of the sensitivity of inclined pinhole apertures with small acceptance angles, will only proof useful in practice when these variations can be taken into account.

9.2.2 Multipinhole SPECT

The theoretical study of single and multipinhole SPECT imaging of chapter 6 is only a first attempt to fully understand the differences between single and multipinhole imaging. Most of the current approaches to multipinhole SPECT imaging [2–4] are at least partially based on intuition with experimental validation and prove to be successful, but a fundamental theory about the topic remains yet to be developed. Such theory should focus on sampling (data sufficiency), resolution, sensitivity, noise and the effects of overlapping projections. Eventually, the theory should make it possible to design optimal configurations of pinhole apertures for multipinhole imaging.

9.2.3 Resolution Recovery

Pinhole imaging is always a trade-off between spatial resolution and sensitivity: larger pinhole apertures yield better sensitivity, but at the expense of a decreased spatial resolution and vice versa. By resolution recovery techniques, part of the loss in spatial resolution due to the finite size of the pinhole aperture can however be recovered. Consequently, the same spatial resolution of the reconstructed images can be obtained with higher sensitivity (larger pinhole apertures) when resolution recovery is applied. A resolution recovery technique based on multiple ray tracing through the pinhole aperture, has recently been developed at the Vrije Universiteit Brussel by M. Defrise *et al.* [45] and has already been implemented in our pinhole and multipinhole reconstruction software.

The first results obtained with this technique, indicate a clear improvement in the spatial resolution of the reconstruction image. The improvement in spatial resolution is illustrated in figure 9.1. The figure shows the reconstruction of a small hot rod phantom with (right) and without (left) resolution recovery (The use of the phantom is courtesy of N. U. Schramm, Research Center Juelich GmbH, Germany). The resolution recovery is performed by tracing 7 rays through the pinhole aperture with 3 mm diameter D and 120^o acceptance angle α. The phantom was imaged on a Siemens ECAM camera by 64 equidistant projections over 360^o in a 128x128 projection matrix with 1.95 mm detector pixels. The focal length f was 170 mm and the distance d^* was 39 mm. OSEM reconstruction was performed with 0.6 mm cubic voxels and with a decreasing number of subsets: 10x16, 10x12, 10x8, 10x4, 10x2, 10x1 in which the first figure denotes the number of iterations and the second figure the number subsets. The reconstructed images were post-smoothed with a 1.5 mm FWHM Gaussian kernel. With resolution recovery, the rods in the sectors with the 3.0 mm, 2.7 mm, 2.4 mm and 2.1 mm rods are visible, while the 2.1 mm rods are not visible in the reconstruction without resolution recovery. Furthermore, the rods in the reconstruction without resolution recovery clearly have

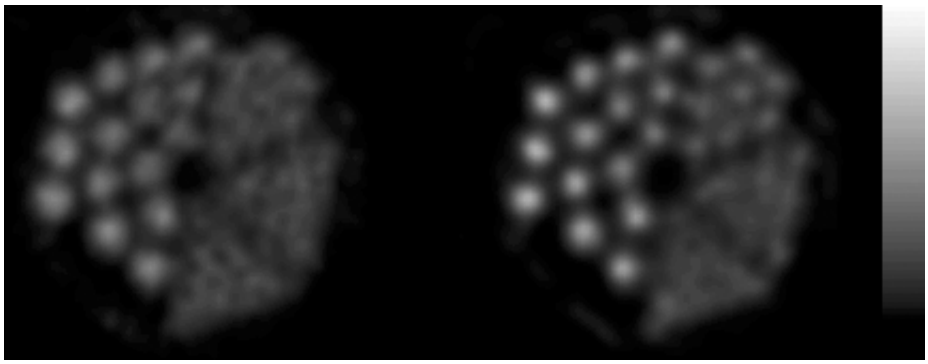

Figure 9.1: Reconstructions with (right) and without (left) resolution recovery of a hot rod phantom with 3.0 mm, 2.7 mm, 2.4 mm, 2.1 mm, 1.8 mm and 1.5 mm rods. (The use of the phantom is courtesy of N. U. Schramm, Research Center Juelich GmbH, Germany.)

a lower maximum intensity, because of the additional blurring in comparison with the rods with resolution recovery. The resolution recovery technique also appears to have a noise reducing effect on the reconstruction. This noise reduction is attributed to the more accurate model of the pinhole (or multipinhole) projection, which allows for a better match of the projection of the reconstruction image and the actual measurement.

In its current implementation the above resolution recovery technique requires however a significant increase in the reconstruction computation time. The reconstruction of the above example with resolution recovery takes 7 times longer to complete in comparison with the reconstruction without resolution recovery. Further research on more efficient implementations of the above resolution recovery technique is therefore highly desirable.

9.2.4 Multipinhole Calibration

A pinhole acquisition of 3 point sources in combination with the knowledge of 2 of the distances between these point sources is the minimum requirement for the unique geometrical calibration of a traditional pinhole system. This requirement also allows the calibration of the multipinhole systems considered in this work, but may not be strictly necessary. In multipinhole situations it is considerably more difficult to allocate the measured point source projection locations to the correct point source and the correct pinhole aperture. It is thereby interesting to study the minimum requirements for the unique calibration of multipinhole systems, in order to limit the number of point sources used to the minimum number required.

9.2.5 Pinhole Reconstruction using Anatomical Information

Simultaneously to this work, K. Baete *et al.* [64–66] developed at our department a maximum-a-posteriori algorithm to take anatomical information from MRI (Magnetic Resonance Imaging) or CT (Computed Tomography) images into account during image reconstruction. The method is based on a priori knowledge about of the activity distribution in the structures that can be delineated in the anatomical images. The much better spatial resolution of the delineated anatomical structures allows the algorithm to minimize partial volume effects in the reconstruction of the emission tomography images. This improves the quality of reconstruction in terms of quantification. Furthermore, this technique could represent a suitable regularization of the underdetermined problem of pinhole and multipinhole image reconstruction. As a result, we anticipate that the use of the above reconstruction algorithm in pinhole and multipinhole applications will yield a significant improvement in the quality of the reconstructed images.

9.2.6 Attenuation & Scatter

So far attenuation and scatter are not modelled in the current version of our pinhole reconstruction software. The application of corrections for attenuation and scatter should at least in theory further improve the accuracy of the reconstructed images, especially for quantification purposes. Because of the limited size of most laboratory animals, the impact of this correction is however expected to be limited.

Appendix A

Proofs and Derivations

A.1 Small Acceptance Angle Aperture Model

This appendix calculates the overlap E of the projections of the ellipses E_c, E_f and E_b defined in section 2.4.3. Instead of projecting the ellipses directly on a plane orthogonal to the photon paths, the ellipses are first projected on the back plane of the collimator plate (the plane of E_b). The result is then simply multiplied by $\cos\tau$ to obtain the desired result.

Consider the pinhole aperture with diameter D, acceptance angle α and inclination angle η illustrated in figure A.1. The center of the pinhole aperture is located at the distances d_f and d_b from the front and back plane of the collimator plate respectively. First, we calculate the exact shape and position of the ellipses E_f and E_b. The long axis A_f of the ellipse E_f can be readily calculated as

$$A_f = \frac{A_{f1} + A_{f2} + A_{f3}}{2} \tag{A.1}$$

with

$$A_{f1} = (d_f - (D/2)\sin\eta)(\tan\eta - \tan(\eta - \alpha/2)), \tag{A.2}$$

$$A_{f2} = D/\cos\eta, \tag{A.3}$$

$$A_{f3} = (d_f + (D/2)\sin\eta)(\tan(\eta + \alpha/2) - \tan\eta). \tag{A.4}$$

With B_f being the short axis of E_f and with the $x_f y_f$ coordinate system at the center of E_f and with the x_f and y_f axes along the long and short axes of E_f respectively, the ellipse E_f can be expressed as

$$\frac{x_f^2}{A_f^2} + \frac{y_f^2}{B_f^2} = 1. \tag{A.5}$$

From the aperture geometry it is further clear that the $x_f y_f$ origin is displaced with respect to the system central ray by the amounts (note that the angle η is defined

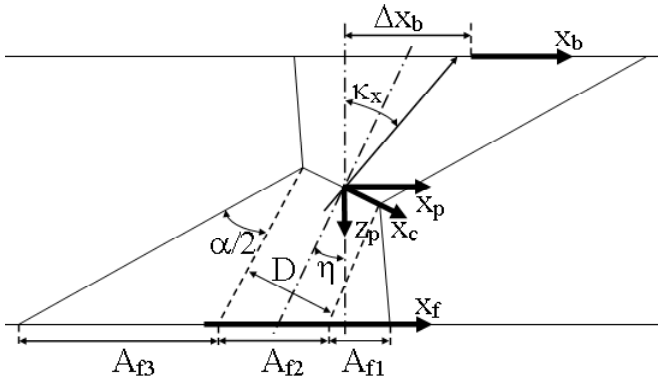

Figure A.1: Model of a small acceptance angle knife edge pinhole aperture.

in the plane of figure A.1)

$$\Delta x_f = -d_f \tan\eta - (A_{f3} - A_{f1})/2, \tag{A.6}$$

$$\Delta y_f = 0. \tag{A.7}$$

At $x_f = -(A_{f3} - A_{f1})/2 = x_f^*$, which is the projection of the focal point of the pinhole aperture on the x_f axis along the pinhole central ray, the width of E_f in the y_f direction further needs to be D^* with

$$D^* = D + 2\frac{d_f}{\cos\eta}\tan(\alpha/2). \tag{A.8}$$

From (A.5), this observation eventually yields B_f

$$B_f = \frac{D^*}{2}\sqrt{\frac{A_f^2}{A_f^2 - x_f^{*2}}}. \tag{A.9}$$

Now the position and shape of E_f is completely determined. An analogous calculation can further be performed to calculate the shape and position of E_b, yielding very similar results, except for some changes in sign.

Now consider a point source at position (x_p, y_p, z_p) in the field of view of the pinhole collimator. From this position we calculate the angle κ between its photon paths and the system central ray and also the projections of this angle on the $x_p z_p$ (κ_x) and $y_p z_p$ (κ_y) planes respectively

$$\kappa = \arctan\left(\frac{\sqrt{x_p^2 + y_p^2}}{z_p}\right), \tag{A.10}$$

$$\kappa_x = \arctan\left(\frac{-x_p}{z_p}\right), \tag{A.11}$$

$$\kappa_y = \arctan\left(\frac{-y_p}{z_p}\right). \tag{A.12}$$

As explained previously, we first project the ellipses E_f, E_c and E_b on the back plane of the collimator plate along the direction κ. The projection of E_b is of course trivial and can be immediately described in the $x_b y_b$ coordinate system.

$$\frac{x_b^2}{A_b^2} + \frac{y_b^2}{B_b^2} = 1. \tag{A.13}$$

As mentioned, the values of A_b, B_b, Δx_b and Δy_b are calculated analogously to (A.1), (A.9), (A.6) and (A.7) respectively. The projection of E_f is straightforward as well, since only its position needs to be recalculated, not its shape and orientation. This immediately results in

$$\frac{(x_b + \Delta x_{fb})^2}{A_f^2} + \frac{(y_b + \Delta y_{fb})^2}{B_f^2} = 1 \tag{A.14}$$

with

$$\Delta x_{fb} = \Delta x_b - \Delta x_f - (d_f + d_b)\tan\kappa_x, \tag{A.15}$$
$$\Delta x_{fb} = \Delta y_b - \Delta y_f - (d_f + d_b)\tan\kappa_y, \tag{A.16}$$

and Δx_f and Δy_f as in (A.6) and (A.7).

The projection of E_c is somewhat more complicated, since this circle is inclined by the angle η with respect to the plane it is projected on. In the $x_c y_c$ coordinate system shown in figure A.1, E_c is easily expressed as

$$\frac{x_c^2}{(D/2)^2} + \frac{y_c^2}{(D/2)^2} = 1. \tag{A.17}$$

Each point (x_c, y_c) of the $x_c y_c$ plane is now projected along the direction κ on the $x_b y_b$ plane, yielding

$$x_b + \Delta x_b = x_c(\cos\eta + \sin\eta\tan\kappa_x) + d_b\tan\kappa_x \tag{A.18}$$
$$y_b + \Delta y_b = y_c + x_c\sin\eta\tan\kappa_y + d_b\tan\kappa_y \tag{A.19}$$

Solving (A.18) and (A.19) for x_c and y_c and substituting them into (A.17) yields

$$\frac{(x_b + \Delta x_{cb})^2}{A_c^2} + \frac{((y_b + \Delta y_{cb}) + g(x_b + \Delta x_{cb}))^2}{B_c^2} = 1 \tag{A.20}$$

with

$$A_c = D(\cos\eta + \sin\eta\tan\kappa_x)/2, \tag{A.21}$$
$$B_c = D/2, \tag{A.22}$$
$$\Delta x_{cb} = \Delta x_b - d_b\tan\kappa_x, \tag{A.23}$$
$$\Delta y_{cb} = \Delta y_b - d_b\tan\kappa_y, \tag{A.24}$$
$$g = \frac{\sin\eta\tan\kappa_y}{\cos\eta + \sin\eta\tan\kappa_x}. \tag{A.25}$$

The term $g(x_b - \Delta x_{cb})$ finds its origin in the fact that the lower part of E_c ($x_c > 0$) is projected by longer projection rays than the upper part ($x_c > 0$), because of the inclination angle η. As a result, the lower parts of E_c are projected at larger absolute values of $(y_b - \Delta y_{cb})$ in comparison with the corresponding upper parts for nonzero angles κ_y, which leads to an ellipse of which the long and short axis are rotated over an angle γ with respect to the axes of the $x_b y_b$ coordinate system.

$$\gamma = \frac{1}{2} \arctan\left(\frac{2g}{1 - g^2 - B_c^2/A_c^2}\right). \tag{A.26}$$

In the rotated coordinate system

$$x_\gamma = (x_b + \Delta x_{cb}) \cos\gamma - (y_b + \Delta y_{cb}) \sin\gamma \tag{A.27}$$

$$y_\gamma = (x_b + \Delta x_{cb}) \sin\gamma + (y_b + \Delta y_{cb}) \cos\gamma \tag{A.28}$$

expression (A.20) reduces to

$$\frac{x_\gamma^2}{A_\gamma^2} + \frac{y_\gamma^2}{B_\gamma^2} = 1 \tag{A.29}$$

with

$$A_\gamma = \left(\frac{\cos\gamma^2}{A_c^2} + \frac{(\sin\gamma + g\cos\gamma)^2}{B_c^2}\right)^{-1/2}, \tag{A.30}$$

$$B_\gamma = \left(\frac{\sin\gamma^2}{A_c^2} + \frac{(\cos\gamma - g\sin\gamma)^2}{B_c^2}\right)^{-1/2}. \tag{A.31}$$

With the projections of E_f, E_c and E_b known analytically, the overlap between them is calculated by simulation and eventually multiplied with $\cos\tau$.

A.2 Coordinate Transformations

Consider the general coordinate systems xyz and uv as defined in section 2.3 and the coordinate systems $x_p y_p z_p$ and $u_p v_p$ specific for pinhole focus p, first introduced in section 2.2.5. This appendix provides the transformations between these different coordinate systems.

First consider the xyz and the $x_p y_p z_p$ coordinate systems. The $x_p y_p z_p$ coordinate system rotates with the detector over the projection angles θ during image acquisition and the $x_p y_p$ plane is parallel to the detector. The xyz coordinate system remains immobile during image acquisition and is generally not aligned with the detector. Therefore it is actually more convenient to establish the relation between the $x'''y'''z'''$ coordinate system (2.9) and the $x_p y_p z_p$ system. The origin of the $x'''y'''z'''$ system is located on the axis of rotation, while the origin of the $x_p y_p z_p$ system is located in the pinhole focal point. Consequently, the $x'''y'''z'''$ system needs to be corrected for the translation of the $x'''y'''z'''$ origin to the pinhole focal point. A second observation is that the x''', z''' axes are aligned with the columns

and rows of the detector pixels, also after correction for the above translation. The x_p, y_p axes on the other hand, are aligned with the inclination η_p of the pinhole central ray. To align both systems, a rotation over the aperture specific angle ζ_p between the systems is required. The combination of the translation and rotation correction yields

$$\begin{bmatrix} x''' \\ y''' \\ z''' \end{bmatrix} = \begin{bmatrix} m_{up} \\ -f_p \\ m_{vp} \end{bmatrix} + \begin{bmatrix} \cos\zeta_p & -\sin\zeta_p & 0 \\ 0 & 0 & 1 \\ \sin\zeta_p & \cos\zeta_p & 0 \end{bmatrix} \begin{bmatrix} x_p \\ y_p \\ z_p \end{bmatrix}. \tag{A.32}$$

Now consider the uv and u_pv_p coordinate systems. Both systems rotate with the detector over the projection angles θ, but the origin of the uv system is defined at the center of the projection images $Q(u, v, \theta)$, while the origin of the u_pv_p system is defined as the orthogonal projection of the pinhole focal point on the detector. Thereby, the translation of the uv origin to the u_pv_p origin requires correction for both the mechanical and electrical offsets. Further, the same rotation correction as above is required to align the axis of both systems, which leads to

$$\begin{bmatrix} u \\ v \end{bmatrix} = \begin{bmatrix} m_{up} + e_u \\ m_{vp} + e_v \end{bmatrix} + \begin{bmatrix} \cos\zeta_p & -\sin\zeta_p \\ \sin\zeta_p & \cos\zeta_p \end{bmatrix} \begin{bmatrix} u_p \\ v_p \end{bmatrix}. \tag{A.33}$$

For clarity, the electrical shifts e_u and e_v are the mixed intrinsic and extrinsic electrical shifts e_u^* and e_v^* of (2.19) and (2.20).

The inverse relations are further readily derived as

$$\begin{bmatrix} x_p \\ y_p \\ z_p \end{bmatrix} = \begin{bmatrix} \cos\zeta_p & \sin\zeta_p & 0 \\ 0 & 0 & 1 \\ -\sin\zeta_p & \cos\zeta_p & 0 \end{bmatrix} \left(\begin{bmatrix} x''' \\ y''' \\ z''' \end{bmatrix} - \begin{bmatrix} m_{up} \\ -f_p \\ m_{vp} \end{bmatrix} \right) \tag{A.34}$$

and

$$\begin{bmatrix} u_p \\ v_p \end{bmatrix} = \begin{bmatrix} \cos\zeta_p & \sin\zeta_p \\ -\sin\zeta_p & \cos\zeta_p \end{bmatrix} \left(\begin{bmatrix} u \\ v \end{bmatrix} - \begin{bmatrix} m_{up} + e_u \\ m_{vp} + e_v \end{bmatrix} \right). \tag{A.35}$$

A.3 Pinhole Calibration Equations

This appendix derives the equations (4.9) to (4.18) by equating the right hand sides of equations (4.1) and (4.2) expressed in two different sets of parameters and point source coordinates (4.4) and (4.5). Using the cylindrical coordinates, defined by equations (4.6) to (4.8), the equations (4.1) and (4.2) are first rewritten as

$$u^* = f \frac{m\cos\Psi + z\cos\Phi\sin\Psi - r\cos\alpha^*\cos\Psi + r\sin\alpha^*\sin\Phi\sin\Psi}{d^* + r\cos\Phi\sin\alpha^* - z\sin\Phi} \tag{A.36}$$

$$v^* = f \frac{m\sin\Psi - z\cos\Phi\cos\Psi - r\cos\alpha^*\sin\Psi - r\sin\alpha^*\sin\Phi\cos\Psi}{d^* + r\cos\Phi\sin\alpha^* - z\sin\Phi} \tag{A.37}$$

with

$$\alpha^* = \alpha - \theta \tag{A.38}$$

$$u^* = u - m\cos\Psi - e_u \tag{A.39}$$

$$v^* = v - m\sin\Psi - e_v \tag{A.40}$$

and in which the subscript i, indicating the point source number, has been dropped for convenience. Since the point source is assumed to be located off the rotation axis (z-axis) and the detector tilt Φ must lie in the interval $\left]-\frac{\pi}{2}, \frac{\pi}{2}\right[$, the coefficient $r\cos\Phi$ in the denominator is nonzero and the above equations can further be rewritten as

$$u = \frac{a_u \cos(\alpha-\theta) + b_u \sin(\alpha-\theta) + c_u}{\sin(\alpha-\theta) + g}, \tag{A.41}$$

$$v = \frac{a_v \cos(\alpha-\theta) + b_v \sin(\alpha-\theta) + c_v}{\sin(\alpha-\theta) + g}, \tag{A.42}$$

with

$$a_u = -f\frac{\cos\Psi}{\cos\Phi}, \tag{A.43}$$

$$a_v = -f\frac{\sin\Psi}{\cos\Phi}, \tag{A.44}$$

$$b_u = f\frac{\sin\Phi\sin\Psi}{\cos\Phi} + m\cos\Psi + e_u, \tag{A.45}$$

$$b_v = -f\frac{\sin\Phi\cos\Psi}{\cos\Phi} + m\sin\Psi + e_v, \tag{A.46}$$

$$c_u = f\left(\frac{m\cos\Psi}{r\cos\Phi} + \frac{z\sin\Psi}{r}\right) + g\left(m\cos\Psi + e_u\right), \tag{A.47}$$

$$c_v = f\left(\frac{m\sin\Psi}{r\cos\Phi} + \frac{z\cos\Psi}{r}\right) + g\left(m\sin\Psi + e_v\right), \tag{A.48}$$

$$g = \frac{d^* - z\sin\Phi}{r\cos\Phi}. \tag{A.49}$$

With the equations (4.1) and (4.2) written in this form, the first objective of this calculation is to prove that

$$\widetilde{a}_u = a_u \quad \text{and} \quad \widetilde{a}_v = a_v, \tag{A.50}$$

$$\widetilde{b}_u = b_u \quad \text{and} \quad \widetilde{b}_v = b_v, \tag{A.51}$$

$$\widetilde{c}_u = c_u \quad \text{and} \quad \widetilde{c}_v = c_v, \tag{A.52}$$

$$\widetilde{g} = g, \tag{A.53}$$

$$\widetilde{\alpha} = \alpha, \tag{A.54}$$

with $a_u, a_v, b_u, b_v, c_u, c_v, g, \alpha$ and $\widetilde{a}_u, \widetilde{a}_v, \widetilde{b}_u, \widetilde{b}_v, \widetilde{c}_u, \widetilde{c}_v, \widetilde{g}, \widetilde{\alpha}$ being expressed in the different parameter sets (4.4) and (4.5). Before proceeding, it should be noticed that the above equations (A.41) and (A.42) are only valid for $g > 1$. Geometrically, this restriction simply states that the point source must be located in the field of view for every possible projection angle θ. This remark must be satisfied by any acceptable parameter set, implying that also $\widetilde{g} > 1$.

Equating now the right hand side of equation (A.41) expressed in the different parameter sets and multiplying with both numerators yields

$$\begin{aligned} &a_u \sin\widetilde{\gamma}\cos\gamma + b_u \sin\widetilde{\gamma}\sin\gamma + (c_u - \widetilde{b_u} g)\sin\widetilde{\gamma} + a_u\widetilde{g}\cos\gamma + c_u\widetilde{g} = \\ &\widetilde{a}_u \sin\gamma\cos\widetilde{\gamma} + \widetilde{b_u}\sin\gamma\sin\widetilde{\gamma} + (\widetilde{c_u} - b_u\widetilde{g})\sin\gamma + \widetilde{a}_u g\cos\widetilde{\gamma} + \widetilde{c_u} g \end{aligned} \tag{A.55}$$

with

$$\gamma = \alpha - \theta, \tag{A.56}$$
$$\widetilde{\gamma} = \widetilde{\alpha} - \theta. \tag{A.57}$$

The products of sines and cosines can further be rewritten, yielding

$$\begin{aligned} &\tfrac{1}{2}(a_u - \widetilde{a}_u)\sin(\gamma + \widetilde{\gamma}) + \tfrac{1}{2}(b_u - \widetilde{b_u})\cos(\gamma + \widetilde{\gamma}) \\ &+(c_u - \widetilde{b_u} g)\sin\widetilde{\gamma} - (\widetilde{c_u} - b_u\widetilde{g})\sin\gamma + a_u\widetilde{g}\cos\gamma - \widetilde{a}_u g\cos\widetilde{\gamma} \\ &+\tfrac{1}{2}(a_u + \widetilde{a}_u)\sin(\widetilde{\alpha} - \alpha) + \tfrac{1}{2}(b_u - \widetilde{b}_u)\cos(\widetilde{\alpha} - \alpha) + c_u\widetilde{g} - \widetilde{c_u} g = 0. \end{aligned} \tag{A.58}$$

Performing the same operation on equation (A.42) yields an analogous result, which can be obtained by replacing the subscripts u by v in equation (A.55) and (A.58).

The above equation contains a constant part, a part varying with the projection angle θ and a part varying with 2θ. Since the relation must be satisfied for every possible projection angle, these parts may each individually be set equal zero. Doing so for the 2θ-part yields

$$(a_u - \widetilde{a}_u)\sin(\gamma + \widetilde{\gamma}) = (b_u - \widetilde{b_u})\cos(\gamma + \widetilde{\gamma}). \tag{A.59}$$

Setting the coefficients of the sine and cosine functions equal to zero results in the equations (A.50) and (A.51). Setting the other parts of equation (A.58) now equal to zero, taking into account the above results, yields

$$(c_u - b_u g)\sin\widetilde{\gamma} + a_u g\cos\widetilde{\gamma} = (\widetilde{c_u} - b_u\widetilde{g})\sin\gamma + a_u\widetilde{g}\cos\gamma \tag{A.60}$$

and

$$a_u\sin(\widetilde{\alpha} - \alpha) + c_u\widetilde{g} - \widetilde{c_u} g = 0. \tag{A.61}$$

Both the left and right hand side of equation (A.60) can be written as a cosine with a specific amplitude and phase. Setting the phase of both sides equal to each other yields

$$\widetilde{\alpha} - \alpha = \arctan\left(\frac{\frac{\widetilde{c}_u}{\widetilde{g}} - b_u}{a_u}\right) - \arctan\left(\frac{\frac{c_u}{g} - b_u}{a_u}\right) \tag{A.62}$$

with $a_u \neq 0$, because $f > 0$ and $\Psi \in \left]-\frac{\pi}{2}, \frac{\pi}{2}\right[$. Further, since $g > 1$, equation (A.61) can be written as

$$\widetilde{c}_u = c_u\frac{\widetilde{g}}{g} + \frac{a_u}{g}\sin(\widetilde{\alpha} - \alpha). \tag{A.63}$$

Substituting this relation into equation (A.62) yields

$$\widetilde{\alpha} - \alpha = \arctan\left(\frac{\frac{c_u}{g} - b_u}{a_u} - \frac{1}{g\widetilde{g}}\sin(\widetilde{\alpha} - \alpha)\right) - \arctan\left(\frac{\frac{c_u}{g} - b_u}{a_u}\right). \tag{A.64}$$

The above equation (A.64) can be written as

$$H(\beta) = \beta - \arctan(x - y\sin\beta) + \arctan(x) = 0, \tag{A.65}$$

with

$$\beta = \widetilde{\alpha} - \alpha, \tag{A.66}$$

$$x = \frac{\frac{c_u}{g} - b_u}{a_u}, \tag{A.67}$$

$$y = \frac{1}{g\widetilde{g}}. \tag{A.68}$$

Since the function $H(\beta)$, with $0 < y < 1$, is strictly increasing,

$$\frac{\partial H(\beta)}{\partial \beta} = 1 - \frac{y\cos(\beta)}{1 + (x - y\sin(\beta))^2} > 0, \tag{A.69}$$

equation (A.65) has a unique solution $\beta = 0$ or equivalently $\widetilde{\alpha} = \alpha$. Substituting this result back into equation (A.60) and (A.61) eventually yields the equations (A.52) and (A.53). Note that the relations (A.50) to (A.54) remain equally valid when replacing $m\cos\Phi$ and $m\sin\Phi$ by m_u and m_v respectively in (A.43) to (A.49).

The above part derives the equations (A.50) to (A.54) for the projection of a point source off the rotation axis. In principle these are already the equations (4.9) to (4.18), although in a different form. The remainder of this appendix systematically transforms each of the equations (A.50) to (A.54) into the corresponding equations of (4.9) to (4.18).

The relations $\widetilde{a}_u = a_u$ and $\widetilde{a}_v = a_v$ yield respectively

$$f\frac{\cos\Psi}{\cos\Phi} = \widetilde{f}\frac{\cos\widetilde{\Psi}}{\cos\widetilde{\Phi}}, \tag{A.70}$$

$$f\frac{\sin\Psi}{\cos\Phi} = \widetilde{f}\frac{\sin\widetilde{\Psi}}{\cos\widetilde{\Phi}}. \tag{A.71}$$

Dividing equation (A.71) by equation (A.70) leads to equation (4.9) and substituting this result back into equation (A.70) or (A.71) further yields equation (4.10). The substitution of the equations (4.9) and (4.10) into the relations $\widetilde{b}_u = b_u$ and $\widetilde{b}_v = b_v$ immediately yields the equations (4.15) and (4.16). The equations $\widetilde{c}_u = c_u$ and $\widetilde{c}_v = c_v$ yield respectively

$$\begin{aligned}\frac{fm}{r\cos\Phi}\cos\Psi + \frac{fz}{r}\sin\Psi + g(m\cos\Psi + e_u) = \\ \frac{f\widetilde{m}}{\widetilde{r}\cos\Phi}\cos\Psi + \frac{\widetilde{f}\widetilde{z}}{\widetilde{r}}\sin\Psi + g(\widetilde{m}\cos\Psi + \widetilde{e_u})\end{aligned} \tag{A.72}$$

and

$$\begin{aligned}\frac{fm}{r\cos\Phi}\sin\Psi - \frac{fz}{r}\cos\Psi + g(m\sin\Psi + e_v) = \\ \frac{f\widetilde{m}}{\widetilde{r}\cos\Phi}\sin\Psi - \frac{\widetilde{f}\widetilde{z}}{\widetilde{r}}\cos\Psi + g(\widetilde{m}\sin\Psi + \widetilde{e_v})\end{aligned} \tag{A.73}$$

in which $\widetilde{g} = g$ and equation (4.10) have already been used. Further, with equations (4.15) and (4.16), $(\widetilde{m}\cos\Psi + \widetilde{e_u})$ and $(\widetilde{m}\sin\Psi + \widetilde{e_v})$ can be written in function of $(m\cos\Psi + e_u)$ and $(m\sin\Psi + e_v)$ respectively, yielding

$$\frac{f\widetilde{m}}{\widetilde{r}\cos\Phi}\cos\Psi + \frac{f\widetilde{z}}{\widetilde{r}}\sin\Psi + g\left(\frac{f(\sin\Phi - \sin\widetilde{\Phi})}{\cos\Phi}\right)\sin\Psi = \frac{fm}{r\cos\Phi}\cos\Psi + \frac{fz}{r}\sin\Psi \tag{A.74}$$

and

$$\frac{f\widetilde{m}}{\widetilde{r}\cos\Phi}\sin\Psi - \frac{f\widetilde{z}}{\widetilde{r}}\cos\Psi - g\left(\frac{f(\sin\Phi - \sin\widetilde{\Phi})}{\cos\Phi}\right)\cos\Psi = \frac{fm}{r\cos\Phi}\sin\Psi - \frac{fz}{r}\cos\Psi. \tag{A.75}$$

Multiplying equation (A.74) and (A.75) by $\cos\Psi$ and $\sin\Psi$ respectively, adding the results and using equation (4.10) eventually yields equation (4.14). The substitution of equation (4.14) and (4.10) into equation (A.74) or (A.75) further yields equation (4.12), with a and b as in (4.17) and (4.18) respectively. Using this result to substitute the term $\frac{\widetilde{z}}{\widetilde{r}}$ in $\widetilde{g} = g$ finally yields equation (4.13).

A.4 Calibration Phantom Position

Section 4.2.2 explains how the positions (x_i, y_i, z_i) of the calibration point sources $i = 1, 2, 3$ have to be expressed in terms of 3 translations t_x, t_y, t_z, 3 rotations ρ_1, ρ_2, ρ_3 and the distances s_{12}, s_{13}, s_{23} between the point sources. This appendix illustrates how this can be done. The transformation proposed first places the phantom in the field of view with point 1 in the xyz origin, point 2 on the positive x axis and point 3 in the xy half plane of positive y coordinates. The phantom is then rotated 3 times over the angles ρ_1, ρ_2, ρ_3 along different axes to its correct orientation and eventually it is translated in the x, y and z directions by t_x, t_y, t_z to the correct position in the field of view. Doing so, yields the transformation

$$\begin{bmatrix} x_i \\ y_i \\ z_i \end{bmatrix} = \begin{bmatrix} t_x \\ t_y \\ t_z \end{bmatrix} + R_3\, R_2\, R_1 \begin{bmatrix} c_{xi} \\ c_{yi} \\ c_{zi} \end{bmatrix} \tag{A.76}$$

with

$$R_1 = \begin{bmatrix} cos\rho_1 & -sin\rho_1 & 0 \\ sin\rho_1 & cos\rho_1 & 0 \\ 0 & 0 & 1 \end{bmatrix} \tag{A.77}$$

$$R_2 = \begin{bmatrix} cos\rho_2 & 0 & -sin\rho_2 \\ 0 & 1 & 0 \\ sin\rho_2 & 0 & cos\rho_2 \end{bmatrix} \tag{A.78}$$

$$R_3 = \begin{bmatrix} cos\rho_3 & -sin\rho_3 & 0 \\ sin\rho_3 & cos\rho_3 & 0 \\ 0 & 0 & 1 \end{bmatrix} \tag{A.79}$$

and with

$$\begin{bmatrix} c_{x1} \\ c_{y1} \\ c_{z1} \end{bmatrix} = \begin{bmatrix} 0 \\ 0 \\ 0 \end{bmatrix} \tag{A.80}$$

$$\begin{bmatrix} c_{x2} \\ c_{y2} \\ c_{z2} \end{bmatrix} = \begin{bmatrix} s_{12} \\ 0 \\ 0 \end{bmatrix} \tag{A.81}$$

$$\begin{bmatrix} c_{x3} \\ c_{y3} \\ c_{z3} \end{bmatrix} = \begin{bmatrix} \frac{s_{12}^2+s_{13}^2-s_{23}^2}{2s_{12}} \\ \sqrt{s_{13}^2 - \left(\frac{s_{12}^2+s_{13}^2-s_{23}^2}{2s_{12}}\right)^2} \\ 0 \end{bmatrix}. \tag{A.82}$$

A.5 Covariance Matrix Decomposition

This section demonstrates a recursive method to calculate the matrix Γ of (5.8) for a small 3x3 covariance matrix

$$\mathrm{cov}(P) = \begin{bmatrix} \sigma_{xx} & \sigma_{xy} & \sigma_{xz} \\ \sigma_{xy} & \sigma_{yy} & \sigma_{yz} \\ \sigma_{xz} & \sigma_{yz} & \sigma_{zz} \end{bmatrix}. \tag{A.83}$$

The first column of Γ, which equals $\frac{\Delta P_1}{2}$, is calculated as

$$\frac{\Delta P_1}{2} = \begin{bmatrix} \sqrt{\sigma_{xx}} \\ \alpha\sqrt{\sigma_{xx}} \\ \beta\sqrt{\sigma_{xx}} \end{bmatrix} \tag{A.84}$$

with

$$\alpha = \frac{\sigma_{xy}}{\sigma_{xx}} \tag{A.85}$$

$$\beta = \frac{\sigma_{xz}}{\sigma_{xx}} \tag{A.86}$$

and $\mathrm{cov}(P)$ is modified into $\mathrm{cov}(P_1)$

$$\mathrm{cov}(P_1) = \begin{bmatrix} 0 & 0 & 0 \\ 0 & \sigma_{yy} - \alpha^2\sigma_{xx} & \sigma_{yz} - \alpha\beta\sigma_{xx} \\ 0 & \sigma_{yz} - \alpha\beta\sigma_{xx} & \sigma_{zz} - \beta^2\sigma_{xx} \end{bmatrix}. \tag{A.87}$$

In this new covariance matrix $\mathrm{cov}(P_1)$, the variance of x has been eliminated and the variances of y and z have been reduced by the appropriate amount, according to their covariances with the parameter x. The covariance σ_{yz} has also been adapted to the new values of the variances of y and z. The above procedure is now systematically repeated for the other diagonal elements, yielding the other columns of Γ. For the above 3x3 covariance matrix $\mathrm{cov}(P)$ this procedure yields

$$\Gamma = \begin{bmatrix} \sqrt{\sigma_{xx}} & 0 & 0 \\ \alpha\sqrt{\sigma_{xx}} & \sqrt{\sigma_{yy} - \alpha^2\sigma_{xx}} & 0 \\ \beta\sqrt{\sigma_{xx}} & \gamma\sqrt{\sigma_{yy} - \alpha^2\sigma_{xx}} & \sqrt{\begin{matrix}\sigma_{zz} - \gamma^2\sigma_{yy} + \\ (\alpha^2\gamma^2 - \beta^2)\sigma_{xx}\end{matrix}} \end{bmatrix} \tag{A.88}$$

with

$$\gamma = \frac{\sigma_{yz} - \alpha\beta\sigma_{xx}}{\sigma_{yy} - \alpha^2\sigma_{xx}}. \tag{A.89}$$

From (A.88), it is easy to prove that $\mathrm{cov}(P) = \Gamma\Gamma^T$ (5.8) and extension of the method to larger covariance matrices is straightforward.

A.6 Pinhole SPECT Field of View

This appendix calculates the shape of the field of view of a pinhole camera with a circular detector orbit and the overlap with the largest sphere inscribed in this field of view. The results are valid for zero mechanical offset m and zero tilt angle Φ.

Consider a point source rotating around an axis at a distance d^* in front of a stationary pinhole camera, as shown in figure A.2. During rotation, the point source describes a circle with radius r in a plane at a distance z from the central ray of the pinhole camera. At each position θ, the point source projection ray intersects the pinhole central ray at an angle τ

$$\tau = \arctan\left(\frac{\sqrt{r^2\cos^2\theta + z^2}}{d^* - r\sin\theta}\right). \tag{A.90}$$

To be located in the field of view, the ray angle τ of the point source projection must be less than half of the acceptance angle α of the pinhole aperture. At each z location, the maximum radius r is thereby limited. During rotation, the angle τ maximizes to

$$\tau_{max} = \arctan\left(\tfrac{z}{d^* \pm r}\right) \qquad \text{if } r^2 + z^2 \geq rd^* \tag{A.91}$$

$$\tau_{max} = \arctan\left(\sqrt{\tfrac{r^2+z^2}{d^{*2}-r^2-z^2}}\right) \quad \text{if } r^2 + z^2 < rd^*. \tag{A.92}$$

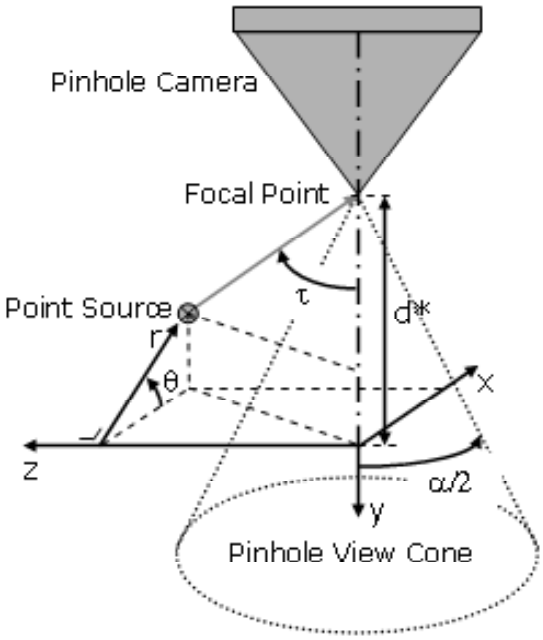

Figure A.2: Point source rotating in front of a stationary pinhole camera.

At this maximum angle position of the point source τ_{max}, the radius of rotation r_{max} that yields $\tau_{max} = \alpha/2$ can be calculated

$$r_{max} = d^* - \frac{z}{\tan(\alpha/2)} \qquad \text{if } z \geq d^* \sin(\alpha/2)\cos(\alpha/2) \tag{A.93}$$

$$r_{max} = \sqrt{d^{*2}\sin^2(\alpha/2) - z^2} \quad \text{if } z < d^* \sin(\alpha/2)\cos(\alpha/2). \tag{A.94}$$

Figure A.3 illustrates the shape of this field of view. The field of view consists of a central spherical zone ($z < d^* \sin(\alpha/2)\cos(\alpha/2)$) with two conical extensions along the rotation axis ($z \geq d^* \sin(\alpha/2)\cos(\alpha/2)$). From this observation, it is easy to calculate the volume V_{fov} of this field of view.

$$V_{fov} = \frac{4}{3}\pi d^{*3} \sin^3(\alpha/2)\ \frac{\cos^2(\alpha/2)+1}{2\ \cos(\alpha/2)}. \tag{A.95}$$

Further, it is obvious from (A.93,A.94) that the largest sphere that can be inscribed in this field of view, is a sphere with radius $d^{*3}\sin(\alpha/2)$ located at the center of the field of view. The volume V_{sphere} is readily calculated as

$$V_{sphere} = \frac{4}{3}\pi d^{*3} \sin^3(\alpha/2). \tag{A.96}$$

The overlap between this sphere and the actual field of view only depends on the aperture angle α of the pinhole system.

$$\frac{V_{sphere}}{V_{fov}} = \frac{2\ \cos(\alpha/2)}{\cos^2(\alpha/2)+1}. \tag{A.97}$$

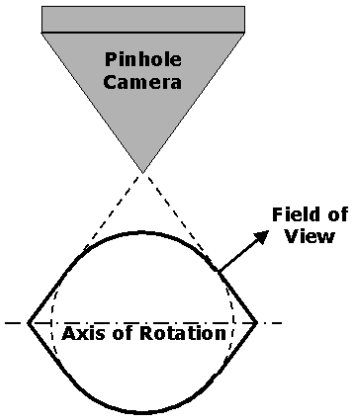

Figure A.3: Pinhole SPECT Field of View.

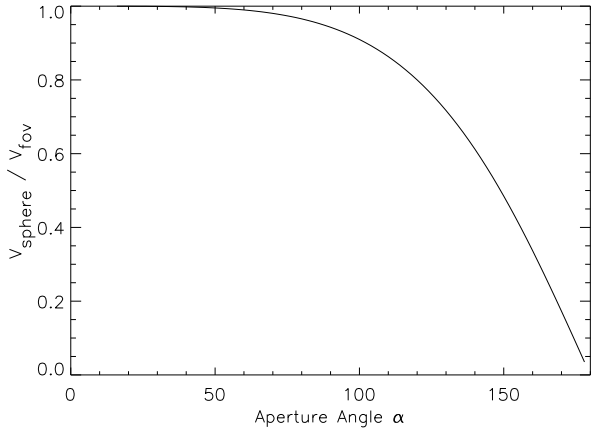

Figure A.4: Fractional overlap of a spherical approximation (V_{sphere}) of the pinhole field of view and the true field of view (V_{fov}) as a function of the pinhole aperture angle α.

Figure A.4 shows the overlap of the sphere and the actual field of view. For small to moderate aperture angles, the sphere covers almost the entire field of view.

List of Publications

International Journal

1. J. Nuyts, K. Baete, **D. Bequé**, and P. Dupont, "Comparison between MAP and post-processed ML for incorporating anatomical knowledge in emission tomography," Submitted to *IEEE Trans. Med. Imag.*

2. **D. Bequé**, J. Nuyts, P. Suetens, and G. Bormans, "Optimization of Geometrical Calibration in Pinhole SPECT," Accepted for publication in *IEEE Trans. Med. Imag.*

3. **D. Bequé**, J. Nuyts, G. Bormans, P. Suetens, and P. Dupont, "Characterization of Acquisition Geometry of Pinhole SPECT," *IEEE Trans. Med. Imag.*, vol. 22(5), pp. 599-612, 2003.

4. J. Nuyts, **D. Bequé**, P. Dupont, and L. Mortelmans, "A concave prior penalizing relative differences for maximum-a-posteriori reconstruction in emission tomography," *IEEE Trans. Nucl. Sci.*, Vol. 49, pp. 56-60, 2002.

International Conference Proceeding

1. **D. Bequé**, C. Vanhove, A. Andreyev, J. Nuyts, and M. Defrise, "Correction for Imperfect Camera Motion and Resolution Recovery in Pinhole SPECT, " IEEE Nuclear Science Symposium and Medical Imaging Conference 2004, Rome, Italy.

2. **D. Bequé**, J. Nuyts, G. Bormans, P. Suetens, and P. Dupont, "Optimization of Pinhole SPECT Calibration," Proceedings of IEEE Nuclear Science Symposium and Medical Imaging Conference 2003, Portland, Oregon, USA.

International Abstract

1. K. Van Laere, E. Lauwers, **D. Bequé**, J. Nuyts, J. Van den Eynden, P. Vermaelen, B. Vanbilloen, L. Mortelmans, A. Verbruggen, B. Nuttin, G. Bormans, Z. Debyzer, V. Baekelandt, "Quantitative comparison of 123I-FP-CIT

microSPECT dopamine transporter binding and histology in a rodent model for Parkinson's disease by lentiviral vector-mediated overexpression of α-synuclein," Annual Congress of the European Association of Nuclear Medicine 2004, Helsinki, Finland.

2. **D. Bequé**, E. Lauwers, J. Nuyts, G. Bormans, P. Vermaelen, J. Van den Eynden, Z. Debyser, V. Baekelandt, A. Verbruggen, L. Mortelmans, and K. Van Laere, "Micro-SPECT validation of a rodent model for Parkinson's disease by lentiviral vector-mediated overexpression of α-synuclein," Annual Meeting Society of Nuclear Medicine 2004, Philadelphia, Pennsylvania, USA.

3. **D. Bequé**, J. Nuyts, G. Bormans, P. Suetens, and P. Dupont, "Characterization of Acquisition Geometry of Pinhole SPECT, " IEEE Nuclear Science Symposium and Medical Imaging Conference 2002, Norfolk, Virginia, USA.

Local Abstract

1. **D. Bequé**, J. Nuyts, G. Bormans, P. Suetens, M. Defrise, and P. Dupont, "Optimization of Pinhole SPECT Calibration," Symposium of the Belgian Society of Nuclear Medicine May 2003, Knokke, Belgium.

Book Chapter

1. J. Nuyts and **D. Bequé**, "Image formation and data processing", in "Diagnostic Nuclear Medicine", C. Schiepers edt, Springer. In Press.

Master's Thesis

1. **D. Bequé** and Y. Vanden Hende, "Measurement of Local Heat Transfer Coefficients by means of Liquid Crystal Thermography," Katholieke Universiteit Leuven, Belgium, 1999.

Thesis

1. **D. Bequé**, "The use of a priori knowledge in positron emission tomography," Katholieke Universiteit Leuven, Belgium, 2000.

Curriculum Vitae

Dirk Bequé
March 25, 1976.

Education

1. Doctoraatsopleiding in de Toegepaste Wetenschappen.
   K.U.Leuven, 2000-2005.
2. GAS Biomedische en Klinische Ingenieurstechnieken en Medische Fysica, Optie Medische Stralingsfysica. K.U.Leuven, 1999-2000.
3. Burgerlijk Werktuigkundig-Elektrotechnisch Ingenieur, Richting Mechanica.
   K.U.Leuven, 1996-1999.
4. Kandidaat Burgerlijk Ingenieur. K.U.Leuven, 1994-1996.

Training

1. Short Course: "Detectors for SPECT and PET" by H. Barrett.
   NSS-MIC October 18, 2004, Rome, Italy.
2. Summer Internship at CT-lab, GE Global Research, Niskayuna, NY.
   Period: July 21 to October 17, 2003.
   Subject: iterative image reconstruction in CT applications.
3. Short Course: "Statistical Methods for Image Reconstruction" by J.A. Fessler.
   NSS-MIC November 12, 2002, Norfolk, VA.

Award

1. Laureaat 1999-2000 "Eindwerkonderzoek in de Biomedische Ingenieurstechnieken en Medische Fysica", Belgisch Genootschap Biomedische Techniek & Gezondheidszorg.

Bibliography

[1] M. A. King, G. J. Hademenos, and S. J. Glick, "A dual photopeak window method for scatter correction," *J. Nucl. Med.*, Vol. 33, pp. 605–613, 1992.

[2] N. U. Schramm, G. Ebel, U. Engeland, T. Schurrat, M. Béhé, and T. M. Behr, "High-Resolution SPECT Using Multipinhole Collimation," *IEEE Trans. Nucl. Sci.*, Vol. 50(3), pp. 315–320, 2003.

[3] S. R. Meikle, R. R. Fulton, S. Eberl, M. Dahlbom, K.-P. Wong, and M. J. Fulham, "An Investigation of Coded Aperture Imaging for Small Animal SPECT," *IEEE Trans. Nucl. Sci.*, Vol. 48(3), pp. 816–821, 2001.

[4] S. R. Meikle, P. K. Kench, A. G. Weisenberger, R. Wojcik, M. F. Smith, S. Majewski, S. Eberl, R. R. Fulton, A. Rosenfeld, and M. J. Fulham, "A Prototype Coded Aperture Detector for Small Animal SPECT," *IEEE Trans. Nucl. Sci.*, Vol. 49(5), pp. 2167–2171, 2002.

[5] H. K. Tuy, "An inversion formula for cone-beam reconstruction," *SIAM J. Appl. Math.*, Vol. 43(3), pp. 546–552, 1983.

[6] B. D. Smith, "Image Reconstruction from Cone-Beam Projections: Necessary and Sufficient Conditions and Reconstruction Methods," *IEEE Trans. Med. Imag.*, Vol. 4(1), pp.14–25, 1985.

[7] S. D. Metzler, J. E. Bowsher, and R. J. Jaszczak, "Geometrical Similarities of the Orlov and Tuy Sampling Criteria and a Numerical Algorithm for Assessing Sampling Completeness," *IEEE Trans. Nucl. Sci.*, Vol. 50(5), pp. 1550–1555, 2003.

[8] S. H. Manglos, and B. D. Smith, "Practical Evaluation of Several Cone Beam Orbits for SPECT," *IEEE Trans. Nucl. Sci.*, Vol. 40(4), pp. 1134–1139, 1993.

[9] S. D. Metzler, k. L. Greer, K. Bobkov, and R. J. Jaszczak, "Laser Alignment System for Helical Pinhole SPECT," *IEEE Trans. Nucl. Sci.*, Vol. 51(3), pp. 603–610, 2004.

[10] S. D. Metzler, k. L. Greer, and R. J. Jaszczak, "Helical Pinhole SPECT for Small-Animal Imaging: A Method for Addressing Sampling Completeness," *IEEE Trans. Nucl. Sci.*, Vol. 50(5), pp. 1575–1583, 2003.

[11] T. Zeniya, H. Watabe, T. Aoi, K. M. Kim, N. Teramoto, T. Hayashi, A. Sohlberg, H. Kudo, H. Iida, "A new reconstruction strategy for image improvement in pinhole SPECT," *Eur. J. Nucl. Med.*, Vol. 31, pp. 1166–1172, 2004.

[12] S. S. Orlov, "Theory of three dimensional reconstruction. I. Conditions for a complete set of projections," *Sov. Phys. Crystallogr.*, Vol. 20(3), pp. 312–314, 1975.

[13] A. Seret, M. Defrise, and D. Blocklet, "180 degree pinhole SPECT with tilted detector and OSEM reconstruction: phantom studies and potential clinical applications," *Eur. J. Nucl. Med.*, Vol. 28, pp. 1836–1841, 2001.

[14] M. F. Smith, and R. J. Jaszczak, "The effect of gamma ray penetration on angle-dependent sensitivity of pinhole collimation in nuclear medicine," *Med. Phys.*, vol. 24(11), pp. 1701–1709, 1997.

[15] R. Accorsi, and S. D. Metzler, "Analytic Determination of the Resolution-Equivalent Effective Diameter of a Pinhole Collimator," *IEEE Trans. Med. Imag.*, Vol. 23(6), pp. 750–763, 2004.

[16] S. D. Metzler, J. E. Bowsher, M. F. Smith, and R. J. Jaszczak, "Analytic Determination of Pinhole Collimator Sensitivity With Penetration," *IEEE Trans. Med. Imag.*, Vol. 20(8), pp. 730–741, 2001.

[17] M. F. Smith, and R. J. Jaszczak, "An analytic model of pinhole aperture penetration for 3D pinhole SPECT image reconstruction, "*Phys. Med. Biol.*, vol. 43, pp. 761–775, 1998.

[18] L. A. Shepp, and Y. Vardi, "Maximum Likelihood Reconstruction for Emission Tomography," *IEEE Trans. Med. Imag.*, Vol. 1(2), pp. 113–122, 1982.

[19] K. Lange, and R. Carson, "EM Reconstruction Algorithms for Emission and Transmission Tomography," *Journal of Computer Assisted Tomography*, Vol. 8(2), pp. 306–316, 1984.

[20] A. R. De Pierro, "On the relation between the ISRA and the EM algorithm for positron emission tomography," *IEEE Trans. Med. Imag.*, Vol. 12(2), pp. 328–333, 1993.

[21] L. A. Feldkamp, L. C. Davis, and J. W. Kress, "Practical cone beam algorithm," *J. Opt. Soc. Am.*, A1, pp. 612–619, 1984.

[22] J. Li, R. J. Jaszczak, and R. E. Coleman, "Quantitative Small Field-of-View Pinhole SPECT Imaging: Initial Evaluation," *IEEE Trans. Nucl. Sci.*, Vol. 42(4), pp. 1109–1113, 1995.

[23] J. Li, R. J. Jaszczak, K. L. Greer, and R. E. Coleman, "A filtered backprojection algorithm for pinhole SPECT with a displaced centre of rotation," *Phys. Med. Biol.*, Vol. 39, pp. 165–176, 1994.

[24] J. Li, R. J. Jaszczak, K. L. Greer, R. E. Coleman, Z.-J. Cao, and B. M. W Tsui, "Direct cone beam SPECT reconstruction with camera tilt," *Phys. Med. Biol.*, Vol. 38, pp. 241–258, 1993.

[25] F. Noo, R. Clack, M. Defrise, "Cone-beam Reconstruction from General Discrete Vertex Sets using Radon Rebinning Algorithms," *IEEE Trans. Nucl. Sci.*, Vol. 44(3), pp. 1309–1316, 1997.

[26] M. Karolczak, S. Schaller, K. Engelke, A. Lutz, U. Taubenreuther, K. Wiesent, W. Kalender, "Implementation of a cone-beam reconstruction algorithm for single-circle source orbit with embedded misalignment correction using homogeneous coordinates," *Med. Phys.*, Vol. 28(10), 2050-2069, 2001.

[27] M. Defrise, and R. Clack, "A cone-beam reconstruction algorithm using shift variant filtering and cone-beam backprojection," *IEEE Trans. Med. Imag.*, Vol. 13, pp. 186–195, 1994.

[28] J. Li, R. J. Jaszczak, and R. E. Coleman, "Maximum Likelihood Reconstruction for Pinhole SPECT with a Displaced Centre-of-Rotation," *IEEE Trans. Med. Imag.*, Vol. 14(2), pp. 407–409, 1995.

[29] D. Bequé, J. Nuyts, G. Bormans, P. Suetens, and P. Dupont, "Characterization of Pinhole SPECT Acquisition Geometry, " *IEEE Trans. Med. Imag.*, Vol. 22(5), pp. 599-612, 2003.

[30] Ph. Rizo, P. Grangeat, and R. Guillemaud, "Geometric Calibration Method for Multiple-Head Cone-Beam SPECT System," *IEEE Trans. Nucl. Sci.*, Vol. 41(6), pp. 2748–2757, 1994.

[31] F. Noo, R. Clackdoyle, C. Mennessier, T. A. White, and T. J. Roney, "Analytic method based on identification of ellipse parameters for scanner calibration in cone-beam tomography," *Phys. Med. Biol.*, Vol. 45, pp. 3489–3508, 2000.

[32] J. Li, R. J. Jaszczak, H. Wang, K. L. Greer and, R. E. Coleman, "Determination of both mechanical and electronic shifts in cone beam SPECT," *Phys. Med. Biol.*, Vol. 39, pp. 743–754, 1993.

[33] G. T. Gullberg, B. M. W. Tsui, C. R. Crawford, J. G. Ballard, and J. T. Hagius, "Estimation of geometrical parameters and collimator evaluation for cone beam tomography," *Med. Phys.*, Vol. 17(2), pp. 264–272, 1990.

[34] H. Wang, M. F. Smith, C. D. Stone, and R. J. Jaszczak, "Astigmatic single photon emission computed tomography imaging with a displaced center of rotation," *Med. Phys.*, Vol. 25(8), pp. 1493–1501, 1998.

[35] K. J. Kyriakopoulos, P. Yiannakos, V. Kallipolites, and K. Domales, "A Geometric Calibration Methodology for Single-Head Cone-Beam X-Ray Systems," *Journal of Intelligent and Robotic Systems*, Vol. 24, pp. 151–174, 1999.

[36] A. V. Bronnikov, "Virtual alignment of x-ray cone-beam tomography system using two calibration aperture measurements," *Opt. Eng.*, Vol. 38(2), pp. 381–386, 1999.

[37] W. H. Press, B. P. Flannery, S. A.Teukolksky, and W. T. Vetterling, *Numerical Recipes : the Art of Scientific Computing.* Cambridge: Cambridge University Press, 1986, pp.294–301.

[38] H. M. Hudson, and R. S. Larkin, "Accelerated Image Reconstruction Using Ordered Subsets of Projection Data," *IEEE Trans. Med. Imag.*, Vol. 13(4), pp. 601–609, 1994.

[39] C. Vanhove, M. Defrise, P. R. Franken, H. Everaert, F. Deconinck, and A. Bossuyt, "Interest of ordered subsets expectation maximization (OS-EM) algorithm in pinhole single-photon emission tomography reconstruction: a phantom study," *Eur. J. Nucl. Med.*, Vol. 27(2), pp. 140–146, 2000.

[40] D. Bequé, J. Nuyts, P. Suetens, and G. Bormans, "Optimization of Geometrical Calibration in Pinhole SPECT, " *IEEE Trans. Med. Imag.*, in Press.

[41] J. A. Fessler and W. L. Rogers, "Spatial resolution properties of penalized-likelihood image reconstruction: space-invariant tomographs," *IEEE Trans. Image Proc.*, Vol. 5, pp. 1346–1358, 1996.

[42] J. A. Fessler, "Mean and Variance of Implicitely Defined Estimators (such as Penalized Maximum Likelihood): Applications to Tomography," *IEEE Trans. Med. Imag.*, Vol. 5(3), pp. 493–506, 1996.

[43] J. Qi and R. Leahy, "A theoretical Study of the Contrast Recovery and Variance of MAP Reconstructions from PET Data," *IEEE Trans. Med. Imag.*, Vol. 18(4), pp. 293–305, 1999.

[44] J. Qi and R. Leahy, "Resolution and Noise Properties of MAP Reconstruction for Fully 3-D PET," *IEEE Trans. Med. Imag.*, Vol. 19(5), pp. 493–506, 2000.

[45] D. Bequé, C. Vanhove, A. Andreyev, J. Nuyts, and M. Defrise, "Correction for Imperfect Camera Motion and Resolution Recovery in Pinhole SPECT, " IEEE Nuclear Science Symposium and Medical Imaging Conference 2004, Rome, Italy.

[46] A. Spanu, G. Dettori, F. Chessa, A. Porcu, P. Cottu, P. Solinas, A. Falchi, M. E. Solinas, A. M. Scanu, S. Nuvoli, and G. Madeddu, "99mTc-Tetrofosmin pinhole-SPECT (P-SPECT) and radioguided sentinel node (SN) biopsy and in breast cancer axillary lymph node staging," *Cancer Biother. Radiopharm.*, Vol. 16(6), pp. 501–513, 2001.

[47] Y. W. Bahk, S. K. Chung, Y. H. Park, S. H. Kim, and H. K. Lee, "Pinhole SPECT imaging in normal and morbid ankles,"*J. Nucl. Med.*, Vol. 39, pp. 130–139, 1998.

[48] P. M. Wanet, A. Sand, and J. Abramovici, "Physical and Clinical Evaluation of High-Resolution Thyroid Pinhole Tomography," *J. Nucl. Med.*, Vol. 37, pp. 2017–2020, 1996.

[49] P. D. Acton, S. Choi, K. Plössl, and H. F. Kung, "Quantification of dopamine transporters in the mouse brain using ultra-high resolution single-photon emission tomography," *Eur. J. Nucl. Med.*, Vol. 29, pp. 691–698, 2002.

[50] P. D. Acton, C. Hou, M.-P. Kung, K. Plössl, C. L. Keeney, H. F. Kung, "Occupancy of dopamine D_2receptors in the mouse brain measured using ultra-high-resolution single-photon emission tomography and [^{123}]IBF," *Eur. J. Nucl. Med.*, Vol. 29(11), pp. 1507–1515, 2002.

[51] D. A. Weber, and M. Ivanovic, "Ultra-high resolution imaging of small animals: implementations for preclinical and research studies," *J. Nucl. Cardiol.*, Vol. 6, pp.332-344, 1999.

[52] J. B. A. Habraken, K. de Bruin, M. Shehata, J. Booij, R. Bennink, B. L. F. van Eck Smit, and E. B. Sokole, "Evaluation of High-Resolution Pinhole SPECT Using a Small Rotating Animal," *J. Nucl. Med.*, Vol. 42, pp. 1863–1869, 2001.

[53] L. R. MacDonald, B. E. Patt, J. S. Iwanczyk, B. M. W. Tsui, Y. Wang, E. C. Frey, D. E. Wessel, P. D. Acton, and H. F. Kung, "Pinhole SPECT of Mice Using the LumaGEM Gamma Camera," *IEEE Trans. Nucl. Sci.*, Vol. 48(3), pp. 830–836, 2001.

[54] M. C. Wu, H. R. Tang, D. W. Gao, A. Ido, J. W. O'Connell, B. H. Hasegawa, and M. W. Dae, "ECG-Gated Pinhole SPECT in Mice with Millimeter Spatial Resolution," *IEEE Trans. Nucl. Sci.*, Vol. 47(3), pp. 1218–1221, 2000.

[55] M. C. Wu, H. R. Tang, J. W. O'Connell, D. W. Gao, A. Ido, A. J. Da Silva, K. Iwata, B. H. Hasegawa, and M. W. Dae, "An Ultra High Resolution ECG-Gated Myocardial Imaging System for Small Animals," *IEEE Trans. Nucl. Sci.*, Vol. 46(4), pp. 1199–1202.

[56] T. Hirai, R. Nohara, R. Hosokawa, M. Tanaka, H. Inada, Y. Fukibayashi, M. Fujita, J. Konishi, and S. Sasayama, "Evaluation of myocardial infarct size in rat heart by pinhole SPECT," *J. Nucl. Cardiol.*, Vol. 7(2), pp. 107–111, 2000.

[57] K. Ogawa, T. Kawade, K. Nakamura, A. Kubo, and T. Ichihara, "Ultra high resolution pinhole SPECT for small animal study," *IEEE Trans. Nucl. Sci.*, Vol. 45(6), pp. 3122–3126, 1998.

[58] K. Ishizu, T. Mukai, Y. Yonekura, M. Pagani, T. Fujita, Y. Magata, S. Nishizawa, N. Tamaki, H. Shibasaki, and J. Konishi, "Ultra-high Resolution SPECT System Using Four Pinhole Collimators for Small Animal Studies," *J. Nucl. Med.*, Vol. 36(12), pp. 2282-2287, 1995.

[59] C. Scherfler, E. Donnemiller, M. Schocke, K. Dierkes, C. Decristoforo, M. Oberladstätter, C. Kolbitsch, F. Zschiegner, G. Riccabona, W. Poewe, and G. Wenning, "Evaluation of Striatal Dopamine Transporter Function in Rats by in Vivo β-[^{123}I]CIT Pinhole SPECT," NeuroImage, Vol. 17, pp. 128–141, 2002.

[60] F. J. Beekman, D. P. McElroy, F. Berger S. S. Gambhir, E. J. Hoffman, and S. R. Cherry, "Towards in vivo nuclear microscopy: iodine-125 imaging in mice using micro-pinholes," *Eur. J. Nucl. Med.*, Vol. 29(7), pp. 933-938, 2002.

[61] J. Booij, K. de Bruin, M. M. L. de Win, C. L. Lavini, G. J. den Heeten, J. B. A. Habraken, "Imaging of striatal dopamine transporters in rat brain with single pinhole SPECT and co-aligned MRI is highly reproducible," *Nucl. Med. and Biol.*, Vol. 30, pp. 643-649, 2003.

[62] E. Lauwers, "Development of New Animal Models for Parkinson's Disease based on Vector-mediated Overexpression of α-synuclein," Ph.D. thesis, Katholieke Universiteit Leuven, Belgium, 2004.

[63] E. Lauwers, Z. Debyser, J. Van Dorpe,B. De Strooper, B. Nuttin, V. Baekelandt, "Neuropathology and neurodegeneration in rodent brain induced by lentiviral vector-mediated overexpression of α-synuclein," *Brain Pathol.*, Vol. 13(3), pp. 364–372, 2003.

[64] K. Baete, J. Nuyts, K. Van Laere, W. Van Paesschen, S. Ceyssens, L. De Ceuninck, O. Gheysens, A. Kelles, J. Van den Eynden, P. Suetens, and P. Dupont, "Evaluation of anatomy based reconstruction for partial volume correction in brain FDG-PET," *NeuroImage*, Vol. 23(1), pp. 305–317, 2004.

[65] K. Baete, J. Nuyts, W. Van Paesschen, P. Suetens, and P. Dupont, "Anatomical based FDG-PET reconstruction for the detection of hypo-metabolic regions in epilepsy," *IEEE Trans. Med. Imag.*, Vol. 23(4), pp. 510–519, 2004.

[66] J. Nuyts, K. Baete, D. Bequé, and P. Dupont, "Comparison between MAP and post-processed ML for image reconstruction in emission tomography when anatomical knowledge is available," Submitted to *IEEE Trans. Med. Imag.*